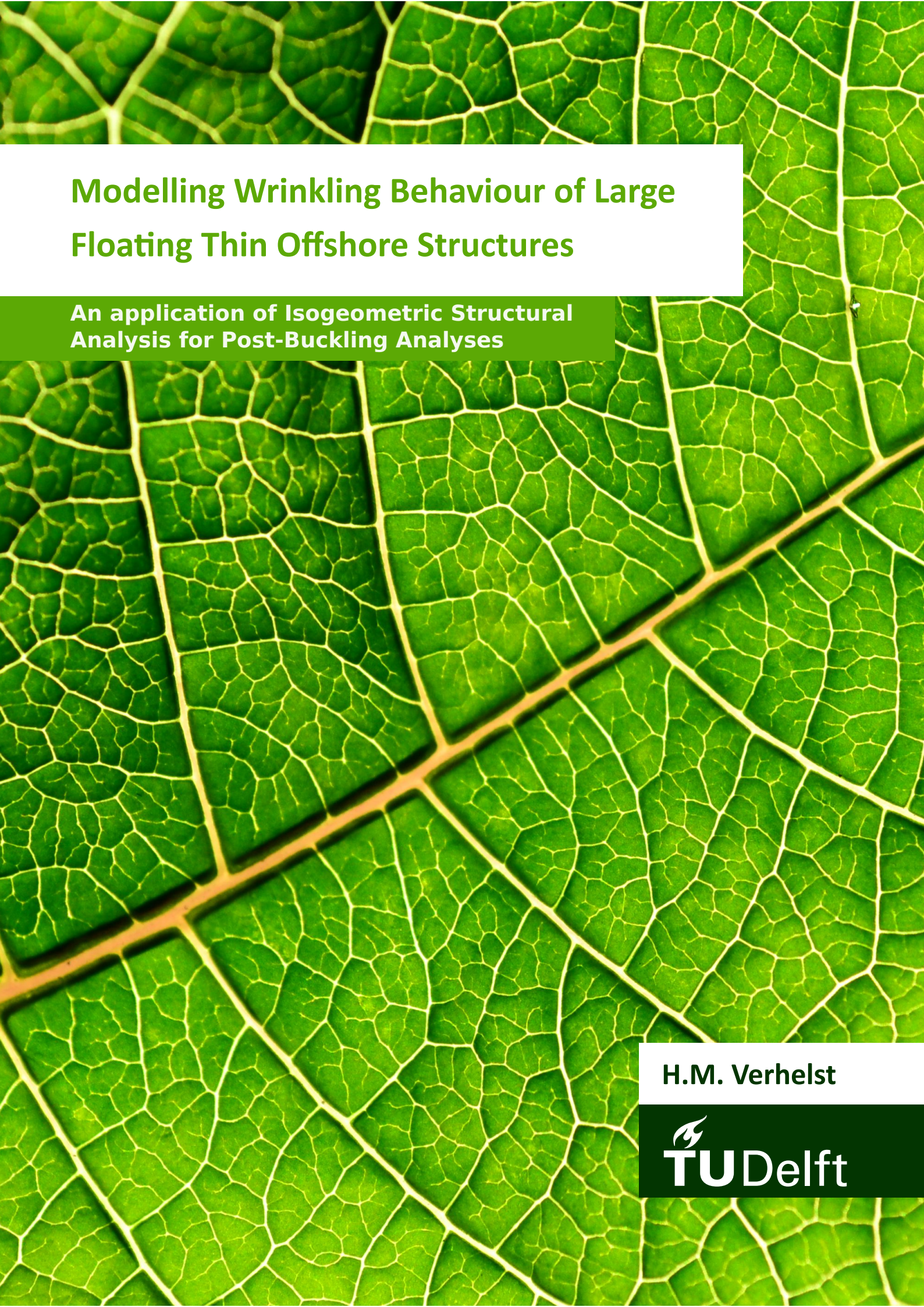

Modelling Wrinkling Behaviour of Large Floating Thin Offshore Structures

An application of Isogeometric Structural Analysis for Post-Buckling Analyses

H.M. Verhelst

TU Delft

Modelling Wrinkling Behaviour of Large Floating Thin Structures

An Application of Isogeometric Structural Analysis and Arc-Length Methods

H.M. (Hugo) Verhelst

to obtain the degrees of,
Master of Science in Marine Technology,
Master of Science in Applied Mathematics,
at the Delft University of Technology,
to be defended publicly on Monday July 22, 2019 at 13:30.

Examination committee:
Prof. Dr. ir. M.L. Kaminski,
Full professor Ship and Offshore Structures, TU Delft
Prof. Dr. R.R. Negenborn,
Full professor Multi-Machine Operations and Logistics, TU Delft
Dr. ir. F.J. Vermolen,
Associate professor Numerical Analysis, TU Delft
Dr. ir. H.M. Schuttelaars,
Associate professor Mathematical Physics, TU Delft
Dr. ir. J.H. den Besten,
Assistant professor Ship and Offshore Structures, TU Delft
Dr. ir. M. Möller,
Assistant professor Numerical Analysis, TU Delft

The leaf on the cover of this thesis forms a thin structure where reinforcement and distribution of energy are provided by nerves. As leafs possibly float on the water surface (e.g. water lilies), leafs are a perfect example of floating solar energy generation. Image from Wikipedia.

Preface

This thesis on modelling wrinkling behaviour of offshore solar platforms has been written as parts of the Master of Science degrees in Applied Mathematics and Marine Technology at the Delft University of Technology. The research was performed under the supervision of Prof. Dr. Ir. Mirek Kaminski and Dr. Ir. Henk den Besten for the Marine Technology part and under supervision of Dr. Ir. Fred Vermolen and Dr. rer.nat Matthias Möller for the Applied Mathematics part. On page iii, a reading guide for people with backgrounds in Applied Mathematics, Marine Technology or other fields of the engineering sciences is provided.

During one year of research for this thesis, the scope of the work changed from Fluid-Structure Interaction modelling of offshore solar platforms in waves towards modelling of wrinkling in floating offshore platforms. Peer discussions, seminars but also questions as '*Hugo, what are you actually doing in one year of MSc. thesis?*' all contributed to the scope of the present research and the scope of the suggested further research.
First and foremost, I would like to thank my supervisors Fred, Henk, Matthias and Mirek. Fred, you taught me three courses in numerical analysis, where I really enjoyed your analytical point of view on numerics, your humour and your high level of improvization. Henk, we spent some time discussing physics but also numerics and I really appreciate the time, effort and great precision you put in discussions and about my work. Matthias, you convinced me to work in `G+smo`; providing a very steep learning curve in `C++`, but also as great contacts in the community and nice conversations in our weekly meeting. Mirek, thanks a lot for inspiring and encouraging me to study the various topics I enjoyed in my years at TU Delft and thanks for numerous opportunities you provided me to enrich myself even further. Last but not least, I want to thank my two external committee members Dr. Ir. Henk Schuttelaars and Prof. Dr. Rudy Negenborn who both thoroughly read and discussed this work to guarantee its quality.

Besides my graduation committee, I would like to thank Sebastian Schreier for the time and effort he put in having discussions about offshore solar platforms, for reviewing the proposal I wrote as part of my Honours Programme Master and for involving me in the process of writing a proposal. Additionally, I would like to thank from our department, Ido Akkerman, Reinier Bos, Marco ten Eijkelder and Carey Walters for in-depth conversations and inspiration related to this thesis. Special thanks go to Martin van der Eijk for proof-reading parts of this thesis. Furthermore, lots of appreciation goes to Angelos Mantzaflaris (INRIA) for his support in `G+smo`. Additionally, I thank Roel Tielen (TU Delft) for nice chats and helping me out with `G+smo` in the very beginning, Alexander Shamanskiy (TU Kaiserslautern) for his support related to mesh deformation and the elasticity module and Florian Beiser (TU München) for his thoughts on adaptive refinement using THB-splines.

Furthermore, I want to thank my family and friends in Delft and anywhere else for providing me support, humour, coffee/lunch/diner-breaks or drinks and simple questions with very hard answers. I think it is essential to thank my love Lonneke, for being my greatest support and my oasis of rest, for her questions and interest in the mathematics and physics I have been dealing with but which were new to her and finally for proofreading parts of this thesis. Not only as a token of politeness, but also as a sign of my deepest appreciation and love, I would lastly like to thank my parents and my brothers for their support, inspiration, questions and answers during my six years in Delft.

Delft, July 2019 Hugo Verhelst

Reading Guide

This thesis is a final work for the Masters Programmes in Applied Mathematics (Computational Science and Engineering) and Marine Technology (Ship and Offshore Structures) at Delft University of Technology. These two programmes will both be finished based on the assessment of this final work, under the regulations of the Double Degree for Master Programmes at the Delft University of Technology. To facilitate the neutral, honest and to-the-point assessment of both programmes, a reading guide is an obligatory part of this thesis.

For those with a strong interest and background in *Applied Mathematics*, the following chapters are advised:

Chapter 1 Introduction The introduction of this thesis defining motivation, the main question and main goals of this research.

Chapter 2 Literature Review The literature study of this research, mainly for the part about Isogeometric Analysis for Structural Mechanics.

Chapter 3 Structural Model This is the mathematical heart of the model that is used and developed in this research. The chapter uses the basics of differential geometry (introduced in Section 3.1) and principles from linear algebra and vector and tensor algebra. Reference works to the relevant topics are cited in the chapter.

Chapter 4 Isogeometric Structural Analysis This chapter covers the routines from computational structural mechanics that are used in this work. Basically, the chapter describes how static, modal, (post-)buckling and dynamic problems are solved given a formulation of the (tangential) stiffness matrix, the mass and damping matrices and load and residual vectors.

Chapter 5 Benchmark Problems Benchmarks to the structural analysis routines are presented in this chapter. Hence, models are verified in this chapter and performance is assessed.

Chapter 7 Conclusions and Chapter 8 Further Research These chapters are advised as they answer, reflect on and provide future insights on the main question and main goals of this research.

Appendices A to D These appendices support the relevant chapters.

For those with a strong interest and background in *Marine Technology*, the following chapters are advised:

Chapter 1 Introduction The introduction of this thesis defining motivation, the main question and main goals of this research'.

Chapter 2 Literature Review The literature study of this research, mainly for the part about the Response of Very Large Floating Structures (VLFSs) in Waves and on the Wrinkling of Thin Sheets.

Chapter 4 Isogeometric Structural Analysis This chapter covers the routines from computational structural mechanics that are used in this work. Basically, the chapter describes how static, modal, (post-)buckling and dynamic problems are solved given a formulation of the (tangential) stiffness matrix, the mass and damping matrices and load and residual vectors.

Chapter 5 Benchmark Problems Benchmarks to the structural analysis routines are presented in this chapter. Hence, models are verified in this chapter and performance is assessed.

Chapter 6 Application: Wrinkling of Thin Sheets In this chapter, the mathematical model is applied to a few case studies to showcase the model on cases where wrinkling of thin sheets occurs. This chapter also provides design considerations for the design of floating solar platforms and some conclusions on the applicability of the present model on these designs.

Chapter 7 Conclusions and Chapter 8 Further Research These chapters are advised as they answer, reflect on and provide future insights on the main question and main goals of this research.

Appendices C to E These appendices support the relevant chapters.

For those with a strong interest and background in *Engineering Sciences*, chapters related to Marine Technology are advised. However, as the text is written for people with backgrounds in structural mechanics, in particular, the reader should consult reference works that are cited in the chapters.

Contents

Abstract

With increasing attention to climate change, renewable energy generation has become a major topic for research and development. Wind and solar energy are generated on land, whereas wave, wind and tidal energy generators are getting attention in the offshore domain. A novel extension of onshore solar energy is the concept of offshore solar energy using floating platforms. As little research has been performed on the concept of offshore solar energy generations, main challenges in the field are related to consequences to the marine ecology, economics and production and structural design of the platforms. In this thesis, a numerical model to assess wrinkling behaviour of thin, floating sheets with application to the structural design of offshore solar platforms is developed.

Since wrinkling of thin sheets, in general, is initiated by a structural instability (i.e. buckling), the developed model consists of an arc-length method that is capable to deal with bifurcation points and to switch to bifurcation branches. In this way, buckling and post-buckling behaviour of thin sheets are modelled and wrinkled shapes can be assessed without imposing *a priori* defined unbalancing imperfections or loads. The computational model is developed using a shell discretization with Isogeometric rotation-free Kirchhoff-Love elements, which are higher-order elements with a B-spline or NURBS basis with global support and global higher-order continuity of the solution. For the illustrative purpose and future use, a similar Euler-Bernoulli beam model was developed and numerical solvers for static, dynamic, modal and linear buckling analysis were implemented.

The model was verified using various benchmark studies for static, modal, (post-)buckling and dynamic analysis. In particular, the post-buckling solver was assessed by modelling the collapse of a spherical roof and using (post-)bucking of a cantilever strip. Both benchmarks have shown excellent agreement with previous publications. Additional verification was done on the approaching accuracy and prediction of bifurcation points. It was found that this accuracy showed the accurate prediction of the bifurcation point.

Additionally, the model was applied to three cases where wrinkling is involved. In these cases, sheets with low bending stiffness were modelled such that their post-buckling shapes show multiple half-waves and thus wrinkles. Based on the model of a floating sheet subject to surface traction (e.g. wind or current), design parameters were varied. From this case, it follows a decrease in foundation stiffness or an increase in flexural rigidity (either by varying Young's modulus or thickness) implies the number of wrinkles to decrease and the wrinkling instability to occur for lower loads. Thirdly, based on the wrinkling geometries of a quarter disk, design consideration for Very Large Floating Thin Structures (VLFTSs) for offshore solar energy generation were given. These are: (i) adding reinforcement to arrest wrinkles and to introduce structural hierarchy for structural reliability; (ii) consider the effect of different mooring system connections to the (reinforced) platform; and (iii) investigate the effect of holes and point loads on local wrinkling behaviour.

Based on the results of the study, it is concluded that the isogeometric thin shell formulation is suitable for different structural analyses and that in particular that robustness and accuracy on a per-degree of freedom basis is observed in the isogeometric post-buckling analysis. This adds post-buckling analysis to the seamless integration of Computer Aided Design (CAD) and Analysis of Isogeometric Analysis. Suggestions for further studies include several improvements of the current implementation (patch coupling, boundary condition implementation), utilization of nonlinear material models for modelling of rubber-like materials, adaptive re-meshing using THB-splines to capture local wrinkling phenomena and Fluid-Structure Interaction computations with a nonlinear structural and fluid description of VLFTS in large waves.

Notations

In this thesis, derivations in various mathematical fields are given. It is expected that the reader is familiar with basic concepts in the fields of *vector calculus* and *linear algebra*. Symbols used in the derivations are consistently defined in the text. The following notations related to matrices, vectors and tensors are adopted in this work:

Scalar	$x \in \mathbb{R}$	
Vector	$\mathbf{x} \in \mathbb{R}^{m \times 1}$	$\begin{bmatrix} x_1 \\ x_2 \\ \vdots \\ x_m \end{bmatrix}$
Matrix	$\mathrm{X} \in \mathbb{R}^{m \times n}$	$\begin{bmatrix} X_{11} & \dots & X_{n1} \\ \vdots & \ddots & \vdots \\ X_{m1} & \dots & X_{mn} \end{bmatrix}$
Second-order tensor	$\underline{\underline{\boldsymbol{X}}} \in \mathbb{R}^{m \times n}$	$\underline{\underline{\boldsymbol{X}}} = \begin{bmatrix} X_{11} & X_{12} \\ X_{21} & X_{22} \end{bmatrix}$
Voight notation for 2×2 tensor	$\underline{\underline{\boldsymbol{X}}} \in \mathbb{R}^{2 \times 2}$	$\underline{\underline{\boldsymbol{X}}} = \begin{bmatrix} X_{11} \\ X_{22} \\ X_{12} \end{bmatrix}$
Fourth-order tensor	$\mathcal{X} \in \mathbb{R}^{m \times n \times o \times p}$	
Vector inner-product	$\mathbf{x} \cdot \mathbf{y}$, $\mathbf{x}^T \mathbf{y}$	$\begin{bmatrix} x_1 & \dots & x_n \end{bmatrix} \begin{bmatrix} y_1 \\ \dots \\ y_n \end{bmatrix} = \sum_{j=1}^{n} x_j y_j$
Matrix-vector product	$\mathrm{X}\mathbf{y}$	$\begin{bmatrix} X_{11} & \dots & X_{1n} \\ \vdots & \ddots & \vdots \\ X_{m1} & \dots & X_{mn} \end{bmatrix} \begin{bmatrix} y_1 \\ \dots \\ y_n \end{bmatrix} = \begin{bmatrix} \sum_{j=1}^{n} X_{1j} y_j \\ \dots \\ \sum_{j=1}^{n} X_{mj} y_j \end{bmatrix}$
Double contraction of second-order tensors	$\underline{\underline{\boldsymbol{X}}} : \underline{\underline{\boldsymbol{Y}}}$	$\begin{bmatrix} X_{11} & \dots & X_{1n} \\ \vdots & \ddots & \vdots \\ X_{m1} & \dots & X_{mn} \end{bmatrix} : \begin{bmatrix} Y_{11} & \dots & Y_{1n} \\ \vdots & \ddots & \vdots \\ Y_{m1} & \dots & Y_{mn} \end{bmatrix} = \sum_{i=1}^{m} \sum_{j=1}^{n} X_{ij} Y_{ij}$
Kronecker product for second-order tensors	$\underline{\underline{\boldsymbol{X}}} \otimes \underline{\underline{\boldsymbol{Y}}}$	$\begin{bmatrix} X_{11} & \dots & X_{1n} \\ \vdots & \ddots & \vdots \\ X_{m1} & \dots & X_{mn} \end{bmatrix} \otimes \begin{bmatrix} Y_{11} & \dots & Y_{1n} \\ \vdots & \ddots & \vdots \\ Y_{m1} & \dots & Y_{mn} \end{bmatrix} = \begin{bmatrix} X_{11}\underline{\underline{\boldsymbol{Y}}} & \dots & X_{1n}\underline{\underline{\boldsymbol{Y}}} \\ \vdots & \ddots & \vdots \\ X_{m1}\underline{\underline{\boldsymbol{Y}}} & \dots & X_{mn}\underline{\underline{\boldsymbol{Y}}} \end{bmatrix}$
Hadamard or Schur product	$\mathbf{x} \circ \mathbf{y}$	$\begin{bmatrix} x_1 \\ \vdots \\ x_m \end{bmatrix} \circ \begin{bmatrix} y_1 \\ \vdots \\ y_m \end{bmatrix} = \begin{bmatrix} x_1 y_1 \\ \vdots \\ x_m y_m \end{bmatrix}$

List of Abbreviations

(T)HB Spline (Truncated) Hierarchical B-spline

CAD Computer-Aided Design

DIRK Diagonally Implicit Runge-Kutta

ERK Explicit Runge-Kutta

ESDIRK Explicit first stage Singly Diagonally Implicit Runge-Kutta

EVA Ethylene-Venyl Acetate

FEA Finite Element Analysis

FEM Finite Element Method

FSI Fluid-Structure Interaction

IGA Isogeometric Analysis

NURBS Non-Uniform Rational B-Spline

PDE Partial Differential Equation

PV Photovoltaics (i.e. solar panels)

RK Runge-Kutta

SDIRK Singly Diagonally Implicit Runge-Kutta

VLFSs Very Large Floating Structures

VLFTSs Very Large Floating Thin Structures

1 | Introduction

The attention for climate change and its effect on societies rapidly increased over the past decade. As a consequence, worldwide political debate and investments changed towards renewable energies, letting the fossil fuels behind. With the Paris Agreement [1] - ratified by 180 states and signed by 197 states - members agree that the increase in global average temperature should stay below 2°C above pre-industrial levels and persuading efforts to limit the increase to 1.5°C above pre-industrial levels. As an addition, the submitted contribution of the European Union to the agreement states that the greenhouse gas emissions should be cut by 40% in 2030 and with long-term goal 80-95% before 2050, all compared to the year 1990 [2].

In the run for cleaner energies to reduce greenhouse gas emissions, different offshore energy generation concepts have been developed. Especially in Europe, offshore wind energy is providing sustainable energy for countries as Great Britain, The Netherlands, Germany and Denmark. Furthermore, investigations on wave and tidal energies are ongoing [3]. Additionally, on-land photovoltaics (PV), i.e. solar panels, appear on rooftops and land, providing societies solar-generated energy. A novel idea for the expansion of solar energy on land is offshore solar energy generation. Research on the potential and practicalities of this novel energy source is however limited. This work is a contribution to the structural analysis of a flexible offshore structure to be used as a solar energy platform. Before going into details on the specific goals and the outline of the thesis, which are given in Section 1.2 and Section 1.3, respectively, an introduction to offshore energy solutions is given in Section 1.1. Although this thesis is not a motivation for offshore solar energy, the following section illustrates a *quick and dirty* line of reasoning for offshore solar energy as an alternative to offshore wind and wave energy.

1.1 Offshore Solar Energy: A Motivation

In this section, a brief motivation for the use of offshore solar energy compared to other renewable offshore energy alternatives is provided. Current renewable offshore energy alternatives include fixed/floating wind turbines, wave energy converters and tidal energy converters.

In the past years, the attention for offshore energy generation using *wind turbines* increased. According to the data of the Global Wind Energy Council, 4.5 $[GW]$ of offshore wind capacity was installed in the year 2018, contributing to a total global capacity of 23.1 $[GW]$ offshore. Key players in the offshore wind market are the United Kingdom (34% of the total, 29% of newly installed), Germany (28% of the total, 22% of new) and China (20% of the total, 40% of new) [9]. These wind turbines are all located in shallow waters with depths around 20 $[m]$ [10]. For water bodies with significant water depths (> 50 $[m]$[11]), floating wind turbines form an alternative for the large supports of bottom-founded turbines. However, floating turbines are less developed compared to the bottom-founded wind turbines. Future work needs to be done on mooring system design and testing [3]. As stated in the reviews by Pisacane et al. [12] and Soukissian et al. [13], current and future research and development on floating wind turbines are expected to have a large impact on the utilization of offshore wind energy in deeper seas such as the Mediterranean Sea.

An alternative to floating wind turbines is *wave energy*. The principle of wave energy is to extract the energy that is contained in a standing wave and transform it into electrical energy. Most wave energy converters discussed in literature operate in shallow waters [14, 15] but the potential in deep waters (i.e. along the Scandinavian coast [16] or the Brazilian coast [17]) allows for utilization of wave farms in the order of hundreds of megawatts up to tenths of gigawatts. Kalogeri et al. [5] investigates a combined wind and wave energy farm which is optimized

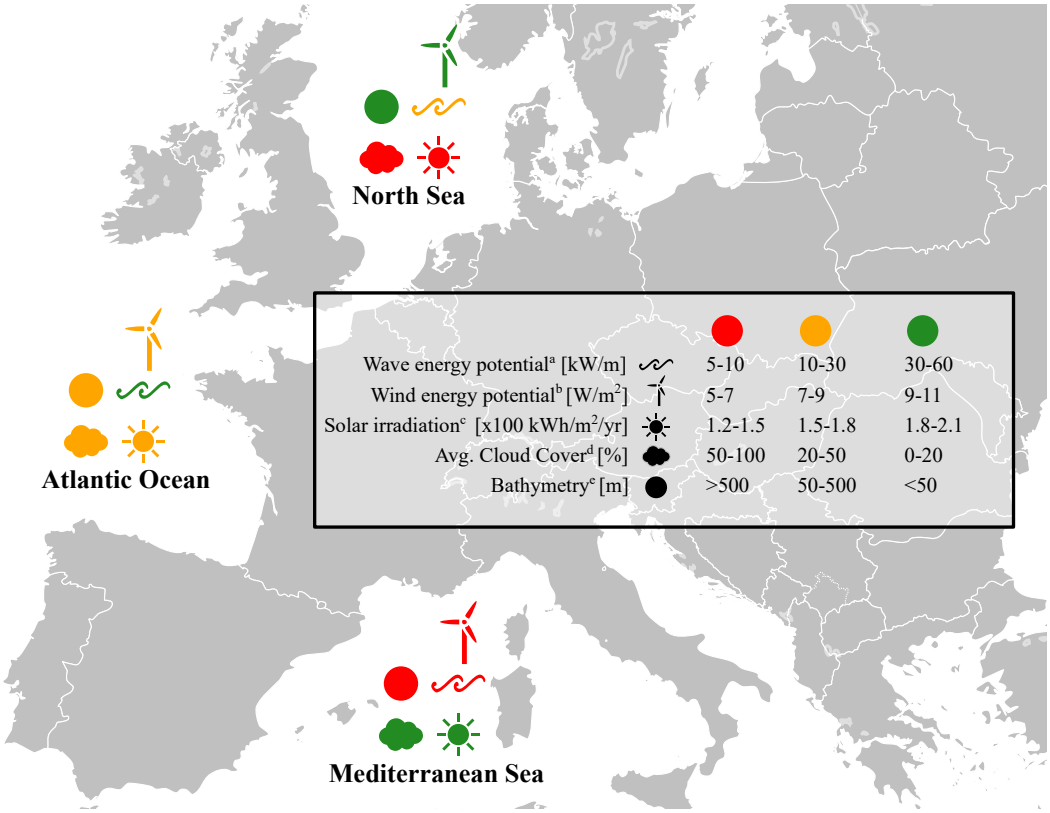

Figure 1.1: Map of the North Sea, Atlantic and Mediterranean coasts of Europe. In the map, the wave energy potential in $[W/m^2]$, the wind energy potential in $[kW/m]$, the solar radiation in $[100kWh/m^2/yr]$, the average cloud cover in [%] and the bathymetry in $[m]$ are depicted in a qualitative way. Data on tidal energy is not included since this is mostly concentrated in the United Kingdom and the English Channel only [4]. Refs a and b) Kalogeri et al. [5], c) Huld et al. [6], d) Meerkötter et al. [7] and e) data from EMODNET [8].

for a constant energy output from these two variable energy resources. Furthermore, Kalogeri et al. shows that along the coast of North-Western Europe, the potential for wind and/or wave energy is the highest and that mainly the wave energy potential decreases for waters where the fetch length is low (i.e. the Mediterranean area). However, as mentioned by Lavidas [18] and Arena et al. [19], the low variability of waves due to the basin-shape of the Mediterranean sea allows for smaller wave energy converters and relatively constant power output compared to the Atlantic coast for instance, although the wave energy potential is substantially lower.

Besides wave and wind energy, *tidal energy* are a nearshore and offshore energy resource that is mainly investigated in the North-Western states of the European Union [20]. Within the concept of tidal energy, two methods for power generation are identified. On the one hand, tidal barrages are used to subtract tidal energy from tidal amplitude differences and tidal turbines are used to generate tidal energy based on tidal currents. One of the benefits of tidal energy compared to wave and wind energy is that power output is highly predictable, as tides are least influenced by other environmental factors [21]. As seen from the number of concepts, current power generation and R&D budgets [20] and as seen from the results of Campbell et al. [4], Guillou et al. [22] and Segura et al. [23], tidal energy has high potential in the estuaries in the United Kingdom and the English Channel. On the contrary, Pisacane et al. [12] and Soukissian et al. [13] mention that research on tidal energy in the Mediterranean sea is very limited, but that the potential of tidal energy is considered low based on the low tidal currents in the Mediterranean sea.

Another possible offshore energy resource is *solar energy* as a novel extension of the land-based solar energy generation (i.e. photovoltaics (PV)). Offshore solar energy is mainly beneficial in areas where the wind and wave energy potential is relatively low but where cloud cover and solar irradiance is particularly high [24, 7], e.g.

in basins such as the Mediterranean area or near islands. Additionally, floating PV has the advantage that the panels are cooled by the sea water, achieving good efficiencies of the panels [25, 26]. However, the motions and possible deformation of the offshore solar platform due to waves require flexible solar panels or hinged modules and advanced tracking systems [27]. Similar to floating wind turbines and wave energy converters, floating solar platforms require a mooring system which becomes more complicated as depths increase.

To assess the possibility and advantages of offshore solar energy, potentially annual power generation is to be computed and compared with other offshore energy concepts in different regions. As this is not within the scope of this project, Figure 1.1 provides a *qualitative comparison* for the wave and wind energy potentials, solar radiation and cloud cover and the bathymetry for the North Sea area, the European Atlantic Coast and the Mediterranean Area, based on different literature resources [5, 6, 8, 7]. Data about tidal energy was not included since the success of this technology is highly location dependent and mainly concentrated in the United Kingdom and the English Channel. It should be noted that computation of the offshore solar energy potential has not been done yet, but that the work of Huld et al. [6] can be used to compute the solar energy potential, including the effects of for instance air temperature and wind speeds in the future.

As seen in Figure 1.1, relatively high solar radiation and low cloud cover are observed in the Mediterranean sea. Additionally, due to the basin-shape of this sea, the wind and wave energy potentials are relatively low. Hence, the combination of these factors in the Mediterranean sea motivate for more research and development for floating offshore solar energy generation. Furthermore, it can also be seen that high wind energy potential combined with the shallow water clarifies the observation of Gao et al. [3] of the large development in offshore wind on the North Sea.

A recently published paper by Patterson et al. [28] considers the use of large flexible circular floating platforms for offshore solar energy generation for offshore synthetic fuel production. As mentioned in this paper, water on deck and slamming loads can be minimized by designing a structure that follows the waves up to a large extent. However, a detailed design for the structure was not provided, leaving open challenges for *structural design and analysis* and *installation and maintenance* of the platform. Another challenge for offshore solar energy generation is related to *economics and the business model*, i.e. if offshore solar energy should be used for fuel production or for direct power supply to coastal regions and the projected costs. Lastly, a point that is not addressed by Patterson et al. [28] but which is considered important by the author of this thesis is the effect of offshore solar platforms on the *marine ecosystem* as it blocks sunlight on the ocean surface but could provide shelter for animals. In the next section, the goal of this thesis related to structural design and analysis of offshore solar platforms is presented.

1.2 Thesis Goal

Inspired by the idea of offshore solar energy generation, this thesis considers the structural analysis of large floating thin offshore structures. More specifically, a numerical model is applied to study static, quasi-static and dynamic characteristics of floating thin offshore structures. Without giving full detailed specifications for the platform, the working characteristics of the platform that are adopted including their motivation are listed below:

Circular & Large scale To generate a future-proof framework for the analysis of such structures, it is assumed that the structure that is considered is very large, i.e. the surface area is of order $\mathcal{O}\left(km^2\right)$. The platforms considered by Kashiwagi[29] amongst others, are of similar size and are referred to as Very Large Floating Structures (VLFSs). With this assumption, it is reasonable that current and wind speeds are non-uniform and have different direction over the whole platform. Furthermore, it is assumed that the in-plane characteristic length of the platform is larger than the wavelengths exciting the platform. The geometry of the platform is considered to be circular, but analyses can be performed for other geometries without loss of generality.

Continuum As concept designs are not yet available, it is assumed that the platform is a continuum. In other words, the platform does not consist of modules, but rather can be seen as a *continuous structure* without

hinges. This assumption is made since hinge forces are expected to be large[1]. Structures that have local stiffening or holes are not considered in the present study.

Low Payload: Lightweight Structure The main task of the platform is to carry the PV modules. Hence the payload of the platform is several kilograms per square metre (kg/m^2). Hence, the payload of the platform is characterized to be low compared to other offshore structures. This allows for a relatively light-weight structure to carry the panels.

Flexible As briefly motivated by Patterson et al. [28], flexible structures allow to follow waves to a large extent and thus minimise water on deck and slamming loads. Therefore, the bending stiffness of the structure is considered to be low and hence structural response is governed by both bending and membrane stiffness.

Based on the platform characteristics, a numerical model for Very Large Floating Thin Structures (VLFTSs) is developed in this research, ultimately to be applied to the analysis of offshore solar platforms. Because the platform is assumed to be thin and floating on a fluid, the phenomena of *wrinkling* (i.e. formation of multiple half-waves as a result of structural instability) is expected to occur for (combinations of) in-plane loads on the platform. Based on similarities with the physics of wrinkling for thin sheets and the use of a state-of-the-art numerical modelling technique *isogeometric analysis*, a numerical mathematical is developed that to model the wrinkling phenomenon and support structural design and analysis of VLFTSs for offshore solar energy generation. Hence, the main question of this research is:

> *How can wrinkling formation of floating thin structures be numerically modelled with Isogeometric Analysis?*

Separating the development and application of the model, this thesis is based on two goals. The first goal, focussing on the development of the nonlinear shell model for wrinkling of thin sheets, reads:

> *Develop a geometrically nonlinear shell model based on Kirchhoff-Love shell theory and Isogeometric Analysis for post-buckling analysis.*

Whereas the second goal, based on applications of the mathematical model in structural analysis and on wrinkling patterns of (floating) thin sheets, is:

> *Apply the Isogeometric shell model on common structural analysis computations, and in particular on post-buckling computations of wrinkling formation in floating sheets.*

Moreover, in order to achieve the goal of this thesis, a number of subgoals are defined. They are described as follows:

1. *Identify governing equations for the structural model of a floating thin sheet and motivate the assumptions.* To facilitate a background for the reader and to clarify limits of certain models, the governing equations structural behaviour will be derived.

2. *Discuss the use of Isogeometric Analysis and apply it in the model problem.* Isogeometric Analysis is a method that is similar to the Finite Element Method (FEM) to solve Partial Differential Equations (PDEs). This method, its applications and its (dis)advantages compared to the FEM are of importance to the justification of the final model.

3. *Develop and implement different structural analyses in the Isogeometric structural model and discuss their use on the model problem.* Using the Isogeometric structural model, different structural analysis (e.g. static, dynamic, buckling) can be performed using computational mechanics procedures used in FEM. Although post-buckling analysis will only be used in wrinkling analyses in this study, the other structural analyses are of interest because they can be used in further studies. For instance, dynamic analysis relates with Fluid-Structure Interaction (FSI) and modal analysis can be used to assess the eigenfrequencies and mode shapes of VLFTSs with respect to different wave frequencies.

[1] Waals presented hinge loads of the concept of the H2020 project SPACE@SEA in March 2018 at MARIN's "The Floating Future Seminar". For their platform with interconnected triangles of sides with dimension 100m, hinge loads of 20,000t were measured in waves with $H_s = 15.5m$. [30]

4. *Verify the model using benchmark cases and discuss improvements of (parts of) the model.* The performance of the present structural model will be assessed based on available benchmark results from the literature. Based on these verifications, the model can be justified for further application.

5. *Apply the present model on the problem of wrinkling formation of thin sheets and discuss relevant physical parameters.* Based on the characteristics of the offshore solar platform, a case-study of a floating thin sheet can be defined. Based on this case study, the effect of different design parameters (e.g. stiffness, length scales) can be investigated and compared to known results from the literature.

6. *Give design considerations and model improvements for membrane-like structures in the ocean environment.* Based on the findings related to the previous subgoal, the last subgoal relates to design considerations of VLFTSs in the ocean environment from wrinkling perspective. Additionally, model improvements could be provided which will enhance in future research.

Subgoals 1 and 2 mainly correspond to the first objective (mathematical model development), subgoals 3 and 4 correspond to both objectives and subgoal 5 and 6 correspond to the second objective of this work (applications on wrinkling of sheets). The conclusions and recommendations at the end of this thesis evaluate on the main goals and main question and provide suggestions for future work.

1.3 Outline

The report is structured as follows. Firstly, in Chapter 2 a *literature review* of the state-of-the-art of research disciplines related to the main goals of this thesis is given. This review includes the topics *response of very large floating structures in waves*, *wrinkling of thin sheets* and *isogeometric structural analysis* and provides background knowledge for subgoals 2, 5 and 6.

After the background is provided in the literature study, Chapters 3 to 5 lay the foundation for the numerical method that is developed and used in this thesis. Chapter 3 presents the justification of the assumptions (subgoal 1), the mathematical derivation and the implementation aspects of the numerical shell models and a beam model for illustrational purposes. This chapter does not make any assumptions for the Isogeometric Analysis framework but covers general implementation aspects and hence relates to subgoal 3 as well. In Chapter 4, the *Isogeometric Analysis* framework is introduced and the different concepts for *computational structural mechanics* are treated, relating this chapter to subgoal 3. Hereafter, Chapter 5 presents results of the present model on different benchmark problems, hence dealing as *verification* (subgoal 4).

The model is applied to cases of floating sheets in Chapter 6. Here, the benchmarked structural model is applied on the phenomenon of wrinkling of thin sheets (subgoal 5), identifying the influence of different design parameters on the wrinkled shapes. Additionally, the chapter presents design considerations for VLFTSs based on the wrinkling perspective, associated with subgoal 6.

Lastly, this thesis finishes with conclusions and recommendations for further research in Chapter 7 and Chapter 8, respectively.

2 | Literature Review

In this chapter, a literature review is presented for topics relating to the present research. Firstly, a brief literature review on past research on Very Large Floating Structures (VLFSs) is presented to identify the state-of-the-art of previously used analysis methods for such structures and to check their applicability on Very Large Floating Thin Structures (VLFTSs). This provides background information related to the sixth subgoal of this thesis. Secondly, the phenomena of wrinkling of thin membranes on substrates or fluid are investigated, relating to subgoal 5 of this thesis. The mechanism of wrinkling of thin membranes is presented and state-of-the-art experimental results, as well as numerical methods, are investigated. Thereafter, the state-of-the-art of Isogeometric Analysis is presented, covering works from 2005 up to 2019. This section mainly emphasises isogeometric structural analysis, but the general philosophy behind IGA, meshing techniques and a comparison between IGA and Finite Element Analysis (FEA) are also presented. These aspects are used to motivate the use of IGA in this research, which relates to the second subgoal of this thesis. The basics of IGA including examples are discussed in Section 4.1. This chapter finishes with concluding remarks where knowledge gaps for the present research are identified.

2.1 The Response of Very Large Floating Structures (VLFSs) in Waves

The available literature on the response of Very Large Floating Structures (VLFSs) is mainly based on structures that have large cross-sections and stiffness and hence have large bending stiffness. The literature on Very Large Floating Thin Structures (VLFTSs) was not found by the time of writing (2019). Therefore, focussing on Very Large Floating Structures, research on their response started with the investigation of a near-shore *floating airport* in Japan in the early 2000s by Kashiwagi et al. [32, 31, 33]. These works cover various methods to compute the response of VLFSs in waves. This includes a modal-expansion method where the pressure integral is computed using a B-spline Galerkin method [32], modelling of an aeroplane landing on a floating membrane structure [33] and a general overview of the research on VLFSs before the 2000s [31].

Additionally, Andrianov [34] developed an analytical model for the response of VLFSs in waves. In this PhD thesis, an extensive summary of existing VLFS projects is given (additionally, one can consult the work of Lamas-Pardo et al. [35] for a more recent review of different concepts of VLFSs). Andrianov provides an overview of the assumptions that are made in the analysis of VLFSs. They are:

- VLFSs are modelled as thin, elastic (isotropic/orthotropic) plates with free edges,
- Potential flow is used as a fluid model,
- The amplitude of the incident wave and the motions of the VLFS are small. Furthermore, the motions of the VLFS are considered in the vertical direction only,
- There is no gap between the VLFS and the water surface, i.e. air entrainment effects are not considered,
- Bathymetry effects are not considered, i.e. the sea bottom is assumed to be flat.

Using these assumptions, an analytical model for the hydroelasticity of VLFSs was developed and applied for different shapes of the VLFS. The response of the VLFS for non-constant bathymetry was studied by Gerostathis et al. [36].

Other studies on the response of VLFSs in waves include the works of Hamamoto [37], Khabakhpasheva and Korobkin [38], Riyansyah et al. [39], Wang and Tay [40] and Wei et al. [41]. Hamamoto [37] uses (wet) modal superposition to obtain the response of a (moored) floating beam subject to wave, wind or earthquake loading. The works of Khabakhpasheva and Korobkin [38] and Riyansyah et al. [39] focus on floating beams with a hinge connection using a coupling of wet mode shapes [38] or using coupling of a Boundary Element Method (BEM) for the fluid problem and the Finite Element Method (FEM) for the beam problem [39]. The coupling of the BEM and the FEM has also been used by Wang and Tay [40] to model the response of a two-dimensional VLFS in waves. The authors used a one-way coupling approach by applying the pressures from the velocity potential of the fluid on the finite element model. Lastly, the work of Wei et al. [41] investigates the hydroelastic response of a VLFS in inhomogeneous waves using a time-domain approach, contrary to the spectral approach by Wang and Tay [40] amongst others.

All studies which are presented in this section have in common that the structural models that are used are *linear* models for beams or plates. Hence, the assumption of small (only vertical) deflections is made. Additionally, the models include the assumption of potential flow (or ideal flow) which implies that the flow is incompressible and irrotational [42], which is reasonably valid for small waves and thus small structural deflections. However, as stressed by Andrianov [34], further research on VLFSs includes modelling of the structure in large waves, modelling the structure with a non-flat hull and modelling of the response for different mooring solutions. Furthermore, Wang and Tay [40] recommend investigating the response of the VLFS due to nonlinear wave impact and analysis using a Navier-Stokes fluid model. Additionally, the recommendations on the use of nonlinear models (especially for the structure) are expected to be even more relevant in the case of Very Large Floating Thin Structures (VLFTSs), as their bending stiffness is low and therefore their response is expected to be significantly determined by nonlinear structural behaviour such as *stretching*.

2.2 Wrinkling of Thin Sheets

Wrinkling is the phenomena of out-of-plane pattern formation in thin sheets subject to in-plane loads. Due to low Young's moduli and low thickness, soft membranes are sensitive to *buckling*, which initiates wrinkling patterns on its turn. In the sequel, buckling will be referred to as a structural instability and *post-buckling* is the behaviour of a structure after it buckled. Both buckling and post-buckling can be seen as types of structural analyses. *Wrinkling* is considered as physical deformation pattern formation and propagation of a thin sheet, and from a structural analysis perspective formed due to structural instability (buckling) and propagating as post-buckling phenomena.

Figure 2.1 and Figure 2.2 show respectively wrinkles in a stretched thin sheet [43] and the wrinkle to fold transition of a sheet on a foundation [44]. In both cases, wrinkles are formed as a buckling instability where the number of wrinkles is determined by a balance between the membrane stiffness and the tensional force (Figure 2.1) or the foundation stiffness (Figure 2.2).

In this section, a review on *experimental* (see Section 2.2.1), *analytical* (see Section 2.2.2) and *numerical* (see Section 2.2.3) analyses of wrinkles of stretched thin sheets or sheets on an elastic foundation (e.g. fluid-supported sheets) is given. A general review on wrinkling of sheets on elastic foundation has been written in 2012 by Li et al. [45]. As shown in this paper, research interests from biological applications (e.g. growth induced wrinkles of *mucosa* which is an organ class that includes airways [46]), inflated membrane applications (e.g. wrinkles in an inflated beach ball studied by Vella et al. [47] and Taffetani and Vella [48]) or fluid-supported nanomaterials (e.g. wrinkles in graphene sheets studied by Androulidakis et al. [49]). Additionally, wrinkling formation as a result of in-plane loads on sheets without elastic foundations is studied in the works of Wong and Pellegrino [50], motivated by the application of solar sails for spacecraft. In ocean or marine engineering, wrinkling is hardly considered as it is irrelevant for structures with high bending stiffness. Instead, structures are often designed far from structural instabilities. [1]. When using sandwich materials, wrinkling is considered as a failure mode of the material itself (see for instance the paper by Hadi [53]).

[1] For references about buckling in general or in marine structures the works of Brush et al. [51] or Hughes et al. [52].

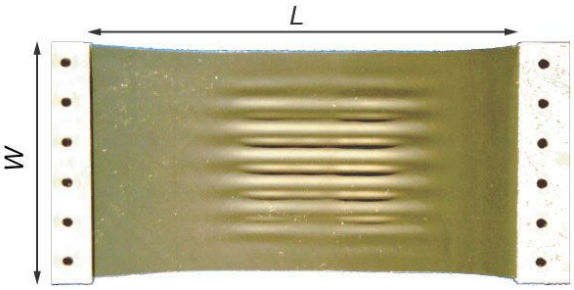

Figure 2.1: Wrinkling due to stretching of a thin sheet. Experiment and image published by Cerda et al. [43].

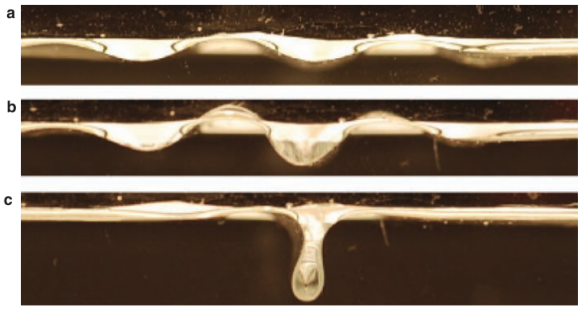

Figure 2.2: Wrinkle to fold transition of a sheet on a substrate. Displacements in compressive direction are applied in increasing order between figures a, b and c. Experiment and image published by Pocivavsek et al. [44].

2.2.1 Phenomena and Experimental Work

Within research on the wrinkling phenomena, two set-ups can be identified, which do not necessarily have to be disjoint as will be illustrated later. In the first place, research has been performed on wrinkling of membranes supported by a fluid or a solid (see Li et al. [45] for a review). This includes the application of fluid-supported nano-materials and the pressurized membranes mentioned earlier. In the second place, research has been performed on wrinkles occurring due to tension of a membrane.

Wrinkling of membranes on a foundation has been studied experimentally by Pocivavsek et al. [44] (see Figure 2.2) and was also elaborated by Cerda and Mahadevan [54]. In the latter paper, the authors note that the foundation stiffness penalises long wavelengths, similar to stretching stiffness. In this paper, the authors considered human skin resting on fat and wrinkles on the skin of an apple, induced by shrinkage of the flesh to assess their scaling laws. Pocivavsek et al. [44] considered wrinkling of membranes supported by a fluid which are compressed (uni-axially). Pocivavsek et al. considered the wrinkle-to-fold transition on different scales by using dimensionless scaling of the potential energy of the foundation (i.e. the hydrostatic contribution of the supporting fluid) as well as dimensionless scaling of the potential energy due to bending of the membrane. In this scaling analysis, it is assumed that the potential energy due to axial compression of the membrane is negligible, i.e. that the membrane is *inextensible*. In the paper by Pocivavsek et al., a formulation for the critical compression for the initiation of wrinkles was also given. Lastly, similar experiments with a thin film between two fluids with different densities and a film with a mass were performed by Jambon-Puillet et al. [55]. These authors identified that the two-fluid situation and contact of the membrane affects wrinkle-to-fold transition and the shape of the final fold.

In the work by Cerda et al. [43], wrinkling of an elastic sheet under tension is experimentally considered (see Figure 2.1). According to the authors, the wrinkles are formed because of lateral contractions in the material due to constraints at boundaries combined with pre-stress of the membrane and they occur when a critical stretching strain (depending in the Poisson ratio) is exceeded. In the work, the authors use the bending and stretching energies in the membrane to derive a scaling law for the wavelength and amplitude of the occurring wrinkles. The physics, which are elaborated further by Cerda and Mahadevan [54] are described by a balance between bending stiffness that penalises short wavelengths and stretching which penalises large amplitudes and hence large wavelengths. The balance between these two effects yields wrinkles of moderate length. For the scaling laws, the reader is referred to the cited publications in this paragraph.

Two different configurations tested by Wong and Pellegrino [50], which are depicted in Figure 2.3a and Figure 2.3. The former case depicts a thin square membrane subjected to two pairs of equal and opposite diagonal forces at the corners and the latter case depicts a rectangular membrane under simple shear. In both cases, the material was linear elastic and isotropic. Clearly, the cases in Figures 2.3 and 2.3a show wrinkles occurring in the sheet. In two other papers by the same authors analytical [56] and numerical solutions [57] to the present case were developed.

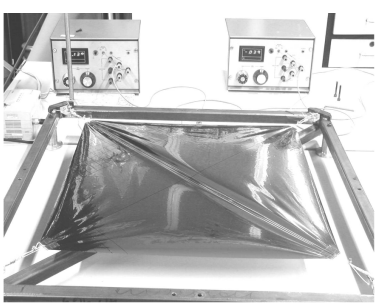

(a) Thin sheet subject to tensional corner loads. The force pair top left and bottom right has 4 times the magnitude of the force pair bottom left and top right.

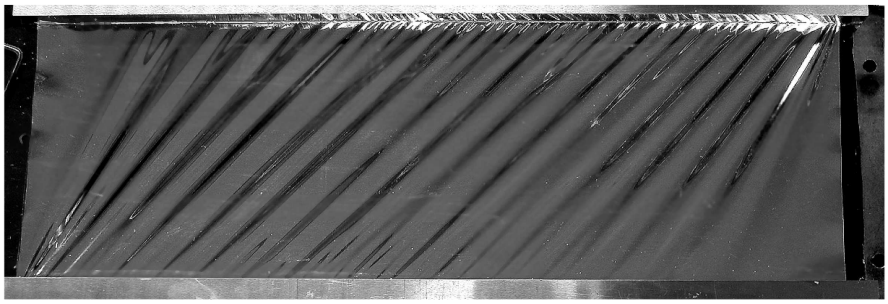

(b) Thin membrane subject to shear. The left and right edges are free, the top edge is displacement controlled and the bottom edge is free.

Figure 2.3: Thin membrane subject to corner loads (left) and thin membrane subject to shear (right). Experiments and figures by Wong and Pellegrino [50].

As discussed in the previous paragraphs, wrinkles occur when a membrane is loaded under tension and exceeds certain tensional stress, or when a membrane supported by a foundation is loaded under compression. As mentioned above, Cerda and Mahadevan [54] mentioned that in both cases, the wrinkle wavelengths and amplitudes are governed by the balance between short and long wavelength penalising quantities, namely the bending stiffness and the stretch or foundation stiffness respectively. For the sequel, it should be noted that the tension and compression wrinkling phenomena are not necessarily distinct. For instance, when considering a membrane on a foundation which is loaded under tension, wrinkles are formed by the balance between bending stiffness, axial stiffness and foundation stiffness.

Recommended further reading material out of the scope of this research includes the work of Evans et al. [58] about the role of elastocapillary effects on buckling, wrinkling and folding instabilities. Also, Wagner [59] looked at elastocapillary and its role in adhesion of thin sheets. Another work for further reading is the work of Wagner and Vella [60] about delamination of elastic sheets resting on fluids. Lastly, the work of Abi Ghanem et al. [61] about experimental and numerical investigation wave impacts on sheets resting on a fluid is an interesting work for further research and reading.

2.2.2 Analytical Mathematical Modelling

Inspired by the work of Cerda et al. [43], Puntel et al. [62] developed a mathematical model for the case of the stretched elastic sheet. The model includes the effects of stretching and the elastic foundation. Furthermore, it provides an analytical expression for a sequence of stretches for which different numbers of wrinkles appear. Additionally, the mathematical model corresponds to the scaling laws for the wavelength and amplitude for the wrinkled configurations observed by Cerda et al. [43] and Cerda and Mahadevan [54].

Based on the experiments of Pocivavsek et al. [44], analytical models for wrinkling and folding behaviour for a floating sheet under compression have been developed. In the works of Diamant and Witten [63] and Rivetti [64] analytical solutions for a floating rod (i.e. a 1D sheet) were given. Diamant and Witten presented a nonlinear ordinary differential equation in terms of an unknown rotation of the rod, corresponding with Euler's *elastica* problem. The analytical solutions given by the authors, however, contained both symmetrical, antisymmetrical and non-symmetrical folds, with similar total energy levels. In the paper by Audoly [65] the work of Diamant and Witten was extended since it was shown that their Ansatz for the solution is optimal. Furthermore, Audoly also showed that the wrinkle-to-fold transition from the experiments of Pocivavsek et al. is an instance of a series of localized buckling. As stressed by Rivetti based on the paper of Diamant and Witten, the unsolved problem remained whether symmetric or antisymmetric folds are formed based on a certain perturbation. In the paper by Rivetti and Neukirch [66], the so-called *mode-branching* (i.e. the localized buckling discussed by

Audoly [65]) was further considered. From this paper, it was clear that this mode-branching route is a process where the shape of the rod alternates between symmetric and anti-symmetric modes, with great dependence on the non-dimensionalized foundation stiffness and compression.

Lastly, Wong and Pellegrino [56] developed analytical solutions for the cases in Wong and Pellegrino [50]. The authors use two-dimensional stress-field analysis to analytically determine bounds on the corner displacement of the case in Figure 2.3a and to estimate the number of wrinkles that will occur in the sheet and in its corners. For the membrane in shear (see Figure 2.3b), they also use stress-field analysis to identify locations where wrinkles occur and subsequently they utilise stress and strain equilibria to obtain an estimate for the wrinkling wavelength and amplitude. For both cases, scaling laws were derived based on the analytical formulations for wrinkle wavelength and amplitude.

2.2.3 Numerical Modelling

Numerical modelling of wrinkles has been done by different authors for different applications. Here, some works amongst others are highlighted, focussing on modelling approaches. Illustrations of the model problems are given as examples for the applications of wrinkling models.

In the papers by Wong et al. [68, 67, 57], numerical simulations for thin membranes in space applications have been performed. In the papers, the results of numerical models have been compared to analytical and experimental solutions (see references [50] and [56], respectively and see Figures 2.3 and 2.3a for the set-up). The numerical approach that has been used by Wong et al. is based on a general procedure for wrinkling computations in a finite element code. This procedure is, in brief, explained by the following steps: (i) Define Finite Element model including boundary conditions and material properties; (ii) Set initial conditions by applying a pre-described stress field to enforce out-of-plane deformations using nonlinear computations; (iii) Apply initial imperfections based on a linear combination of buckling modes of the pre-stressed membrane; (iv) Compute load steps using nonlinear Newton iterations and solve singularities in the time domain using a dynamic analysis. Important to note is that the superposition of the modes as *initial imperfection* is required to obtain wrinkles as magnifications in the forthcoming analysis. Additionally, the authors mention that the stabilization of the dynamic step for wrinkle transition should be low enough to not influence the solution, but high enough to stabilise the iterations. A similar analysis has been performed by Wang et al. [69], but initial forces were used for generation of the buckling mode shape for the initial deformation. Bisagni [70] applied measured initial imperfection to a composite cylinder (not a thin membrane) and performed a dynamic analysis to investigate dynamic buckling loads. These were concluded to be significantly higher than the static buckling load.

Inspired by the experimental work of Cerda et al. [43] (see Figure 2.1), numerical solutions were developed using different material models and considering the effects of Poisson's ratio and geometric ratios [71, 72, 73, 74, 75, 76]. Taylor et al. [73] additionally also considers the experiments of Wong and Pellegrino [50]. Firstly, Nayyar et al. used levels of compressive stresses occurring due to a non-zero Poisson's ratio in the material as a pre-stress for the buckling analysis. The post-buckling analysis is again started by imposing a number of eigenmodes from the buckling analysis as *initial imperfection*, in order to initiate wrinkles. Contrary to the dynamic solution step for singularities (or bifurcation points) used by Wong et al. [67], Nayyar et al. [72] use the arc-length-based Riks method[2]. The findings of their work were that the numerical results corresponded to the experimental results of Cerda and Mahadevan for the wrinkling wavelength, but that the wrinkling amplitude was not monotonically increasing with the applied tensile strain. Additionally, the work of Taylor et al. [73] uses Koiter's nonlinear plate theory combined with the *dynamic relaxation method* to solve the post-buckling phenomena of wrinkle formation. The dynamic relaxation method basically constructs an equilibrium problem into an artificially dynamic system where the mass and damping parameters do not have a physical meaning but are tuning parameters [77]. The results showing excellent agreements with reference results. Although initial imperfections were applied, the authors stress that the solution is not depending on *a priori* assumptions of the wrinkling shape, which is a great advantage. In the work of Sipos and Fehér [74] experiments were performed for different aspect ratios and showed the existence of two packets of wrinkles for large aspect ratios. One of the recommendations based on their findings is to use other material models (e.g. Neo-Hookean and Mooney-Rivlin) for the behaviour of

[2] More information on arc-length methods and singular points will follow later in this work in Section 4.4.

rubber-like sheets. This work was done by Li and Healey [75], Fu et al. [78] and Wang et al. [76]. In the work of Wang et al. [76], a three-dimensional phase-diagram for the characterization of wrinkles, including aspect ratio, dimensionless thickness and strain was developed. Additionally, both Wang et al. [76] and Fu et al. [78] show the influence of the Poisson's ratio on the formation or absence of wrinkles.

As inspired by the experimental work of Pocivavsek et al. [44] (see Figure 2.2), Cao et al. [79] and Ning et al. [80] performed numerical studies of a sheet resting on a foundation. Cao et al. performed a numerical study of an elasto*plastic* film on a soft substrate. In this study, the substrate was modelled as an elastic 'foam' and the film was modelled as a membrane with a certain yield strength. When the applied displacement on the boundaries of the film was above a certain critical value, wrinkles occurred. Additionally, an increase of the displacements resulted in localized creasing. According to the authors, creasing occurred due to plastic deformation of the substrate. Analogous to the creasing definition of creasing of Li et al. [45], the crease is probably formed by formation of a plastic hinge in the wrinkles. Period-doubling folds, however, were not observed in the work of Cao et al.. In the work of Ning et al. [80] a beam model was used to model a rod on an elastic support. The rod was modelled with a non-uniform stiffness distribution. It was observed that on the places where the Young's modulus is lowest, buckling and fold formation occurs.

The two papers by Javili et al. [81] and Dortdivanlioglu et al. [82] consider cases where wrinkles are formed based on bifurcations due to internal growth of materials (i.e. biological membranes) rather than externally applied forces or displacements. They model a growing sheet on an elastic foundation, which has similarities with the case from Pocivavsek et al. [44]. In the first paper by Javili et al., the authors make a distinction between prescribed perturbations and eigenvalue analysis to capture growth-induced instabilities. The former method uses small perturbations in the residual of the Newton iterations such that instabilities occur. However, as stressed by the authors, too small perturbations can cause instabilities not to occur whereas too large perturbations causes 'subjective' perturbations, i.e. perturbations that overwrite the actual solution. The latter method uses the eigenvalues of the stiffness matrix of the system. If one of the eigenvalues becomes negative for a certain growth value, a bi-section or secant method can be used to compute the eigenvalue for which the matrix has a zero eigenvalue and the corresponding eigenvector then corresponds to the instability mode[3]. In the paper of Dortdivanlioglu et al. [82], Isogeometric Analysis (IGA) has been used to model similar growth-induced instabilities. Here, the eigenvalue approach as discussed in the paper of Javili et al. was used. The findings of the paper were that the solutions from IGA were superior to those of FEM. Furthermore, the authors concluded that arc-length methods were to be further discussed for modelling creases and ridges.

2.3 Isogeometric Analysis

Isogeometric Analysis is a computational framework introduced by Hughes et al. [83] in 2005[4] inspired to facilitate seamless integration between Computer Aided Design (CAD) and Finite Element Analysis (FEA). Using CAD geometry representations (e.g. Non-Rational B-Splines (NURBS)) and additional routines for geometry refinement to reduce the computational costs of the meshing procedure required for FEA. Since isogeometric analysis is based on a parametric domain description rather than parametric elements, higher-order continuity properties of the basis functions are found over the complete domain resulting in accuracy and robustness on a degree-of-freedom basis compared to conventional FEA.

Figure 2.4 presents an example of a CAD geometry and analysis based on this geometry is depicted as an example. This figure is taken from Hsu et al. [86], where a bioprosthetic heart valve was parametrically modelled in CAD software and analysed by a Fluid-Structure Interaction solver in the Isogeometric Analysis framework.

In this section, an overview of the progress of isogeometric analysis for structural mechanics will be given. Firstly, focussing on structural analysis, shell, beam and cable models will be investigated and afterwards,

[3] This method relates to the arc-length method which is used later on in this research, see Section 4.4

[4] Later, in 2009, a the first book on Isogeometric Analysis was published by Cottrell et al. [84]. This book is highly recommended as an overview of the basics of IGA and its applications. Additionally, Nguyen et al. [85] published a paper in 2015, which gives a general overview of the state-of-the-art in that time. This paper covers applications, alternative discretizations and notes on computational aspects.

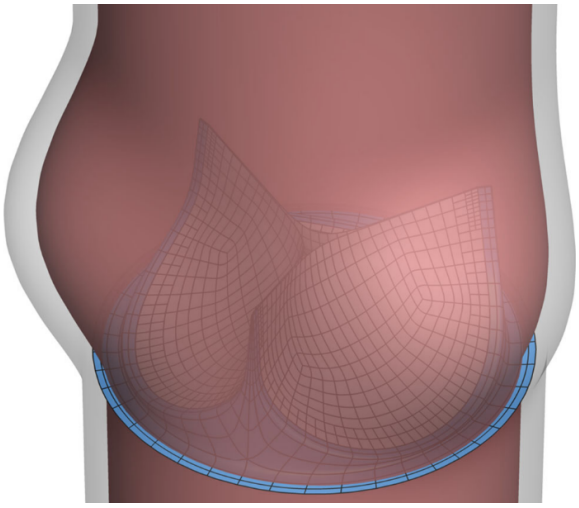

(a) CAD geometry of the bioprosthetic heart valve with refinement using T-splines (see Section 2.3.3)

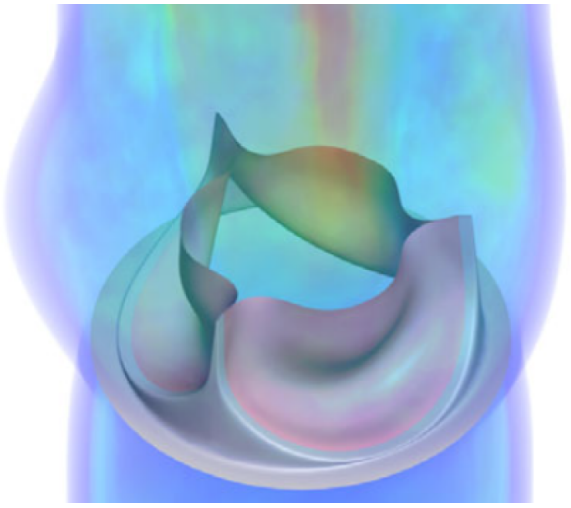

(b) Flow velocity and deformation of the arterial wall and the heart valve on a time instance.

Figure 2.4: Dynamic fluid-stricture interaction model for a bioprosthetic heart valve. The left picture represents the Computer Aided Design (CAD) geometry of the heart valve surrounded by an arterial wall. The right picture depicts the deformation of the heart valve and the arterial wall with coloured flow velocities. For details, the reader is referred to the original work of Hsu et al. [86].

progress in different structural analyses will be investigated. Secondly, comparisons of IGA and FEA from the literature will be recalled for structural analysis specifically. Afterwards, meshing techniques for general isogeometric analysis will be presented. This section closes with a brief overview of computational aspects.

2.3.1 Isogeometric Analysis for Structural Mechanics

Isogeometric Analysis for structural mechanics has been developed over the past years. The Kirchhoff-Love shell, the Reissner-Mindlin shell, solid, cable and beam elements have been developed. The range of applications of the different structural models varies from thin or moderately thick shells (Kirchhoff-Love shell and Reissner-Mindlin shell, respectively) or solids to one-dimensional elements for cables and beams. The present study mainly focusses on the use of Kirchhoff-Love shell elements since the offshore solar platform is assumed to be thin. However, Reissner-Mindlin shell models or solid models for thicker parts of the platform might be of interest in a later stadium. Furthermore, beam elements for reinforcement and cable elements for mooring systems of offshore solar platforms might be relevant in later stadia of development (see also Chapter 8).

A brief literature review is presented in the first part of this section. A review on isogeometric models for beam, cable, and shell elements is presented first. Hereafter, a review on isogeometric structural analyses that have been performed is given.

Isogeometric Shell, Beam and Cable Models

When structures are thin[5], i.e. when cross-sectional shear can be neglected (this is the so-called Kirchhoff hypothesis, see Section 3.2), *Kirchhoff-Love shells* can be used to model the structure. Kiendl et al. published several papers on the Kirchhoff-Love formulation in the Isogeometric Analysis framework [87, 88, 89]. In the work of Kiendl et al. [87], the formulation was developed for thin shell structures with large deformations and negligible through-thickness deformations induced by shear effects. Kirchhoff-Love elements require C^1 continuity between elements, which can be challenging with standard polynomial basis functions in FEA. However, using spline basis functions (e.g. B-splines), higher-order continuity between elements can be facilitated.

[5] A shell is considered *thin* when the ratio between its (shortest) in-plane length dimension L over its thickness t is larger than 20, i.e. $L/T > 20$. In this case, Kirchhoff-Love theory is applicable. If $L/t > 1000$, shells are considered *very thin* and geometric nonlinearities are necessary. If $L/t < 20$, shells are considered *moderately thick* and Reissner-Mindlin shells need to be applied. [87]

Therefore, this model is called *rotation-free* since rotational degrees of freedom are solved by derivatives of the displacement. Later on, the *Bending Strip Method* was developed by Kiendl et al. [88] to couple multiple NURBS patches. Additional work on shell coupling was performed by Coox et al.[90, 91] for non-conforming patches (i.e. patches where the parametrization does not match). Lastly, Kiendl et al. [89] extends the Kirchhoff-Love shell formulation for hyperelastic materials, such as rubber-like materials and biological tissues. Applications of different material models on biological tissues are also given in Roohbakhshan and Sauer [92].

When shells are moderately thick[6], shear deformation of the cross-section significantly influences the deformations of the shell. The so-called *Reissner-Mindlin shell* element for moderately thick shells was modelled using isogeometric analysis by Benson et al. [93]. The derived elements were tested on one linear elastic case (pinched cylinder) and four nonlinear elastoplastic cases, including the buckling of a cylinder and square tube. The element is implemented as a user-defined element in LS-DYNA and the implementation shows the effective use of quadratic and quartic shells. Furthermore, Beirão da Veiga et al. [94] presents an isogeometric method for the Reissner-Mindlin shell formulation which is locking-free, i.e. preventing over-stiff solutions in the thin plate limit [95]. Furthermore, they show for general boundary conditions that the method is uniformly stable and that it satisfies optimal convergence estimates. The derivations are formally mathematical. In the paper of Benson et al. [96], a method to combine Kirchhoff-Love and Reissner-Mindlin shells to so-called *blended shells* is proposed, combining the accuracy of the latter with the computational efficiency of the former.

Cable elements are of special interest when modelling mooring systems in marine applications. Raknes et al. [97] derive a cable element from 3D continuum mechanics equations. In their formulation, bending stiffness is included, under the Kirchhoff hypothesis. Besides providing some interesting validation cases, such as the bow and arrow problem to couple cables and beams, or the opening umbrella to couple a truss and a Kirchhoff-plate, they conclude that the bending term in the cable element formulation works as a stabilising factor in the computations. This is especially the case when modelling beams under compression. Additionally, Thai et al. [98] developed an isogeometric cable element under self-weight and elaborated on sagging cable nets using a penalty technique to calculate the equilibrium configuration.

As discussed in the previous paragraph, the work of Raknes et al. [97] also discusses the coupling of beam and shell elements. For offshore solar platform design, the structure might locally be reinforced by relatively stiff beams. Therefore, *Timoshenko beams* (moderately thick) or *Euler-Bernoulli beams* (thin) might be of interest. Firstly, Lee and Park [99] and Luu et al. [100] derive Timoshenko beam models with an isogeometric approach. In the former paper, it is concluded that the beam model is very efficient and robust with k refinements. Furthermore, they found that higher order elements do not show shear-locking effect and the mode shapes are represented compared to FEA results. In the latter paper by Luu et al. [100], the focus is on the free-form vibration of *curved beams*. They conclude that rotary inertia and shear are important for thick, elliptic rings and that the use of NURBS allows for efficient modelling of arbitrarily curved beams. Secondly, in the work of Weeger et al. [101] a nonlinear non-rotational Euler-Bernoulli beam formulation using isogeometric analysis is presented and applied to nonlinear structural vibration analysis. Lastly, the works of Cazzani et al.[103] consider curved beams with IGA. Basically, this is an extension of the 'regular' IGA beam elements. Besides the formulations and implementation of the curved beam elements, both papers provide validation cases for similar structures. In the conclusion of the paper by Cazzani et al. [103], the authors stress that the use of 'regular' IGA beam elements works for relatively small curved beams. When the initial curvature is present, however, the need for their constitutive model for curved beams needs to be adopted.

Isogeometric Structural Analysis

Based on the isogeometric structural elements presented in the previous part of this section, different applications in structural analysis have been presented in the literature. In this subsection, a brief overview is given on the performed structural analyses in the Isogeometric Analysis framework. In Chapter 4, details about the numerical procedures of different structural analyses are given.

Firstly, the works of Weeger et al., Kolman et al., Luu et al., Qin et al.[101, 104, 100, 105] focus on *structural*

[6] See Footnote 5

vibrations, i.e. *modal analysis*. Applications of IGA for structural vibrations is beneficial for panels with curved stiffeners (see [105]), curved geometries such as rings [100]. Additionally, several publications have shown that IGA outperforms the Finite Element Method (FEM) for beam vibrations [101, 106], shell vibrations [107] or simply shaped solids [104]. For more details on the comparison to the finite element method, the reader is referred to Section 2.3.2.

In the works of Valizadeh et al. [108], Thai et al. [109] and Shojaee et al. [110], *buckling* of isogeometric shell elements (respectively the first with Kirchhoff-Love elements and the second and third with Reissner-Mindlin elements) is considered for isotropic and composite panels. Similarly to the modal analysis, buckling solutions are obtained by solving an eigenvalue problem. From the study of Shojaee et al., it turns out that isogeometric shell elements for buckling analysis (including meshing procedures) are efficient, robust and accurate compared to other available methods.

Guo et al. [111] presents an implementation of *post-buckling methods*, in particular arc-length or path-following methods (see Section 4.4), on isogeometric Kirchhoff-Love shell elements. In their work, the path-following algorithm that is implemented is not capable of finding bifurcation (i.e. buckling) points and hence initial perturbations have to be applied. However, the paper does show that the results compare very well to reference solutions in ABAQUS and that local effects are captured by the higher-order continuity of the NURBS basis. A similar study was included in the work of Luo et al. [112].

Isogeometric shell discretizations have been applied in a various amount of *dynamic problems*. Besides applications in Fluid-Structure Interaction (FSI), which is out of the scope of this thesis but a suggestion for further research (see Chapter 8), studies have been performed on dynamics of shells. In the work of Benson et al. [113], a Reissner-Mindlin shell for large deformations was developed and benchmarked on different cases with different mass matrix formulations. In the work of Wang et al. [114] more information can be found on mass-matrix lumping to reduce the bandwidth but to remain accuracy in case of vibration (and subsequently dynamic) analyses.

Lastly, recent developments that are relevant for isogeometric structural mechanics, but not necessarily for this study, include dynamic contact models in general [115] and used for cloth modelling [116], the Kirchhoff-Love shell formulation including plasticity [117] and Spectral Stochastic Isogeometric Analysis (SSIGA) for the analysis of the influence of stochastic parameter distributions in linear elasticity, vibration and buckling analyses [118, 119, 120].

2.3.2 Comparison to Finite Element Analysis

As mentioned at the beginning of this section, Isogeometric Analysis originates from the idea of seamless integration between CAD and Finite Element Analysis (FEA). The fundamental difference between Isogeometric Analysis and FEA, however, is that basis functions have a compact support (element-wise) in case of FEA, whereas they have a global (patch-wise) support in Isogeometric Analysis. A domain can be subdivided into multiple patches and per patch, there are usually multiple non-zero basis functions. More detail will be given in Section 4.1.

Regarding the performance of FEA and Isogeometric Analysis, few comparing studies have been performed in the past. Furthermore, most (dis)advantages of Isogeometric Analysis compared to FEA are shown by means of application or hypothesis, rather than by formal mathematical proofs. First of all, Hughes et al. [121] compared p-method finite elements with a NURBS-based approach and concluded that for structural dynamics, the whole frequency spectrum converges with p whereas in FEA the errors in the higher-order modes even diverge with p. In the works of Auricchio et al. [122] and Morganti et al. [123] two applications comparing Isogeometric Analysis with FEA were given. In the present studies, stunning accuracy and fast computing times were observed for Isogeometric Analysis compared to FEA.

Regarding structural vibrations, Weeger et al. [101] studied nonlinear vibrations of an Euler-Bernoulli beam in the IGA and FEA framework. The conclusions were that IGA outperforms FEA since IGA does not show so-called optical branches (see Section 4.5) and that the number of degrees of freedom to reach a certain accuracy is

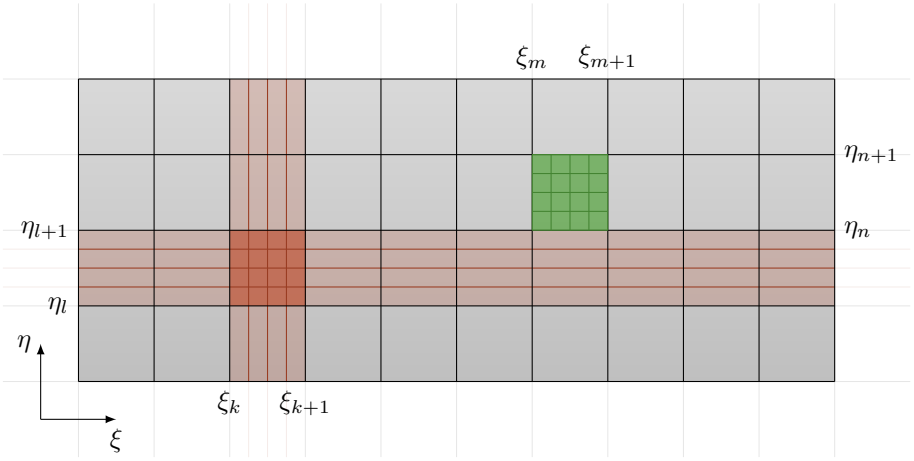

Figure 2.5: Local refinement of an element in an arbitrary piece of the parametric domain with knot vectors $\Xi = \{\xi_1, \ldots, \xi_k, \xi_{k+1}, \ldots, \xi_m, \xi_{m+1}, \xi_N\}$ and $\mathcal{H} = \{\eta_1, \ldots, \eta_l, \eta_{l+1}, \ldots, \eta_n, \eta_{n+1}, \eta_M\}$. Regions to be refined are coloured. Ordinary refinement of the tensor product is depicted in green with additional refined elements lightly coloured. T-spline refinement is depicted in orange.

lower. Additionally, Kolman et al. [104] performed an analysis of free vibrations of simple-shaped elastic samples using solid elements and also found that the number of degrees of freedom that is needed for IGA and FEM for similar accuracy is significantly smaller for IGA, and that the number of Gauss-evaluations for assembly of the system is also smaller, although IGA has less-sparse systems. Qin et al. [105] considered stiffened panels with curved stiffeners and compared IGA to FEA. Besides the advantage that IGA can exactly describe curved stiffeners, it was found that IGA outperformed FEA on accuracy for a smaller amount of degrees of freedom compared to FEA.

2.3.3 Meshing Techniques

B-splines and NURBS are defined by a set of knots in a knot vector. A disadvantage of those is that they are generally not able to represent topologies that contain holes. Furthermore, as they are defined by a tensor product of knot vectors, local refinements are inefficient, as shown in Figure 5.6, since additional regions are refined by the tensor product refinement. A solution to this is the use of T-splines, which are introduced by Sederberg et al. [124]. This technique prevents the use of global tensor product knot insertion by introducing T-junctions in the parametric mesh (see Figure 5.6). As discussed by Bazilevs et al. [125], T-splines allow for watertight merging of patches and efficient local mesh refinement, which is also discussed by Dörfel et al. [126].

Another refinement strategy is based on so-called Hierarchical B-splines (HB-splines) and was introduced by Vuong et al. [127]. The name *hierarchical B-splines* comes from the fact that the splines are refined based on a finer B-spline basis, i.e. a basis with another hierarchy in the refinement. Within the tensor product basis of arbitrary dimension, basis functions can be refined by replacing them with basis functions with a higher level of refinement. Another concept of refinement is based on Truncated Hierarchical B-splines (THB-splines) [128]. In this case, the basis functions around the eliminated basis function are truncated to have smaller support and conserve the *partition of unity* property (see Section 4.1 for properties of B-spline bases). In Figure 5.6 in Section 4.1, the concepts of uniform refinement, HB-refinement and THB-refinement are illustrated for a one-dimensional B-spline basis. Figure 2.6 depicts a THB-refined mesh in de bow of a vessel, used to increase the number of control points to model a bulbous bow.

THB-splines can be used as the basis for adaptive mesh refinements. These refinements are of particular interest when a certain part of the domain requires a high level of detail. For instance, when wrinkles with wavelengths of a few centimetres occur in a platform with dimensions of hundreds of meters, *multiple spatial scales* are involved and adaptive meshing can provide fine meshes in wrinkled regions, but coarse meshes outside. This keeps computational costs low for a certain level of accuracy in wrinkling prediction. Carraturo et al. [129] describe

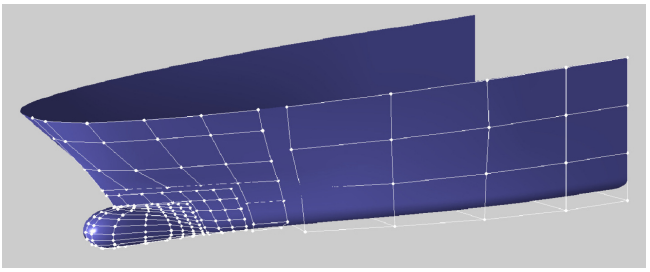

Figure 2.6: Application of THB-splines to increase the number of control points to shape a bulbous bow of a vessel. Image from Giannelli et al. [130].

the application of THB-splines on adaptive refinement with application to a heat equation on the problem of a small laser beam on a plate. The adaptive meshing procedure from this paper is based on refinement and a coarsening scheme to refine regions where an *a posteriori* error estimation based on a previous time step or iteration is used to indicate refinement or coarsening regions. The paper concludes that the proposed method provides an excellent trade-off between accuracy and system degrees of freedom (i.e. computational costs). Recommendations given by the authors are to look at three-dimensional, nonlinear or multi-physics problems.

2.3.4 Computational Aspects

Principally, Isogeometric Analysis is based on variational forms, similarly to FEA[7]. The integrals in the variational form are usually computed using quadrature rules (e.g. Gauss Quadrature) per element. In case of NURBS and B-splines, such quadrature rules are far from efficient, due to the fact that NURBS and B-splines pose some degree of smoothness across element boundaries, as illustrated in the paper of Hughes et al. [132]. Hence, a computationally very expensive step in Isogeometric Analysis is the integration of the variational form and hence assembly of the system. As this thesis will not further look into optimal quadrature for Isogeometric Analysis, the reader is advised to read the papers of Hughes et al. [132] and Auricchio et al. [133] for *improved quadrature rules*. In this work, Gauss quadrature is used for integration.

Collier et al. [134] discusses the computational costs that are associated with k-refinements (i.e. refinement of the continuity) for *direct solvers* [134] and for *iterative solvers* [135]. Garcia et al. [136] provides the 'refined IGA' (rIGA) method which uses separators in the domain (lines of reduced continuity) that make the resulting linear system more suitable to solve for direct solvers. In this work, considerations of computational costs associated with refinements and the resulting matrix structures are out of scope since the global structural response will be modelled with a small number of elements and hence computational costs for solving linear systems are assumed to be relatively small.

Lastly, as already mentioned in Section 2.3.1 an advantage of Isogeometric Analysis is the fact that the basis functions provide higher-order continuity between elements. This property is utilized in the Kirchhoff-Love shell formulation and reduces the global system size since rotational degrees of freedom do not have to be solved.

2.4 Concluding Remarks

In this chapter, a review of three topics in literature (response of VLFSs in waves, Isogeometric Analysis and the wrinkling phenomena) was given. Based on these three reviews, conclusions can be drawn for the (un)available knowledge related to this study:

- The response of Very Large Floating Structures in waves using linear models for fluid and structure has been computed by other authors. However, modelling of large, geometrically nonlinear, responses of these structures in more severe conditions (e.g. large waves, but also wind and current) has not been done yet, but it is recommended according to literature. Additionally, no literature was found for structural failure mode analysis of VLFSs. Reflecting subgoal 6, this gives a background on the development of (structural)

[7] See the work of Bischoff et al. [131] amongst others for an overview of the Finite Element Method.

models for the response of VLFSs in different loading conditions.

- In the field of wrinkling and folding of thin membranes, different experiments have been performed. Amongst these experiments are the floating sheet by Pocivavsek et al. [44] and the stretched thin sheet by Cerda et al. [43]. All applications and numerical models considered in this literature review, focussed on small scales. Additionally, numerical studies use arc length methods with *a priori* user input (see the previous bullet) or other methods to model the formation of wrinkles. Contributions in this field would hence include numerical simulations based on arc length methods without *a priori* user input. Additionally, scaling laws and parameter studies of sheets on foundations under different loading conditions and on large scales are sparse and would hence also contribute in the field. Considering subgoal 5, it can be concluded that the relevant parameters in the physical mechanism of wrinkling formation are the stiffness of the membrane (governed by material parameters or thickness), the stiffness of the elastic foundation (determined by the density of the fluid and the gravitational acceleration), the material properties and the shape or size. The numerous experiments and benchmarks that have been studied can be used for validation or verification of numerical models.

- The field of Isogeometric Analysis (IGA) has expanded since its origins in 2005. In particular, shell models have been developed based on different assumptions (e.g. rotation-free Kirchhoff-Love shells, Reissner-Mindlin shells, different material models) and has shown its advantages over Finite Element Methods (FEM) in different structural analyses. Additionally, the fact that isogeometric bases provide higher-order continuity over the whole domain implies that this technique is suitable for the Kirchhoff-Love shell implementation. This partially relates to the second subgoal of this thesis as implementation will be presented in the next chapter. However, in the field of post-buckling analysis, arc-length methods have yet only been applied based on initial perturbations, hence *a priori* user input. As will be shown in Section 4.4, methods are available to prevent the use of these perturbations.

Based on the above, the goal of this study, which is to model wrinkling of floating sheets (for failure mode analysis of VLFSs) in the Isogeometric Analysis framework using arc-length methods, contributes in different fields of study. The Kirchhoff-Love shell formulation will be used with the assumption that the considered shells are thin ($L/t > 20$) or very thin ($L/t > 1000$) [87] and the isogeometric analysis framework is utilized to facilitate higher-order continuity (minimal C^1) between elements. As will be discussed in Chapter 8, Fluid-Structure Interaction (FSI) simulations of VLFSs, corresponding to the first bullet, are out of the scope of this research.

3 | Structural Model

In this chapter, the foundations for the beam and shell models are laid. The goal of this chapter is to provide a motivation for and an explanation of the structural models that are used in this research, hence related to the first subgoal of this thesis. Additionally, the chapter provides implementation aspects of the model without specifying the type of basis functions of the method, i.e. without making a distinction between Finite Element Analysis (FEA) or Isogeometric Analysis (IGA). These implementation aspects are related to the third subgoal of this thesis. The beam model is presented for illustrational purpose as the derivation implementation is more straight-forward and thus requires less advanced coding procedures or mathematical procedures.

In the first section, relations from continuum mechanics are briefly recalled. This includes the *Kirchhoff hypothesis* for thin shells and relations between displacements, stresses and strains. First, Section 3.1 gives the basics of *differential geometry*, which is relevant for shell surface descriptions. In Section 3.2, the governing equations for beam or shell models models are given. Thereafter, in Section 3.3 and Section 3.4 the equations for respectively the beam and shell models are derived and discretized specifically.

3.1 Basics of Differential Geometry

Before the derivation of an isogeometric shell element is given, this section will briefly cover the basics of differential geometry of curved surfaces [1]. Let $\mathbf{S}(\boldsymbol{\theta}) : \mathbb{R}^2 \rightarrow \mathbb{R}^3$ be a surface representation which maps between normalized parametric coordinates $(\theta_1, \theta_2) \in [0, 1]^2$ and physical space Ω. Then, the *covariant* curvilinear basis vector $\mathbf{a}_\alpha$, $\alpha = 1.2$ is simply found by computing the partial derivatives of all three components of $\mathbf{S}$ with respect to the parameters θ_1 and θ_2. That is,

$$\mathbf{a}_\alpha = \frac{\partial \mathbf{S}}{\partial \theta_\alpha}, \qquad \text{or, element-wise,} \qquad (a_\alpha)_i = \frac{\partial \mathbf{S}_i}{\partial \theta_\alpha} \qquad \text{with:} \qquad \alpha = 1, 2;\ i = 1, 2, 3.$$

Based on the covariant basis vector, the covariant basis is usually represented by $\mathbf{a}_\alpha \otimes \mathbf{a}_\beta$ where the indices depend on the number of parametric dimensions [2] and where $\otimes$ represents the Kronecker product [138]. Some geometric representations, i.e. Cartesian bases, spherical/cylindrical bases, have the property that the covariant basis is orthogonal (see Appendix A.1), i.e. that $\mathbf{a}_i \cdot \mathbf{a}_j = 0$ for $i \neq j$, however this is generally not true. Based on the covariant basis, the *covariant metric tensor* $g_{\alpha\beta}$ can be derived. The elements of this second-order tensor are defined as:

$$g_{\alpha\beta} = \mathbf{a}_\alpha \cdot \mathbf{a}_\beta, \qquad \text{with:} \qquad \alpha, \beta = 1, 2.$$

The square root of the determinant of the covariant metric tensor, $\sqrt{\det(g_{\alpha\beta})}$, is referred to as the *measure*, but is also known as the Jacobian when bases of integrals are changed[3]. Using this tensor, the second basis of the geometry (in this case surface $\mathbf{S}$) can be derived: the *contravariant basis* $\mathbf{a}^\alpha \otimes \mathbf{a}^\beta$. This basis has the property that $\mathbf{a}_\alpha \cdot \mathbf{a}^\beta = \delta_{\alpha\beta}$ where $\delta_{\alpha\beta}$ is the Kronecker delta which is 1 for equal indices and 0 for unequal indices. The contravariant basis can be derived from the covariant basis using the contravariant metric tensor

[1] For theoretical background on the content of this section, the reader is referred to the second chapter of the dissertation of Kiendl [137] or the book of Holzapfel [138].

[2] In the latter sections, the basis will be represented by two surface coordinates θ_1, θ_2 and one out-of-plane normal coordinate θ_3. Hence, the indices will be $i, j = 1, 2, 3$.

[3] The reader is referred to basic calculus books such as Stewart [139] for the domain change of integrals

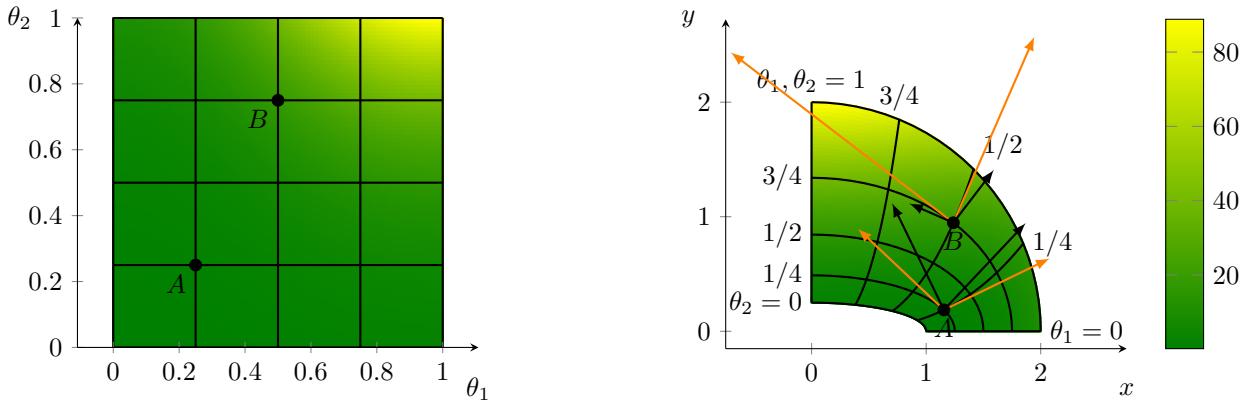

Figure 3.1: Illustration of the covariant and contravariant (coloured **orange** and **black**, respectively) for the surface with formula from Equation (3.1). The parametric points A and B are plotted in both parametric domain (left) and on the surface (right). The surfaces are coloured by the *measure* of the mapping $\mathbf{S} : \Omega^* \to \Omega$.

$[g^{\alpha\beta}] = [g_{\alpha\beta}]^{-1}$ by taking the scalar product of the *contravariant metric tensor* coefficients and a covariant basis vector:

$$\mathbf{a}^\alpha = g^{\alpha\beta}\mathbf{a}_\beta = g^{\alpha 1}\mathbf{a}_1 + g^{\alpha 2}\mathbf{a}_2, \qquad \text{for} \qquad \alpha, \beta = 1, 2.$$

To illustrate the meaning of contravariant and covariant bases, Figure 3.1 presents the surface with the formulation from Equation (3.1) with the parametric domain Ω^* and in the physical domain $\Omega = (x, y)$ such that $\mathbf{S} : \Omega^* \to \Omega$. The covariant and contravariant vectors on the points A and B are displayed and it can clearly be seen that the covariant vector in 'radial' (i.e. θ_2) direction is orthogonal to the contravariant vector in the 'angular' (i.e. θ_1) direction and vice versa. In Appendix A.2, the formulations of the covariant and contravariant basis vectors are given.

$$\mathbf{S}(\theta_1, \theta_2) = \begin{bmatrix} (r(\theta_2) + 1)\cos(\phi(\theta_1)) \\ \frac{(r(\theta_2)+1)^3}{4}\sin(\phi(\theta_2)) \end{bmatrix}, \qquad \text{where:} \qquad \phi(\theta_1) = \frac{\pi}{2}\theta_1 \qquad \text{and} \qquad r(\theta_2) = \theta_2. \tag{3.1}$$

3.2 Fundamentals of Continuum Mechanics for Thin Beams and Shells

From continuum mechanics, general relations between displacements, strains and stresses are adopted for thin shells specifically. In the sequel, the assumption is made that the dimension of the thickness of the shell is smaller than any in-plane dimension, e.g. $t \ll B$ and $t \ll L$ where B and L are some length and width dimensions of the geometry and t is the thickness of the shell.

3.2.1 Coordinate System

Suppose a piece of material is first in a *reference state* and due to deformation, it turns into a *deformed state*. Suppose that any point in the material can be represented by the parametric coordinates $\boldsymbol{\theta} = (\theta_1, \theta_2, \theta_3)$. Figure 3.2 illustrates the coordinate system that is used using two-dimensional in-plane deformation, without loss of generality. Then, any point in the undeformed configuration is represented by $\mathbf{X}(\boldsymbol{\theta})$ and any point in the deformed configuration is represented by $\mathbf{x}(\boldsymbol{\theta})$. In the sequel, capitals will be used for quantities in the undeformed state whereas lower-case letters will be used for quantities in the deformed state. As discussed in Section 3.1, $\mathbf{X}$ and $\mathbf{x}$ are mappings from the coordinate system $\boldsymbol{\theta}$ to a point in space, or from a parameter space $\boldsymbol{\theta} \in \hat{\Omega}$ to a point in physical space $\mathbf{x} \in \hat{\Omega}^*$.

The basis of Euler-Bernoulli beam theory and Kirchhoff-Love shell theory is the *Kirchhoff Hypothesis*. The Kirchhoff Hypothesis defines thin shell or beam coordinate systems relative to the mid-plane of the shell and

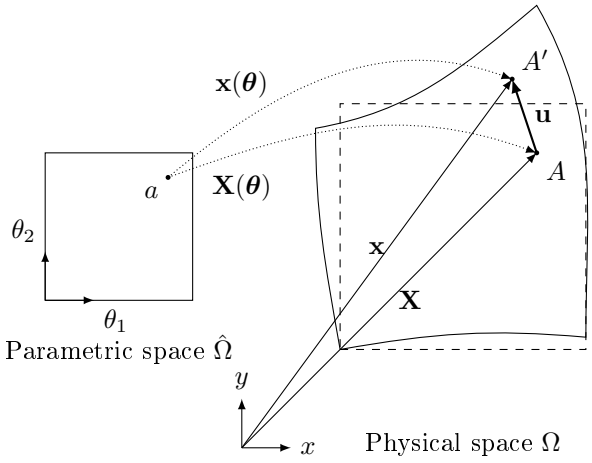

Figure 3.2: Arbitrary physical domain $\Omega \in \mathbb{R}^2$ (dashed) and its deformation (solid). The parametric domain $\hat{\Omega} \in \mathbb{R}^2$ is also plotted. The point $a \in \hat{\Omega}$ is mapped on the deformed and undeformed domains to A' and A by mappings $\mathbf{x}(\boldsymbol{\theta})$ and $\mathbf{X}(\boldsymbol{\theta})$, respectively. These mappings represent coordinate vectors and the different between the vectors is $\mathbf{u} = \mathbf{x} - \mathbf{X}$. The same notations hold in the three-dimensional space $\Omega^* = \Omega \cup [-t/2, t/2]$ using the coordinate system in 3.2.

beam and a director (i.e. a normal vector). The Kirchhoff Hypothesis makes the following three assumptions for the displacement field [140]:

1. Straight lines perpendicular to the mid-surface (i.e. transverse normals) before deformation, *remain straight after deformation*,
2. The transverse normals rotate such that they *remain perpendicular* to the mid-surface after deformation.
3. The transverse normals do not experience *elongation* (i.e. they are *inextensible*),

Consequently, the first assumption implies that the through thickness strain distribution is linear, the second assumption implies that the geometry can be represented by its mid-surface only and combined with the first assumption it implies that the cross-section does not shear. Additionally, the second assumption implies that the thickness of the cross-section does not change due to deformation. This does not necessarily mean that the thickness of the cross-section cannot be variable over the mid-plane. [137]

Based on the Kirchhoff Hypothesis, the coordinate system of the deformed (undeformed) shell can be defined based on the mid-plane surface $\mathbf{c}(\theta_1, \theta_2)$ ($\mathbf{C}(\theta_1, \theta_2)$) and the normal vector to this surface $\hat{\mathbf{n}}$ ($\hat{\mathbf{N}}$) as:

$$\mathbf{x}(\boldsymbol{\theta}) = \mathbf{c}(\theta_1, \theta_2) + \theta_3 \hat{\mathbf{n}} \qquad \text{and} \qquad \mathbf{X}(\boldsymbol{\theta}) = \mathbf{C}(\theta_1, \theta_2) + \theta_3 \hat{\mathbf{N}}. \tag{3.2}$$

The covariant basis (see Section 3.1) is defined by the covariant basis of a surface, i.e. the surface tangents (subscripts 1 and 2), and the normal vector. The Greek indices α and β are used for the in-plane parameters, i.e. $\alpha, \beta = 1, 2$. The following definitions of the covariant and contravariant bases will be given for the deformed configuration only, but the the results are valid for any shell geometry and hence also the undeformed variant. The covariant basis vectors $\mathbf{g}_i$ $i = 1, 2, 3$ are defined as:

$$\mathbf{g}_\alpha = \frac{\partial \mathbf{x}}{\partial \theta_\alpha} \qquad \text{and} \qquad \mathbf{g}_3 = \hat{\mathbf{n}} = \frac{\frac{\partial \mathbf{c}}{\partial \theta_1} \times \frac{\partial \mathbf{c}}{\partial \theta_2}}{\left\| \frac{\partial \mathbf{c}}{\partial \theta_1} \times \frac{\partial \mathbf{c}}{\partial \theta_2} \right\|}.$$

Using this basis, the coefficients of the covariant metric tensor for the in-plane basis $g_{\alpha\beta}$ are

$$\begin{aligned} g_{\alpha\beta} = \mathbf{g}_\alpha \cdot \mathbf{g}_\beta &= \left(\frac{\partial \mathbf{c}}{\partial \theta_\alpha} + \theta_3 \frac{\partial \hat{\mathbf{n}}}{\partial \theta_\alpha} \right) \cdot \left(\frac{\partial \mathbf{c}}{\partial \theta_\beta} + \theta_3 \frac{\partial \hat{\mathbf{n}}}{\partial \theta_\beta} \right) \\ &= \frac{\partial \mathbf{c}}{\partial \theta_\alpha} \cdot \frac{\partial \mathbf{c}}{\partial \theta_\beta} + \theta_3 \left(\frac{\partial \mathbf{c}}{\partial \theta_\alpha} \cdot \frac{\partial \hat{\mathbf{n}}}{\partial \theta_\beta} + \frac{\partial \mathbf{c}}{\partial \theta_\beta} \cdot \frac{\partial \hat{\mathbf{n}}}{\partial \theta_\alpha} \right) + \theta_3^2 \frac{\partial \hat{\mathbf{n}}}{\partial \theta_\alpha} \frac{\partial \hat{\mathbf{n}}}{\partial \theta_\beta}. \end{aligned}$$

The terms of order θ_3^2 are neglected in the sequel by the assumption of small thickness, i.e. a thin shell assumption. Furthermore, the term of order θ_3 can be simplified using the following result from Kiendl [137] amongst others:

$$\frac{\partial \mathbf{c}}{\partial \theta_\alpha} \cdot \frac{\partial \hat{\mathbf{n}}}{\partial \theta_\beta} = \frac{\partial \mathbf{c}}{\partial \theta_\beta} \cdot \frac{\partial \hat{\mathbf{n}}}{\partial \theta_\alpha} = -\frac{\partial^2 \mathbf{c}}{\partial \theta_\alpha \partial \theta_\beta} \cdot \hat{\mathbf{n}}.$$

The coefficients of the covariant metric tensor related to the director coordinate θ_3 are

$$g_{\alpha 3} = \mathbf{g}_\alpha \cdot \mathbf{g}_3 = \left(\frac{\partial \mathbf{c}}{\partial \theta_\alpha} + \theta_3 \frac{\partial \hat{\mathbf{n}}}{\partial \theta_\alpha} \right) \cdot \hat{\mathbf{n}} = 0, \tag{3.3}$$

$$g_{33} = \mathbf{g}_3 \cdot \mathbf{g}_3 = \hat{\mathbf{n}} \cdot \hat{\mathbf{n}} = 1. \tag{3.4}$$

Where the first line is equal to zero because the product of the normal vector is orthogonal to the derivative of the surface tangents and since the derivatives of $\hat{\mathbf{n}}$ with respect to the surface coordinates (θ_1, θ_2) is zero.

3.2.2 Shell Kinematics

In the previous section, the coordinate system for thin shells was derived together with the covariant metric tensors. In this section, the shell kinematics are derived, which relate deformations between two configurations of the shells using the covariant bases in the deformed and undeformed configuration using the *strain tensor*. The derivation of Kiendl is used as guideline in this section. The reader is referred to the works of Holzapfel [138] and Başar and Weichert [141] for further details. In the work of Goyal [142], a different approach is used, but the outcome of the strain tensor is equal.

When a shell is deforming, the difference between the undeformed configuration $\mathbf{X}$ and the deformed configuration $\mathbf{x}$ is denoted by the vector $\mathbf{u}$. By definition, (see Figure 3.2)

$$\mathbf{x} = \mathbf{X} + \mathbf{u} \iff \mathbf{u} = \mathbf{x} - \mathbf{X}.$$

Furthermore, consider a line segment $\mathrm{d}\mathbf{X}$ in the undeformed configuration. After deformation, the same line segment is deformed to $\mathrm{d}\mathbf{x}$. The relation between both segments is described by the *deformation gradient* $\underline{\underline{\boldsymbol{F}}}$ as follows

$$\mathrm{d}\mathbf{x} = \underline{\underline{\boldsymbol{F}}} \cdot \mathrm{d}\mathbf{X}.$$

Denoting the covariant and contravariant basis of the deformed and undeformed configuration by $\mathbf{g}_i$, $\mathbf{g}^i$, $\mathbf{G}_i$ and $\mathbf{G}^i$, the following relations of the deformation gradient $\mathbf{F}$ hold [137, 141], where:

$$\underline{\underline{\boldsymbol{F}}} = \mathbf{g}_i \otimes \mathbf{G}^i, \qquad \underline{\underline{\boldsymbol{F}}}^T = \mathbf{G}^i \otimes \mathbf{g}_i,$$
$$\underline{\underline{\boldsymbol{F}}}^{-1} = \mathbf{G}_i \otimes \mathbf{g}^i, \qquad \underline{\underline{\boldsymbol{F}}}^{-T} = \mathbf{g}^i \otimes \mathbf{G}_i.$$

For index $i = 1, 2, 3$. The strain model that is used in the Kirchhoff-Love shell model is the *Green-Lagrange strain tensor*. This tensor describes a nonlinear relationship between deformations and strains and it is defined as[4]

$$\underline{\underline{\boldsymbol{E}}} = \frac{1}{2} \left(\underline{\underline{\boldsymbol{F}}}^T \underline{\underline{\boldsymbol{F}}} - \underline{\underline{\boldsymbol{I}}} \right) \tag{3.5}$$

Please note that the strain and identity tensors, $\underline{\underline{\boldsymbol{E}}}$ and $\underline{\underline{\boldsymbol{I}}}$, are of second order. Substituting the relations of the deformation gradient $\underline{\underline{\boldsymbol{F}}}$ and its transpose, gives the following definition of the Green-Lagrange strain tensor with respect to the undeformed basis $\mathbf{G}^i \otimes \mathbf{G}^j$:

$$\underline{\underline{\boldsymbol{E}}} = \frac{1}{2} \left(g_{ij} - G_{ij} \right) \mathbf{G}^i \otimes \mathbf{G}^j. \tag{3.6}$$

[4] For introductory strain definitions, the reader is directed to the works of Sadd [143] and Reddy [95]. In the book of Sadd the derivation of simple linear strain is clearly derived from the typical deformations of a rectangular element. In the work of Reddy, the formulation $\mathbf{E} = \frac{1}{2} \left((\nabla \mathbf{u})^T + \nabla \mathbf{u} + (\nabla \mathbf{u})^T \nabla \mathbf{u} \right)$ is used and derived and used in Cartesian and polar coordinates.

Substituting the relations of g_{ij} from Section 3.1 (which also hold for the deformed configuration, giving G_{ij}) gives

$$\underline{\underline{\boldsymbol{E}}} = \frac{1}{2}\begin{bmatrix} \frac{\partial \mathbf{c}}{\partial\theta_1}\cdot\frac{\partial \mathbf{c}}{\partial\theta_1} - \frac{\partial \mathbf{C}}{\partial\theta_1}\cdot\frac{\partial \mathbf{C}}{\partial\theta_1} & \frac{\partial \mathbf{c}}{\partial\theta_1}\cdot\frac{\partial \mathbf{c}}{\partial\theta_2} - \frac{\partial \mathbf{C}}{\partial\theta_1}\cdot\frac{\partial \mathbf{C}}{\partial\theta_2} & 0 \\ \frac{\partial \mathbf{c}}{\partial\theta_1}\cdot\frac{\partial \mathbf{c}}{\partial\theta_2} - \frac{\partial \mathbf{C}}{\partial\theta_1}\cdot\frac{\partial \mathbf{C}}{\partial\theta_2} & \frac{\partial \mathbf{c}}{\partial\theta_2}\cdot\frac{\partial \mathbf{c}}{\partial\theta_2} - \frac{\partial \mathbf{C}}{\partial\theta_2}\cdot\frac{\partial \mathbf{C}}{\partial\theta_2} & 0 \\ 0 & 0 & 0 \end{bmatrix} + \theta_3 \begin{bmatrix} \frac{\partial^2 \mathbf{C}}{\partial\theta_1^2}\cdot\hat{\mathbf{N}} - \frac{\partial^2 \mathbf{c}}{\partial\theta_1^2}\cdot\hat{\mathbf{n}} & \frac{\partial^2 \mathbf{C}}{\partial\theta_1\partial\theta_2}\cdot\hat{\mathbf{N}} - \frac{\partial^2 \mathbf{c}}{\partial\theta_1\partial\theta_2}\cdot\hat{\mathbf{n}} & 0 \\ \frac{\partial^2 \mathbf{C}}{\partial\theta_1\partial\theta_2}\cdot\hat{\mathbf{N}} - \frac{\partial^2 \mathbf{c}}{\partial\theta_1\partial\theta_2}\cdot\hat{\mathbf{n}} & \frac{\partial^2 \mathbf{C}}{\partial\theta_2^2}\cdot\hat{\mathbf{N}} - \frac{\partial^2 \mathbf{c}}{\partial\theta_1^2}\cdot\hat{\mathbf{n}} & 0 \\ 0 & 0 & 0 \end{bmatrix} \tag{3.7}$$

$$= \underline{\underline{\boldsymbol{\varepsilon}}} + \theta_3 \underline{\underline{\boldsymbol{\kappa}}}.$$

From these equations, it can be seen that the strain tensor for a Kirchhoff-Love thin shell can be decomposed in a *normal strain component* $\underline{\underline{\boldsymbol{\varepsilon}}}$ and a *curvature component* $\underline{\underline{\boldsymbol{\kappa}}}$. In both components, the last column and rows are zero by the results of Equations (3.3) and (3.4) (see Remark 3.4 of Goyal [142]).

3.2.3 Constitutive Equations

The constitutive relations describe the relations between stresses and strains. In this section, the constitutive relations used in the Kirchhoff-Love shell are presented. The formulations are adopted from Kiendl [137] and Goyal [142]. The formulations given in these works are different since Goyal uses the curvilinear basis of the shell element in the analysis, whereas Kiendl uses a Cartesian transformation. In general, backgrounds on the equations given in this section can be found in the books of Başar and Weichert, Reddy [141, 95] amongst others.

Depending on the material law, different constitutive relations are obtained. The energy conjugate to the Green-Lagrange strain tensor is the *second Piola-Kirchhoff stress tensor* $\underline{\underline{\boldsymbol{S}}}$. From this tensor, physical stresses can be obtained using the *Cauchy stress tensor* (defined in the deformed covariant basis $\mathbf{g}_i \otimes \mathbf{g}_j$) [95, 137, 141]:

$$\underline{\underline{\boldsymbol{\sigma}}} = (\det\mathbf{F})^{-1}\underline{\underline{\boldsymbol{F}}}\,\underline{\underline{\boldsymbol{S}}}\,\underline{\underline{\boldsymbol{F}}}^T. \tag{3.8}$$

In the Kirchhoff-Love shell model, the *Saint Venant-Kirchhoff material model* is used, which describes a linear relation between the stress tensor $\underline{\underline{\boldsymbol{S}}}$ and strain tensor $\underline{\underline{\boldsymbol{E}}}$ by the fourth order material tensor $\mathcal{C}$ using the following relation:

$$\underline{\underline{\boldsymbol{S}}} = \mathcal{C} : \underline{\underline{\boldsymbol{E}}}. \tag{3.9}$$

This quantity is defined in the covariant undeformed basis $(\mathbf{G}_i \otimes \mathbf{G}_j)$. The : denote *double contraction* (see Başar and Weichert [141] or the notations of this thesis). For isotropic materials, i.e. materials where the Young's modulus E and the Poisson ratio ν are constant in all directions, the *Lamé parameters* λ, μ are often used in the definition of the material tensor. These parameters are defined by:

$$\lambda = \frac{E\nu}{(1+\nu)(1-2\nu)} \qquad \text{and} \qquad \mu = \frac{E}{2(1+\nu)}. \tag{3.10}$$

In the curvilinear undeformed basis $\mathbf{G}^i \otimes \mathbf{G}^j$, the coefficients of the fourth-order *material tensor* $\mathcal{C}$ is defined by [142]:

$$\mathcal{C}^{\alpha\beta\sigma\tau} = 2\frac{\lambda\mu}{\lambda+2\mu}G_{\alpha\beta}G_{\sigma\tau} + \mu(G_{\alpha\sigma}G_{\beta\tau} + G_{\alpha\tau}G_{\beta\sigma}). \tag{3.11}$$

Here, $G_{\alpha\beta}$ denotes the undeformed covariant metric tensor (see Section 3.1. It is more common to transform the strain tensor to a local Cartesian basis (such that the Cartesian strain tensor is $\hat{\underline{\underline{\boldsymbol{E}}}}$) to obtain the a Saint Venant-Kirchhoff stress tensor of the following form [131, 137][5]. The material tensor $\underline{\underline{\boldsymbol{D}}}$ in Cartesian coordinates becomes:

$$\mathrm{D} = \begin{bmatrix} \tilde{\mathcal{C}}^{1111} & \tilde{\mathcal{C}}^{1122} & \tilde{\mathcal{C}}^{1112} \\ \tilde{\mathcal{C}}^{2211} & \tilde{\mathcal{C}}^{2222} & \tilde{\mathcal{C}}^{2212} \\ \tilde{\mathcal{C}}^{1112} & \tilde{\mathcal{C}}^{2212} & \tilde{\mathcal{C}}^{1111} \end{bmatrix} = \frac{E}{1-\nu^2}\begin{bmatrix} 1 & \nu & 0 \\ \nu & 1 & 0 \\ 0 & 0 & \frac{1-\nu}{2} \end{bmatrix}. \tag{3.12}$$

Theorem 1. *The material tensor of Equation* (3.12) *on a local Cartesian basis and the material tensor from Equation* (3.11) *on a curvilinear basis are equivalent.*

[5] In this work, however, the model from Goyal [142] is adopted and therefore the material tensor from Equation (3.11) is used. It should be noted that the strain energy used by Goyal [142] is multiplied by $\frac{1}{2}$ and that Equation (3.11) is multiplied by 2.

Proof. The proof is given in Section B.1.1. □

Theorem 2. *The material tensor $\mathcal{C}$ is symmetric, i.e. $\mathcal{C} = \mathcal{C}^T$ (**note:** in Section B.1.1, the notion of symmetry for fourth-order tensors is refined and the theorem is slightly reformulated.)*

Proof. The proof is given in Section B.1.1. □

Up to the definition of the stress tensor $\underline{\underline{\boldsymbol{S}}}$, no assumptions have been made regarding the thin shell. However, by the Kirchhoff Hypothesis, it is known that the thickness remains constant when the shell deforms. Therefore, the stress tensor can be integrated over the thickness to reduce the domain of integration from the three-dimensional physical domain $\Omega^* = \Omega \cup [-t/2, t/2]$ to the mid-plane surface Ω only. For later reference, the definitions of the *force* and *moment tensor* of the shell are given by [137]:

$$\underline{\underline{\boldsymbol{n}}} = \int_{[-\frac{t}{2},\frac{t}{2}]} \underline{\underline{\boldsymbol{S}}} \, \mathrm{d}\theta_3 = \int_{[-\frac{t}{2},\frac{t}{2}]} \mathcal{C} : (\underline{\underline{\boldsymbol{\varepsilon}}} + \theta_3 \underline{\underline{\boldsymbol{\kappa}}}) \, \mathrm{d}\theta_3 = t\mathcal{C} : \underline{\underline{\boldsymbol{\varepsilon}}}, \tag{3.13}$$

$$\underline{\underline{\boldsymbol{m}}} = \int_{[-\frac{t}{2},\frac{t}{2}]} \theta_3 \underline{\underline{\boldsymbol{S}}} \, \mathrm{d}\theta_3 = \int_{[-\frac{t}{2},\frac{t}{2}]} \mathcal{C} : (\theta_3 \underline{\underline{\boldsymbol{\varepsilon}}} + \theta_3^2 \underline{\underline{\boldsymbol{\kappa}}}) \, \mathrm{d}\theta_3 = \frac{t^3}{12} \mathcal{C} : \underline{\underline{\boldsymbol{\kappa}}}. \tag{3.14}$$

Or in Voight notation:

$$\begin{bmatrix} N_{11} \\ N_{22} \\ N_{12} \end{bmatrix} = t \begin{bmatrix} \mathcal{C}^{1111} & \mathcal{C}^{1122} & \mathcal{C}^{1112} \\ \mathcal{C}^{2211} & \mathcal{C}^{2222} & \mathcal{C}^{2212} \\ \mathcal{C}^{1112} & \mathcal{C}^{2212} & \mathcal{C}^{1111} \end{bmatrix} \begin{bmatrix} \varepsilon_{11} \\ \varepsilon_{22} \\ \varepsilon_{12} \end{bmatrix} \quad \text{and} \quad \begin{bmatrix} M_{11} \\ M_{22} \\ M_{12} \end{bmatrix} = \frac{t^3}{12} \begin{bmatrix} \mathcal{C}^{1111} & \mathcal{C}^{1122} & \mathcal{C}^{1112} \\ \mathcal{C}^{2211} & \mathcal{C}^{2222} & \mathcal{C}^{2212} \\ \mathcal{C}^{1112} & \mathcal{C}^{2212} & \mathcal{C}^{1111} \end{bmatrix} \begin{bmatrix} \kappa_{11} \\ \kappa_{22} \\ \kappa_{12} \end{bmatrix}. \tag{3.15}$$

3.2.4 Energy Relations

In the previous section, the constitutive relation between stresses and strains has been defined. Numerical codes such as Finite Element Methods (FEMs) or Isogeometric Analysis (IGA) rely on the *minimization of energy* in a system [144]. In this section, the formulations for the internal, external and kinetic energies are given. In the next section, these formulations will be used to derive the variational form of the shell equations, which is the basis for the FEM or for IGA[6].

The *internal energy* in a deformed body is defined by the stress and strains present in the body. In particular [141, 138, 143],

$$W_{\text{int}} = \frac{1}{2} \int_\Omega \underline{\underline{\boldsymbol{S}}} : \underline{\underline{\boldsymbol{E}}} \, \mathrm{d}\Omega.$$

Here, $\underline{\underline{\boldsymbol{S}}}$ and $\underline{\underline{\boldsymbol{E}}}$ is depending on the displacements $\mathbf{u}$. When the decomposition of the strain into membrane and flexural elements and the definitions of the internal force and moment, the internal energy becomes:

$$W_{\text{int}} = \frac{1}{2} \int_\Omega \underline{\underline{\boldsymbol{n}}} : \underline{\underline{\boldsymbol{\varepsilon}}} + \underline{\underline{\boldsymbol{m}}} : \underline{\underline{\boldsymbol{\kappa}}} \, \mathrm{d}\Omega \tag{3.16}$$

Note that the integral over the whole domain has been replaced by the integral over the surface mid-plane since $\Omega^* = \Omega \times [-t/2, t/2]$. The *external energy* on the body is defined as [137, 142]:

$$W_{\text{ext}} = -\int_\Omega \mathbf{t} \cdot \mathbf{u} \, \mathrm{d}\Omega. \tag{3.17}$$

Where $\underline{\underline{\boldsymbol{t}}}$ is the surface traction tensor. In the book of Goyal [142], more expressions for the external energies are given. These formulations will be used in Section 3.3, where the beam model is derived from the variational form. In that case, boundary forces and moments will be multiplied with displacements and rotations on the boundary.

The *kinetic energy* of the body is given by:

$$K = \frac{1}{2} \int_\Omega \rho \dot{\mathbf{x}} \cdot \dot{\mathbf{x}} \, \mathrm{d}\Omega.$$

[6] For more details, the reader is again referred to the books of Başar and Weichert [141], Holzapfel [138] and Sadd [143] and for thin shells in particular to the work of Kiendl [137]. The work of Goyal [142] will be used later. In this section, this work is not used because the internal strain energy is not consistent with the other references (see Footnote 5)

Where the dot represents the time-derivative. Using the shell coordinate system $\mathbf{x} = \mathbf{c} + \theta_3\hat{\mathbf{n}}$ and integration over the thickness, this simplifies to

$$K = \frac{1}{2}\int_\Omega \rho\left[t\dot{\mathbf{c}}\cdot\dot{\mathbf{c}} + \frac{t^3}{12}\dot{\hat{\mathbf{n}}}\cdot\dot{\hat{\mathbf{n}}}\right]\,\mathrm{d}\Omega. \tag{3.18}$$

Here, ρ is the density of the material and t is the thickness of the shell. The first term in this integral represents the translational inertia of the shell, whereas the second term represents *rotational inertia* of the shell. In this work, it is assumed that the rotary inertia of the shell is negligible compared to translational inertia.

3.2.5 Variational Form

The *variational form* of an energy equation is a form which describes the energy of a system due to small variations of a functional. For Finite Element Methods and Isogeometric Analysis, the variational form is often used to derive an energy minimiser using *Hamilton's principle* to finally find a system which minimises energy. In this section, Hamilton's principle is defined and used to derive the variational formulation for the Kirchhoff-Love shell.[7]

Hamilton's principle states that [95]:

> Of all possible paths that a material particle could travel from its position at time τ_1 to its position at time τ_2, its actual path will be one for which the integral
>
> $$\int_{\tau_1}^{\tau_2}\mathcal{L}\,\mathrm{d}\tau \tag{3.19}$$
>
> is an extremum.

Here, $\mathcal{L}$ is the *Lagrangian* of the system, which is defined to be a functional of the difference between kinetic and potential energy functions in terms of the displacements $\mathbf{u}$ and its time derivative $\dot{\mathbf{u}}$, i.e.

$$\mathcal{L} = K(\dot{\mathbf{u}}) - (W_{\text{int}}(\mathbf{u}) + W_{\text{ext}}(\mathbf{u})).$$

Furthermore, the extremum in Hamilton's principle is found by the use of variations of the energies between the time steps τ_0 and τ_1. The path for which Hamilton's principle results in an extremum is found by taking the derivative of the energy integral with respect to the displacement vector, i.e. by applying calculus of variations. Let us first define the *energy functional* by [142]:

$$J(\theta) = \int_{\tau_0}^{\tau_1}\mathcal{L}(\mathbf{u}+\theta\mathbf{v})\,\mathrm{d}\tau. \tag{3.20}$$

Here, $\mathbf{u}$ is the displacement vector of the body and $\theta\mathbf{v}$ is a variation of the displacements by using the *admissible* test function $\mathbf{v}$. The variation $\theta\mathbf{v}$ is admissible if and only if $\mathbf{u}+\theta\mathbf{v}$ satisfies the boundary conditions for all $\theta\in\mathbb{R}$ and for all times τ and such that $\mathbf{u}+\theta\mathbf{v} = \mathbf{u}$ for all $\theta\in\mathbb{R}$ on times τ_0 and τ_1. This implies that the variation should be zero on the boundary all time. Furthermore, for two times τ_0 and τ_1, the variation is zero for all $\theta\in\Omega$. From this energy functional, energy variation can now be derived by first taking the *Gateaux derivative* [145, 146], i.e.

$$\left.\frac{\mathrm{d}J}{\mathrm{d}\theta}\right|_{\theta=0} = 0. \tag{3.21}$$

This implies (see Equation (B.5))

$$\int_{\hat{\Omega}}\rho\ddot{\mathbf{c}}\cdot\mathbf{v}\,\mathrm{d}\hat{\Omega} + \int_\Omega \underline{\underline{\boldsymbol{n}}}:\underline{\underline{\boldsymbol{\varepsilon}}}' + \underline{\underline{\boldsymbol{m}}}:\underline{\underline{\boldsymbol{\kappa}}}'\,\mathrm{d}\Omega - \int_\Omega \mathbf{t}\cdot\mathbf{v}\,\mathrm{d}\Omega = 0. \tag{3.22}$$

Here, $\underline{\underline{\boldsymbol{\varepsilon}}}'$ and $\underline{\underline{\boldsymbol{\kappa}}}'$ are the Gateaux derivatives of the strain and curvature. They will be determined for the beam and shell element separately in the coming sections (see Section 3.3 and Section 3.4, respectively). From the above form, the energy variations (i.e. generalized forces) are:

$$\delta K = -\int_\Omega \rho t\ddot{\mathbf{u}}\cdot\mathbf{v}\,\mathrm{d}\Omega, \qquad \delta W_{\text{int}} = -\int_\Omega \underline{\underline{\boldsymbol{n}}}:\underline{\underline{\boldsymbol{\varepsilon}}}' + \underline{\underline{\boldsymbol{m}}}:\underline{\underline{\boldsymbol{\kappa}}}'\,\mathrm{d}\Omega \qquad \text{and} \qquad \delta W_{\text{ext}} = \int_\Omega \mathbf{t}\cdot\mathbf{v}\,\mathrm{d}\Omega. \tag{3.23}$$

[7] For more details about variational calculus, the reader is referred to the books of Dacorogna [145] or Cassel [146]

The variations δW_{int} and δW_{ext} are in fact the partial derivatives of the internal and external energies with respect to the displacement vectors, and thus by Castigliano's first theorem (see Reddy [95]), they are equal to the generalized internal and external forces. Note that all quantities are scalar quantities by the definition of the double contraction : for second-order tensors and the inner-product for vectors.

Since the generalized internal force δW_{int} is nonlinear for the displacement vector $\mathbf{u}$, Newton iterations will be needed in the solution procedure (see Section 4.2). This method uses the Jacobian of the system to be solved to iteratively solve for the solution of the system. To obtain the tangential stiffness matrix, the second variation of the internal stiffness matrix needs to be derived [142, 137]. Taking the Gateaux derivative of the variation of the internal energy yields (see Equation (B.6)):

$$j(\mathbf{u},\mathbf{v},\mathbf{w}) = \frac{\mathrm{d}\delta W_{\text{int}}}{\mathrm{d}\theta}(\mathbf{u}+\theta\mathbf{w},\mathbf{v})\bigg|_{\theta=0} = -\int_\Omega \underline{\underline{\boldsymbol{n}}}' : \underline{\underline{\boldsymbol{\varepsilon}}}' + \underline{\underline{\boldsymbol{n}}} : \underline{\underline{\boldsymbol{\varepsilon}}}'' + \underline{\underline{\underline{\boldsymbol{m}}}}' : \underline{\underline{\boldsymbol{\kappa}}}' + \underline{\underline{\underline{\boldsymbol{m}}}} : \underline{\underline{\boldsymbol{\kappa}}}'' \,\mathrm{d}\Omega. \tag{3.24}$$

Here, $\underline{\underline{\boldsymbol{\varepsilon}}}''$ and $\underline{\underline{\boldsymbol{\kappa}}}''$ are the second Gateaux derivatives of the strain and curvature and $\underline{\underline{\boldsymbol{n}}}'$ and $\underline{\underline{\underline{\boldsymbol{m}}}}'$ are the Gateaux derivatives of the internal force and moment. When the basis functions of the method are specified, numerical discretization of Equation (3.24) will result in the Jacobian matrix (see Section 3.2.7)

3.2.6 Follower (Hydrostatic) Pressures

In the special case when the load is depending on the solution, the expression for the external work becomes:

$$W_{\text{ext}} = \int_\Omega \mathbf{f}(\mathbf{u}) \cdot \mathbf{u} \,\mathrm{d}\Omega.$$

Where $\mathbf{f}(\mathbf{u})$ is a function depending on the displacements $\mathbf{u}$. Suppose we have $\mathbf{f} = \hat{p}\hat{\mathbf{n}}$ where $\hat{p}$ is a pressure working in normal direction $\hat{\mathbf{n}}$ on the shell. Note that the normal depends on the solution $\mathbf{u}$ when it is evaluated on the deformed configuration $\mathbf{x}$. The variation of the virtual work and the Jacobian contribution are then defined as (see Kiendl et al. [89]):

$$\delta W_{\text{ext}} = \int_\Omega \mathbf{f}\cdot\mathbf{v}\,\mathrm{d}\Omega = \int_\Omega \hat{p}\hat{\mathbf{n}}\cdot\mathbf{v}\,\mathrm{d}\Omega, \tag{3.25}$$

$$j_{\text{ext}} = -\int_\Omega \mathbf{f}'\cdot\mathbf{v}\,\mathrm{d}\Omega = \int_\Omega \hat{p}\hat{\mathbf{n}}'\cdot\mathbf{v}\,\mathrm{d}\Omega. \tag{3.26}$$

Where $\hat{\mathbf{n}}'$ is the Gateaux derivative of the normal vector. Additionally, *hydrostatic pressures* can be modelled by a spring foundation under a plate. By Bernoulli's law, hydrostatic pressure is defined by $p = \rho g \mathbf{e}_3 \circ \mathbf{u}$ where $\mathbf{e}_3$ is a unit vector that is 1 for the vertical direction and 0 elsewhere and $\circ$ denotes and element-wise vector product, i.e. the Hadamard-product (or Schur-product) [147]. Using the definitions in Equation (3.25) and Equation (3.26), the variation of the external virtual work and the Jacobian contribution due to hydrostatic pressure become:

$$\delta W_{\text{ext}} = \int_\Omega \rho g \mathbf{e}_3 \circ \mathbf{u}\cdot\mathbf{v}\,\mathrm{d}\Omega, \tag{3.27}$$

$$j_{\text{ext}} = \int_\Omega \rho g \mathbf{e}_3 \circ \mathbf{w}\cdot\mathbf{v}\,\mathrm{d}\Omega. \tag{3.28}$$

3.2.7 Numerical Discretization

For discretization and finally numerical implementation of the beam and shell models the *Rayleigh-Ritz* method, an alternative to the commonly used Galerkin method, is used as a starting point. The Rayleigh-Ritz method uses the variational formulation and imposes an approximation of the solution to find a system of equations [146]. The choice of the basis functions in this approximation leads to the finite element method or Isogeometric analysis. Let us approximate the unknown, deformed configuration using an infinite series of basis functions and weighting functions, i.e.

$$\mathbf{x} = \sum_{j=1}^{\infty} x_j(\tau)\boldsymbol{\Psi}_j(\boldsymbol{\theta}) = \sum_{j=1}^{\infty}(X_j(\tau)+u_j(\tau))\boldsymbol{\Psi}_j(\boldsymbol{\theta}) \approx \sum_{j=1}^{N}(X_j(\tau)+u_j(\tau))\boldsymbol{\Psi}_j(\boldsymbol{\theta}). \tag{3.29}$$

Here, N is a finite number of degrees of freedom, hence the third equality is an approximation. Furthermore, the coefficients $x_j(\tau) = X_j(\tau) + u_j(\tau)$ are time-dependent coefficients corresponding to basis functions $\mathbf{\Psi}_j$ and are to be determined. Accordingly, $\mathbf{\Psi}_j$ is a tensor product basis to be chosen for the Finite Element Method or Isogeometric Analysis. In Finite Element Methods, the tensor product basis is defined element-wise. In the context of Isogeometric Analysis, the tensor product basis is the CAD basis of the undeformed geometry with coefficients X_j. Hence, the coefficients u_j are to be determined for both beam and shell models.

In case of a beam, the tensor basis $\mathbf{\Psi}_j$ has a one-dimensional domain $\Omega \in \mathbb{R}$ and the solution consists of a in-plane and out-of-plane deformations, thus the solution has two degrees of freedom. For the shell, the basis is two-dimensional, i.e. $\Omega \in \mathbb{R}^2$, and the dimensionality of the solution is three. In the sections Section 3.3 and Section 3.4 the discretizations for the beam and shell models, respectively, are further derived.

When the bases are substituted in the variational formulations of the beam and shell models, respectively, the analytical formulation for the Jacobian from Equation (3.24) becomes a matrix $\mathrm{K}_T(\mathbf{u}_h) \in \mathbb{R}^{N\times N}$ where N denotes the total number of degrees of freedom and the matrix K_T is referred to as the *tangential stiffness matrix* depending on the discrete displacement vector $\mathbf{u}_h$. This matrix is obtained by substituting for the variation $\mathbf{v}$ the basis functions $\mathbf{\Psi}_i$ and for the variation $\mathbf{w}$ the solution $\mathbf{u}$ in terms of the unknown coefficients $\mathbf{u}_j(\tau)$ and basis functions $\mathbf{\Psi}_j$. When using the Newton-Raphson method to solve the nonlinear system of equations (see Section 4.2), the residual vector $\mathbf{R}(\mathbf{u_h})$ needs to be obtained together with the tangential stiffness matrix K_T. The residual vector is the nonlinear equation to be solved, which in case of the beam and shell model is the difference between the discretized generalized forces, i.e. $\mathbf{R}(\mathbf{u}_h) = \delta\mathbf{W}_{\text{int}}(\mathbf{u}_h) - \delta\mathbf{W}_{\text{ext}}(\mathbf{u}_h) = \mathbf{N}(\mathbf{u}_h) - Q(\mathbf{u}_h) - \mathbf{P}$. Here $\delta\mathbf{W}_{\text{int}}$ and $\delta\mathbf{W}_{\text{ext}}$ are obtained by substituting the discretized approximation in Equations (3.16) and (3.17) and in Chapter 4 the notations $\mathbf{N}(\mathbf{u})$, $\mathbf{Q}(\mathbf{u})$ and $\mathbf{P}$ will be used to denote the internal forces, the external forces depending on the displacements and the independent external forces, respectively.

Function space requirements for the basis functions $\mathbf{\Psi}$ follow from the derivatives of the mid-plane of the shell ($\mathbf{c}$) with respect to the parametric coordinates $\boldsymbol{\theta}$. As seen from the derivations in the previous section and in Section B.3.1, it can be seen that derivatives of up to second order are occurring. Since these derivatives occur in the variational form (see Equation (3.22)), they need to be integrable as well. Hence, the function space requirements for the basis functions are:

$$\mathbf{\Psi} \in H^2(\hat{\Omega}) = \left\{ \mathbf{\Psi} : \hat{\Omega} \to \mathbb{R}^2 \middle| \mathbf{\Psi}(\hat{\Omega}), \mathbf{\Psi}_{,\alpha}(\hat{\Omega}), \mathbf{\Psi}_{,\alpha,\beta}(\hat{\Omega}) \in L^2(\hat{\Omega}) \right\}. \tag{3.30}$$

Where $\hat{\Omega}$ is the parametric domain, $\mathbf{\Psi}(\hat{\Omega})$ are the basis functions, $\mathbf{\Psi}_{,\alpha}(\hat{\Omega})$ denotes the first partial derivative of the basis with respect to θ_α and $\mathbf{\Psi}(\hat{\Omega})$ denotes the second partial derivative of the basis with respect to combinations of θ_α and θ_β for $\alpha, \beta = 1, 2$. Furthermore, $L^2(\hat{\Omega})$ denotes the function space of all squared integrable functions, i.e.

$$\mathbf{\Psi} \in L^2(\hat{\Omega}) = \left\{ \mathbf{\Psi} : \hat{\Omega} \to \mathbb{R}^2 \middle| \int_{\hat{\Omega}} \left\| \mathbf{\Psi}(\hat{\Omega}) \right\|^2 \, \mathrm{d}\hat{\Omega} < \infty \right\}. \tag{3.31}$$

Where $\|\cdot\|^2$ denotes the Euclidean norm.

3.3 Euler-Bernoulli Beam Model

The first model that is derived from the equations from Section 3.2 is the *Euler-Bernoulli beam* model. This beam model is a 1D version of the thin shell theory. By this means, the Euler-Bernoulli beam assumes that the Kirchhoff Hypothesis is valid, contrary to the Timoshenko beam theory. Furthermore, the beam model derived in this section holds for a straight beam.[8] Throughout the whole section, the domain of the beam is $x \in \Omega \subset \mathbb{R}$ and the definitions presented in Figure 3.3 is used.

[8] For derivations of the finite element method for straight beams, the reader is referred to the book of Reddy [95]. Furthermore, for derivation of an isogeometric beam model the reader is referred to the paper of Weeger et al. [101] and for linear curved beam models, the reader is referred to the works of Cazzani et al.[102, 103]. The latter was implemented in this research but not considered relevant for application.

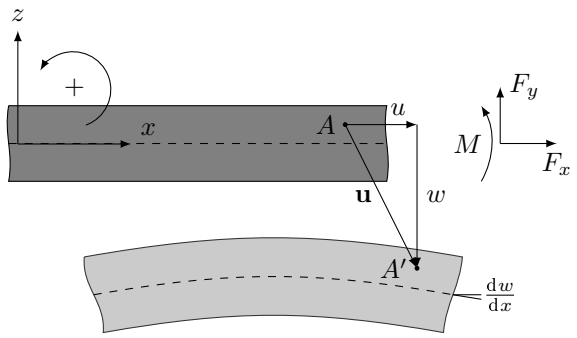

Figure 3.3: Coordinate system and definitions of the displacements $\mathbf{u} = [u, w]$ and loads F_x, F_y and M. A and A' are coordinates in the deformed and undeformed configuration, respectively.

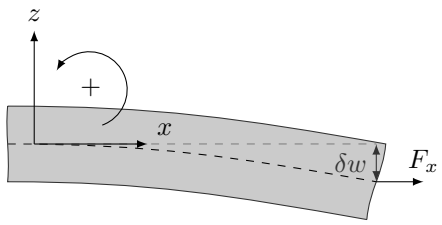

Figure 3.4: Illustration of the imposed moment $F_x \delta w$ due to a horizontal force F_x and a virtual displacement δw. The moment has positive magnitude according to the coordinate system.

In the previous section, the generalized internal and external forces have been derived (see Equation (3.23)), depending on the Gateaux derivatives of the strain and curvature tensors $\underline{\underline{\boldsymbol{\varepsilon}}}$ and $\underline{\underline{\boldsymbol{\kappa}}}$, respectively. These tensors, subsequently, are derived based on the definition of the strain which can be deduced from the deformation gradient. For the Euler-Bernoulli beam, the derivation is started with the *Von Kármán strain* (see Section B.2.1 for a derivation):

$$E_{11} = \frac{\mathrm{d}u}{\mathrm{d}x} - z\frac{\mathrm{d}^2 w}{\mathrm{d}x^2} + \frac{1}{2}\left(\frac{\mathrm{d}w}{\mathrm{d}x}\right)^2 + \boxed{\frac{\mathrm{d}w^*}{\mathrm{d}x}\frac{\mathrm{d}w}{\mathrm{d}x}}. \tag{3.32}$$

Additionally, a strain component due to an initial vertical deflection field $w^*(x)$ has been added in the derivation to be optionally used to apply initial deflections for buckling analysis in future studies. The terms coming from this component will be boxed in the sequel. The strain and curvature components are:

$$\varepsilon_{11} = \frac{\mathrm{d}u}{\mathrm{d}x} + \frac{1}{2}\left(\frac{\mathrm{d}w}{\mathrm{d}x}\right)^2 + \boxed{\frac{\mathrm{d}w^*}{\mathrm{d}x}\frac{\mathrm{d}w}{\mathrm{d}x}} \qquad \text{and} \qquad \kappa_{11} = -\frac{\mathrm{d}^2 w}{\mathrm{d}x^2}. \tag{3.33}$$

Here, w is the vertical deflection of the beam, u is the horizontal deflection and x is the length coordinate of the beam. Since a straight beam is modelled, the Cartesian material matrix from Equation (3.12) can be used. For a beam, Poisson's ratio is equal to zero, which simplifies the non-zero component of the stress tensor to:

$$S_{11} = E(\varepsilon_{11} + z\kappa_{11}). \tag{3.34}$$

And the normal force and bending moment in the beam are, according to Equation (3.15)

$$N_{11} = tE\varepsilon_{11} \qquad \text{and} \qquad M_{11} = \frac{t^3}{12}E\kappa_{11}. \tag{3.35}$$

In order to derive the variational formulation, the Gateaux derivatives of the strain and curvature have to be derived. Let $\mathbf{u} = (u, w)$ and let $\mathbf{v} = (\delta w, \delta w)$. Then, the variation of the displacement field is $\mathbf{u} = (u + \theta\delta u, w + \theta\delta w)$ and the Gateaux derivative of the strain and curvature (denoted with a prime $'$) become:

$$\begin{aligned}
\varepsilon'_{11} &= \frac{\mathrm{d}}{\mathrm{d}\theta}\left[\frac{\mathrm{d}u}{\mathrm{d}x} + \theta\frac{\mathrm{d}\delta u}{\mathrm{d}x} + \frac{1}{2}\left(\frac{\mathrm{d}w}{\mathrm{d}x} + \theta\frac{\mathrm{d}\delta w}{\mathrm{d}x}\right)^2 + \boxed{\frac{\mathrm{d}w^*}{\mathrm{d}x}\frac{\mathrm{d}w}{\mathrm{d}x} + \theta\frac{\mathrm{d}w^*}{\mathrm{d}x}\frac{\mathrm{d}\delta w}{\mathrm{d}x}}\right]\Bigg|_{\theta=0} \\
&= \frac{\mathrm{d}\delta u}{\mathrm{d}x} + \frac{\mathrm{d}w}{\mathrm{d}x}\frac{\mathrm{d}\delta w}{\mathrm{d}x} + \boxed{\frac{\mathrm{d}w^*}{\mathrm{d}x}\frac{\mathrm{d}\delta w}{\mathrm{d}x}} \qquad \text{and} \\
\kappa'_{11} &= \frac{\mathrm{d}}{\mathrm{d}\theta}\left(-\frac{\mathrm{d}^2 w}{\mathrm{d}x^2} - \theta\frac{\mathrm{d}^2\delta w}{\mathrm{d}x^2}\right)\Bigg|_{\theta=0} = -\frac{\mathrm{d}^2\delta w}{\mathrm{d}x^2}.
\end{aligned} \tag{3.36}$$

Using the result from Equation (3.36) and Equation (3.35), the variational form from Equation (3.22) can be

derived:

$$b\int_\Omega -\rho t\left(\ddot{u}\delta u+\ddot{w}\delta w\right)-tE\left(\frac{\mathrm{d}u}{\mathrm{d}x}+\frac{1}{2}\left(\frac{\mathrm{d}w}{\mathrm{d}x}\right)^2+\boxed{\frac{\mathrm{d}w^*}{\mathrm{d}x}\frac{\mathrm{d}w}{\mathrm{d}x}}\right)\left(\frac{\mathrm{d}\delta u}{\mathrm{d}x}+\frac{\mathrm{d}w}{\mathrm{d}x}\frac{\mathrm{d}\delta w}{\mathrm{d}x}+\boxed{\frac{\mathrm{d}w^*}{\mathrm{d}x}\frac{\mathrm{d}\delta w}{\mathrm{d}x}}\right)$$
$$-\frac{t^3}{12}E\frac{\mathrm{d}^2w}{\mathrm{d}x^2}\frac{\mathrm{d}^2\delta w}{\mathrm{d}x^2}+\mathbf{t}\cdot\mathbf{v}\,\mathrm{d}\Omega=0.$$

Where the integral has been evaluated over the width b of the beam since the solution is constant in this direction. The external work, represented by the term $\mathbf{t}\cdot\mathbf{v}$ is not specified yet. For the beam, the external work will be decomposed by a surface pressure $p(x)$ working in vertical direction, a surface traction $t(x)$ working in horizontal direction, a pressure $\hat{p}(x)\hat{\mathbf{n}}$ following the normal direction $\hat{\mathbf{n}}$ of the beam and a horizontal force $F_x(x_i)$, a vertical force $F_y(x_i)$ and a moment $M(x_i)$ working on the end points x_i of the beam. The work of the moment is computed by multiplying the moment by the virtual rotation $\frac{\mathrm{d}\delta w}{\mathrm{d}x}$ of the beam, whereas the other force components are multiplied by the virtual displacements δu and δw (see Figure 3.4). Furthermore, in the small angle approximation, the horizontal force also exerts work in the form of a moment. The following variational form is obtained:

$$\int_\Omega \rho A\left(\ddot{u}\delta u+\ddot{w}\delta w\right)+EA\left(\frac{\mathrm{d}u}{\mathrm{d}x}+\frac{1}{2}\left(\frac{\mathrm{d}w}{\mathrm{d}x}\right)^2+\boxed{\frac{\mathrm{d}w^*}{\mathrm{d}x}\frac{\mathrm{d}w}{\mathrm{d}x}}\right)\left(\frac{\mathrm{d}\delta u}{\mathrm{d}x}+\frac{\mathrm{d}w}{\mathrm{d}x}\frac{\mathrm{d}\delta w}{\mathrm{d}x}+\boxed{\frac{\mathrm{d}w^*}{\mathrm{d}x}\frac{\mathrm{d}\delta w}{\mathrm{d}x}}\right)$$
$$+EI\frac{\mathrm{d}^2w}{\mathrm{d}x^2}\frac{\mathrm{d}^2\delta w}{\mathrm{d}x^2}\,\mathrm{d}\Omega=b\int_\Omega t\delta u+p\delta w\,\mathrm{d}\Omega+\left[F_x\left(\delta u+\delta w\frac{\mathrm{d}w}{\mathrm{d}x}\right)+F_y\delta w+M\frac{\mathrm{d}\delta w}{\mathrm{d}x}\right]\Bigg|_{x_1}^{x_2},\quad(3.37)$$

Where

$$A=bt\qquad\text{and}\qquad I=\frac{bt^3}{12}.$$

For nonlinear computations as briefly mentioned in the end of Section 3.2, the Jacobian matrix from Equation (3.24) needs to be derived. Computation of this term requires the Gateaux derivatives of ε'_{11}, κ'_{11}, N_{11} and M_{11}. These Gateaux derivatives are computed using the variations $\Delta\mathbf{u}=(\Delta u,\Delta v)$ to which will later be referred as the increments of the Newton iterations. The Gateaux derivatives are:

$$\begin{aligned}
\varepsilon''_{11}&=\frac{\mathrm{d}}{\mathrm{d}\theta}\left[\frac{\mathrm{d}\delta u}{\mathrm{d}x}+\frac{\mathrm{d}w}{\mathrm{d}x}\frac{\mathrm{d}\delta w}{\mathrm{d}x}+\theta\frac{\mathrm{d}\Delta w}{\mathrm{d}x}\frac{\mathrm{d}\delta w}{\mathrm{d}x}+\boxed{\frac{\mathrm{d}w^*}{\mathrm{d}x}\frac{\mathrm{d}\delta w}{\mathrm{d}x}}\right]\Bigg|_{\theta=0}=\frac{\mathrm{d}\Delta w}{\mathrm{d}x}\frac{\mathrm{d}\delta w}{\mathrm{d}x},\\
\kappa''_{11}&=\frac{\mathrm{d}}{\mathrm{d}\theta}\left(-\frac{\mathrm{d}^2\delta w}{\mathrm{d}x^2}\right)\Bigg|_{\theta=0}=0,\\
N'_{11}&=tE\varepsilon'_{11}=tE\left(\frac{\mathrm{d}\Delta u}{\mathrm{d}x}+\frac{\mathrm{d}w}{\mathrm{d}x}\frac{\mathrm{d}\Delta w}{\mathrm{d}x}+\boxed{\frac{\mathrm{d}w^*}{\mathrm{d}x}\frac{\mathrm{d}\Delta w}{\mathrm{d}x}}\right)\qquad\text{and}\\
M'_{11}&=\frac{t^3}{12}E\kappa'_{11}=-\frac{t^3}{12}E\frac{\mathrm{d}^2\Delta w}{\mathrm{d}x^2}.
\end{aligned}$$

Such that the Jacobian of the internal force becomes:

$$\begin{aligned}
K_T(\mathbf{u},\delta\mathbf{u},\Delta\mathbf{u})&=\int_\Omega N_{11}\varepsilon''_{11}+N'_{11}\varepsilon'_{11}+M_{11}\kappa''_{11}+M'_{11}\kappa'_{11}\,\mathrm{d}\Omega\\
&=\int_\Omega EA\left(\frac{\mathrm{d}u}{\mathrm{d}x}+\frac{1}{2}\left(\frac{\mathrm{d}w}{\mathrm{d}x}\right)^2+\boxed{\frac{\mathrm{d}w^*}{\mathrm{d}x}\frac{\mathrm{d}w}{\mathrm{d}x}}\right)\frac{\mathrm{d}\Delta w}{\mathrm{d}x}\frac{\mathrm{d}\delta w}{\mathrm{d}x}\\
&\quad+EA\left(\frac{\mathrm{d}\Delta u}{\mathrm{d}x}+\frac{\mathrm{d}w}{\mathrm{d}x}\frac{\mathrm{d}\Delta w}{\mathrm{d}x}+\boxed{\frac{\mathrm{d}w^*}{\mathrm{d}x}\frac{\mathrm{d}\Delta w}{\mathrm{d}x}}\right)\left(\frac{\mathrm{d}\delta u}{\mathrm{d}x}+\frac{\mathrm{d}w}{\mathrm{d}x}\frac{\mathrm{d}\delta w}{\mathrm{d}x}+\boxed{\frac{\mathrm{d}w^*}{\mathrm{d}x}\frac{\mathrm{d}\delta w}{\mathrm{d}x}}\right)\\
&\quad+EI\frac{\mathrm{d}^2\Delta w}{\mathrm{d}x^2}\frac{\mathrm{d}^2\delta w}{\mathrm{d}x^2}\,\mathrm{d}\Omega.
\end{aligned}\qquad(3.38)$$

3.3.1 Numerical Discretization

Numerical discretization of the beam model is performed by using the Rayleigh-Ritz method on the variational formulation of Equation (3.37). The tensor basis $\mathbf{\Psi}_j$ corresponding to the approximation from Equation (3.29) is a vector of basis functions for the approximation of the in-plane and out-of-plane deformations $u(x)$ and $w(x)$ with bases $\psi(x)$ and $\varphi(x)$, respectively, which can be of different polynomial order. The tensor product basis is defined by:

$$\mathbf{\Psi}_j = \begin{bmatrix} \psi_j \\ \varphi_j \end{bmatrix} \circ \mathbf{e}_j. \tag{3.39}$$

Here, $\circ$ denotes and element-wise vector product, i.e. the Hadamard-product (or Schur-product) [147], and the vector $\mathbf{e_j}$ is the unit vector which is equal to $[1 \quad 0]^T$ for the first n degrees of freedom and $[0 \quad 1]^T$ for the last m degrees of freedom. In other words, $j = 0, \ldots, n, n+1, \ldots, n+m = N$, where N denotes the total number of degrees of freedom of the system, after implementation of Dirichlet boundaries (see Section 3.3.2). In this way, the Rayleigh-Ritz approximation becomes:

$$\mathbf{u} = \begin{bmatrix} u \\ w \end{bmatrix} \approx \sum_{j=1}^{N} \alpha_j \begin{bmatrix} \psi_j \\ \varphi_j \end{bmatrix} \circ \mathbf{e}_j = \mathbf{u}_h. \tag{3.40}$$

The coefficients α_j are to be determined and the unit vector $\mathbf{e}_j$ switches on index n which is determined by the number of basis functions for the in-plane and out-of-plane solutions u and w. Based on the weak formulation of the beam equation in Equation (3.37), a splitting to a system of equations for the variations δu and δw separately can be introduced since the variations are chosen arbitrarily from relevant function spaces. This results in the *weak formulation*

$$\begin{cases} \text{Find } u \in H^1(\Omega),\ w \in H^2(\Omega) \text{ with } \Omega = (x_1, x_2) \in \mathbb{R}^1 \text{ such that} \\ \displaystyle\int_\Omega \rho A \ddot{u} \delta u + EA \left(\frac{\mathrm{d}u}{\mathrm{d}x} + \frac{1}{2} \left(\frac{\mathrm{d}w}{\mathrm{d}x} \right)^2 + \boxed{\frac{\mathrm{d}w^*}{\mathrm{d}x} \frac{\mathrm{d}w}{\mathrm{d}x}} \right) \frac{\mathrm{d}\delta u}{\mathrm{d}x} \,\mathrm{d}\Omega = b \int_\Omega t \delta u \,\mathrm{d}\Omega + F_x \delta u \Big|_{x_1}^{x_2} \\ \displaystyle\int_\Omega \rho A \ddot{w} \delta w + EA \left(\frac{\mathrm{d}u}{\mathrm{d}x} + \frac{1}{2} \left(\frac{\mathrm{d}w}{\mathrm{d}x} \right)^2 + \boxed{\frac{\mathrm{d}w^*}{\mathrm{d}x} \frac{\mathrm{d}w}{\mathrm{d}x}} \right) \left(\frac{\mathrm{d}w}{\mathrm{d}x} \frac{\mathrm{d}\delta w}{\mathrm{d}x} + \boxed{\frac{\mathrm{d}w^*}{\mathrm{d}x} \frac{\mathrm{d}\delta w}{\mathrm{d}x}} \right) + EI \frac{\mathrm{d}^2 w}{\mathrm{d}x^2} \frac{\mathrm{d}^2 \delta w}{\mathrm{d}x^2} \,\mathrm{d}\Omega \\ = b \displaystyle\int_\Omega p \delta w \,\mathrm{d}\Omega + \left[F_x \delta w \frac{\mathrm{d}w}{\mathrm{d}x} + F_y \delta w + M \frac{\mathrm{d}\delta w}{\mathrm{d}x} \right] \Big|_{x_1}^{x_2} \\ \forall \delta u \in H^1(\Omega) \text{ and } \delta w \in H^2(\Omega). \end{cases} \tag{3.41}$$

Now, suppose that the discretized solution $\mathbf{u}_h \in \Sigma$, where $\Sigma(\Omega)$ is a function space such that the solution vector $\mathbf{u}_h$ complies with the boundary conditions of the beam and for which $(u_h, w_h) \in \{u, w \in H^1(\Omega) \times H^2(\Omega)\}$. Then, the variations of $\mathbf{u}$, $\delta\mathbf{u}$ are also in $\Sigma(\Omega)$. This means that we can let

$$\delta\mathbf{u} = \begin{bmatrix} \psi_j \\ \varphi_j \end{bmatrix} \circ \mathbf{e}_j,$$

and combined with the other assumptions, the variational form becomes (see Equation (3.37))

$$\mathrm{M}\ddot{\alpha} + \mathbf{R}(\mathbf{u}_h) = \mathbf{0}. \tag{3.42}$$

Here, the mass matrix M is defined as:

$$\mathrm{M} = \begin{bmatrix} \mathrm{M}_A & 0 \\ 0 & \mathrm{M}_B \end{bmatrix} \quad \text{with} \quad \mathrm{M}_{A,ij} = \int_{\hat{\Omega}} \rho A \psi_i \psi_j \sqrt{\det(g_{\alpha\beta})} \,\mathrm{d}\hat{\Omega} \quad \text{and} \quad \mathrm{M}_{B,ij} = \int_{\hat{\Omega}} \rho A \varphi_i \varphi_j \sqrt{\det(g_{\alpha\beta})} \,\mathrm{d}\hat{\Omega} \tag{3.43}$$

With $\sqrt{\det(g_{\alpha\beta})}$ the *measure* of the mapping between the parameter space and the physical space. For a normalized knot vector with uniform spacing $\Delta\xi$, this factor is equal to the length L of the beam. The residual vector $\mathbf{R}(\mathbf{u}_h)$ is defined as:

$$\mathbf{R}(\mathbf{u}_h) = [R_1(\mathbf{u}_h) R_2(\mathbf{u}_h)]^T. \tag{3.44}$$

With:

$$R_1(\mathbf{u}_h) = \int_{\hat{\Omega}} EA\left(\frac{\mathrm{d}u}{\mathrm{d}x} + \frac{1}{2}\left(\frac{\mathrm{d}w}{\mathrm{d}x}\right)^2 + \boxed{\frac{\mathrm{d}w^*}{\mathrm{d}x}\frac{\mathrm{d}w}{\mathrm{d}x}}\right)\frac{\mathrm{d}\psi_i}{\mathrm{d}x}\,\mathrm{d}\Omega - b\int_{\Omega} t\psi_i\sqrt{\det(g_{\alpha\beta})}\,\mathrm{d}\hat{\Omega} - F_x\delta u\Big|_{x_1}^{x_2},$$

$$R_2(\mathbf{u}_h) = \int_{\hat{\Omega}}\left[EA\left(\frac{\mathrm{d}u}{\mathrm{d}x} + \frac{1}{2}\left(\frac{\mathrm{d}w}{\mathrm{d}x}\right)^2 + \boxed{\frac{\mathrm{d}w^*}{\mathrm{d}x}\frac{\mathrm{d}w}{\mathrm{d}x}}\right)\left(\frac{\mathrm{d}w}{\mathrm{d}x}\frac{\mathrm{d}\varphi_i}{\mathrm{d}x} + \boxed{\frac{\mathrm{d}w^*}{\mathrm{d}x}\frac{\mathrm{d}\varphi_i}{\mathrm{d}x}}\right) + EI\frac{\mathrm{d}^2w}{\mathrm{d}x^2}\frac{\mathrm{d}^2\varphi_i}{\mathrm{d}x^2}\right]\sqrt{\det(g_{\alpha\beta})}\,\mathrm{d}\hat{\Omega}$$
$$-b\int_{\hat{\Omega}} p\delta w\sqrt{\det(g_{\alpha\beta})}\,\mathrm{d}\hat{\Omega} - \left[F_x\delta w\frac{\mathrm{d}w}{\mathrm{d}x} + F_y\delta w + M\frac{\mathrm{d}\delta w}{\mathrm{d}x}\right]\Big|_{x_1}^{x_2}.$$

Since the basis functions are defined on the parametric domain Ω, the measure $\sqrt{\det(g_{\alpha\beta})}$ is again used for integration of the basis functions in the domain $\hat{\Omega}$. Furthermore, the Jacobian matrix is constructed based on the variations $\delta\mathbf{u}$ and $\Delta\mathbf{u}$. Here, the second variation represents the differentials of the Jacobian entries hence these variations should be approximated using a finite series analogously to Equation (3.29). Since both $\delta\mathbf{u}$ and $\Delta\mathbf{u}$ are variations of the solution $\mathbf{u}$, they have to be chosen from $\Sigma(\Omega)$. Therefore, the same basis functions φ_j and ψ_j can be used in the Jacobian and thus

$$\Delta\mathbf{u} = \sum_{j=1}^{N}\alpha_j\begin{bmatrix}\psi_j\\ \varphi_j\end{bmatrix}\circ\mathbf{e}_j \qquad \text{and} \qquad \delta\mathbf{u} = \begin{bmatrix}\psi_i\\ \varphi_i\end{bmatrix}\circ\mathbf{e}_i. \tag{3.45}$$

Such that the Jacobian from Equation (3.38) becomes:

$$\mathrm{K}_T = \begin{bmatrix}\mathrm{K}_{T,11} & \mathrm{K}_{T,12}\\ \mathrm{K}_{T,21} & \mathrm{K}_{T,22}\end{bmatrix}, \tag{3.46}$$

where:

$$\begin{aligned}
\mathrm{K}_{T,11,ij} = \mathrm{K}_{T,\delta u\Delta u} &= \int_{\hat{\Omega}}\left(EA\frac{\mathrm{d}\psi_i}{\mathrm{d}x}\frac{\mathrm{d}\psi_j}{\mathrm{d}x}\right)\sqrt{\det(g_{\alpha\beta})}\,\mathrm{d}\hat{\Omega},\\
\mathrm{K}_{T,12,ij} = \mathrm{K}_{T,\delta u\Delta w} &= \int_{\hat{\Omega}}\left(EA\frac{\mathrm{d}w}{\mathrm{d}x}\frac{\mathrm{d}\varphi_j}{\mathrm{d}x}\frac{\mathrm{d}\psi_i}{\mathrm{d}x} + \boxed{\frac{\mathrm{d}w^*}{\mathrm{d}x}\frac{\mathrm{d}\varphi_j}{\mathrm{d}x}\frac{\mathrm{d}\psi_i}{\mathrm{d}x}}\right)\sqrt{\det(g_{\alpha\beta})}\,\mathrm{d}\hat{\Omega},\\
\mathrm{K}_{T,21,ij} = \mathrm{K}_{T,\delta w\Delta u} &= \int_{\hat{\Omega}}\frac{\mathrm{d}\psi_j}{\mathrm{d}x}\frac{\mathrm{d}\varphi_i}{\mathrm{d}x}\left(\frac{\mathrm{d}\delta w}{\mathrm{d}x} + \boxed{\frac{\mathrm{d}w^*}{\mathrm{d}x}}\right)\sqrt{\det(g_{\alpha\beta})}\,\mathrm{d}\hat{\Omega}, \qquad \text{and}\\
\mathrm{K}_{T,22,ij} = \mathrm{K}_{T,\delta w\Delta w} &= \int_{\hat{\Omega}}\left(EA\left(\frac{\mathrm{d}u}{\mathrm{d}x} + \boxed{\frac{\mathrm{d}w^*}{\mathrm{d}x}\frac{\mathrm{d}w}{\mathrm{d}x}}\right)\frac{\mathrm{d}\varphi_i}{\mathrm{d}x}\frac{\mathrm{d}\varphi_j}{\mathrm{d}x} + \frac{3}{2}\left(\frac{\mathrm{d}w}{\mathrm{d}x}\right)^2\frac{\mathrm{d}\varphi_i}{\mathrm{d}x}\frac{\mathrm{d}\varphi_j}{\mathrm{d}x}\right.\\
&\quad\left. + \boxed{2EA\frac{\mathrm{d}w^*}{\mathrm{d}x}\frac{\mathrm{d}w}{\mathrm{d}x}\frac{\mathrm{d}\varphi_i}{\mathrm{d}x}\frac{\mathrm{d}\varphi_j}{\mathrm{d}x} + EA\left(\frac{\mathrm{d}w^*}{\mathrm{d}x}\right)^2\frac{\mathrm{d}\varphi_i}{\mathrm{d}x}\frac{\mathrm{d}\varphi_j}{\mathrm{d}x}} + EI\frac{\mathrm{d}^2\varphi_i}{\mathrm{d}x^2}\frac{\mathrm{d}^2\varphi_j}{\mathrm{d}x^2}\right)\sqrt{\det(g_{\alpha\beta})}\,\mathrm{d}\hat{\Omega}.
\end{aligned} \tag{3.47}$$

Here, $\sqrt{\det(g_{\alpha\beta})}$ denotes the measure of the mapping from the parametric domain $\hat{\Omega}$ to the physical domain Ω. For convenience of the derivation, the entry $\mathrm{K}_{T,11,\delta u\Delta u}$ is the Jacobian entry that is derived by collecting all terms of Equation (3.38) with the product $\Delta u\delta u$ and similar notations hold for other combinations of Δu and Δw with δu and δw. Furthermore, the present formulations are then obtained by replacing Δu with ψ_j, Δw with φ_j, δu with ψ_i and δw with φ_i, according to Equation (3.45). The solution $\mathbf{u}$ will represent the solution in a previous iteration later.

3.3.2 Implementation Aspects

Using the tangential stiffness matrix from Equation (3.46) and the residual from Equation (3.44), the solution for the nonlinear beam can almost be computed. In this section, numerical procedures for the beam will be covered.

Numerical Integration

In the formulation of the Jacobian matrix and residual, integrals over the domain x, or more specifically the length of the beam, are yet to be computed. In the present analysis, the basis functions are chosen to be B-splines (i.e. NURBS with weights 1). This means that no analytical quadrature rules are available. One could for instance use the quadrature rules described by Hughes et al. [132] and Auricchio et al. [133]. Although not optimal according to Hughes et al.[132] Gauss quadrature rules are used to evaluate the integrals for matrix assembly. More specifically, *Gauss-Lobatto quadrature*, which includes end points of the interval, is used. This integration rule is exact for polynomial functions with degree $2n-3$, $n=p+1$ for spline degree p and has the advantage over Gauss integration since the end-points of the piece-wise polynomials overlap with other intervals, but have to be calculated only once [148, 149]. Generally, Gauss and Gauss-Lobatto integration given weights w_i and quadrature points x_i is given by (given that the order is sufficiently high that integration is exact):

$$\int_{-1}^{1} f(x)\,\mathrm{d}\Omega = \sum_{j=1}^{N} w_j f(x_j). \tag{3.48}$$

For some function $f(x)$. Alternatively, for an interval $[0,1]$ which is typical for normalized knot vectors,

$$\int_{0}^{1} f(x)\,\mathrm{d}\Omega = \frac{1}{2}\sum_{j=1}^{N} w_j f\left(\frac{x_j+1}{2}\right). \tag{3.49}$$

The weights and quadrature point of Gauss and Gauss-Lobatto rules can be found in many textbooks, including the extensive work by Abramowitz et al.[150].

Boundary Conditions

For the beam boundary conditions, two types are distinguished: *essential* and *natural* boundary conditions. Combining these boundary conditions gives the ability to model free end-points (zero force and moment), pinned end-points (zero moment, zero vertical displacement and horizontal), clamped end-points (zero rotations and vertical and horizontal displacement), rolled end-points (zero rotations and vertical displacement, zero horizontal force) or any combination of prescribed forces, moments, rotations and displacements.[9]

Essential Boundary Conditions

In case of essential boundary conditions, rotations or displacements on the beam end-points are prescribed. In the present beam model, the boundary conditions are imposed by modifying the row of the system matrix and the right-hand side vector corresponding to the end-point x_i such that for an imposed displacement δ_i

$$\sum_{j=1}^{N} \alpha_j \mathbf{\Psi}_j(x_i) = \delta_i.$$

A similar procedure can be followed for the prescribed rotation. In case of homogeneous Dirichlet boundary conditions, i.e. Dirichlet boundary conditions with value 0, the function space $\Sigma(\Omega)$ is restricted. Hereby, when the horizontal or vertical displacements, u or w, are zero on an end-point, the basis functions are zero here and hence these degrees of freedom are not taken into account. Similarly, zero rotations on the end-point can be implemented.

Natural Boundary Conditions

In case of natural boundary conditions, forces and/or moments are applied on the end-points of the beam. As can be seen in the weak formulation in Equation (3.41), forces and moments appear on the boundary integrals and hence their implementation is rather straightforward and thus *natural*. For example, if a horizontal load is applied on the beam end x_k, then the boundary integrals in both equations in Equation (3.41) result in a right-hand side contribution of $F_x\psi_i(x_k)$ for all ψ_i that are nonzero on x_k for the first equation and a matrix contribution of $F_x\varphi_i(x_k)\frac{\mathrm{d}\varphi_j}{\mathrm{d}x}$ for the row corresponding to the control point of the beam end at x_k in case of the second equation. In the case of homogeneous natural boundary conditions, i.e. zero forces or moments, the boundary terms simply vanish.

[9] For elementary details on beam boundary conditions, the reader is referred to textbooks of Hibbeler [151], amongst others.

3.4 Kirchhoff-Love Shell Model

The formulations for the strain tensors, the stress tensors and the normal force and moment tensors are presented in Equations (3.7), (3.8), (3.13) and (3.14), respectively. Those formulations are valid for deforming surfaces, i.e. shell elements and hence form the basis of Kirchhoff-Love shell theory. In this section, the Gateaux derivatives of the strain, stress and force and moment tensors are derived in order to complete the derivation of the weak form using Equation (3.23) and Equation (3.22). Additionally, the relevant terms for computation of the tangential stiffness matrix from Equation (3.24) are derived.

Firstly, in order to formulate the variational formulation for the shell problem (see Equation (3.22)), the variation of the strain and curvature tensors $\underline{\underline{\boldsymbol{\varepsilon}}}$ and $\underline{\underline{\boldsymbol{\kappa}}}$ are required. From Equations (B.18) and (B.19) in Section B.3.1 these terms are (in Voight notation)

$$\underline{\underline{\boldsymbol{\varepsilon}}}' = \begin{bmatrix} \varepsilon'_{11} \\ \varepsilon'_{22} \\ 2\varepsilon'_{12} \end{bmatrix} = \begin{bmatrix} \frac{\partial \mathbf{v}}{\partial \theta_1} \cdot \frac{\partial \mathbf{c}}{\partial \theta_1} \\ \frac{1}{2}\frac{\partial \mathbf{v}}{\partial \theta_2} \cdot \frac{\partial \mathbf{c}}{\partial \theta_1} \\ \frac{\partial \mathbf{v}}{\partial \theta_1} \cdot \frac{\partial \mathbf{c}}{\partial \theta_2} + \frac{\partial \mathbf{v}}{\partial \theta_1} \cdot \frac{\partial \mathbf{c}}{\partial \theta_2} \end{bmatrix} \qquad \text{and} \qquad \underline{\underline{\boldsymbol{\kappa}}}' = \begin{bmatrix} \kappa'_{11} \\ \kappa'_{22} \\ \kappa'_{12} \end{bmatrix} = \begin{bmatrix} -\frac{\partial^2 \mathbf{v}}{\partial \theta_1^2} \cdot \hat{\mathbf{n}} - \frac{\partial^2 \mathbf{c}}{\partial \theta_1^2} \cdot \hat{\mathbf{n}}'(\mathbf{c}) \\ -\frac{\partial^2 \mathbf{v}}{\partial \theta_2^2} \cdot \hat{\mathbf{n}} - \frac{\partial^2 \mathbf{c}}{\partial \theta_2^2} \cdot \hat{\mathbf{n}}'(\mathbf{c}) \\ -\frac{\partial^2 \mathbf{v}}{\partial \theta_1 \partial \theta_2} \cdot \hat{\mathbf{n}} - \frac{\partial^2 \mathbf{c}}{\partial \theta_1 \partial \theta_2} \cdot \hat{\mathbf{n}}' \end{bmatrix}.$$

And the variation of the normal vector, $\hat{\mathbf{n}}'$ is given by Equation (B.20) (see also Section B.3.1)

$$\hat{\mathbf{n}}'(\mathbf{u}, \mathbf{v}) = \frac{\frac{\partial \mathbf{v}}{\partial \theta^1} \times \frac{\partial \mathbf{c}}{\partial \theta^2} + \frac{\partial \mathbf{c}}{\partial \theta^1} \times \frac{\partial \mathbf{v}}{\partial \theta^2}}{\left\| \frac{\partial \mathbf{c}}{\partial \theta^1} \times \frac{\partial \mathbf{c}}{\partial \theta^2} \right\|} + \left[-\frac{1}{\left\| \frac{\partial \mathbf{c}}{\partial \theta^1} \times \frac{\partial \mathbf{c}}{\partial \theta^2} \right\|^2} \frac{\frac{\partial \mathbf{c}}{\partial \theta^1} \times \frac{\partial \mathbf{c}}{\partial \theta^2}}{\left\| \frac{\partial \mathbf{c}}{\partial \theta^1} \times \frac{\partial \mathbf{c}}{\partial \theta^2} \right\|} \left(\frac{\partial \mathbf{v}}{\partial \theta^1} \times \frac{\partial \mathbf{c}}{\partial \theta^2} + \frac{\partial \mathbf{c}}{\partial \theta^1} \times \frac{\partial \mathbf{v}}{\partial \theta^2} \right) \right].$$

Using the formulations for the variation of the strain tensor, the curvature tensor and the normal vector, the internal and external energies can be computed from Equation (3.23). Furthermore, for the Jacobian of the variational form system from Equation (3.22) for a Kirchhoff-Love shell requires computation of the second variations of the strain and curvature tensors and the first variations of the normal and moment tensors. These quantities are also derived in Section B.3.1 in Equations (B.22) to (B.25).

$$\underline{\underline{\boldsymbol{\varepsilon}}}'' = \begin{bmatrix} \varepsilon''_{11} \\ \varepsilon''_{22} \\ 2\varepsilon''_{12} \end{bmatrix} = \begin{bmatrix} \frac{\partial \mathbf{v}}{\partial \theta_1} \cdot \frac{\partial \mathbf{w}}{\partial \theta_1} \\ \frac{\partial \mathbf{v}}{\partial \theta_2} \cdot \frac{\partial \mathbf{w}}{\partial \theta_2} \\ \frac{\partial \mathbf{v}}{\partial \theta_1} \cdot \frac{\partial \mathbf{w}}{\partial \theta_2} + \frac{\partial \mathbf{v}}{\partial \theta_1} \cdot \frac{\partial \mathbf{w}}{\partial \theta_2} \end{bmatrix}, \qquad \underline{\underline{\boldsymbol{\kappa}}}'(\mathbf{u}, \mathbf{v}) = \begin{bmatrix} \kappa''_{11} \\ \kappa''_{22} \\ \kappa''_{12} \end{bmatrix} = \begin{bmatrix} -\frac{\partial^2 \mathbf{v}}{\partial \theta_1^2} \cdot \hat{\mathbf{n}}' - \left(\frac{\partial^2 \mathbf{w}}{\partial \theta_1^2} \cdot \hat{\mathbf{n}}' + \frac{\partial^2 \mathbf{w}}{\partial \theta_1^2} \cdot \hat{\mathbf{n}}'' \right) \\ -\frac{\partial^2 \mathbf{v}}{\partial \theta_1^2} \cdot \hat{\mathbf{n}}' - \left(\frac{\partial^2 \mathbf{w}}{\partial \theta_1^2} \cdot \hat{\mathbf{n}}' + \frac{\partial^2 \mathbf{w}}{\partial \theta_1^2} \cdot \hat{\mathbf{n}}'' \right) \\ -\frac{\partial^2 \mathbf{v}}{\partial \theta_1 \partial \theta_2} \cdot \hat{\mathbf{n}} - \left(\frac{\partial^2 \mathbf{w}}{\partial \theta_1 \partial \theta_2} \cdot \hat{\mathbf{n}}' + \frac{\partial^2 \mathbf{c}}{\partial \theta_1 \partial \theta_2} \cdot \hat{\mathbf{n}}'' \right) \end{bmatrix},$$

$$\underline{\underline{\boldsymbol{N}}}' = t\mathcal{C} : \underline{\underline{\boldsymbol{\varepsilon}}}'(\mathbf{u}, \mathbf{v}), \qquad \text{and} \qquad \underline{\underline{\boldsymbol{M}}}'(\mathbf{u}, \mathbf{v}) = \frac{t^3}{12}\mathcal{C} : \underline{\underline{\boldsymbol{\kappa}}}'(\mathbf{u}, \mathbf{v}).$$

3.4.1 Numerical Discretization

Numerical discretization of the shell model is also performed by using the Rayleigh-Ritz method on the variational formulation of Equation (3.22). Since the coordinate system is governed by Equation (3.2), the approximation of the displacement field $\mathbf{u}_h$ should be substituted in the formulation of the deformed mid-plane configuration $\mathbf{c}_h$ and the corresponding normal vector $\hat{\mathbf{n}}_h$ to discretize the Jacobian matrix from Equation (3.24) and the generalised force residual. The approximation of the displacement field $\mathbf{u}_h$ is again approximated by the Rayleigh-Ritz method (see Equation (3.29)),

$$\mathbf{u}_h = \sum_{j=1}^{N} \boldsymbol{\Psi}_j \alpha_j(\tau). \tag{3.50}$$

Here, $\alpha_j(\tau)$ are again time-dependent coefficients to be determined and $\boldsymbol{\Psi}_j$ are the basis functions for the shell. Analogously to the work of Goyal [142], the basis functions are (NUR)B-spline *tensor products* (see Section 4.1 for details) and the basis functions are the same for each displacement unknown, i.e.

$$\boldsymbol{\Psi}_j = \mathbf{e}_j R_{kl,pq}. \tag{3.51}$$

Were $\mathbf{e}_j$ is a unit vector which is used in a similar way as for the beam model, but then for three degrees of freedom and $R_{kl,pq}$ is the (NUR)B-spline tensor product with indices k and l in the first and second bases

of orders p and q, respectively. Substituting the approximation from Equations (3.50) and (3.51) for the displacements and substituting the basis from Equation (3.51) for the variation $\mathbf{v}$ in the weak formulation gives the mass matrix for the kinetic energy contribution [142].

$$\mathrm{M}_{ij} = \int_{\Omega} \rho t \boldsymbol{\Psi}(\mathbf{x})_j \cdot \boldsymbol{\Psi}(\mathbf{x})_i \, \mathrm{d}\Omega = \int_{\hat{\Omega}} \rho t \boldsymbol{\Psi}(\boldsymbol{\theta})_j \cdot \boldsymbol{\Psi}(\boldsymbol{\theta})_i \sqrt{\det(g_{\alpha\beta})} \, \mathrm{d}\hat{\Omega}. \tag{3.52}$$

Here, the second equality represents the integral over the parametric domain Ω. Note that the use of the vector $\mathbf{e}_j$ in the definition of $\boldsymbol{\Psi}_j$ results in a per-degree of freedom block-structure of the mass matrix. Similar to the beam model, we can use the Rayleigh-Ritz method to approximate the increment of the Newton iterations (see Section 4.2 for details about Newton Iterations) and hence to substitute for the variation $\mathbf{w}$ in Equation (3.24). Substituting for the variation $\mathbf{v}$ again the basis functions $\boldsymbol{\Psi}_i$ gives the Jacobian matrix or the Tangential Stiffness matrix of the shell. These quantities are computed per Gaussian integration point using the expressions in Equations (B.18), (B.19) and (B.22) to (B.25).

3.4.2 Implementation Aspects

The implementation of the shell model is adopted from the work of Goyal [142], hence the reader is referred to his work for more details[10]. When this research started, the implementation contained assembly of the linear and tangential stiffness matrices and the mass matrix. Hence, the routines discussed in this section were already present in the model and are repeated for the sake of completeness. The section covers, numerical evaluation of the integrals in the variational form (see Equation (3.22)) and implementation of boundary conditions.

Evaluation of the integrals

The integrals that appear in the variational formulation (see Equation (3.22)) are evaluated using Gauss quadrature. Consequently, the products between the strain tensor, the curvature tensor, their derivatives and the material matrix are computed on each quadrature point and block matrices with the size of the number of active basis functions. As an example, the membrane strain tensor $\underline{\underline{\boldsymbol{\varepsilon}}}$ on quadrature point $\mathbf{x}_k$ is evaluated as follows:

$$\underline{\underline{\boldsymbol{\varepsilon}}}(\mathbf{x}_k) = \begin{bmatrix} \varepsilon_{11} \\ \varepsilon_{22} \\ 2\varepsilon_{12} \end{bmatrix} = \begin{bmatrix} \frac{\partial R_{kl,pq}}{\partial \theta_1} \cdot \frac{\partial \mathbf{c}}{\partial \theta_1}(\mathbf{x}_k) \\ \frac{\partial R_{kl,pq}}{\partial \theta_2} \cdot \frac{\partial \mathbf{c}}{\partial \theta_2}(\mathbf{x}_k) \\ \frac{\partial R_{kl,pq}}{\partial \theta_1} \cdot \frac{\partial \mathbf{c}}{\partial \theta_2}(\mathbf{x}_k) + \frac{\partial R_{kl,pq}}{\partial \theta_2} \cdot \frac{\partial \mathbf{c}}{\partial \theta_1}(\mathbf{x}_k) \end{bmatrix}. \tag{3.53}$$

Where the surface coordinate $\mathbf{c}(\mathbf{x}_k)$ is computed based on the deformed surface in the previous Newton iteration. For basis function $R_{kl,pq}$ evaluated on $\mathbf{x}_k$. Here, the partial derivatives of the basis function Ψ_j are known from the (NUR)B-splines and the partial derivatives of the mid-plane surface $\mathbf{c}$ are the covariant basis vectors, i.e. $\mathbf{a}_i = \partial \mathbf{c} / \partial \theta_i$. These quantities are implemented in the routines of `G+smo`. After evaluation on the quadrature point, the result is weighted and summed according to Guass quadrature subsequently.

Treatment of Boundary Conditions

When forces are imposed on the boundary, the relevant terms of the external energy contribution from Equation (3.17) should be included in the assembly of the system. In the present shell model, point loads and distributed line loads over the boundary of the mid-plane $\mathbf{c}$ are implemented in a similar way as in the beam model, i.e. by evaluating the loads on the boundary and multiplying them by the active basis functions.

Imposed boundary displacements (Dirichlet boundary conditions) are imposed by elimination. This yields that the prescribed unknowns are eliminated from the system and added to the solution later on. Note that for the Jacobian matrix, the eliminated unknowns are not added to the update of the displacement vector. Additionally, the current implementation does not support a changing residual vector when Dirichlet boundary conditions are modified during iterations. This is a major drawback since it does not support the arc length method with Dirichlet boundary conditions (see Section 4.4).

[10] In the time of writing (July 2019), the shell library in `G+smo` is still under development and hence not made public.

Lastly, in the derivation of the shell model, rotational degrees of freedom are not implemented. This means that prescription of rotations on the boundaries is not as straightforward as for the beam model. In the present model, rotations are restricted (e.g. in case of clamped boundaries) by the technique mentioned by Kiendl [137]. That is, the out-of-plane degrees of freedom of the nodes (hence control points) next to a clamped edge are also restricted in the out-of-plane direction. Similar techniques have successfully been applied on multi-patch coupling and arbitrary patch coupling, better known as the Bending Strip Method [88]. This technique, however, is not yet available in the present shell model.

3.5 Remarks on Other Material Models

In the derivation of the current shell model, the strain-displacement relationship is governed by the Green-Langrange strain tensor and the relation between stress and strain is assumed to be linear, governed by the Saint Venant-Kirchhoff constitutive relation. Depending on the application of the shell model, different constitutive models are proposed in literature. A brief description of the material models is given below. The Saint Venant-Kirchhoff model is discussed for completeness. Reference works include the books of Ogden [152] or Başar and Weichert [141].

For small strains, the Saint-Venant Kirchhoff material model suffices. In this case, a linear relationship between stresses and strains is assumed. The material model can be used with a nonlinear Green-Lagrange strain tensor to allow for large displacements but not necessarily large strains. [153]

For moderate strains (up to 40%) the Neo-Hookean material model can be used. This material model is commonly used for rubber-like materials (for a stretched sheet, recall the works of Li and Healey [75], Fu et al. [78] and Wang et al. [76]) or biological tissues [92] and is a simplified version of the Mooney-Rivlin material model. The Neo-Hookean model is similar to the Saint-Venant Kirchhoff model for small strains, but the stress-strain relation flattens for larger strains. [153]

For strains up to 100%, the Mooney-Rivlin material model is suitable. This model was used for modelling stretched thin sheets of rubber-like materials. However, the model was found to inadequately describe compressions and to the stress-stiffening effect. For larger strains, Ogden's material can be used, which has shown acceptable accuracy with test results for strains up to 700%. [153]

3.6 Concluding Remarks

In this chapter, the derivation and implementation of isogeometric beam and shell models have been presented. Reflecting on the first subgoal of this thesis, the underlying assumptions in the model are:

- *Low thickness* compared to in-plane dimensions allows for using the Kirchhoff Hypothesis (see Section 3.2.1). Consequently, the shell is modelled by deformations of the mid-plane under the assumption that its cross-section does not deform and that normals remain normal after deformation.
- *Rotary inertia* of the shell is ignored, based on the low thickness of the shell (see Section 3.2.4).
- The *Saint Venant-Kirchhoff material model* was used, using a linear relationship between stress and strains (see Section 3.2.3).

Additionally, subgoal 3 relates to the implementation of the shell model. Although no basis functions have been specified yet, the following can be concluded. The derivations are based on the Ritz method, rather than the Galerkin method, since the Rayleigh-Ritz method allows for direct derivation of the weak formulation based on the variational form. Hence, the strong form of the beam and shell equations was not used. The shell model is based on the Isogeometric Kirchhoff-Love shell model from the works of Goyal [142] and Kiendl [137]. The beam model was derived in a similar way.

4 | Isogeometric Structural Analysis

In present structural analysis, numerical models play an important role. As structural analysis supports structural design, different analysis tools are used to assess the structural failure and structural behaviour in general. In this section, an overview of numerical structural analyses and their implementation used for this research is given. This relates to subgoal 3 of this thesis. For the analyses, structural mass matrices damping and tangential stiffness matrices M, C and $\mathrm{K}_T(\mathbf{u})$ and the internal and external force vectors $\mathbf{N}(\mathbf{u})$ and $\mathbf{P}$ are relevant. Without loss of generality, it is assumed in this section that these matrices are available for any element (e.g. beam, shell, solid) using any method (e.g. FEM, IGA). In the following sections, however, these matrices will be derived using IGA for beams and shells.

Static analysis is the analysis of structures involving only displacements and constant loading conditions, solving for an equilibrium between internal and external forces. *Quasi-static analysis* is a type of analysis where velocities and accelerations of the structure are not considered, but where loads change in *load steps*. This type of analysis is often used with *buckling* and *post-buckling* analyses. *Modal* or *spectral analysis* is the analysis of vibrations in the spectral, i.e. frequency, domain. This means that eigenfrequencies and vibration modes are considered. This type of analysis can be used to solve dynamic problems under the assumption that the dynamic response is a linear combination of the vibration modes. Lastly, *temporal* or *dynamic analysis* involves the full dynamic simulation of structures, including structural velocities, optionally accelerations and dynamic (i.e. time-dependent) forcing.

4.1 Basics of Isogeometric Analysis (IGA)

The concept of isogeometric (IGA) was introduced in Section 2.3 in a literature review focussing on structural analysis. In this section, the basics of IGA are covered by providing one-dimensional examples of the construction of *B-spline* and *Non-Uniform Rational B-spline* (NURBS) basis functions. That is, the concept of *control points* to construct curves and surfaces as known from *Computer Aided Design* (CAD) is presented and the principle of knot insertion (or so-called h-refinement) is introduced. Thereafter, the concept of THB-splines for adaptive mesh refinement is illustrated. This section closes with an example of a one-dimensional linear elasticity problem solved using B-spline basis functions.

4.1.1 B-splines and NURBS

By the time of the introduction of IGA, in 2005, the basis functions were B-splines or NURBS [83]. Later on, T-splines and other splines that were developed in the CAD community (e.g. [124]) were also used as a basis for IGA [125]. B-splines are curves that are defined by so-called *knot vectors* that are described by knot vectors. A knot vector is a non-decreasing sequence of coordinates in the parameter space. Thus, $\Xi = \{\xi_1, \xi_2, \ldots, \xi_{n+p+1}\}$ where $\xi_i \geq \xi_j$ for $i > j$ and $\xi_k \in \mathbb{R}$ for all k. Here, n is the number of basis functions and p is the degree of the basis functions that construct the B-spline.

Construction of B-splines is done recursively. Let $N_{i,p}$ denote the i^{th} basis function of order p. The 0^{th} order basis function in parametric coordinate ξ is defined by:

$$N_{i,0}(\xi) = \begin{cases} 1 & \text{if } \xi_i \leq \xi < \xi_{i+1} \\ 0 & \text{elsewhere} \end{cases}.$$

Now, the higher-degree basis functions ($p \geq 1$) are constructed with the *Cox-De Boor recursion formula* [154, 155]:

$$N_{i,p}(\xi) = \frac{\xi - \xi_i}{\xi_{i+p} - \xi_i} N_{i,p-1}(\xi) + \frac{\xi - \xi_{i+1}}{\xi_{i+p+1} - \xi_{i+1}} N_{i+1,p-1}(\xi).$$

For repeated indices, so in case $\xi_i = \xi_{i+1}$, then the basis function is defined to be zero everywhere. Additionally, the Cox-De Boor formula needs an assumption for the case that $\frac{0}{0}$, which is assumed to be equal to zero for the construction of the basis function. Hence, one can see that all basis functions are zero between two identical indices.Generally, properties of B-spline basis functions are [84, 137, 125]:

- *Local support*: A basis function with index i and order p, $N_{i,p}(\xi)$, is non-zero everywhere, i.e.

$$N_{i,p}(\xi) \geq 0 \, \forall \xi \in [\xi_i, \xi_{i+p+1}].$$

- *Partition of unity*: The basis functions form a partition of unity, i.e.

$$\sum_{i=1}^{N} N_{i,p}(\xi) = 1 \, \forall \xi \in [\xi_1, \xi_{n+p+1}].$$

- *Non-negativity*: All basis functions are non-negative, i.e.

$$N_{i,p}(\xi) \geq 0 \, \forall \xi \in [\xi_1, \xi_{n+p+1}].$$

- *Linear independence*: The basis functions are linearly independent, i.e.

$$\sum_{i=1}^{N} \alpha_i N_{i,p}(\xi) = 0 \iff \alpha_j = 0 \, j = 1, 2, \ldots, n \, \forall \xi \in [\xi_1, \xi_{n+p+1}].$$

- *Control of continuity*: B-splines possess order $p - k$ continuity on control points with multiplicity k.

Based on the first three properties, B-splines curves convey the so-called *affine covariance property*, the *convex hull property* and the *variation diminishing property*. The affine covariance property means that transformations of B-splines are obtained by applying the transformations to the control points. The convex hull property means that the B-spline of order p is completely contained in the convex hull defined by its $p+1$ control points and that . The variation diminishing property means that curves cannot cross a line more times than its control polygon does. The latter two properties make the method robust for oscillatory behaviour of the solutions since for higher-order bases the effect of individual control points on the solution decreases and since basis functions are not oscillating between two knots. The partition of unity property is furthermore beneficial when using row-sum mass-matrix lumping to reduce the degrees of freedom of the mass matrix for dynamic computations [84]. The control of continuity property of the basis allows for flexibility in the use of derivatives for instance for rotational degrees of freedom in the present beam and shell models.

The derivatives of the basis function N_i are determined in the following way:

$$\frac{\mathrm{d}}{\mathrm{d}\xi} N_{i,p}(\xi) = \frac{p}{\xi_{i+p} - \xi_i} N_{i,p-1}(\xi) - \frac{p}{\xi_{i+p+1} - \xi_{i+1}} N_{i+1,p-1}(\xi).$$

And obtaining higher-order derivatives is done iteratively by taking the derivative of this expression:

$$\frac{\mathrm{d}^k}{\mathrm{d}\xi^k} N_{i,p}(\xi) = \frac{p}{\xi_{i+p} - \xi_i} \left(\frac{\mathrm{d}^{k-1}}{\mathrm{d}\xi^{k-1}} N_{i,p-1}(\xi) \right) - \frac{p}{\xi_{i+p+1} - \xi_{i+1}} \left(\frac{\mathrm{d}^{k-1}}{\mathrm{d}\xi^{k-1}} N_{i+1,p-1}(\xi) \right).$$

As an extension for B-splines, Non-Uniform Rational B-splines are constructed by adding a weight for each basis function. Then, the weighting function $W(\xi)$ is defined by:

$$W(\xi) = \sum_{i=1}^{n} N_{i,p}(\xi) w_i. \tag{4.1}$$

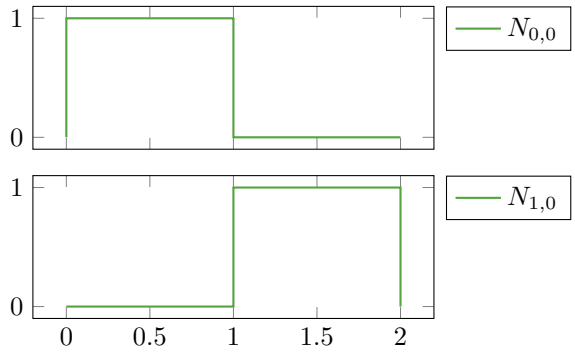

(a) Zeroth order basis functions with knot vector $\Xi = \{0, 1, 2\}$

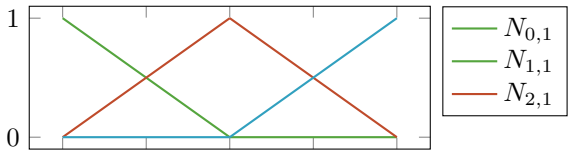

(b) First order basis functions with knot vector $\Xi = \{0, 0, 1, 2, 2\}$

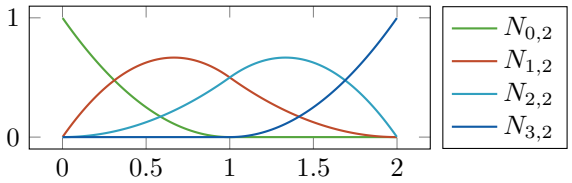

(c) Second order basis functions with knot vector $\Xi = \{0, 0, 0, 1, 2, 2, 2\}$

Figure 4.1: Examples of basis functions of different order and the same *unique* knots. As the order increases, the end knots are repeated $p + 1$ times. Furthermore, these examples also illustrate that the number of basis functions increases as the order increases.

Where w_i is the weight for spline $N_{i,p}$ of order p. Then, the i^{th} NURBS of order p is defined by:

$$R_i^p = \frac{N_{i,p}(\xi) w_i}{W(\xi)}. \tag{4.2}$$

By introducing a weight per basis function, one is able to represent each geometry accurately. An example is presented in Section 4.1.1.

In order to generate spline curves in 2D or 3D, the basis functions N_i based on one or more knot vectors $\Xi, \mathcal{H}$ can be utilized. Define a curve l in 2D and let $\mathbf{S}_i$ be control points in the 2D plane. Then, the curve is constructed by (see Figure 4.2):

$$\mathbf{C}(\xi) = \sum_{i=1}^{n} R_i^p(\xi) \mathbf{B}_i. \tag{4.3}$$

Where R_i^p can also be a B-spline if all weights are equal. Furthermore, $\mathbf{B}_i$ contains the coordinates of a control point in 2 or 3 dimensions. Furthermore, for the generation of surfaces, or volumes, the parametric domain $\xi \in \mathbb{R}^1$ is extended to $(\xi, \eta) \in \mathbb{R}^2$ or $(\xi, \eta) \in \mathbb{R}^3$. The formulations for surfaces (and similarly for solids) are then (see Figure 4.3):

$$\mathbf{S}(\xi, \eta) = \sum_{i=1}^{n} \sum_{j=1}^{m} R_i^p(\xi) P_j^q(\eta) \mathbf{B}_{i,j}. \tag{4.4}$$

Where R_i^p, P_j^q and T_k^r are NURBS of orders p, q and r. Furthermore, with preservation of the exact geometry, it is possible to insert a control point of a curve (or surface or volumes) for refinement purposes. This is called *knot insertion* (see Figure 4.4). The principle of knot insertion is based on redefining the control points such that one is added but that the geometry remains the same. Let $\bar{\mathbf{B}}$ be the vector of new control points and let $\mathbf{B}$ be the old control points and let the new knot $\bar{\xi}$ be added between ξ_k and ξ_{k+1}. Then, the new control points are determined by:

$$\bar{B}_i = \alpha_i B_i + (1 - \alpha_i) B_{i-1}.$$

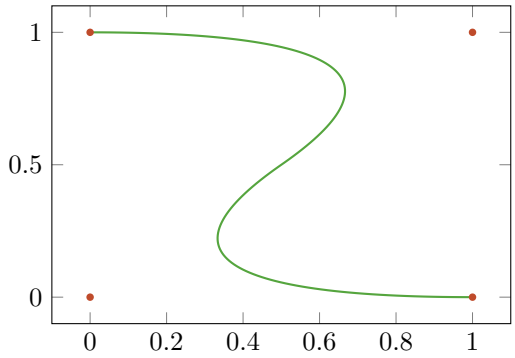

Figure 4.2: Curve generated with the control points as shown in the figure and with knot vector $\Xi = \{0, 0, 0, 0.5, 1, 1, 1\}$ (see Figure 4.4c).

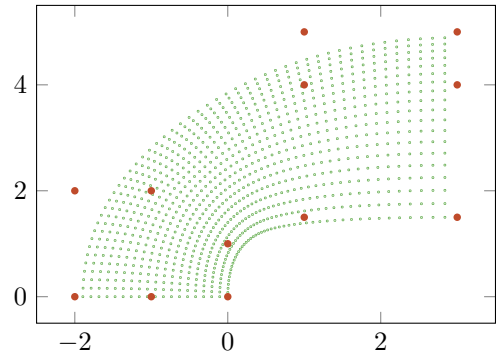

Figure 4.3: Surface generated with the control points as shown in the figure and with knot vectors $\Xi = \{0, 0, 0, 0.5, 1, 1, 1\}$ (horizontal, see Figure 4.4c) and $\mathcal{H} = \{0, 0, 0, 1, 1, 1\}$ (vertical, see Figure 4.4a).

With

$$\alpha_i = \begin{cases} 1, & 1 \leq i \leq k-1 \\ \dfrac{\bar{\xi} - \xi_i}{\xi_{i+p} - \xi_i}, & k-p+1 \leq i \leq k \\ 0, & k+1 \leq i \leq n+p+2 \end{cases} .$$

Lastly, order elevation of B-splines is performed by increasing the multiplicity of *each* knot without adding new knot values. In this way, the original basis functions are increased by order. When knot insertion is followed by order elevation, the equivalence of a p-refinement in FEA is constructed. In this way, the basis of the basis functions does not increase, but their order does. When order elevation is followed by knot insertion the so-called k refinement is constructed, in which continuity of basis function on internal knots can be increased.

4.1.2 Adaptive Refinement using THB-Splines

As discussed in Chapter 2, Truncated Hierarchical B-splines can be used for local refinement of tensor product bases. Contrary to ordinary refinement of knot vectors in the spline tensor products, local refinement of bases reduce the number of auxiliary refinements (see Figure 5.6). In Figure 4.6, refinement using Hierarchical B-splines (HP-splines) [127] and Truncated Hierarchical B-splines (THB-splines) [128] is illustrated.

As seen in Figure 4.6, the concept of Hierarchical B-splines is to replace one or more basis functions from the original basis and replace it with a number of functions from a basis with one or more levels of refinement. In the case of HB-splines, the basis functions from the higher level are inserted in the refined basis function without any modifications. This, however, violates the *partition of unity* property. Therefore, truncation of neighbouring basis functions leads to THB-splines and to the preservation of the partition of unity property such that the *convex hull property* and the *affine transformation property* are preserved. Additionally, the basis forms a smaller support [128] which shows improvements related to matrix sparsity.

In this work, THB-splines will be used on a static case to show the potential of the refinement with respect to accuracy for a number of degrees of freedom. An adaptive refinement strategy is presented in the works of Giannelli et al. [130] and Carraturo et al. [129] and is suggested for further research in Chapter 8.

4.1.3 Isogeometric Analysis

As mentioned before, Isogeometric Analysis is similar to Finite Element Analysis. Basically, Isogeometric Analysis utilises spline basis functions that have global support. Hence, discretization according to the Isogeometric Analysis framework is done in a similar way compared to FEA. Firstly, given a PDE (or a system of PDEs),

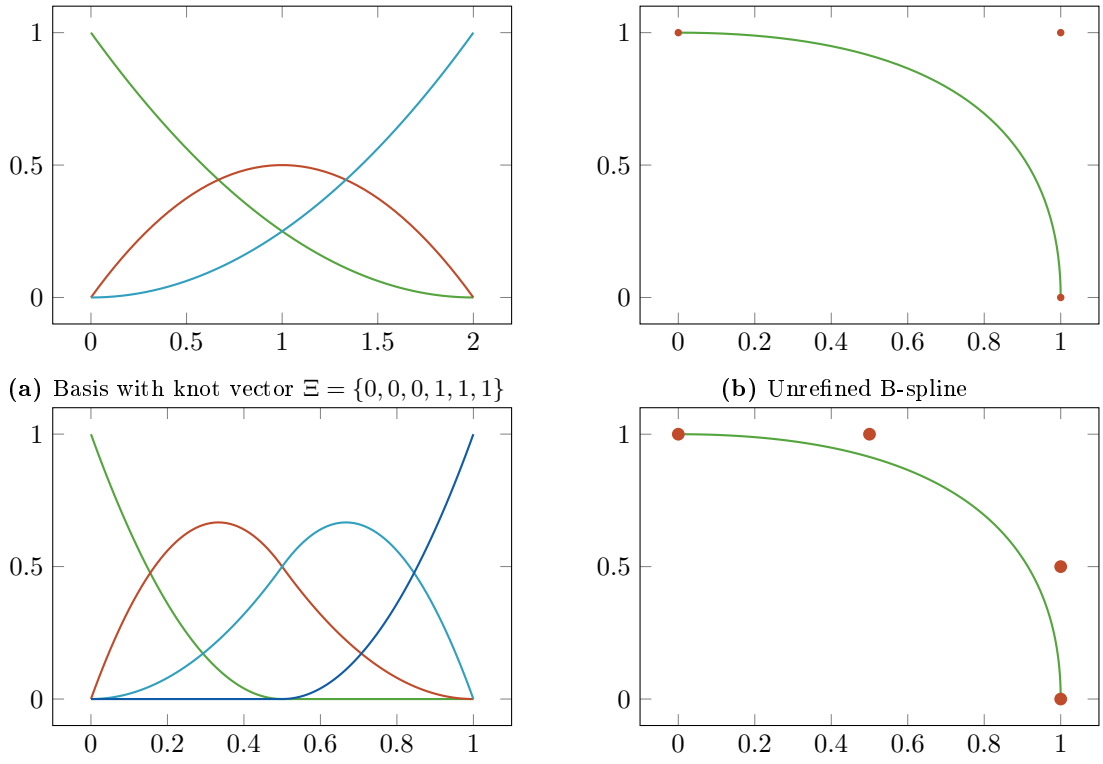

(a) Basis with knot vector $\Xi = \{0, 0, 0, 1, 1, 1\}$

(b) Unrefined B-spline

(c) Basis with knot vector $\Xi = \{0, 0, 0, 0.5, 1, 1, 1\}$

(d) Refined B-spline

Figure 4.4: Principle of knot insertion. On top, a B-spline of order 2 with three basis functions for the knot vector $\Xi = \{0, 0, 0, 1, 1, 1\}$ is presented. On the bottom, a B-spline of order 2 with four basis functions and modified knot vector $\Xi = \{0, 0, 0, 0.5, 1, 1, 1\}$ is presented. Knot insertion moves the control point such that the B-spline remains the same.

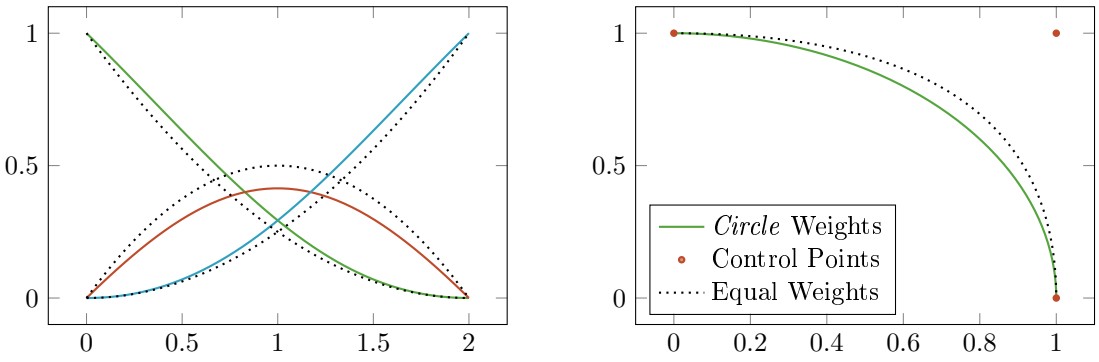

(a) Basis functions

(b) Curve

Figure 4.5: NURBS (weights $\{1, 1/\sqrt{2}, 1\}$) curve versus B-spline. On the left, the basis functions of the B-spline curve are dotted and the basis functions of the NURBS are coloured. On the right, the B-spline is dotted and the NURBS curve is coloured. With these weights, the NURBS exactly represents a quarter of a circle. [156]

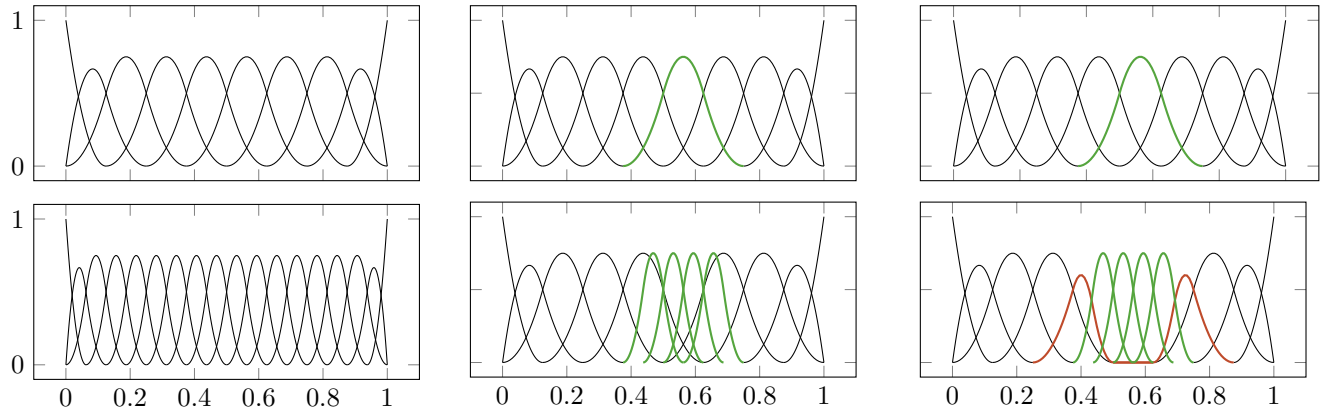

(a) B-spline basis **(b)** HB-spline basis **(c)** THB-spline basis

Figure 4.6: Principles of refinement for different spline bases. The top figures represent the undeformed basis, optionally with refined basis functions coloured green and truncated basis functions coloured orange. Bottom pictures represent refined bases. a) uniform refinement; b) HB-refinement; c) THB-refinement. Note that the basis functions used for refinement are derived from the uniform refined B-spline basis (fig. a, bottom). The unrefined unique knot vector in all cases is $\Xi = \{0, 1/8, 2/8, \ldots, 7/8, 1\}$ and the order of the splines is 2. The bases are generated in `G+smo` [157].

the weak form is determined by multiplying the PDE by a test function and integrating it over the domain. Partial integration is applied to incorporate boundary conditions. Up to this point, there is no difference with classical FEA. Secondly, when the weak form is known, the solution is approximated by a finite number of the product of a basis function and a weight. Here, in terms of the basis functions, differences come into play.

Given a weak form, denote by the following combination of a bi-linear operator $a(\cdot, \cdot)$ and an inner product $(\cdot, \cdot)$,

$$a(u, \varphi) = (\varphi, f).$$

Here, φ is the basis function, u is the solution and f is the forcing term of the PDE. Using the Galerkin approximation

$$u = \sum_{j=1}^{\infty} \alpha_j \varphi_j \approx \sum_{j=1}^{n} \alpha_j \varphi_j,$$

and substituting $\varphi = \varphi_i$, the weak form changes to (given linearity of $a(\cdot, \cdot)$):

$$\sum_{j=1}^{n} \alpha_j a(\varphi_j, \varphi_i) = (\varphi_i, f), \ \forall i.$$

In case of classical FEA, the integrals in $a(\cdot, \cdot)$ and in the inner product can be simplified to band matrices, since the basis functions have a local support. When B-splines or NURBS are used as basis functions, this simplification cannot be made. Hence, the system to be solved cannot be simplified further and domain integrals have to be calculated for all combinations of basis functions φ_i, φ_j. In sequel, an example of Isogeometric Analysis is given for the linear Euler beam equation. Here, the discretization procedure using B-splines is briefly explained, but it is applied in the models described in Chapter 3.

4.1.4 An Example: Clamped-Clamped Linear Euler Beam

Let us consider a linear Euler-Bernoulli beam with length 1, which is clamped at both ends and which is subject to a uniform pressure load $q = -1\ N/m$. As we have seen in Section B.2.2, Equation (B.15), the governing

equation for a linear beam is:

$$EI\frac{\partial^4 w}{\partial x^4} = q,$$
$$w(0) = \frac{\mathrm{d}w}{\mathrm{d}x}(0) = w(1) = \frac{\mathrm{d}w}{\mathrm{d}x}(1) = 0, \qquad \text{i.e. clamped boundary conditions on both sides.}$$

The weak form is, using:

$$\begin{cases} \text{Find } w \in \Sigma(\Omega) = \left\{ w \in H^2(\Omega) | w(0) = \dfrac{\mathrm{d}w}{\mathrm{d}x}(0) = w(1) = \dfrac{\mathrm{d}w}{\mathrm{d}x}(1) = 0 \right\}, \ \Omega = (0,1) \in \mathbb{R}^1 \text{ s.t.} \\ \\ \displaystyle\int_0^1 EI \frac{\mathrm{d}^2\varphi}{\mathrm{d}x^2}\frac{\mathrm{d}^2 w}{\mathrm{d}x^2}\,\mathrm{d}x = \int_0^1 \varphi q\,\mathrm{d}x \\ \\ \forall \varphi \in \Sigma(\Omega). \end{cases} \tag{4.5}$$

Here, the boundary terms drop out because the clamped boundary conditions are essential boundary conditions. The spatial discretization, which is also treated in Section 3.3, is done by the Galerkin method. Here, it is assumed that the solution w can be approximated by the following:

$$u(x) = \sum_{j=1}^{\infty} c_j N_j(x) \approx \sum_{j=1}^{n} c_j N_j(x).$$

With c_j, $j = 1, \ldots, n$ unknown constants. Substituting this into the obtained weak formulation gives a linear system (see Section 3.3 for the details):

$$\mathbf{K}\mathbf{c} = \mathbf{f},$$

Where,

$$K_{ij} = \int_0^1 EI \frac{\mathrm{d}^2\varphi_i}{\mathrm{d}x^2}\frac{\mathrm{d}^2\varphi_j}{\mathrm{d}x^2}\,\mathrm{d}x,$$
$$f_i = \int_0^1 \varphi_i p\,\mathrm{d}x,$$
$$\mathbf{c} = \begin{bmatrix} c_1 & c_2 & \ldots & c_n \end{bmatrix}^T.$$

Using this linear system, the coefficients $\mathbf{c}$ can be calculated and an approximation of the solution u_n can be constructed using the Galerkin method. In Figure 4.7 and Figure 4.8, the basis functions and their decomposition to the solution of the problem, respectively, are presented. As seen in this figure, the second-order basis with unique knot vector $\Xi = \{0, 1\}$ does not provide any basis functions that comply with the clamped boundary conditions, hence no solution is available. Furthermore, the fourth order basis functions represent the analytical solution since it is a fourth order polynomial. Another observation that can be made is that the basis functions are indeed global, which is a property of the IGA framework. Since they have this global support, the basis functions that overlap with others do not have the property that they represent the solution on nodes, as we know from basic Finite Element Methods.

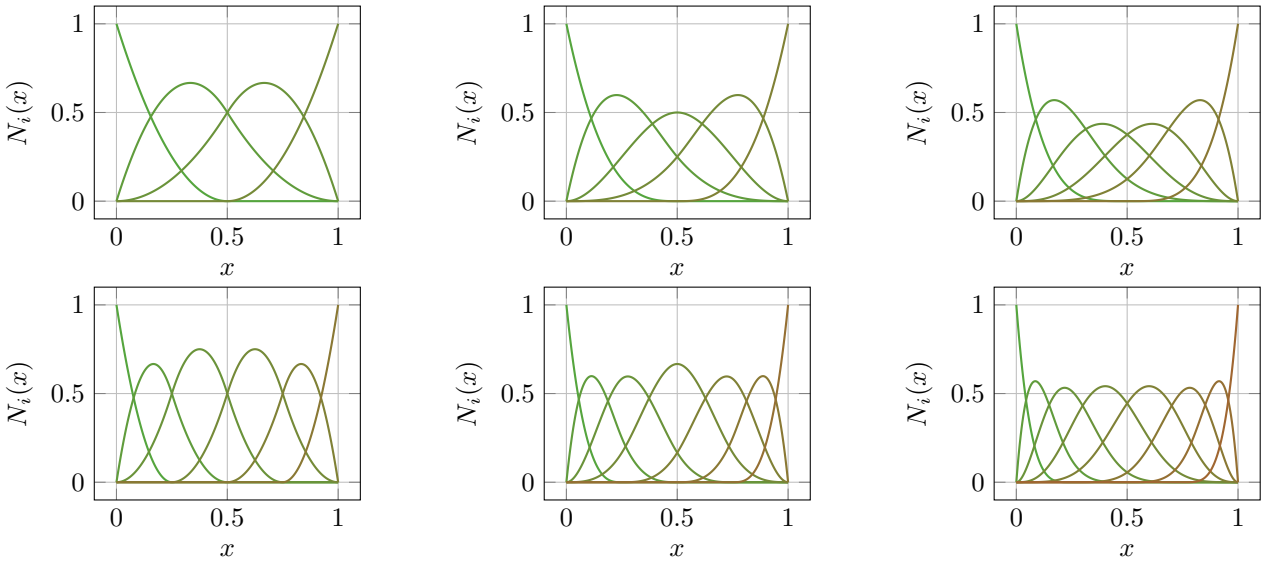

Figure 4.7: Basis functions of order p 2 (left), 3 (mid) and 4 (right) for knot vectors $\Xi = \{0.0, 1.0\}$ (top) and $\Xi = \{0.0, 0.5, 1.0\}$ (bottom). **Note:** Only unique knots are presented. The first and last knots are repeated $p+1$ times.

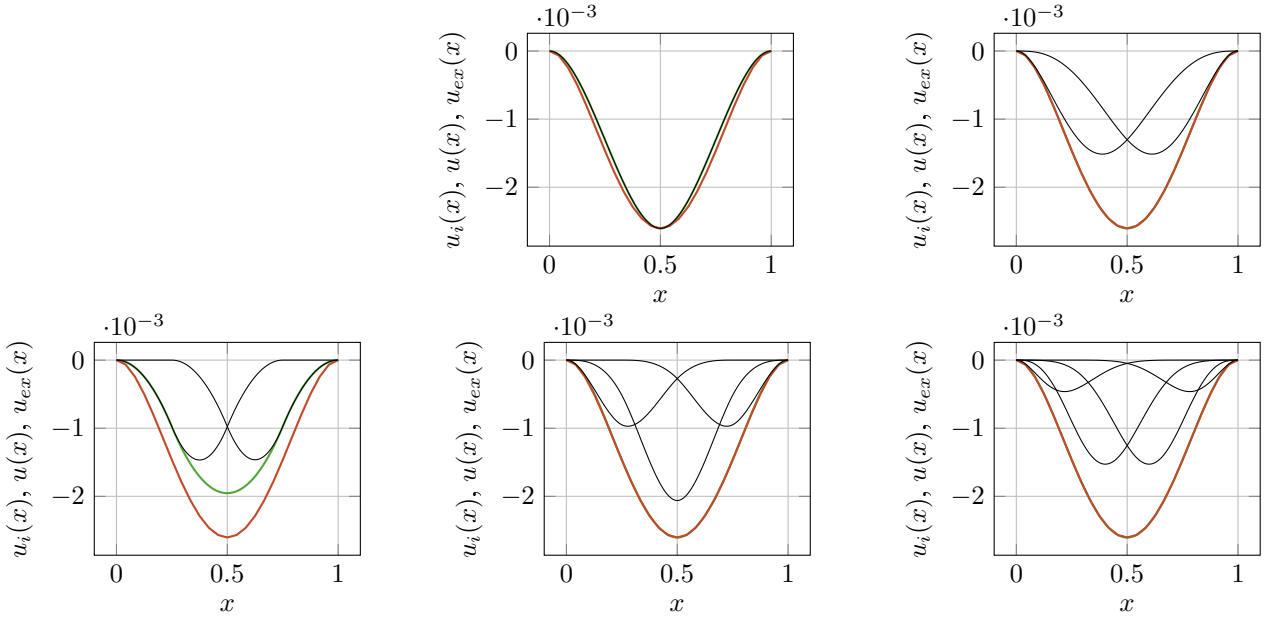

Figure 4.8: Analytical solution (green), numerical solution (orange) and decomposition of the solution (black) for basis function of order p 2 (left), 3 (mid) and 4 (right) for knot vectors $\Xi = \{0.0, 1.0\}$ (top) and $\Xi = \{0.0, 0.5, 1.0\}$ (bottom). **Note:** No solution exists for $p = 2$ and the coarsest knot vector (top left), since there are no basis functions that comply with the boundary conditions $N_i(x) = \frac{\mathrm{d}N_i}{\mathrm{d}x}(x) = 0$ for $x \in \{0, 1\}$.

4.2 (Nonlinear) Static Analysis

In static analyses, kinetic energies are by definition assumed to be equal to zero. This implies that velocities and accelerations of the structures are zero and hence that any effect of structural mass (material density ρ) are not considered. Therefore, the difference $\mathbf{G}$ between internal and external forces, respectively $\mathbf{N}(\mathbf{u})$ and $\mathbf{Q}(\mathbf{i}) + \mathbf{P}$, needs to be zero for an unknown displacement vector $\mathbf{u}$:

$$\mathbf{G}(\mathbf{u}) = \mathbf{N}(\mathbf{u}) - \mathbf{P} = \mathbf{0}. \tag{4.6}$$

When a linear problem is solved, the internal forces are described by a linear stiffness matrix K_L times the displacement field $\mathbf{u}$, so that a linear system needs to be solved:

$$\mathrm{K}_L\mathbf{u} = \mathbf{P}.$$

Here, K_L is the linear stiffness matrix, neglecting all terms depending on the solution vector $\mathbf{u}$. In case of a nonlinear system, a nonlinear solution strategy should be applied to solve Equation (4.6). When the stiffness matrix of the system, depending on the displacements $\mathbf{u}$ is known, *Picard iterations* (or *fixed-point iterations*) can be used. This method is known to be robust, but slow converging. A commonly used alternative is to exploit Newton-Raphson iterations [1]. This method works by linearising the system in Equation (4.6) around the displacement field $\mathbf{u}$:

$$\mathbf{G}(\mathbf{u} + \Delta\mathbf{u}) \approx \mathbf{G}(\mathbf{u}) + \frac{\partial \mathbf{G}}{\partial \mathbf{u}}(\mathbf{u})\Delta\mathbf{u} + \mathcal{O}(\Delta\mathbf{u}). \tag{4.7}$$

Here, $\mathcal{O}(\Delta\mathbf{u})$ denotes an error of *order* $\Delta\mathbf{u}$. Note that this method is second-order accurate in $\Delta\mathbf{u}$ by the Taylor expansion (linearization) in Equation (4.7). Now, let us assume that the increment $\Delta\mathbf{u}$ is such that $\mathbf{G}(\mathbf{u} + \Delta\mathbf{u}) = \mathbf{0}$, the method simplifies to:

$$\frac{\partial \mathbf{G}}{\partial \mathbf{u}}(\mathbf{u})\Delta\mathbf{u} = -\mathbf{G}(\mathbf{u}). \tag{4.8}$$

The term $\frac{\partial \mathbf{G}}{\partial \mathbf{u}}(\mathbf{u})$ is the Jacobian or the *tangential stiffness matrix* $\mathrm{K}_T(\mathbf{u})$. Generally, evaluating the system in Equation (4.8) does not yield a residual $\mathbf{G}(\mathbf{u} + \Delta\mathbf{u}) = \mathbf{0}$. Therefore, the method is in practice iterated until the residual $\mathbf{G}(\mathbf{u})$ satisfies a certain error measure. Algorithm 1 presents the solution algorithm for the Newton-Raphson method.

Algorithm 1 Newton-Raphson method for solving nonlinear system $\mathrm{G}(\mathbf{u}) = \mathbf{0}$

1: Initialise solution vector $\mathbf{u}_0$,
2: Define maximum number of iterations k_{max} and tolerance TOL,
3: Initialise iteration counter k and residual ϵ,
4: **while** $\epsilon <$TOL and $k < k_{max}$ **do**,
5: Compute $\mathbf{G}(\mathbf{u}_k)$ and $\frac{\partial \mathbf{G}}{\partial \mathbf{u}}(\mathbf{u})$,
6: Solve $\frac{\partial \mathbf{G}}{\partial \mathbf{u}}(\mathbf{u})\Delta\mathbf{u}_{k+1} = -\mathbf{G}(\mathbf{u}_k)$ for increment $\Delta\mathbf{u}_{k+1}$,
7: Update solution $\mathbf{u}_{k+1} = \mathbf{u}_k + \Delta\mathbf{u}_{k+1}$,
8: Compute residual $\epsilon = \mathbf{G}(\mathbf{u}_{k+1})$.
9: **end while**

Alternatives to the Newton-Raphson method, such as the *Quasi-Newton method* or *Broyden's method* can be used. The former method approximates the inverse of the Jacobian matrix based on this matrix in the previous iterations and the latter method approximates the inverse of the Jacobian matrix and hence does not even need an expression for the Jacobian matrix itself [159, 158]. However, in this study, the Newton-Raphson method is used and hence the Jacobian or tangential stiffness matrix should be required. These formulations were derived in Chapter 3.

[1] The books of Wriggers[158] or de Borst et al.[159] can be used as reference for this widely-known method in nonlinear finite elements

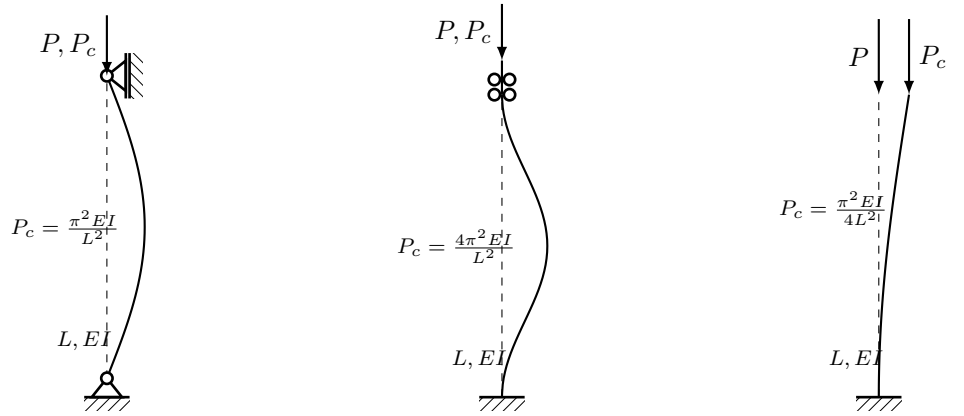

(a) Pinned-pinned beam **(b)** Clamped-clamped beam **(c)** Clamped-free beam

Figure 4.9: Buckling of a beam with length L and stiffness EI, giving the critical buckling load $P = P_c$ for different boundary conditions.

4.3 Buckling Analysis

Buckling is a *structural instability* that occurs when a critical load is exceeded. For example, consider the beams as depicted in Figure 4.9. When the compressive load exceeds the value of $P = P_c$ the initially straight (dashed line) structure buckles in the shape represented by the solid line. For different boundary conditions, different formulations for the critical buckling load (also referred to as the *Euler critical load*) are valid. In Appendix C.2, the critical load is derived for a clamped-clamped beam on an elastic foundation, which will be used in Section 5.2 for benchmarking of the numerical models. For other analytical solutions, the reader is referred to the book of Roark et al. [160].

Wriggers [158] describes linear buckling analysis using the tangential stiffness or Jacobian matrix of the internal forces in a structure, referring to the work of Brendel and Ramm [161]. Mathematically speaking, the buckling instability occurs when the determinant of the tangential stiffness matrix is equal to zero, or equivalently, where

$$\mathrm{K}_T(\boldsymbol{\phi})\boldsymbol{\phi} = 0.$$

Where $\boldsymbol{\phi}$ is the mode shape corresponding to the buckling mode shape. To compute the critical buckling load parameter λ such that buckling occurs for a load vector $\lambda\mathbf{P}$ in mode shape $\boldsymbol{\phi}$, the method proposed by [161] is to solve the eigenvalue problem with a splitting of the tangential stiffness matrix into a linear and a nonlinear part

$$\mathrm{K}_T(\mathbf{u}) = \mathrm{K}_L + \mathrm{K}_{NL}(\mathbf{u}).$$

Here, the linear part K_L does not depend on the displacement vector $\mathbf{u}$, whereas the nonlinear part K_{NL} does. Suppose now that the nonlinear stiffness matrix is computed on a linearized (non-buckled) state $\mathbf{u}_L$, with corresponding matrix $\mathrm{K}_{NL}\mathbf{u}_L$, the buckling eigenvalue problem becomes:

$$\left[\mathrm{K}_L + \lambda \mathrm{K}_{NL}(\mathbf{u}_L)\right]\boldsymbol{\phi} = \mathbf{0}.$$

Here, the eigenvalue λ is the magnification factor of the load that was applied in the linearized case for obtaining the solution $\mathbf{u}_L$. An algorithm for computing the critical buckling load and the corresponding mode shape is given in Algorithm 2.

4.4 Quasi-Static Analysis: Arc-Length Methods

In order to assess the behaviour of structures that show unstable behaviour, arc-length methods are used. For quasi-static analysis, zero velocities and accelerations of the structure are assumed. However, the loads on the structure are varying. Therefore, quasi-static analyses can be considered as cases where structural damping is large enough to damp all velocities and that are inertia forces are negligible. When quasi-static analysis is

Algorithm 2 Algorithm for computing the critical buckling load $\mathbf{P}_c$ and the corresponding buckling mode shape $\boldsymbol{\phi}$. From Wriggers [158]

1: Define problem, i.e. compute linear stiffness matrix K_L and load vector $\mathbf{P}$ according to applied boundary conditions and forces.
2: Solve $\mathrm{K}_L\mathbf{u}_L = \mathbf{P}$ for $\mathbf{u}_L$,
3: Compute tangential stiffness matrix $\mathrm{K}_T(\mathbf{u}_L)$,
4: Compute nonlinear stiffness matrix $\mathrm{K}_{NL}(\mathbf{u}_L) = \mathrm{K}_T(\mathbf{u}_L) - \mathrm{K}_L$,
5: Compute generalized eigenvalue problem $\mathrm{K}_L\boldsymbol{\phi} = \lambda_c\mathrm{K}_{NL}\boldsymbol{\phi}$,
6: Compute critical load $\mathbf{P}_c = \lambda_c\mathbf{P}$.

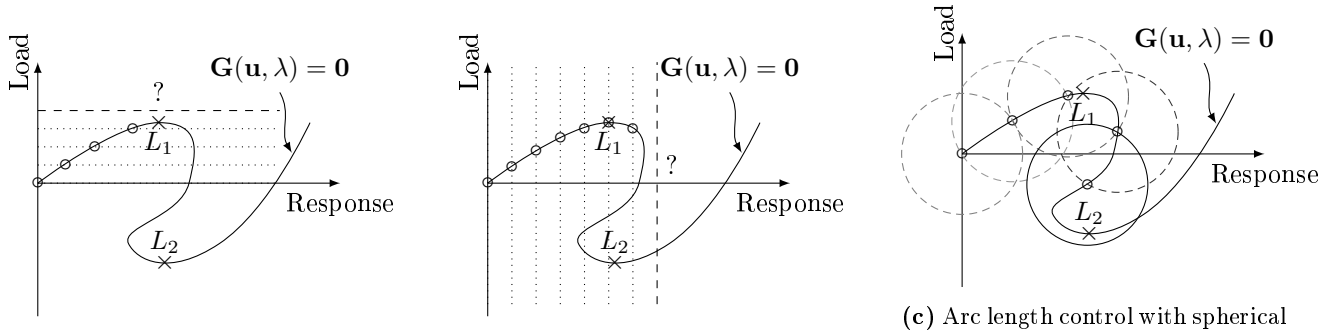

(a) Load control **(b)** Displacement control. **(c)** Arc length control with spherical constraint equation.

Figure 4.10: Load (left), displacement (mid) and arc length (right) control on a load-response curve on which the sum of internal and external forces is zero for a load factor λ and a resulting displacement vector $\mathbf{u}$, i.e. $\mathbf{G}(\mathbf{u}, \lambda) = \mathbf{0}$. The points L_1 and L_2 are *limit points*.

applied in combination with bucking, it is referred to as *post-buckling analysis*. In the sequel, let us assume that the load is applied as a multiple of a *reference load vector* $\mathbf{P}$. Introducing a *load factor* λ, the nonlinear system Equation (4.6) is:

$$\mathbf{G}(\mathbf{u}, \lambda) = \mathbf{N}(\mathbf{u}) - \mathbf{Q}(\mathbf{u}) - \lambda\mathbf{P} = \mathbf{0}. \tag{4.9}$$

Here, $\mathbf{Q}(\mathbf{u})$ is an external load vector which could be depending on the displacements $\mathbf{u}$ but not on the load factor λ. In the sequel, this term is combined with $\mathbf{N}(\mathbf{u})$. For example, if $\mathbf{P}$ is a load vector corresponding to an applied reference displacement, then $\lambda = 1$ would correspond to application of this displacement and increasing λ would provide a larger applied displacement. $\mathbf{Q}(\mathbf{u})$ can, for example, represent a foundation which is compressed as consequence of displacements $\mathbf{u}$.

Quasi-static analysis can be performed in different forms. For example, one can increase λ in steps and compute for each step the response. If the reference load vector corresponds to end-point displacements, *displacement control* is applied, whereas if the reference load vector corresponds to an applied surface load or load at the endpoints, *load control* is applied. In both cases, the Newton-Raphson method can be applied in each load step, using the converged solution from the previous load step as an initial guess. Displacement control and load control are sketched in Figure 4.10c using so-called *load-response curves*. When buckling is involved, initial imperfection can be applied to the structure to obtain a smooth curve and to avoid unstable branches (see Figure 4.11). However, in the following, a method is presented where bifurcations can be modelled without the need of initial imperfections.

4.4.1 Arc-Length Methods

Arc length methods, or path following methods, a system of nonlinear equations subject to a reference load or condition is solved for both the solution $\mathbf{u} \in \mathbb{R}^{N\times 1}$ as well as for the load factor λ with an additional constraint equation (e.g. a circle in the $\mathbf{u}, \lambda$-space, see Figure 4.10c). By this means, the solution $\mathbf{w} = [\mathbf{u}, \lambda]$ consists of $N + 1$ degrees of freedom, i.e. $\mathbf{w} \in \mathbb{R}^{(N+1)\times 1}$. This means that besides the partial differential equations to solve $\mathbf{u}$, an additional equation is needed to solve for the scalar λ. This equation often works as a constraint

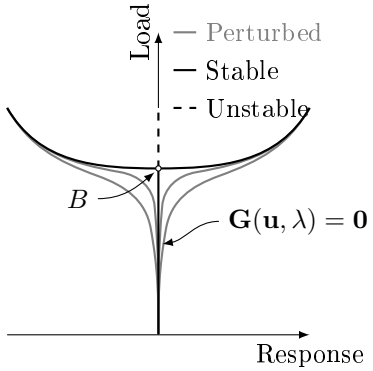

Figure 4.11: Effect of initial perturbations to avoid passing bifurcation points.

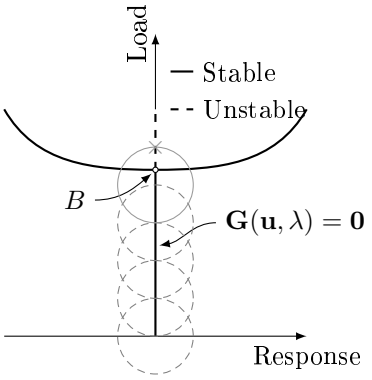

Figure 4.12: Arc length method applied on pitchfork bifurcation. When passing a bifurcation point, the unstable branch (dashed) is found.

equation on λ and $\mathbf{u}$ and different variants have been proposed in the field of structural mechanics. Given any constraint equation $f(\mathbf{u},\lambda)$, linearization of the system in Equation (4.9) yields a Newton-Raphson method for the constrained system [158]

$$\tilde{\mathbf{G}}(\mathbf{w}) = \begin{bmatrix}\mathbf{G}(\mathbf{w}) \\ f(\mathbf{w})\end{bmatrix} = \mathbf{0}, \qquad \text{with linearisation} \qquad \begin{bmatrix}\mathrm{K}_T & \mathbf{P} \\ \nabla_u f & \frac{\mathrm{d}f}{\mathrm{d}\lambda}\end{bmatrix} \Delta\mathbf{w} = -\tilde{\mathbf{G}}. \tag{4.10}$$

Here, ∇_u denotes a gradient with respect to the displacement vector $\mathbf{u}$ and $\Delta\mathbf{w}$ is the increment of the solution vector. All entities are evaluated on iteration i and the incremental solution is computed as $\mathbf{w}_{k+1} = \mathbf{w}_k + \Delta w$. Originally, this method was first published by Riks [162] who introduced a constraint equation that is linear in $\mathbf{u}$ and λ and describes a normal plane perpendicular to the tangent of the last computed equilibrium point. Later, Crisfield [163] proposed a cylindrical or spherical constraint equation, where the solution $\mathbf{w}$ is bounded by a circle with radius Δl, i.e. the arc length.[2] In this work, the constraint condition as proposed by Crisfield is used as basis. This method has the advantage over the method from Riks that it always finds a solution, but the disadvantage is that multiple solutions are often found and hence a choice should be made. The *constraint equation* proposed by Crisfield is:

$$\Delta\mathbf{u}^T\Delta\mathbf{u} + \Psi^2\Delta\lambda^2\mathbf{P}^T\mathbf{P} = \Delta l^2. \tag{4.11}$$

Where Δl is the arc length and $\Delta\mathbf{u}$ and $\Delta\lambda$ are respectively the increment of the displacement and load factor with respect to the previous load step. As the solved equations are nonlinear, $\Delta\mathbf{u}$ and $\Delta\lambda$ are solved incrementally with increments $\delta\mathbf{u}$ and $\delta\lambda$ such that in iteration i, $\Delta\mathbf{u}_i = \Delta\mathbf{u}_{i-1} + \delta\mathbf{u}$ and $\Delta\lambda_i = \Delta\lambda_{i-1} + \delta\lambda$. The parameter Ψ is a scaling parameter which was originally not present in the method of Crisfield. In their case, $\Psi = 0$, to which is referred as the *spherical arc length method*. Alternative choices have been proposed by Schweizerhof and Wriggers [170] and Bellini and Chulya [171] amongst others. In this work, Ψ is defined as follows (referred to as the *elliptical arc length method* [171]):

$$\Psi^2 = \frac{\mathbf{u}_0^T\mathbf{u}_0}{\lambda_0^2\mathbf{P}^T\mathbf{P}}. \tag{4.12}$$

Where $\mathbf{u}_0$ and λ_0 are the solutions of the arc length method on the previously converged point. In the origin, i.e. at $(\mathbf{u},\lambda) = (\mathbf{0},0)$, a prediction using the results from Equation (4.22) will be used with $\Psi^2 = 0$. Crisfield proposed to solve the equation in Equation (4.10) in a segregated way. To this end, the increment of the displacement vector, $\delta\mathbf{u}$ is solved based on the unknown load increment $\delta\lambda$:

$$\mathrm{K}_T\delta\mathbf{u} = \mathbf{G}(\mathbf{u},\lambda) = \mathbf{N}(\mathbf{u}) - \mathbf{Q}(\mathbf{u}) - \delta\lambda\mathbf{P}. \tag{4.13}$$

[2] An overview of arc-length methods is given by Wriggers [158], Crisfield [164], Crisfield [165] and de Borst et al. [159], who are all great contributors to the arc length method applied in numerical structural bifurcation problems. The original works about the arc-length method are cited in this chapter for reference. Further and reviews on arc-length methods include the ones of Fafard and Massicotte [166] who gives a geometrical interpretation of various arc-length methods or Carrera [167] who assesses different methods with a simple example and Memon and Su [168] who describes the development of the method over time. Improvements have been made by Hellweg and Crisfield [169] and arc-length methods with Isogeometric Analysis have been combined in [112, 111]

The iterative displacement increment $\delta\mathbf{u}$ can be split in to two parts such that $\delta\mathbf{u} = \delta\bar{\mathbf{u}} + \delta\lambda\delta\mathbf{u}_t$. Here, the increment from the standard load-controlled Newton-Raphson method $\delta\hat{\mathbf{u}}$ and the increment $\delta\mathbf{u}_t$ due to the iterative change of the load, which are solved by (k is the iteration counter)

$$\mathrm{K}_T\delta\bar{\mathbf{u}} = \mathbf{G}(\mathbf{w}_k), \qquad \text{and} \tag{4.14}$$

$$\mathrm{K}_T\delta\mathbf{u}_t = \mathbf{P}. \tag{4.15}$$

Using this splitting, the factorization of the Jacobian has to be computed once, which is an advantage from computational point of view. A disadvantage, is that no solutions can be found on limit points, since the Jacobian is singular there [164]. In Section 4.4.5 solutions will be given to this problem. Using the constraint equation from Equation (4.11) and using the fact that the iterative increment $\delta\mathbf{u}$ is depending on the unknown $\delta\lambda$, the constraint equation can be written as a polynomial in $\delta\lambda$:

$$a\delta\lambda^2 + b\delta\lambda + c = 0. \tag{4.16}$$

Here:

$$\begin{aligned} a &= \delta\mathbf{u}_t^T\delta\mathbf{u}_t + \Psi^2\mathbf{P}^T\mathbf{P}, \\ b &= 2\left(\delta\mathbf{u}_t^T(\Delta\mathbf{u}_{k-1} + \delta\bar{\mathbf{u}}) + \Delta\lambda_{k-1}\Psi^2\mathbf{P}^T\mathbf{P}\right), \\ c &= (\Delta\mathbf{u} + \delta\bar{\mathbf{u}})^T(\Delta\mathbf{u} + \delta\bar{\mathbf{u}}) + \Delta\lambda^2\Psi^2\mathbf{P}^T\mathbf{P} - \Delta l^2. \end{aligned} \tag{4.17}$$

Based on the work of Schweizerhof and Wriggers [170], *numerical relaxation* is applied to accelerate convergence behaviour. In particular, relaxation with factor α is applied when the load factor of iteration k, $\delta\lambda^k$ is oscillating with respect to the previous iteration $k-1$, $\delta\lambda^{k-1}$. In that case, the load factor $\delta\tilde{\lambda}$ and corresponding displacement update $\delta\tilde{\mathbf{u}}$ are computed based on

$$\delta\lambda^k\delta\lambda^{k-1} < 0 \qquad \text{and} \qquad \left|\delta\lambda^k\right| \leq \left|\delta\lambda^{k-1}\right| \implies \qquad \delta\tilde{\lambda} = \alpha\delta\lambda^k \qquad \text{and} \qquad \delta\tilde{\mathbf{u}} = \alpha\left(\delta\tilde{\lambda}\delta\mathbf{u}_t + \delta\bar{\mathbf{u}}\right).$$

In the current research, the relaxation factor was chosen to be 0.5, similar to Schweizerhof and Wriggers [170]. Additionally, in the implemented arc length method, the error is determined by a relative norm of the residual vector ϵ_R and the displacement vector ϵ_u, separately. Both norms and used tolerances are defined as [159]:

$$\epsilon_R = \frac{\mathbf{r}_i^T\mathbf{r}_i}{\mathbf{r}_0^T\mathbf{r}_0} \leq 10^{-3} \qquad \text{and} \qquad \epsilon_u = \frac{\|d\mathbf{a}_i\|}{\|d\mathbf{a}_0\|} \leq 10^{-6}. \tag{4.18}$$

Lastly, the arc length Δl is not necessarily constant but can be made adaptive. Suggestions given by for instance Riks [172] are to rescale the new arc length Δl^* by the number of iterations of the previous load step:

$$\Delta l_i = \left(\frac{k_{\text{target}}}{k_{i-1}}\right)^{\alpha}\Delta l_{i-1}. \tag{4.19}$$

Here, Δl_i is the arc length in load step i, k_{target} is the number of target iterations, k_{i-1} is the number of iterations in load step $i-1$ and α is a coefficient that can be chosen. As mentioned by Riks [172], the main disadvantage of adaptive arc lengths is that it does not work when there are sudden changes in the curvature path. For this reason, the method is implemented but not used in this study.

4.4.2 Choice of roots

From the quadratic nature of Equation (4.16), two solutions for $\delta\lambda$ and hence two solutions for $\delta\mathbf{u}$ will be produced. Originally, Crisfield [163] proposed to compute the angle between the current iterative correction $\delta\mathbf{u}_k$ and the previous iterative correction $\delta\mathbf{u}_{k-1}$ as follows:

$$\alpha_{1,2} = (\Delta\mathbf{w}_{k+1}^{1,2})^T\Delta\mathbf{w}_k^{1,2}. \tag{4.20}$$

If this number is positive, it means that the iterations are pointing in the same directions. Additionally, the largest root for which α_k is largest is the root for which the current correction and the correction in the previous iteration point in the most similar direction. Therefore, the root of Equation (4.16) that is largest is chosen. If both roots are positive, the root which is closest to the linear approximation $\delta\lambda = -c/b$ is chosen. In other

works, such as by de Borst et al. [159], it is proposed to use the predictor stage instead of the previous iteration as reference. If both inner products are negative, it means that both corrections of the current iteration are pointing in the opposite direction compared to the previous iteration. In this case, the 'angle' α_k that is the smallest, i.e. the closest to zero, is chosen.

An alternative formulation is discussed in the work of Ritto-Corrêa and Camotim [173]. This formulation is based on the fact that the minimal angle is to be found. Minimising the angle for the increment $\delta\lambda$, yields that it suffices to look at the following roots [173]:

$$\vartheta_r = \delta\lambda_r \left(\Delta\mathbf{u}_{i-1}^T \delta\mathbf{u}_t + \Psi^2 \Delta\lambda_{i-1}\right), \qquad r = 1, 2. \tag{4.21}$$

And the root $\delta\lambda_r$ for which ϑ_r is largest is the selected root. In the original work of Crisfield [163] a different method was proposed, where the increment $\Delta\mathbf{u}$ is computed for both values of $\delta\lambda_r$ and the largest inner-product is taken. In this research, both options have been implemented and differences in the behaviour of the algorithm were not observed. The method proposed by Ritto-Corrêa and Camotim [173] was finally used.

4.4.3 Initialization and the Predictor Phase

In case of the first iteration of the first load increment, no information about previous load steps $\Delta\mathbf{w}$ is present, and the residual of the previous load increment or iterations is zero. Therefore, initialization of the arc length method from the origin $(\mathbf{u}, \lambda) = (\mathbf{0}, 0)$ can only be based on the step $\delta\mathbf{u}_t$ and is done by letting [163, 173]:

$$\delta\lambda_0 = \frac{\Delta l}{\delta\mathbf{u}_t^T \delta\mathbf{u}_t + \Psi^2}. \tag{4.22}$$

In the first iteration of a new load step, i.e. the predictor stage, information about the previous load step is available, hence the predictor of the load increment $\delta\lambda$ can be computed using Equation (4.22) where the sign of the step is chosen based on Feng et al.[174, 175]:

$$\text{sign}(\delta\lambda_0) = \text{sign}(\Delta\mathbf{u}_{i-1}^T \delta\mathbf{u}_t + \Delta\lambda_{i-1}\mathbf{P}^T\mathbf{P}). \tag{4.23}$$

Remarks that have been made by Feng et al. include that the determination of the sign using the sign of the Jacobian matrix is a more conventional way, but only works before bifurcations are encountered, as shown in Feng et al. [176]. Another remark that was illustrated in Feng et al. [174] is that the proposed methods on the determination of the predictor step still require a proper selection of the size of the arc-length. Namely, if the load-response curve is too sharp, the constraint equations can intersect more than two times and root selection based on the quadratic equation in Equation (4.16) fails to cover all solutions.

4.4.4 Dealing With Complex Roots (Line Search)

In the case that $b^2 - 4ac < 0$ in Equation (4.16), complex solutions are found for the incremental load step $\delta\lambda$. Using a simplified model, Carrera [167] motivates that complex roots occur when the solution path cannot be found using the tangent plane of the constraint equation. This problem can be avoided by simply reducing the arc length, e.g. bisecting it [171]. However, in the works of Lam and Morley [177] and Zhou and Murray [178], a correction to Equation (4.16) is motivated using a *pseudo line-search technique*. In the following, the method proposed by Zhou and Murray [178] is derived.

Let the update of the displacement increment be $\delta\mathbf{u} = \beta\delta\bar{\mathbf{u}} + \delta\lambda\delta\mathbf{u}_t$ where β is a *line search parameter* proposed by Crisfield [179]. Then, the new polynomial coefficients of the constraint equation become

$$a'\delta\lambda^2 + b'\delta\lambda + c' = 0.$$

Here,

$$\begin{aligned}
a' &= \delta\mathbf{u}_t^T \delta\mathbf{u}_t + \Psi^2 \mathbf{P}^T\mathbf{P} = a_0, \\
b' &= 2\left(\delta\mathbf{u}_t^T \Delta\mathbf{u}_{i-1} + \Delta\lambda_{i-1}\Psi^2\mathbf{P}^T\mathbf{P}\right) + 2\beta\delta\mathbf{u}_t^T\delta\bar{\mathbf{u}} = b_0 + \beta b_1, \\
c' &= \beta^2\delta\bar{\mathbf{u}}^T\delta\bar{\mathbf{u}} + 2\beta\delta\bar{\mathbf{u}}^T\Delta\mathbf{u} + \Delta\mathbf{u}^T\Delta\mathbf{u} + \Delta\lambda^2\Psi^2\mathbf{P}^T\mathbf{P} - \Delta l^2 = c_0 + \beta c_1 + \beta^2 c_2.
\end{aligned} \tag{4.24}$$

When we enforce that the discriminant $b'^2 - 4a'c' = 0$, to avoid complex roots, the coefficients from Equation (4.24) can be substituted such that a quadratic equation in terms of β is found:

$$a_s\beta^2 + b_s\beta + c_s = 0.$$

Where (see 4.24 or Ritto-Corrêa and Camotim [173] for the definition of the coefficients):

$$a_s = b_1^2 - 4a_0c_2, \qquad b_s = 2b_0b_1 - 4a_0c_1 \qquad \text{and} \qquad c_s = b_0^2 - 4a_0c_0. \tag{4.25}$$

Such that $\beta_{1,2} = \left(-b_s \pm \sqrt{b_s^2 - 4a_sc_s}\right)/2a_s$. According to Zhou and Murray [178], the solutions $\beta_{1,2}$ ($\beta_1 < \beta_2$) are of opposite sign and if β is between those roots, the constraint equation is satisfied. Zhou and Murray propose to choose $0 < \beta \leq \beta_{\max}$, where $\beta_{\max} = \min(1, \beta_2)$. If β is close to zero, the iterative method becomes inefficient and it is advised by to cut the arc length [178, 173]. The work of Lam and Morley [177] slightly differs from the work of Zhou and Murray [178] in the sense that they use an out-of-balance load factor in their method and that different conditions for the choice of β are used. This method has also been implemented in this study and showed similar results. Additionally, the work of Lam and Morley does show an illustrative analysis on the influence of the pseudo-line search factor β.

Based on the results in this section and Section 4.4.2, Section 4.4.3 and the original method of Crisfield [179], Algorithm 3 can be used to follow load-displacement paths.

Algorithm 3 Arc-Length method based on the work of Crisfield [163] combined with line search, for load step i.

1: Initialise Δl,
Predictor phase:
2: Compute $\delta\mathbf{u}_t$ from Equation (4.15),
3: Compute $\delta\lambda$ from Equation (4.22),
4: Compute ϵ based on Equation (4.18) using $\delta\mathbf{u}_t$ and $\delta\lambda$,
Corrector phase:
5: **while** $k < k_{\max}$, $k \in \mathbb{N}$ and $\epsilon < \epsilon_{\text{tol}}$ **do**,
6: Compute $\delta\mathbf{u}_t$ from Equation (4.15) and $\delta\bar{\mathbf{u}}$ from Equation (4.14),
7: Compute a, b and c from Equation (4.17) and solve Equation (4.16) to obtain $\delta\lambda_1$ and $\delta\lambda_2$.
8: **if** $b^2 - 4ac < 0$ **then**
9: Compute coefficients a_s, b_s and c_s from Equation (4.25) and compute and select the line-search parameter β from:

$$\beta_{1,2} = \left(-b_s \pm \sqrt{b_s^2 - 4a_sc_s}\right)/2a_s$$

10: Compute a', b' and c' from Equation (4.24). If $b'^2 - 4a'c' < 0$, bisect the arc-length or apply line-search again. If $b'^2 - 4a'c' \geq 0$, compute $\delta\lambda_1$ and $\delta\lambda_2$.
11: **end if**
12: Compute $\delta\mathbf{u}_1$ and $\delta\mathbf{u}_2$:

$$\delta\mathbf{u}_\alpha = \beta\delta\bar{\mathbf{u}}_\alpha + \delta\lambda_\alpha\delta\mathbf{u}_t, \quad \alpha = 1, 2$$

13: Compute angles ϑ_1 and ϑ_2 from Equation (4.21) and choose the largest one,
14: Compute the error ϵ from Equation (4.18),
15: **end while**
16: Go to next load step.

4.4.5 Dealing with Singular Points

Singular points in structural analysis are associated with singularities in the tangential stiffness matrix. As will be discussed in this section, singular points are points where the structure is unstable and possibly, but not necessarily, buckles. In the latter case, the eigenvector corresponding to the lowest eigenvalue of the tangential stiffness matrix is the buckling mode shape. From this principle, linear buckling analysis is also derived (see Section 4.3)[158].

Detection of Singular Points

Singular points are the points where the determinant of the tangential stiffness matrix is equal to zero and hence the matrix is singular. In the partitioning technique that is generally used in Crisfield's method, this implies that the corrections $\delta\mathbf{u}_t$ and $\delta\bar{\mathbf{u}}$ cannot be computed. However, in general, the arc-length method does not pass a singular point directly [158].

On singular points, two types of structural instabilities can be identified. In the first place, the point can be a *limit point*. These are points that are indicated by L_1 and L_2 in Figure 4.10. Secondly, the point can be a *bifurcation point* (see Figure 4.12, point B), i.e. the point where buckling occurs and hence a post-buckling branch connects to the original path. Bifurcation points are the points of which the dot product of the eigenvector of the corresponding tangential stiffness matrix and the force vector is equal to zero, i.e. $\boldsymbol{\phi}^T\mathbf{P}$ or, in numerical codes, within a certain tolerance ϵ from zero [180]. In other cases, the singular point is a limit point. As will be discussed in the next subsection, the eigenvector is included in the algorithms that are used to approach singular points.

As shown in Figures 4.10 and 4.12 bifurcation points form a connection between different branches whereas limit points denote local extremes in the equilibrium curve. In the case of bifurcation points, branch switching is often of interest and hence there is a need to approach the point. This requires special algorithms to approach bifurcation points (see next subsection) and to switch to another branch (see second next subsection). Hence, it is essential to monitor whether buckling occurs in the system in each load step. As discussed in the books of Wriggers [158] and de Borst et al. [159] amongst others, bifurcations are passed when the *determinant of the tangential stiffness matrix changes sign*. Equivalently, this means the *minimum eigenvalue of the tangential stiffness matrix is negative* (hence the matrix is not positive-definite) or that *the product of the entries of the diagonal matrix of the* LDL^T *Cholesky-decomposition of the tangential stiffness matrix* (which is equal to determinant by Vieta's rule [159]) *is negative*. An alternative for the latter approach is to monitor the lowest diagonal values resulting from the decomposition, since an even number of diagonal entries of the diagonal matrix still gives a positive product, but corresponds to an unstable solution [158]. Generally, the last indicator is most beneficial as the Cholesky-decomposition can also be used to compute the equations in Equations (4.14) and (4.15). Furthermore, for a large number of degrees of freedom, the determinant becomes very large and could not even be represented by computer precision. Therefore, the minimal values of the Cholesky-diagonal matrix are monitored in this study.

Approach of Bifurcation Points

When the exact determination of bifurcation points is desired, e.g. in case of computation of bifurcation branches, further methods have to be utilized to approach the bifurcation points, i.e. the points where the determinant of the tangential stiffness matrix is zero.

The first option is to use the *bisection method*. The use of this method for approaching stability was presented by Wagner and Wriggers [181]. This method is elementary, robust [182], but slowly converging [158]. In brief, the algorithm for the method is given in Algorithm 4 and is slightly modified compared to the version in Burden et al. [182] to start from a point with a given step size. The method is then started at a certain load step $(\mathbf{u}, \lambda)_k$ when the next load step $(\mathbf{u}, \lambda)_{k+1}$ using arc-length Δl corresponds to an unstable solution. When load steps are too large, unstable branches might be *overstepped*, as illustrated in Figure 4.13 together with an example. Note that the 'error' ϵ for the loop of the algorithm can, for example, be a function value of the function for which the root is found.

An alternative method to approach singular points is presented by Wriggers et al. [183], called the *extended arc length method*. Basically, the method uses the fact that on a singular point, the determinant of the tangential stiffness matrix is equal to zero, which leads to solving $\mathrm{K}_T\boldsymbol{\phi} = \mathbf{0}$ for the non-trivial eigenvector $\boldsymbol{\phi}$. By this means, Wriggers et al. solve

$$\hat{\mathbf{G}}(\mathbf{u}, \lambda, \boldsymbol{\phi}) = \begin{bmatrix} \mathbf{G}(\mathbf{u}, \lambda) \\ \mathrm{K}_T(\mathbf{u}, \lambda)\boldsymbol{\phi} \\ l(\boldsymbol{\phi}) \end{bmatrix} = \mathbf{0}. \tag{4.26}$$

Algorithm 4 Bisection method to find a bifurcation point. $\mathbf{w} = (\mathbf{u}, \lambda)$ and the error ϵ can be any measure to monitor the stability of the system.

Start at load step $\mathbf{w}_0$ (stable),
Bisect arc length, $\Delta l_0 = \frac{\Delta l}{2}$,
Initialise iteration counter $k = 0$ and define tolerance ϵ_{tol},
while $\varepsilon > \epsilon_{\text{tol}}$ **do**,
    Compute next load step $\mathbf{w}'$ using new arc length Δl_k starting from $\mathbf{w}_{k-1}$,
    if $\mathbf{w}'$ is stable **then**,
        Set $\mathbf{w}_k = \mathbf{w}'$ and $\Delta l_{k+1} = \Delta l_k$,
    else $\mathbf{w}'$ is unstable,
        Set $\mathbf{w}_k = \mathbf{w}_{k-1}$ and bisect the step $\Delta l_{k+1} = \frac{\Delta l_k}{2}$,
    end if
    Compute error ϵ, i.e. determine the stability of the system.
end while

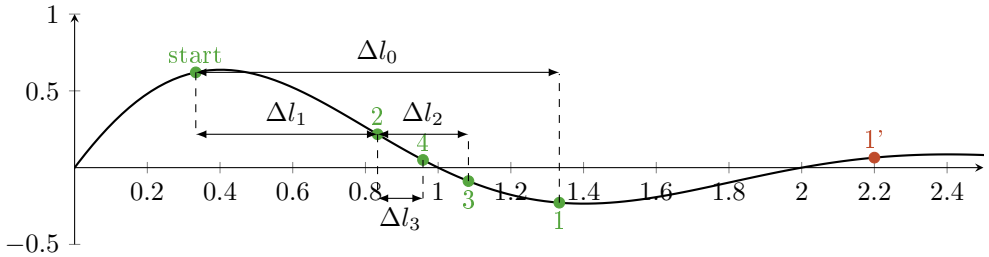

Figure 4.13: Application of the bisection algorithm to find a zero of the function $f(x) = \exp(-x)\sin(\pi x)$. The starting point is on $x = 1/3$ and the initial step Δl_0 gives a zero function value on point 1. Following the bisection procedure, the step length is halved to Δl_1 and point 2 (positive) is found. From this point, the step is again halved to Δl_2 and point 3 is found (negative). Hence, the algorithm continues from point 2 again with a halved step length Δl_3 to find point 4. In case the step between *start* and point 1' was initially taken, the negative part of the function would have been *overstepped*.

Here, $l(\boldsymbol{\phi})$ is a constraint equation to prevent the trivial solution $\boldsymbol{\phi} = \mathbf{0}$ to be found. In the work of Wriggers et al. [183], the equation $l(\boldsymbol{\phi}) = \|\boldsymbol{\phi}\| - 1 = 0$ is used and the same is adopted here. This constraint equation enforces the approach of bifurcation points. Using similar derivations as for the ordinary arc length method, a partitioned system of equations can be derived for the extended method. This yields the algorithm as presented in Algorithm 5. It should be noted that in case of this algorithm and the one in Algorithm 3 that the tangential stiffness matrix $\mathrm{K}_T(\mathbf{u})$ is computed every iteration, but that quasi-Newton or Broyden methods can also be used to reduce computational effort.

Branch Switching

When a bifurcation point is found within a specified tolerance ϵ of the extended arc-length method, the eigenvector $\boldsymbol{\phi}$ is known from this method and the method can switch to the bifurcation branch by perturbation using the buckling mode shape, i.e. using $\boldsymbol{\phi}_1$. Branch switching is simply done by perturbing the bifurcation point $\mathbf{w}_B = (\mathbf{u}_P, \lambda_P)$ by the eigenvector [158, 184]:

$$\mathbf{u} = \mathbf{u}_P + \zeta\bar{\boldsymbol{\phi}} \qquad \text{and} \qquad \lambda = \lambda_P. \tag{4.27}$$

Where $\bar{\boldsymbol{\phi}}_1$ is the normalized buckling mode shape. The factor ζ represents the magnitude of the perturbation and can be chosen sufficiently small [158]. For all applications in the present study, this factor was of order 10^{-4} up to 10^{-3}. Other methods for branch switching were proposed by Wriggers and Simo [180], where the tangent of the branch is determined and the perturbation is applied accordingly. However, the authors of this paper mention that the approach in Equation (4.27) suffices for pitch-fork bifurcations, i.e. the type shown in Figure 4.12. However, more advanced techniques can be used in future studies or for cases where the branch switching algorithm fails.

Algorithm 5 Computation of singular points using the extended method from Wriggers et al. [183].

When close to singular point $\mathbf{u}_b, \lambda_b$:

Initialise an approximation of the eigenvector $\boldsymbol{\phi}_0$ of K_T,
Utilise the power method with $k_{\max}$ iterations to approximate $\boldsymbol{\phi}$,
Compute the Jacobian K_T using displacement vector $\mathbf{u}_b$,
for $k < k_{\max} \in \mathbb{N}$ **do**
    Solve $\mathrm{K}_T \boldsymbol{\phi}_{k+1} = \boldsymbol{\phi}_k$,
    Normalise $\boldsymbol{\phi}_{k+1}$,
end for
Check if inner product of eigenvector and forcing is close to 0, i.e. if the singular point is a bifurcation point.
if $\boldsymbol{\phi}_{k+1}^T \mathbf{f} < e_{\mathrm{tol}}$ **then**
    while $i < i_{\max}$, $i \in \mathbb{N}$ and $\epsilon < \epsilon_{\mathrm{tol}}$ **do**,
        Compute residual $\mathbf{G}(\mathbf{w})$ and Jacobian $\mathrm{K}_T(\mathbf{w})$,
        Compute $\delta \mathbf{u}_t$ from Equation (4.15) and $\delta \bar{\mathbf{u}}$ from Equation (4.14),
        Compute vectors $\mathbf{h}_1$ and $\mathbf{h}_2$ using directional derivatives of K_T (see Wriggers et al. [183]) with specified step ε,

$$\mathbf{h}_1 = \frac{1}{\varepsilon}\left[(\mathrm{K}_T(\mathbf{u} + \varepsilon\boldsymbol{\phi})\delta\mathbf{u}_t) - \mathbf{P}\right],$$
$$\mathbf{h}_2 = \mathrm{K}_T\boldsymbol{\phi} + \frac{1}{\varepsilon}\left[(\mathrm{K}_T(\mathbf{u} + \varepsilon\boldsymbol{\phi})\delta\bar{\mathbf{u}} + \mathbf{G}(\mathbf{w}))\right],$$

        Solve $\mathrm{K}_T \delta\boldsymbol{\phi}_t = -\mathbf{h}_1$ and $\mathrm{K}_T \delta\bar{\boldsymbol{\phi}}_2 = -\mathbf{h}_2$,
        Compute the updates of $\Delta\lambda$, $\Delta\mathbf{u}$ and $\Delta\boldsymbol{\phi}$,

$$\delta\lambda = -\frac{\boldsymbol{\phi}^T \delta\bar{\boldsymbol{\phi}}}{\boldsymbol{\phi}^T \delta\boldsymbol{\phi}_t},$$
$$\delta\mathbf{u} = \delta\lambda\mathbf{u}_t + \bar{\mathbf{u}},$$
$$\delta\boldsymbol{\phi} = \delta\lambda\boldsymbol{\phi}_t + \bar{\boldsymbol{\phi}},$$

        Update $\Delta\lambda$, $\Delta\mathbf{u}$ and $\Delta\boldsymbol{\phi}$ and λ, $\mathbf{u}$ and $\boldsymbol{\phi}$,

$$\Delta\lambda = \Delta\lambda + \delta\lambda \qquad \lambda = \lambda + \Delta\lambda,$$
$$\Delta\mathbf{u} = \Delta\mathbf{u} + \delta\mathbf{u} \qquad \mathbf{u} = \mathbf{u} + \Delta\mathbf{u},$$
$$\Delta\boldsymbol{\phi} = \Delta\boldsymbol{\phi} + \delta\boldsymbol{\phi} \qquad \boldsymbol{\phi} = \boldsymbol{\phi} + \Delta\boldsymbol{\phi},$$

    end while
else
    Continue.
end if

4.5 Modal Analysis

Analysis of *structural vibrations* is useful when one is interested in the behaviour of a structure that is excited by an oscillating load or by sudden pulse loads. With modal analysis, information about natural frequencies, damping factors and mode shapes are inferred to use as a basis for dynamical analysis. Such dynamic analyses use a linear superposition of vibration modes for temporal solutions. Hence, information about the modal properties of a system can be useful for further structural analysis. In this section, the basics of vibration theory and the formulation for the linear vibration problem are given. Further information can be found in the book of Zhi-Fang and Jimin [185].

Given the mass matrix M and stiffness matrix K_L of a dynamic system, free vibration is described by the following:

$$\mathrm{M}\ddot{\mathbf{u}} + \mathrm{K}_L\mathbf{u} = \mathbf{0}.$$

Where $\mathbf{u}$ is a solution vector and the double dot denotes the second time-derivative, i.e. accelerations. In free vibration, the non-trivial solution to the system is denoted by the complex vector:

$$\mathbf{u} = \psi \exp(i\omega t).$$

Here, ω is an eigenfrequency of the system and $\boldsymbol{\phi}$ is an eigenmode of the system. Substituting this into the free vibration equation Section 4.5 gives:

$$\left(-\omega^2\mathrm{M} + \mathrm{K}_L\right)\boldsymbol{\phi} = \mathbf{0}.$$

Which is a generalized eigenvalue problem with eigenvalue ω^2 and eigenvector $\boldsymbol{\phi}$. Since the mass matrix M and the linear stiffness matrix K_L are associated with a finite discretization, the number of eigenvalues and eigenvectors is also finite. When the spatial discretization step increases, the number of eigenfrequencies and eigenmodes increases. Since the vibration modes form an orthogonal basis, modal analysis has attractive properties for solving dynamic systems. For further reading on this topic, the work of Zhi-Fang and Jimin [185] serves as a good introductory reference.

In the year 2006 Cottrell et al. [186] published about modal analyses in the context of isogeometric analysis and showed the advantage of being superior in accuracy compared to conventional finite element methods. Later Weeger et al.[101] published similar results for linear and nonlinear beams in 2013. Where finite element methods show so-called *optical branches* in the frequency spectrum when $n/N > 0.5$, i.e. for upper-half part of the discrete eigenfrequency spectrum, IGA does not show these branches [106]. This leads to a more accurate representation of the eigenvalues. The results of Weeger et al. will serve as a benchmark problem in Section 5.4.

4.6 Dynamic Analysis

Dynamic analysis of linear or nonlinear structures is widely used in various engineering sciences. Especially when loads are time-depending or depending on the deformation of the structure (e.g. in case of Fluid-Structure Interaction), dynamic analysis using superposition of linear modes is not sufficient to accurately describe the transient solution of structures. In that case, dynamic analyses of structures come into place. Let us define the dynamic equation, or equation of motion, for a nonlinear dynamic system. The mass matrix M denotes structural inertia. The linear damping matrix C does not follow from the discretization of the equations of solid mechanics (see Chapter 3). However, in practice, structural damping is observed for example due to viscous effects in the material, internal friction or friction in connections [158]. Furthermore, the nonlinear stiffness of the system will be denoted by $\mathbf{N}(\mathbf{u})$ and the external, time-dependent, force will be denoted by $\mathbf{P}(t)$. Furthermore, the vectors $\ddot{\mathbf{u}}, \dot{\mathbf{u}}, \mathbf{u}$ denote the accelerations, velocities and displacements of the structure, respectively. The dynamic equation then reads:

$$\mathrm{M}\ddot{\mathbf{u}} + \mathrm{C}\dot{\mathbf{u}} + \mathbf{N}(\mathbf{u}) = \mathbf{P}(t). \tag{4.28}$$

To solve this equation, several methods can be used. In this work, a distinction between two types of methods is made, namely *order reduction methods* and *direct methods for second order problems*. In the following, a selection of methods is given. The order reduction methods that are used in this study are the *Euler methods* and the *Runge-Kutta methods*. The direct methods that are presented are the *Newmark method*, the *Wilson-θ*

method and *Bathe's method*. More methods can be found in the works of Subbaraj and Dokainish[187, 188] amongst others. Order reduction methods are generally defined based on the differential equation

$$\dot{y} = f(y, t). \tag{4.29}$$

This is first order in time.

4.6.1 Implicit and Explicit Euler Methods

The implicit and Explicit Euler methods are simple methods for time integration and have been derived by Leonard Euler in 1768 [189]. Basically, the time derivative of a first order initial value problem of Equation (4.29) is approximated by a forward or backward difference step. This yields the Explicit and Implicit Euler methods, respectively. The corresponding equations read [190]:

$$\frac{y^{t+\Delta t} - y^t}{\Delta t} = f(y^t, t) \qquad \text{Explicit Euler Method,} \tag{4.30}$$

$$\frac{y^{t+\Delta t} - y^t}{\Delta t} = f(y^{t+\Delta t}, t + \Delta t) \qquad \text{Implicit Euler Method.} \tag{4.31}$$

Using order reduction methods (see for instance [191]), the Explicit Euler method is derived as

$$\begin{bmatrix}\dot{\mathbf{u}}\\ \dot{\mathbf{v}}\end{bmatrix}^{t+\Delta t} = \Delta t \left(\underbrace{\begin{bmatrix} 0 & I \\ -M^{-1}K & -M^{-1}C \end{bmatrix}}_{\mathrm{A}} \begin{bmatrix}\mathbf{u}\\ \mathbf{v}\end{bmatrix}^t + \begin{bmatrix}\mathbf{0}\\ \mathrm{M}^{-1}\mathbf{P}(t)\end{bmatrix} \right) - \begin{bmatrix}\mathbf{u}\\ \mathbf{v}\end{bmatrix}^t \qquad \text{Linear system,} \tag{4.32}$$

$$\begin{bmatrix}\dot{\mathbf{u}}\\ \dot{\mathbf{v}}\end{bmatrix}^{t+\Delta t} = \Delta t \begin{bmatrix} 0 & I \\ 0 & -M^{-1}C \end{bmatrix} \begin{bmatrix}\mathbf{u}\\ \mathbf{v}\end{bmatrix}^t + \begin{bmatrix}\mathbf{0} + \mathbf{v}^t\\ \mathrm{M}^{-1}\left(-\mathrm{C}\mathbf{v}^t - \mathbf{N}(\mathbf{u}^t)\mathbf{P}(t)\right)\end{bmatrix} - \begin{bmatrix}\mathbf{x}\\ \dot{\mathbf{x}}\end{bmatrix}^t \qquad \text{Nonlinear system.} \tag{4.33}$$

For the implicit Euler method, an implicit system needs to be solved in each time step, since the internal forces in the term $\mathbf{N}(\mathbf{u})$ are evaluated for the displacements on time step $t + \Delta t$. In case of linear stiffness, however, the method simply requires one system solve, namely

$$\left(\mathrm{I} - \Delta t \begin{bmatrix} 0 & I \\ -M^{-1}K & -M^{-1}C \end{bmatrix}\right) \begin{bmatrix}\mathbf{x}\\ \dot{\mathbf{x}}\end{bmatrix}^{t+\Delta t} = \Delta t \begin{bmatrix}\mathbf{0}\\ \mathrm{M}^{-1}\mathbf{P}(t + \Delta t)\end{bmatrix} - \begin{bmatrix}\mathbf{x}\\ \dot{\mathbf{x}}\end{bmatrix}^t. \tag{4.34}$$

In the nonlinear case, Newton iterations can be used to solve the nonlinear system in time. Felippa and Park [192] presents a solution strategy for implicit systems that are used for the derivations of direct methods, i.e. the Newmark, Wilson-θ and Bathe method. For the Implicit Euler method, it is convenient to solve using Newton iterations (see Appendix D for the derivation and the expressions for the Jacobian and the residual).

For the conditions of the Explicit Euler method with respect to stability (the Implicit Euler method is unconditionally stable) and for the Trapezoidal method as a linear combination of the Implicit and Explicit Euler method, the reader is referred to the books of Hairer et al. [189], Butcher [190] and Vuik et al. [191] amongst others.

4.6.2 Runge-Kutta Methods

The family of Runge-Kutta methods contains time integration schemes that are combinations of Explicit and Implicit Euler method steps divided over different *stages*, which are then combined to find an approximation of the solution at time step $t+\Delta t$. From [189], an s-stage Explicit Runge-Kutta Method (ERK) for Equation (4.29) is defined by:

$$\begin{aligned}
k_1 &= f(y_t, t),\\
k_2 &= f(y_t + \Delta t a_{21} k_1, t + c_2 \Delta t),\\
k_3 &= f(y_t + \Delta t(a_{31} k_1 + a_{32} k_2), t + c_3 \Delta t),\\
&\vdots\\
k_s &= f(y_t + \Delta t(a_{s,1} k_1 + \cdots + a_{s,s-1} k_{s-1}), t + c_s \Delta t),\\
y_{t+\Delta t} &= y_t + \Delta t \left(b_1 k_1 + \cdots + b_s k_s\right).
\end{aligned} \tag{4.35}$$

Where the coefficients a_{ij}, b_i and c_j can be presented in a so-called Butcher Tableau [193]:

$$\begin{array}{c|ccccc} c_1 & a_{11} & & & & \\ c_2 & a_{21} & a_{22} & & & \\ c_3 & a_{31} & a_{32} & a_{32} & & \\ \vdots & \vdots & \vdots & \ddots & & \\ c_s & a_{s1} & a_{s,2} & \dots & a_{s,s-1} & a_{s,s} \\ \hline & b_1 & b_2 & \dots & b_{s-1} & b_s \end{array} \tag{4.36}$$

The most 'famous' Runge-Kutta method, which is the Runge-Kutta 4 (RK4) method, is defined by the following Butcher Tableau [194]:

$$\begin{array}{c|cccc} 0 & & & & \\ \frac{1}{2} & \frac{1}{2} & & & \\ \frac{1}{2} & 0 & \frac{1}{2} & & \\ 1 & 0 & 0 & 1 & \\ \hline & \frac{1}{6} & \frac{2}{6} & \frac{2}{6} & \frac{1}{6} \end{array} \tag{4.37}$$

In this work, the well-known fourth order Runge-Kutta method (RK4) will be used. However, variations on the general Runge-Kutta methods are as follows. As an extension to the equations in Equation (4.35), the 'diagonal' coefficients a_{ii} can be added. If at least one of these coefficients is added to the method, the method contains at least one implicit solution step, making it a Diagonal Implicit Runge Kutta Method (DIRK). If, furthermore, all these diagonal elements are equal, the DIRK methods simplify to the Singly DIRK (SDIRK) methods [189]. Lastly, if the first stage of the method is explicit and all the other steps are implicit with the same diagonal coefficients, so-called Explicit first stage, SDIRK (ESDIRK) schemes are obtained [195]. The ESDIRK schemes that are used by van Zuijlen are unconditionally stable. ERK schemes are Explicit Runge Kutta schemes, that contain the previously presented RK4 method. Kanevsky et al. [196] presents the stability region of these methods. Butcher tableaus for the ESDIRK and the ERK scheme families are:

$$\text{ESDIRK:}\quad \begin{array}{c|cccc} c_1 & 0 & 0 & 0 & 0 \\ c_2 & a_{21} & a_{22} & 0 & 0 \\ c_3 & a_{31} & a_{32} & a_{33} & 0 \\ c_4 & a_{41} & a_{42} & a_{43} & a_{44} \\ \hline & b_1 & b_2 & b_3 & b_4 \end{array} \qquad \text{ERK:}\quad \begin{array}{c|cccc} c_1 & 0 & 0 & 0 & 0 \\ c_2 & a_{21} & 0 & 0 & 0 \\ c_3 & a_{31} & a_{32} & 0 & 0 \\ c_4 & a_{41} & a_{42} & a_{43} & 0 \\ \hline & b_1 & b_2 & b_3 & b_4 \end{array} \tag{4.38}$$

Note that the ESDIRK methods require Newton iterations similar to the Implicit Euler method to solve nonlinear structural dynamics. This is seen as a major drawback of the method, despite the fact that the ESDIRK methods can be of high orders.

4.6.3 The Newmark and Wilson-θ Methods

The Newmark method was first published in 1959 by Newmark[197]. The method is widely known in the field of structural dynamics. Derivation of the method is not necessarily based on the form as written in Equation (4.29) but rather on the system in Equation (4.28). Namely, the method relies on the definition of the displacement and velocity on time step $t + \Delta t$ in terms of the acceleration on this time instance. Let y_t, $\dot{y}_t$ and $\ddot{y}_t$ be the displacement, velocity and accelerations at time step t. Then, the Newmark method is defined by solving

$$\left(\frac{1}{\alpha\Delta t^2}\mathrm{M} + \frac{\delta}{\alpha\Delta t}\mathrm{C} + \mathrm{K}_L\right)\mathbf{u}^{t+\Delta t} = \mathbf{P}(t+\Delta t) - \mathrm{M}\left[\frac{1}{\alpha\Delta t^2}\left(-\mathbf{u}^t - \Delta t\dot{\mathbf{u}}^t\right) - \ddot{\mathbf{u}}^t\right] - \mathrm{C}\left[-\frac{\delta}{\alpha\Delta t}\mathbf{u}^t - \dot{\mathbf{u}}^t\right]. \tag{4.39}$$

Or, for a nonlinear system [198]

$$\begin{aligned}\left(\frac{1}{\alpha\Delta t^2}\mathrm{M} + \frac{\delta}{\alpha\Delta t}\mathrm{C} + \mathrm{K}_T(\mathbf{u}_i^{t+\Delta t})\right)\Delta\mathbf{u} = \mathbf{P}(t+\Delta t) - \mathbf{N}(\mathbf{u}_i^{t+\Delta t}) - \mathrm{M}\left[\frac{1}{\alpha\Delta t^2}\left(\mathbf{u}_i^{t+\Delta t} - \mathbf{u}^t - \Delta t\dot{\mathbf{u}}^t\right) - \ddot{\mathbf{u}}^t\right] \\ -\mathrm{C}\left[\mathbf{u}_i^{t+\Delta t} - \frac{\delta}{\alpha\Delta t}\mathbf{u}^t - \dot{\mathbf{u}}^t\right] \\ \text{With } \mathbf{u}_{i+1}^{t+\Delta t} = \mathbf{u}_i^{t+\Delta t} + \Delta\mathbf{u}.\end{aligned} \tag{4.40}$$

In both cases, the accelerations and velocities on the time step $t + \Delta t$ can be computed by:

$$\begin{aligned} \ddot{\mathbf{u}}^{t+\Delta t} &= \frac{1}{\alpha \Delta t^2}(\mathbf{u}^{t+\Delta t} - \mathbf{u}^t - \Delta t \dot{\mathbf{u}}) - \ddot{\mathbf{u}}^t \\ \dot{\mathbf{u}}^{t+\Delta t} &= \frac{\delta}{\alpha \Delta t}(\mathbf{u}^{t+\Delta t} - \mathbf{u}^t) - \dot{\mathbf{u}}^t. \end{aligned} \tag{4.41}$$

For $\delta \geq \frac{1}{2}$ and $\alpha \geq \frac{\left(\delta + \frac{1}{2}\right)^2}{4}$, the method is unconditionally stable and for $\delta = \frac{1}{2}$ the method has second-order accuracy. More variations of the tuning parameters are given in the work of Subbaraj and Dokainish [187].

The Wilson-θ method is a variation on the Newmark method and was first presented in 1973 by Wilson et al.[199]. The method is a variation of the Newmark method since it computes the acceleration on time step $t + \Delta t$ using the following interpolation:

$$\ddot{\mathbf{u}}_{t+\Delta t} = \left(1 - \frac{1}{\theta}\right) \ddot{\mathbf{u}}_t + \frac{1}{\theta} \ddot{\mathbf{u}}_{t+\theta \Delta t}. \tag{4.42}$$

In the case where $\theta = 1$, the method simplifies to the original Newmark method. In case of $\theta > 1$, the method works as an interpolation between the solutions on time step t and on $t + \theta \Delta t$. The latter is calculated using the Newmark method with time step $\theta \Delta t$. As mentioned by Wilson et al. [199], the method is unconditionally stable for $\theta \geq 1.37$. Increasing θ yields an increase in numerical dissipation and accuracy is lost. Furthermore, the method has the tendency to overshoot the exact solution in the first steps of a transient analysis and hence the method is not suitable for impact loads [187]. Basically, this method can be seen as an extension of Newmark's method, as it contains an extra tuning parameter θ.

Another implicit method that can be used is the Houbolt method. In this method, accelerations and velocities are purely described by displacements at the present time step and the previous two time steps. The method is unconditionally stable, but algorithmic damping is introduced and contrary to the Newmark and Wilson-θ methods, this cannot be tuned [187]. Additionally, the method needs a starting procedure because it uses the solution at more than one previous time step. Based on these two drawbacks of the method, it is not included in this study.

4.6.4 The Bathe Method

A relatively new method in the field of time integration methods for structural dynamics is Bathe's metod, which was introduced in 2005 by Bathe and Baig[198]. In later papers, Bathe investigated the method with co-authors [200, 201, 202, 203]. The motivation behind the Bathe method is that for nonlinear dynamic systems, methods such as the Trapezoidal method or the Wilson-θ method lose their property of being unconditionally stable. This is especially the case when long time responses and very large deformations are considered [198]. The method proposed by Bathe and Baig is a single step, double sub-step method. In the first substep a Newmark method[3] is used with time step $\gamma \Delta t$. In the second sub step, an Euler 3-point backward rule is adopted. Hence, the method is specified by the following equations [203] (only for a nonlinear system):

Step 1: (Newmark Method)

Use the substitutions for the Newmark method with time step $\gamma \Delta t$

$$\begin{aligned} \ddot{\mathbf{u}}^{t+\gamma\Delta t} &= \frac{1}{\alpha \gamma^2 \Delta t^2}(\mathbf{u}^{t+\gamma\Delta t} - \mathbf{u}^t - \Delta t \dot{\mathbf{u}}) - \ddot{\mathbf{u}}^t, \\ \dot{\mathbf{u}}^{t+\gamma\Delta t} &= \frac{\delta}{\alpha \gamma \Delta t}(\mathbf{u}^{t+\gamma\Delta t} - \mathbf{u}^t) - \dot{\mathbf{u}}^t. \end{aligned} \tag{4.43}$$

To solve Equation (4.40) iteratively. Then compute $\mathbf{u}_{t+\gamma\Delta t}$ and $\dot{\mathbf{u}}_{t+\gamma\Delta t}$ from Equation (4.43).

Step 2: (Euler 3-point backward rule)

With $\mathbf{u}_{t+\gamma\Delta t}$, $\dot{\mathbf{u}}_{t+\gamma\Delta t}$ and $\ddot{\mathbf{u}}_{t+\gamma\Delta t}$, compute (in terms of $\mathbf{u}_{t+\Delta t}$)

$$\begin{aligned} \mathbf{u}^{t+\Delta t} &= c_1 \mathbf{u}^t + c_2 \mathbf{u}^{t+\gamma\Delta t} + c_3 \mathbf{u}^{t+\Delta t}, \\ \dot{\mathbf{u}}^{t+\Delta t} &= c_1 \dot{\mathbf{u}}^t + c_2 \dot{\mathbf{u}}^{t+\gamma\Delta t} + c_3 \dot{\mathbf{u}}^{t+\Delta t}. \end{aligned} \tag{4.44}$$

[3] Note: in [198, 200, 201, 202] the trapezoidal method is used as a first step. Basically, this is the Newmark method for $\alpha = \frac{1}{4}$ and $\delta = \frac{1}{2}$. Furthermore, in [200, 201, 202], $\gamma = \frac{1}{2}$ is adopted.

Where:

$$c_1 = \frac{1-\gamma}{\gamma \Delta t}, \qquad c_2 = \frac{-1}{(1-\gamma)\gamma \Delta t} \qquad \text{and} \qquad c_3 = \frac{2-\gamma}{(1-\gamma)\Delta t}.$$

Then, solve

$$\mathrm{M}\ddot{\mathbf{u}}^{t+\Delta t} + \mathrm{C}\dot{\mathbf{u}}^{t+\Delta t} + \mathrm{K}\dot{\mathbf{u}}^{t+\Delta t} = \mathbf{P}(t+\Delta t), \tag{4.45}$$

to obtain $\ddot{\mathbf{u}}^{t+\Delta t}$ and substitute this in Equation (4.44) to obtain $\mathbf{u}^{t+\Delta t}$ and $\dot{\mathbf{u}}^{t+\Delta t}$.

The Bathe method is of second order since both the Newmark method and the Euler 3-point backward rule are of second order. Furthermore, the method is unconditionally stable, even in the case of nonlinear equations with large time steps. The latter is a clear advantage compared to the trapezoidal method [200].

In the work of Bathe and Noh [202], the Bathe method is investigated for linear analyses. In this paper, the method was investigated for $\gamma > 1$. As found in the paper, this choice of γ implies large amplitude decays. Furthermore, they investigated the use of $\alpha = 1$, $\delta = 3/4$ and $\gamma = 0.5$ for the first time step, in order to prevent overshoot in the acceleration of one degree of freedom in their test case. However, they recommend to not use these coefficients in the complete simulation, as the method becomes first order accurate and loses its unconditional stability. Based on other analysis, it was concluded that the Bathe method is stable for large time steps and that artificial high-frequency responses are damped out [198, 200, 201, 202].

4.7 Concluding Remarks

In this section, the concept of Isogeometric Analysis was presented and applied on a simple structural beam equation. Additionally, the section presents the derivation of different structural analyses given the linear and tangential stiffness matrices and the damping and mass matrices from a beam, a shell or any structural element. This reflects the third subgoal of this thesis. The main emphasis in this chapter was on dynamic and post-buckling models. The former is not fully related to this research but is more relevant for further research on dynamic simulations of floating sheets (see Chapter 8). The post-buckling analysis, however, is relevant and will be applied in the analysis of buckling and hence wrinkling of thin sheets. In particular, using the identification of singular points, the bisection method and the extended iterations from Wriggers et al. [183] allow to compute the load factor and displacement vector on singular points, including the corresponding buckling modes in case of bifurcations. To this extent, the arc-length method presented in Section 4.4 can be used for post-buckling analysis without *a priori* selection of an initial perturbation, which was discussed in Chapter 2. In the following chapter, the structural analyses using the model from the previous chapter with Isogeometric Analysis are benchmarked using examples from literature.

5 | Benchmark Problems

In this section, benchmark examples for the numerical procedures from the previous section will be given to assess the performance of the Isogeometric beam and shell models. This relates to subgoal 4 of this thesis. Generally, numerical models can be verified in two ways: by *code verification* and *calculation verification*. In the former case, benchmark problems from literature or manufactured solutions[1] are used to check if equations are implemented correctly. In the latter case, consistency of the code is assessed, most commonly by doing a grid convergence study [205, 206]. Throughout the whole section, benchmark problems, manufactured solutions and grid convergence studies will be used to verify the numerical models. Throughout this section, the following error measures will be used:

$$\epsilon_\Omega = \|\mathbf{u}_{\text{num}} - \mathbf{u}_{\text{an}}\|_2 = \left(\int_\Omega (\mathbf{u}_{\text{num}} - \mathbf{u}_{\text{an}})^2 \right)^{\frac{1}{2}} \qquad \text{and} \qquad \epsilon = \frac{|u_{\text{num}} - u_{\text{an}}|}{|u_{\text{an}}|}.$$

Where $\mathbf{u}_{\text{num}}$ is the numerical approximation of the analytical solution $\mathbf{u}_{\text{an}}$ (both vectors) and u_{num} and u_{an} are representative scalar approximations and analytical solutions. ϵ_Ω is the integral L^2-norm and ϵ is the scalar L^1-norm. In the discrete case, the integral sign in the definition of the norm is replaced by a summation.

5.1 Static Analysis

Static analysis for both beam and shell models is considered in the nonlinear cases only. This means that the systems of equations are solved using Newton iterations and the Jacobian (see Section 4.2).

Beam model

Firstly, for the beam model a pinned-pinned beam with length L subject to a uniform load $q = 1\,[N/m]$ is modelled. The bending stiffness and axial stiffness are chosen to be unity, i.e. $EI = 1\,[Nm^2]$ and $EA = 1\,[N]$. The method of manufactured solution is used for verification of the problem. Here, the analytical solution for the linear beam is utilized as vertical displacements, while horizontal displacements are set to zero. Thus, for the pinned-pinned case:

$$\begin{aligned} u_m(x) &= 0, \\ w_m(x) &= \frac{qx}{24EI}\left(L^3 - 2Lx^2 + x^3\right). \end{aligned}$$

Substituting these manufactured solutions in the system of equations (strong form) for the nonlinear beam (see Equation (B.13)) gives the forcings that need to be applied to simulate the manufactured solutions. For the pinned-pinned case:

$$\begin{aligned} f(x) &= \frac{EAq^2(4x^3 - 6Lx^2 + L^3)x(x-L)}{48EI^2}, \\ g(x) &= \frac{(xEA(L-x)(L-2x)^2(L^2 + 2Lx - 2x^2)^2q^2 + 768EI^3)q}{768EI^3}, \quad x \in [0, L]. \end{aligned}$$

[1] The Method of Manufactured Solutions was introduced by Roache [204]. The method assumes a closed form expression u of the solution, not necessarily a physical one. Subsequently, solution u is substituted in the (system of) partial differential equations such that only right-hand side terms remain unknown. If these terms are applied to the numerical system, an approximation of u should follow.

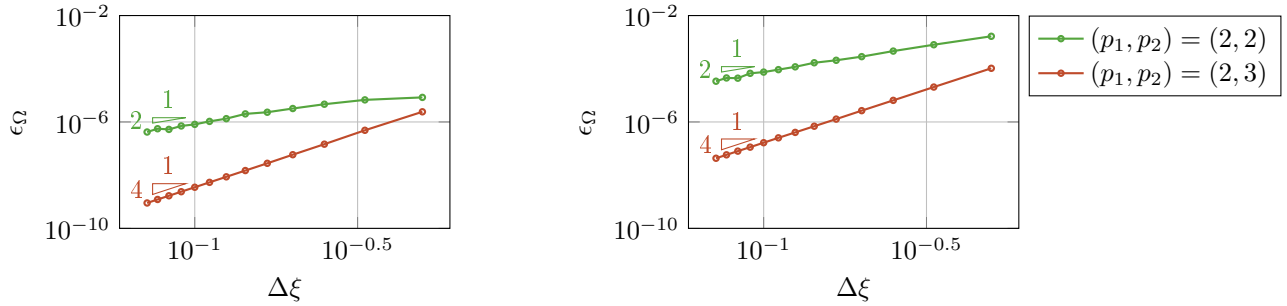

(a) Nonlinear beam, horizontal deflection

(b) Nonlinear beam, vertical deflection

Figure 5.1: Horizontal and vertical deflections for the nonlinear beam for different orders of the knot vector of the knot vectors for the vertical deflection (Ξ_2, p_2) and the horizontal deflection (Ξ_1, p_1). $\Delta\xi$ is the step size in the knot vectors, i.e. unique knot values are $\Xi_i = \{0, \Delta\xi, 2\Delta\xi, \ldots, 1\}$. Furthermore, $EI = 1\ [Nm^2]$, $EA = 1\ [N]$, $q = 1\ [N/m]$, $L = 1\ [m]$.

Consequently, the convergence of the Isogeometric linear and nonlinear beam models with respect to the analytical and manufactured can be calculated to verify the computation as well as the code. The results for the convergence analysis are depicted in Figure 5.1, where the error for the horizontal and vertical directions are plotted for different knot spacings $\Delta\xi$. Furthermore, the order of the B-splines is different for the bases of the solution in these directions. The order of the B-splines that represent the vertical solution is varied between 2 and 4 keeping the horizontal basis of second order.

As can be seen in the figure, second-order convergence is observed for second-order basis functions and the line shows wiggles. From theoretical results, third order is expected since the basis functions are of second order and polynomial. The discrepancy in the order of convergence might be due to the fact that the basis functions are too coarse or that routines for the basis functions or their derivatives provide inaccurate results when knot spans $\Delta\xi$ decrease (e.g. the use of $\leq$ or $<$ for basis function generation). This also holds for upcoming results for the second-order beam model, where wiggles are also found. Furthermore, it can be seen that the basis functions of third order converge with expected fourth order. The basis functions of fourth order are not plotted since they represent the analytical solution since this is of fourth order polynomial form.

Shell model

For the shell model, the Shell Obstacle course as introduced by Belytschko et al. [207] is used for benchmarking. The shell obstacle course consists of three component, namely the *Scordelis-Lo roof*, the *pinched cylinder* and the *hemispherical shell*. In these cases, the linear shell model was used. The geometry definitions are presented in Figure 5.2 together with the parameter values presented in Table 5.1. In Figure 5.3 the contour plots of the deformed geometries are presented and Figure 5.4 presents convergence plots of the benchmarks. Similar to the results of Goyal [142] and Kiendl [137] the numerical solutions are plotted since the shells do not converge to the values of Belytschko et al. [207]. In Figure 5.4 the Richardson extrapolation[208] of the numerical results are also plotted. Table 5.1 also presents the reference solutions of Belytschko et al. [207] (FEM) and Kiendl [137] (IGA) together with the present model.

In the works of Kiendl et al. [87], Coox et al. [209] and Nguyen-Thanh et al. [210] amongst others similar differences of the benchmark solutions from Belytschko et al. [207] were observed. According to Nguyen-Thanh et al. [210] the difference for the Scordelis-Lo roof is explained by treatment of shear deformations in the reference solution and absence of this effect in the Kirchhoff-Love shell. The difference between the obtained results of the present model and the model of Kiendl et al. [87] for the pinched cylinder might be explained by the use of a slightly different basis or the use of the Richardson Extrapolation in the present study to find a converged solution.

Additionally, a benchmark case for follower pressures is adopted from Bouzidi et al. [211]. In this case, a circular plate with simply supported boundary conditions is modelled with follower and non-follower pressures.

Table 5.1: Parameters for the shell obstacle course Belytschko et al. [207]. In the last row, the terms in brackets denote the percentual error between the reference solution and the present solution.

		Scordelis-Lo Roof	Pinched Cylinder	Hemisphere
Boundary conditions	Solid Dashed	$u_x, u_z = 0$ Free	Fixed Symm.	Free Symm.
Material	$E\ [MPa]$ ν	$4.32 \cdot 10^8$ 0.0	$3.0 \cdot 10^6$ 0.3	$6.825 \cdot 10^7$ 0.3
Load	$p\ [N/m^2]/P\ [N]$	90	1	± 2
Geometry	$R\ [m]$ $L\ [m]$ $\theta\ [°]$ $t\ [m]$	25 50 40 0.25	600 300 – 3	10 – – 0.04
Solution at A	$u_{\text{ref}}\ [m]$ [207] $u_{\text{ref}}\ [m]$ [137] $u_{\text{num}}\ [m]$ Present	0.3024 (0.6%) 0.3006 (0.0%) 0.30058	$1.8248 \cdot 10^{-5}$ (0.2%) $1.8264 \cdot 10^{-5}$ (0.1%) $1.8281 \cdot 10^{-5}$	0.0924 (0.0%) 0.0924 (0.0%) 0.0924

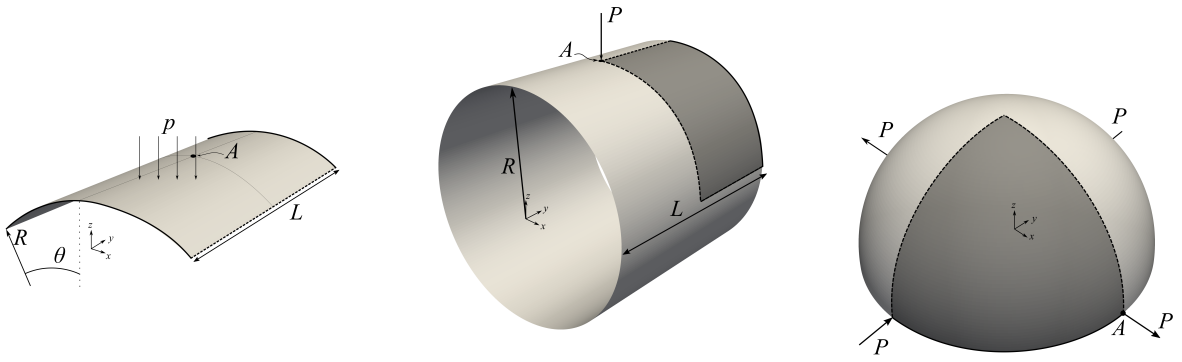

(a) Scordelis Lo roof subject to a uniform pressure.

(b) Pinched cylinder with dark-grey model domain.

(c) Hemisphere subject to point loads with dark-grey model domain.

Figure 5.2: Shell obstacle course, geometry definitions.

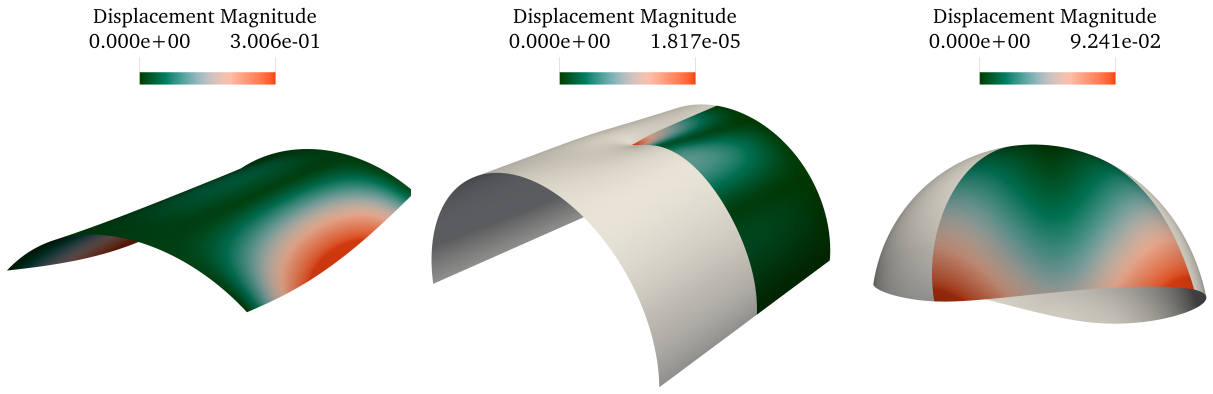

(a) Scordelis-Lo roof. Scaling magnitude: 10

(b) Pinched cylinder. Scaling magnitude: 3×10^6

(c) Hemisphere subject to point loads. Scaling magnitude: 20

Figure 5.3: Shell obstacle course, deformed geometries.

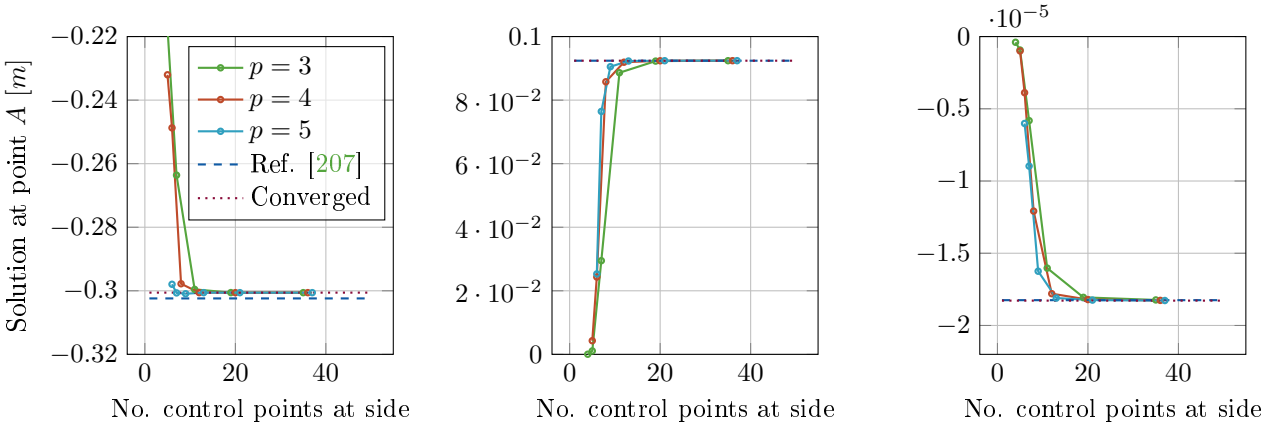

(a) Scordelis-Lo Roof.
$u_{\text{ref}} = 0.3024\ [m]$
$u_{\text{num}} = 0.30058\ [m]$

(b) Hemispherical Shell.
$u_{\text{ref}} = 0.0924\ [m]$
$u_{\text{num}} = 0.0924\ [m]$

(c) Pinched Cylinder.
$u_{\text{ref}} = -1.8264 \cdot 10^{-5}$
$u_{\text{num}} = -1.8281 \cdot 10^{-5}\ [m]$

Figure 5.4: Numerical solutions for different mesh sizes for the three cases of the Shell Obstacle Course. The horizontal axis represents the number of control points at the side of the geometry and the verical axis represents the solution at the reference location A (see Figure 5.2). u_{ref} is the solution of Belytschko et al. [207] and u_{num} is the solution of the present model.

Figure 5.5 presents the radial deformation of the plate for pressure levels 100, 250 and 400 $[kPa]$. As seen in this figure, the present model for non-follower loads matches with the analytical solution of Hencky (see Fichter [212]) and the present model for follower loads corresponds with the model of Fichter [212]. The solution given by Bouzidi et al. [211] shows less correspondence to the Fichter solutions for larger pressure levels, which is by the author clarified by the fact that the Fichter solution is less accurate for large pressures. The proposed element by Bouzidi et al. [211] uses direct minimization of potential energy as an improvement, which is the reason for the difference in the results. For larger pressures, it should be noted that the area of the elements increases significantly due to stretching and hence the area on which the pressures act is larger. This is captured by the finite element formulation of Wu and Ting [213] and left out of scope in this research.

Lastly, a plate subject to pressure is computed with a THB-refined mesh. The refinement procedure that was applied is rather straight forward: (i) compute the deformation of the plate on a coarse mesh; (ii) check the vertical displacements of the plate on the *anchors*, *collocation points* or *Greville absissae* of the element and tag the element; (iii) refine the elements corresponding to the tags. In this case, elements were either refined if their vertical displacement was *below* or *above* a certain tolerance, to which be referred to as *bottom-up* and *top-down* in the sequel. Further adaptive refinement procedures were considered out of the scope of this work and the reader is referred to the work of Carraturo et al. [129] for an adaptive meshing strategy for time-dependent problems.

The result for the THB-refined mesh is depicted in Figure 5.6a for selected meshes and convergence of the meshes with respect to the total number of system degrees of freedom is plotted in Figure 5.6b. From these results, it can be observed that refinements in the boundary region are not effective since the slope of the curve is low at the beginning of the bottom-up approach and at the end of the top-down approach. Furthermore, it can be seen that slopes are higher when regions near the maximum displacement of the plate are refined. However, a combination of the results shows that refinement of the region where the curvature changes sign is most effective (i.e., as the slopes halfway are relatively steep in both cases). Concluding, this benchmark illustrates that refinement based on vertical displacement based on *top-down* refinement is most effective. However, refinement based on curvature fields or stress/strain is to be investigated.

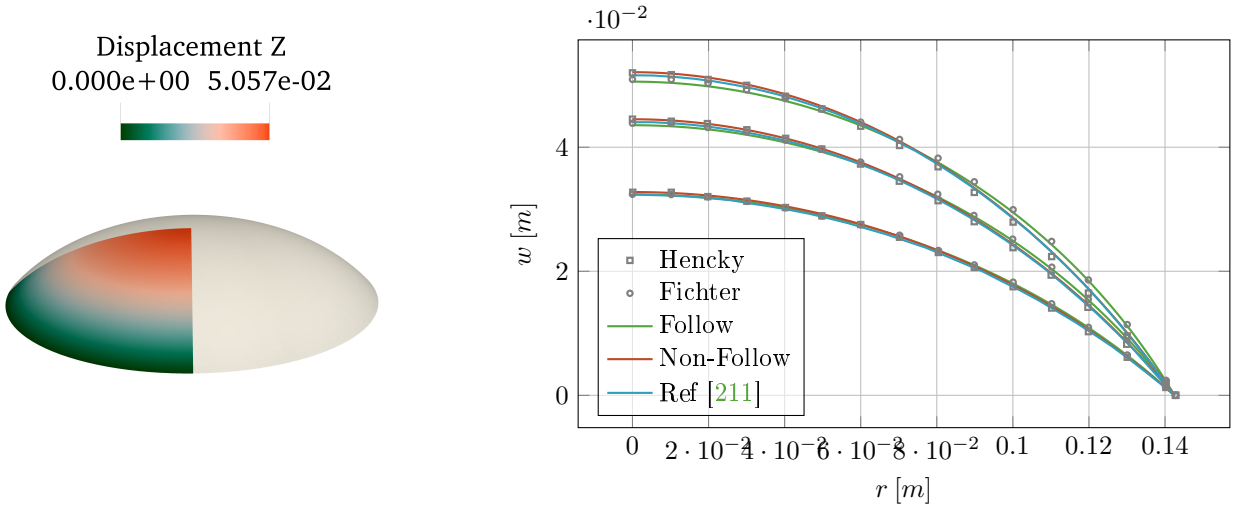

Figure 5.5: Simply supported circular plate subject to (follower) pressure. The analytical solutions of Hencky (non-follower pressure) and Fichter (follower pressure) [212] and the numerical solution of Bouzidi et al. [211] are given as reference solutions. The characteristics of the plate are $E = 31.1488\ [MPa]$, $t = 0.01\ [m]$, $\nu = 0.34$, $R = 0.1425\ [m]$ and pressure levels are $100, 250, 400\ [kPa]$.

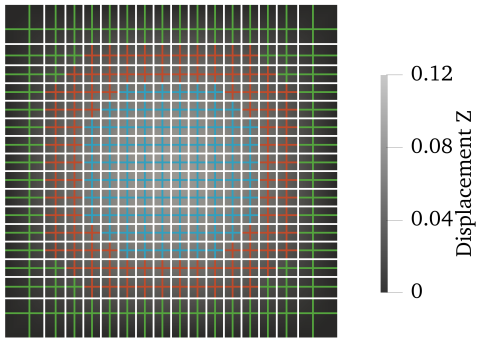

(a) Refinement regions related to displacement levels of 0.12, 0.08, 0.04, 0.0 (original mesh) with colours ■,■,■,□, respectively. In case of *top-down* refinement, adaptive meshing is performed for regions with a displacement above certain levels, hence in the order ■, ■ and ■. In case of *bottom-up* refinement, adaptive meshing is performed for regions with displacement below certain levels, hence in the order ■, ■ and ■ when shifting the tolerance.

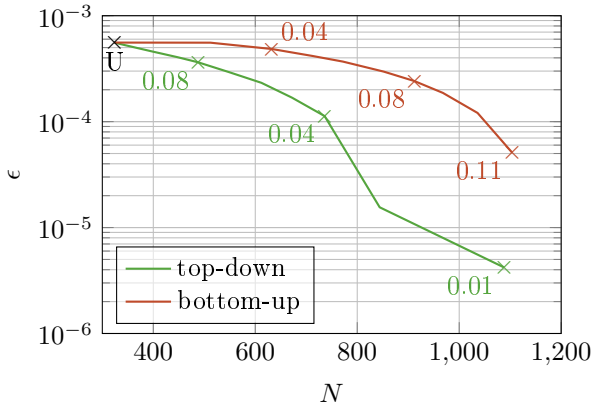

(b) Displacement error ϵ on the plate mid-point with respect to the solution of the finest mesh for different number of degrees of freedom N. Explanation of *top-down* and *bottom-up* refinement can be found in Figure 5.6a. The point corresponding to the unrefined mesh is indicated by U. The other points mark values for which the mesh is refined if the solution is above (below) this tolerance for *top-down* (*bottom-up*) refinement.

Figure 5.6: Adaptive refinement of a fully simply supported plate subject to a distributed load. The geometry has unitary values, i.e. the length and width of the plate are $1\ [m]$. Furthermore, $E = 1\ [Pa]$, $\nu = 0\ [-]$, $t = 0.05\ [m]$ and the load $q = 0.0003\ [N/m^2]$. The left image provides different refinement regions whereas the right figure provides the errors w.r.t. the number of degrees of freedom of the discretised system for a *top-down* and *bottom-up* refinement approach, i.e. refinement of regions where the vertical deflection is above or below a certain tolerance, respectively.

5.2 Buckling Analysis

In this section, verification of the buckling solvers of the beam and shell model is performed. The beam model is verified with a case of a beam on a foundation and the shell model is verified using a bi-axially loaded plate.

Beam Model

For the beam model, verification of the linear buckling model is based on the comparison with analytical solutions to the buckling problem. In this study, buckling verification will be done for a beam on an elastic foundation. The full derivation related to this problem is presented in Appendix C.2. Similar to the analysis of Rivetti and Neukirch [66], the results are given for the non-dimensional foundation/bending stiffness ratio values of $\eta = 0, 2, 7, 10$ (see Equation (5.1)). For a beam with length L, bending stiffness EI and foundation stiffness S, the following dimensionless ratio between the bending stiffness and foundation stiffness is defined.

$$\eta = \frac{L}{L_{eh}} = \frac{L}{\left(\frac{EI}{S}\right)^{\frac{1}{4}}}. \tag{5.1}$$

Figure 5.7 presents convergence plots for the critical buckling load for different values of the nonlinear stiffness ratio η for different polynomial orders with respect to the analytically determined buckling load P_{an} based on Appendix C.2. As can be seen in this figure, coarse meshes provide inaccurate approximations of the buckling load. Finer meshes, however, show convergence in the order of $2p-2$ up to $2p-1$ for bases of order p. However, for fine meshes, oscillations in the convergence behaviour are seen. Although these oscillations occur at relatively low errors (of order $\mathcal{O}\left(10^{-7}\right)$) and although the results from `ANSYS` (`BEAM181` elements) also provide similar oscillations, consistency of the method to lower orders is expected. The reason for the inconsistency can be the fact that a linearized problem is solved and hence the solution used for the tangential stiffness matrix is not representative for the final solution. In literature, no theoretical orders of convergence were found for the beam buckling problem.

Shell Model

Buckling of the thin shell model is verified using a plate that is simply supported on all edges and constrained in the in-plane directions (see Figure 5.9a) such that the plate is bi-axially loaded in case of a non-zero Poisson ratio ν. The reference solution is obtained using formulations from the book of Hughes et al. [52] and is given in Appendix C.3. For a plate with $L = 1\,[m]$, $B = 1\,[m]$, $E = 200\,[GPa]$, $\nu = 0.3$, $t = 10\,[mm]$, the reference critical stresses loads σ_c are $55.62\,[MPa]$, $105.09\,[MPa]$ and $194.36\,[MPa]$ for buckling modes 1, 2 and 3, respectively. The buckling modes corresponding to these loads are depicted in Figure 5.9.

In Figure 5.8, the relative errors between the numerically obtained buckling load and the analytically computed buckling load for the case in Figure 5.9a for the first three buckling modes are given. As seen in these figures, the present model predicts the buckling loads for the square plate accurately and consistently for finer meshes. However, contrary to other analyses, the models do not show improvement in the order of convergence for increasing polynomial order of the elements. Instead, convergences of order 2 up to 3 are observed, regardless of the order of the basis. Thus, it can be concluded that further research is required on convergence of the buckling solver.

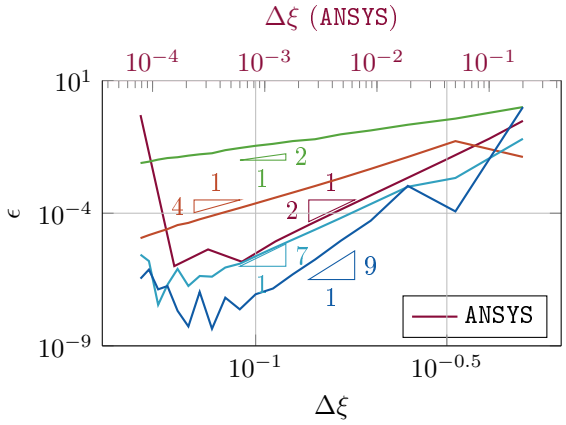

(a) $\eta = 0$, $P_{\text{an}} = 3947.84\ [N]$. **Note:** the solution from ANSYS is plotted on the top-horizontal axis.

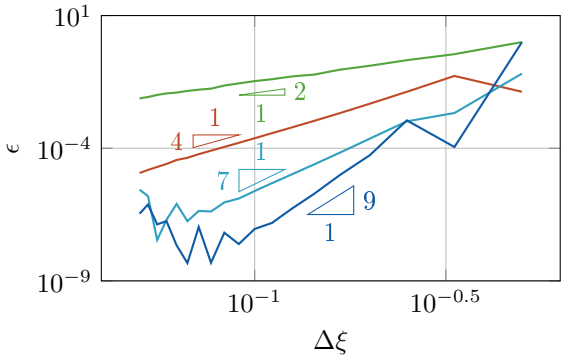

(b) $\eta = 2$, $P_{\text{an}} = 4069.25\ [N]$

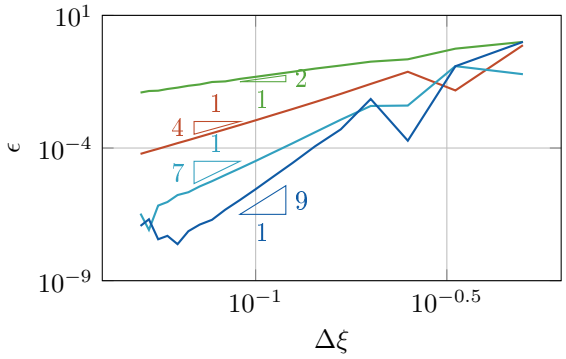

(c) $\eta = 7$, $P_{\text{an}} = 12898.8\ [N]$

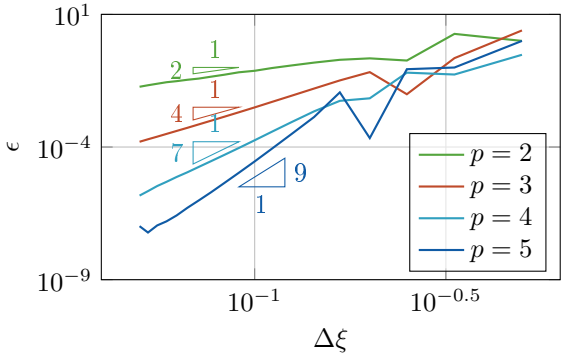

(d) $\eta = 10$, $P_{\text{an}} = 23378.5\ [N]$

Figure 5.7: Convergence of the relative error for the first buckling load of the **beam model**, with respect to analytically determined critical load P_{an} for different values of the non-dimensional stiffness paramteter $\eta \in \{0, 2, 7, 10\}$. The parameters of the beam are: $EA = 10^2\ [N]$, $EI = 10^8\ [Nm^2]$, $L = 1\ [m]$ and the reference load was $P = 10^{-4}\ [N]$. The (unique) knot vector varies between $\Xi = \{0, \Delta\xi, 2\Delta\xi, \ldots, 1\}$ for $\Delta\xi = 1/n$, $n \in \{1, 2, \ldots, 20\}$ and the orders of the knot vector vary between 2 and 5. For the beam without a foundation ($\eta = 0$) reference computations were made with ANSYS with similar parameters but a reference load of $P = 10^2\ [N]$.

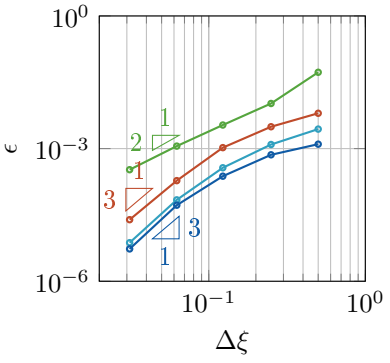

(a) Mode 1, $\sigma_c = 55.62$

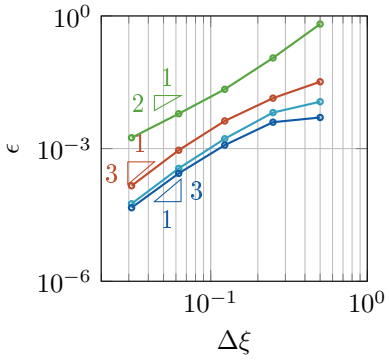

(b) Mode 2, $\sigma_c = 105.09$

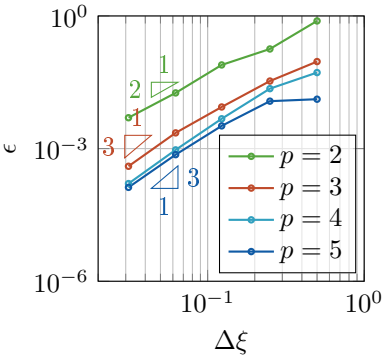

(c) Mode 3, $f_c = 194.37$

Figure 5.8: Convergence of the first three buckling modes for the **shell model** for mesh size or knot span $\Delta\xi$. The error ϵ is an L_2 error between the analytically and numerically obtained critical stress on the boundary. Orders of the knot vectors range from 2 to 5.

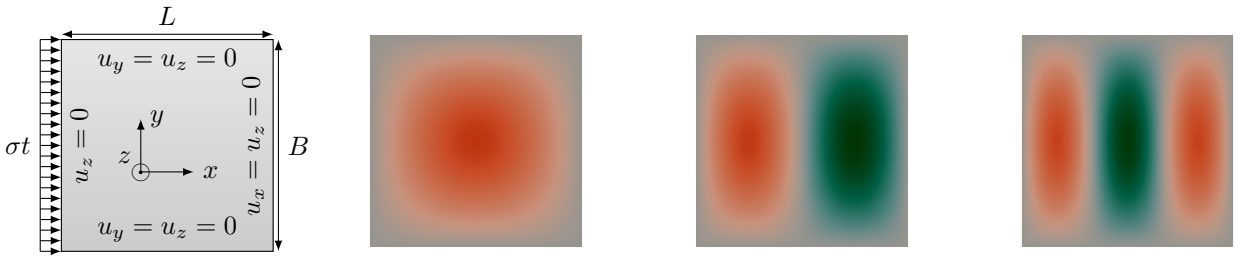

(a) Geometry **(b)** Mode 1 **(c)** Mode 2 **(d)** Mode 3

Figure 5.9: Model and normalised mode shapes for buckling of a simply supported plate which is restrained in the normal direction of each boundary. In the present case, the plate has aspect ratio $L = 1.0\,[m]$, $\beta = L/B = 1.0$, Young's modulus $E = 200\,[GPa]$, Poisson's ratio $\nu = 0.3$, thickness $t = 10\,[mm]$ and applied line load σt.

5.3 Quasi-Static Analysis: Arc-Length Methods

Assessing the models for Quasi-Static and Post-Buckling Analyses implies that the algorithm for handling bifurcation points, i.e. the bi-section method and extended arc length iterations, are considered (see Section 4.4). In this section, bifurcation points are computed using the arc-length procedure for the cases presented in the previous section. Furthermore, the results from benchmark problems for assessing the post-buckling behaviour are given. In the present research, the related algorithms were only implemented for the shell model.

Shell Model

Verification of the post-buckling arc-length model, as described in Section 4.4 for the shell model, is done by considering three cases.

The first benchmark involves incremental loading of a (differently parameterized) Scordelis-Lo roof (see Figure 5.2a) by a point load in the middle, resulting in *snap-back* behaviour of the plate [214]. The reference solution is taken from Sze et al. [214] based on a 16×16 mesh of four-node shell elements in `ABAQUS` for a thickness of 6.35 $[mm]$ and 12.7 $[mm]$. Similar results have been obtained for more parameter combinations in Zhou et al. [215], who also identified secondary unstable paths. Furthermore, Guo et al. [111] used 16×16 and 12×12 isogeometric elements of order 2 for thickness 12.7 and 6.35 $[mm]$. In Figure 5.10 the applied force is plotted against the mid-point displacement of the roof for both thicknesses. As seen in both figures, excellent agreement with the results of Sze et al. [214] is obtained for the isogeometric shell model. As basis function order increases, the results shift more towards the reference results, which shows the model is consistent. Additionally, the results for the order 2 mesh show higher correspondence with the results of Sze et al. [214] than those of Guo et al. [111].

A second benchmark problem that is considered is from, two benchmarks as presented by Pagani and Carrera [216] are considered. The first case represents a cantilever beam subject to a vertical end load. This benchmark does not involve an instability, but it shows a continuous transition between the solution of a linear beam model and the influence of the axial stiffness for larger forces. The second case represents a cantilever beam subject to a horizontal end force. This case involves an instability and the beam is loaded far in the post-buckling regime, such that the beam's direction is 'inverted'. In both cases, the beam has parameters $E = 75\,[MPa]$, $L = 1\,[m]$ and a square cross-section with $t = 0.01\,[m]$.

The results of the benchmarks from Pagani and Carrera [216] are given in Figure 5.11 and Figure 5.12, respectively. The insets in these figures represent the undeformed (dashed) and deformed (solid) configurations. As seen in these pictures, the present model shows good agreement with the results of Pagani and Carrera [216] with a slight deviation in Figure 5.11 which might be due to the fact that their model uses a slightly different technique to eliminate rotational degrees of freedom, which mainly influences for large rotations.

Lastly, assessing the arc-length method on the ability to compute bifurcation points, the first buckling load of

the constrained plate subject to an edge load is computed. The results are presented in Table 5.2. As seen in this table, the first buckling load is computed accurately by the two-step method with the bisection method and extended iterations. Only marginal underestimation is seen for the highest polynomial order with the finest mesh. This can be due to overfitting of the order of the basis function or due to the choice of the tolerance of the extended arc-length method (10^{-6} here) on the singular point indicator (i.e. the minimal diagonal value of the Cholesky Decomposition, see Section 4.4).

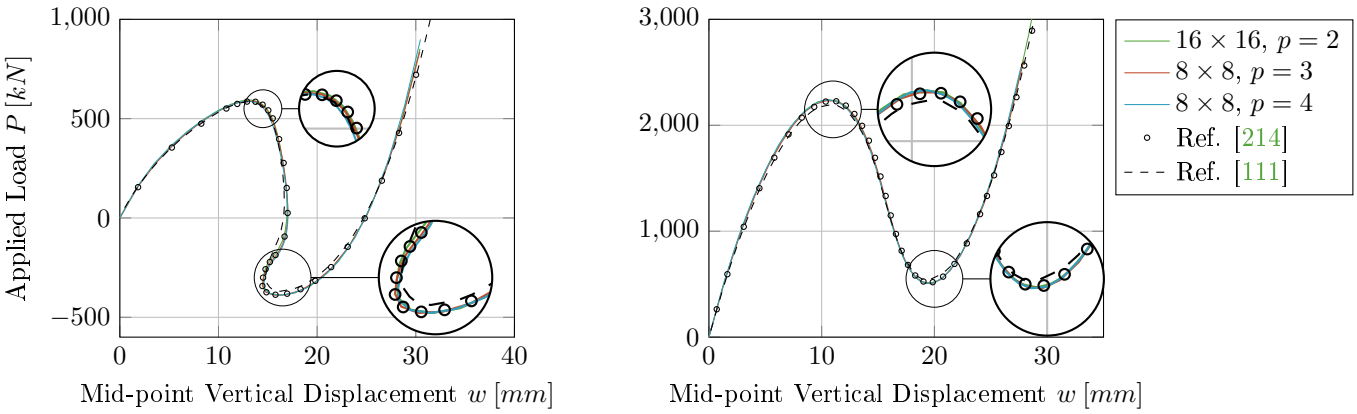

(a) $t = 6.35$ [mm] **(b)** $t = 12.7$ [mm]

Figure 5.10: Scordelis Lo roof subject to a load at the centre for thickness $t = 6.35$ [mm] and $t = 12.7$ [mm]. The reference solutions are from Sze et al. [214] and Guo et al. [111] and the corresponding parameters of the roof (see Figure 5.2a) are $E = 3102.75$ [N/mm^2], $\nu = 0.3$, $L = 254$ [mm], $R = 2540$ [mm], $\phi = 0.1$ [rad]. The numerical results are all computed with fourth order NURBS.

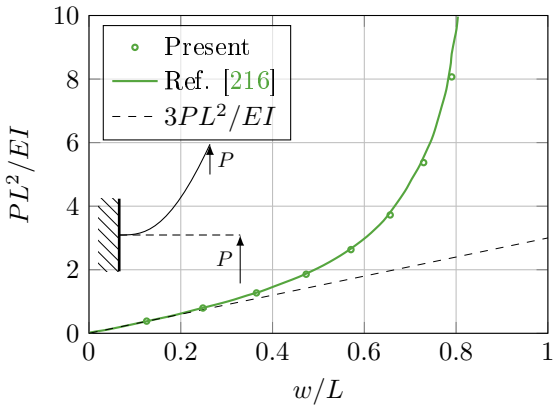

Figure 5.11: Clamped beam with vertical end load. The benchmark results are adopted from Pagani and Carrera [216]. The ratio between the length and the thickness, L/t, is equal 100. The inset represents the undeformed (dashed) and deformed (solid) configuration. The line $3PL^2/EI$ represents the linear bending solution.

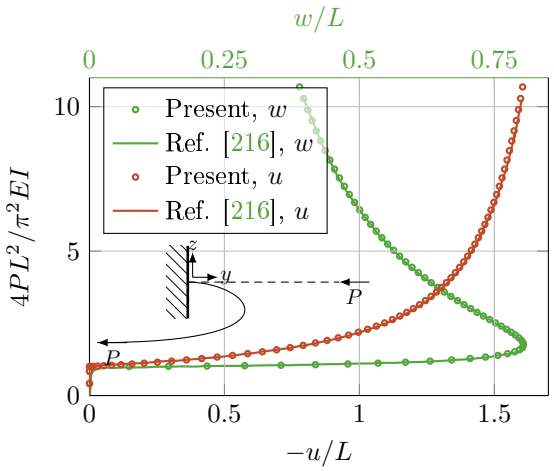

Figure 5.12: Clamped beam with horizontal end load. The benchmark results are adopted from Pagani and Carrera [216]. The inset represents the undeformed (dashed) and deformed (solid) configuration.

5.4 Modal Analysis

Modal analysis was discussed in Section 4.5. Despite this technique is not used in the applications of this research, benchmark results of the model are briefly given here. This verifies the model for future use.

Table 5.2: *Shooting accuracy* of the bisection method and extended iterations implemented in the arc-length method. The values in the table are the loads on the computed bifurcation point for different knot spacings $\Delta\xi$ and different polynomial orders. The numbers in brackets are rounded percentage errors. The exact solution is $\sigma_c = 55.62\,[MPa]$

	p		
$\Delta\xi$	2	3	4
1/2	58.56 (5.29%)	55.96 (0.60%)	55.76 (0.25%)
1/4	56.19 (1.02%)	55.78 (0.29%)	55.67 (0.10%)
1/8	55.80 (0.32%)	55.66 (0.08%)	55.63 (0.01%)
1/16	55.67 (0.09%)	55.62 (0.01%)	55.61 (0.02%)

Beam Model

As discussed in Section 4.5, isogeometric vibration analysis has the advantage over conventional Finite Element Method that eigenfrequency and eigenmode computations are accurate and do not show optical branches [186, 101]. As a benchmark, the spectrum of eigenfrequencies for a pinned-pinned beam is modelled here. The present benchmark is performed for a beam with unit stiffness $EI = 1\,[Nm^2]$, unit area $A = 1\,[m^2]$, unit density $\rho = 1\,[kg/m^3]$ and unit length $L = 1\,[m]$.

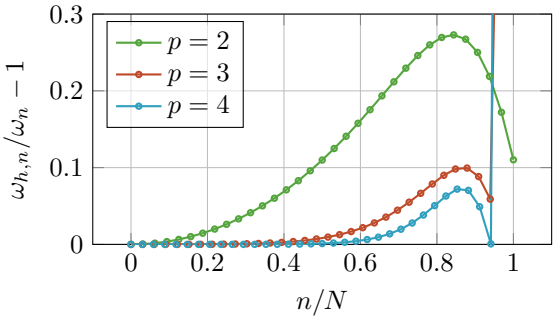

Figure 5.13: Eigenfrequency ratio $\frac{\omega_{h,n}}{\omega_n} - 1$. The (unique) knot vector is $\Xi = \{0, \frac{1}{16}, \frac{2}{16}, \ldots, 1\}$ and the order is $p = 2 \ldots 4$.

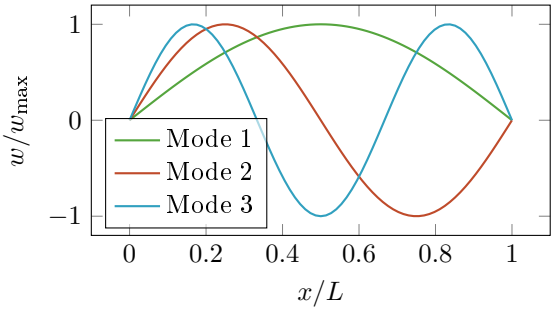

Figure 5.14: Normalised mode shapes (1, 2, 3) for the vibrating simply supported beam. The horizontal coordinate is normalised with the length L of the beam. $w/w_{\max} = \sin(n\pi x)$ for mode n.

In Figure 5.13, the ratio $\omega_{h,n}/\omega_n - 1$ is plotted on the vertical axis, where $\omega_{h,n}$ are numerically obtained eigenfrequencies and ω_n are the analytical eigenfrequencies which are $(n\pi)^2$ for a pinned-pinned beam. On the horizontal axis, the eigenfrequency number n over the number of degrees of freedom n is plotted. Although the resolution is rather low, i.e. N is small, the same height of the curves is obtained as in the works of Cottrell et al. [186] and Weeger et al. [101]. According to this paper, it should indeed not depend on the number of discrete frequencies. Since the number of nodes that are used in the present work (N = 33-35) is significantly smaller than in the work of Cottrell et al. [186] ($N = 2000$), the outliers close to $n/N = 1$ are better visible, although there were reported by Cottrell et al. [186] as well.

Furthermore, another result published by Cottrell et al. [186] is the convergence of the first three eigenfrequencies with respect to the grid size, i.e. the knot vector refinements. Figure 5.15 presents the convergence of the first three eigenfrequencies for different orders of B-splines. The corresponding mode shapes are governed by $\sin(n\pi)$ where n is the mode number. Analogous to the observations in Cottrell et al. [186] the frequencies indeed converge in order $2(p-1)$ for a pinned-pinned beam. However, the basis of order $p = 2$ shows wiggles which were also observed in the static analysis for this basis.

Shell Model

For verification of the modal analysis of the shell model, vibrations of a clamped circular plate are considered. The analytical solution for this problem is derived in Appendix C.1. It should be noted that the eigenfrequencies

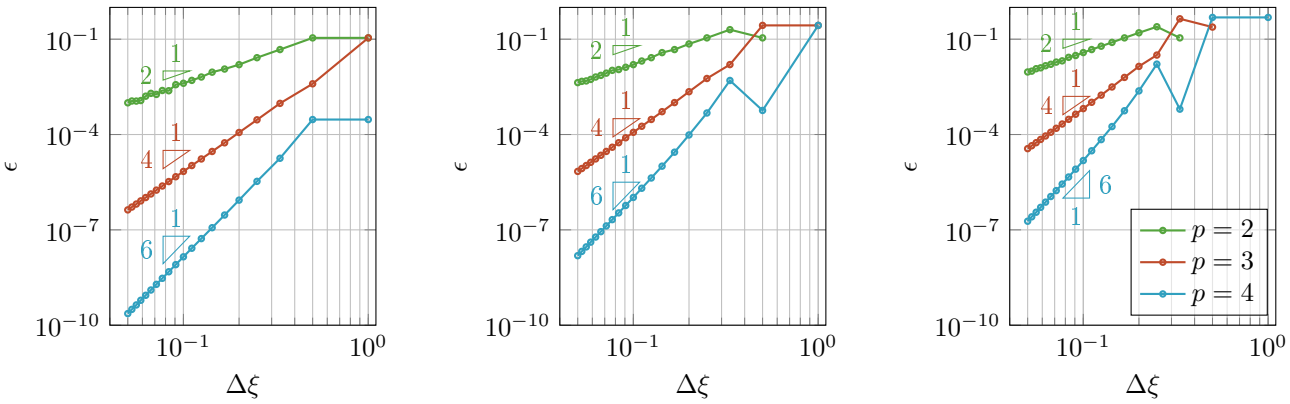

(a) ω_1 **(b)** ω_2 **(c)** ω_3

Figure 5.15: Convergence of the first three eigenfrequencies $\omega_1, \omega_2, \omega_3$ for knot span $\Delta\xi$ for the **beam model**. The error ϵ is an L_1 error between the numerical eigenfrequency ω_n and the analytical eigenfrequency $\omega = (n\pi)^2$. Orders of the knot vectors range from 2 to 4. The value of N is 33 up to 35 for orders 2 up to 4, respectively.

of the plate are approximated numerically due to the occurrence of Bessel functions in the analytical formulations. In Figure 5.17 the first eight mode shapes of the plate resulting from the numerical model are depicted. Furthermore, Figure 5.16 depicts the error of the first three eigenfrequencies over the refinement of bases with different polynomial orders. From these results, one can see that modes 2 and 3 are axisymmetric and hence for these modes the mode shape occurs twice, where the second one is a $\frac{\pi}{2}$ $[rad]$ rotation of the second. Furthermore, one can see that the first three eigenfrequencies converge with at least order $2(p-1)$ for polynomial order p, observing even 9^{th} order convergence for a basis with $p = 5$. Since eigenfrequencies of the analytical problem were numerically obtained, the theoretical order of convergence could not be estimated using similar techniques as used by Cottrell et al. [186] for beam configurations since no analytical solution for the discrete spectrum is known. Additionally, the accuracy of the root finding algorithm used to obtain these solutions (see Appendix C.1) can be the reason for a decrease of the convergence orders for errors of order $\mathcal{O}\left(10^{-13}\right)$.

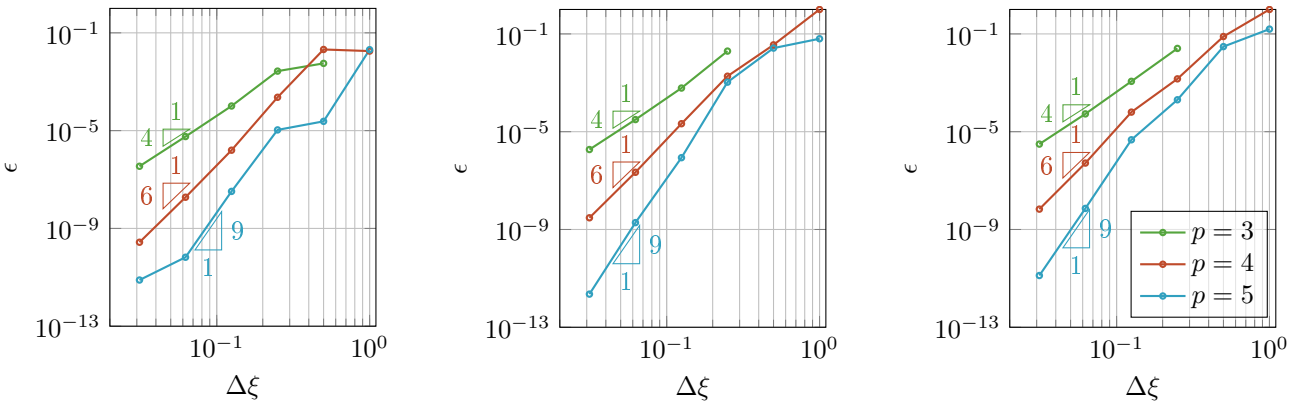

(a) ω_1 **(b)** ω_2 **(c)** ω_3

Figure 5.16: Convergence of the first three eigenfrequencies $\omega_1, \omega_2, \omega_3$ for knot span $\Delta\xi$ for the **shell model**. The error ϵ is an L_1 error between the numerical eigenfrequency ω_i and the analytical eigenfrequency ω which is derived in Appendix C.1 with the mode shapes depicted in Figure 5.17. Orders of the knot vectors range from 3 to 5. For the lowest order, the error for the coarsest mesh is not plotted as the mode shapes were not identifiable with the selected modes.

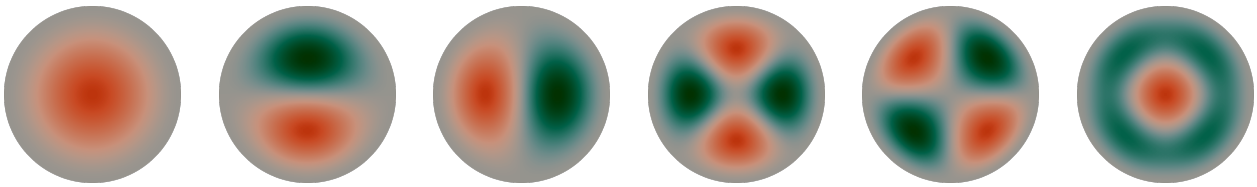

(a) Mode 1 **(b)** Mode 2 **(c)** Mode 2 **(d)** Mode 3 **(e)** Mode 3 **(f)** Mode 4

Figure 5.17: First four mode shapes for a clamped circular plate.

5.5 Dynamic Analysis

In this section, the dynamic analysis of nonlinear structural models will be verified. For the beam model, a variety of time integration schemes is implemented to assess their performance. For the shell model, the Newmark and Bathe method are implemented since these methods are not based on order reduction and hence system size is not doubled.

From literature, orders of convergence for various time integration methods can be found, which are included in the legends in the results in this section. Using these orders of convergence, the discretization errors for both space and time can be made of the same order by the fact that:

$$\mathcal{O}(\varepsilon) = \mathcal{O}\left(\Delta\xi^{p+1}\right) + \mathcal{O}\left(\Delta t^{q}\right), \tag{5.2}$$

Where Δt is the time step, $\Delta\xi$ is the knot spacing, p is the order of the B-splines or NURBS and q is the expected order of the time integration method. To make the total error of the method purely depending on the mesh size, the time step can be scaled according to:

$$\Delta t = (\Delta\xi)^{\frac{p+1}{q}}. \tag{5.3}$$

Alternatively, $\Delta\xi$ can be chosen sufficiently large so that the discretization error is smaller than the temporal discretization error in the considered domain for Δt.

Beam Model

For verification of the dynamic beam model, the method of manufactured solutions is used. To validate the time integration method, it convenient to use a manufactured solution that is polynomial, such that the spatial discretization error (and hence the error of the initial condition) is of the order of the machine precision. The manufactured solution for the beam models is given by:

$$u(x) = 0 \qquad \text{and} \qquad w(x) = \frac{x}{24}\left(1 - 2x^2 + x^3\right)\cos(\omega\pi t)$$

Where ω is a frequency. This solution shows that for $t = 0$ the manufactured solution (thus the initial condition) is equal to a pinned-pinned beam with a unitary distributed load. Substituting this in the (non)linear system of equations in Equation (B.13) gives the following right-hand sides:

$$\begin{aligned} f(x) &= -\frac{EA}{48EI^2}\cos(\omega\pi t)^2(4x^3 - 6x^2 + 1)x(x-1), \\ g(x) &= -\frac{\frac{1}{2}x(x^2 - x - 1/2)^2 EA\left(x - \frac{1}{2}\right)^2(x-1)\cos^2(\omega\pi t)}{24EI^3} \\ &\quad + \frac{\left(\rho A\pi^2\omega^2 x^4 - 2\rho A\pi^2\omega^2 x^3 + \rho A\pi^2\omega^2 x - 24EI\right)\cos(\omega\pi t)}{24EI}. \end{aligned}$$

The results for the linear and non-linear dynamic beams are given in Figure 5.18, where the mesh size was taken constant, but small, and the time step was varied. The methods converge with orders that are equal

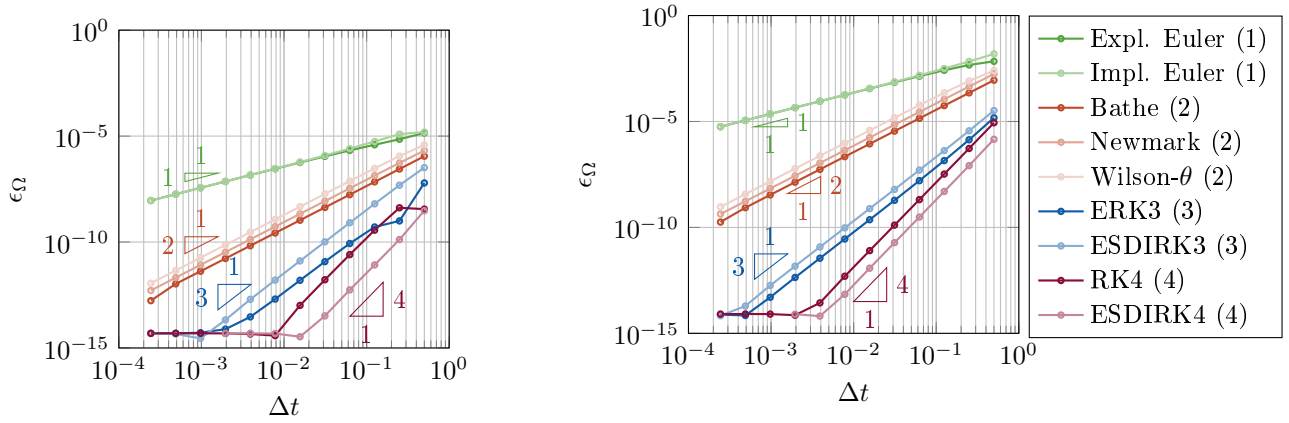

(a) Nonlinear beam, horizontal deflections

(b) Nonlinear beam, horizontal deflections.

Figure 5.18: Convergence plots (top: horizontal deflection error, bottom: vertical deflection error) with the L_2-error ε against the time step Δt for different time integration methods. $EI = 1\,[Nm^2]$, $EA = 1\,[N]$, $\rho A = 10^3\,[kg/m]$ and $t = 2\,[s]$ and the frequency parameter for the manufactured solution is $\omega = 4\,[rad/s]$. The unique knot vector is $\Xi = \{0, 0.5, 1\}$ and the orders of the basis functions are 4 for the vertical deflection and 2 for the horizontal deflection solutions. The numbers in brackets in the legend represent the theoretical order of convergence of each method.

to the theoretical orders of convergence of the methods. Furthermore, it can be seen that machine precision around $\epsilon_\Omega \sim \mathcal{O}\left(10^{-15}\right)$ is obtained for higher-order methods. Only the ERK3 method shows an order of slightly below 3, which could be due to inaccuracy in the implementation of the coefficients of the method (see van Zuijlen [195]). Additionally, the Explicit Euler, ERK3 and RK4 methods show inconsistencies in the order of convergence for large time steps (see Figure 5.18a), which can be because these methods are of explicit nature.

Shell Model

For verification of the dynamic nonlinear shell model, the benchmark case as proposed by Mondkar and Powell [217] is used. That is, a spherical cap is subject to a constant forcing on the centre, for details see Figure 5.19. In the shell model, the Bathe and Newmark methods were implemented, motivated by the fact that these methods are direct and hence do not need order reduction (i.e. doubling of the system size).

Figure 5.20 presents the deflection of the mid-point of the cap over time. The reference solution of Mondkar and Powell [217] is based on a Newmark scheme with a time step of $2\,[\mu s]$, 8-node axisymmetric elements and a lumped mass matrix. The reference solution of Yang and Xia [218] is based on 20 3-node corotational triangular shell elements and the presented energy-decaying/momentum-conserving algorithm with a time step of $2\,[\mu s]$. The results of Wang et al. [220] are based on 96 hexahedral quadratic 20-node solid-shell elements, and unknown but explicit time integration scheme and unknown time step. Finally, the results of Filho and Awruch [219] are based on 750 (2 through thickness) 8-node hexahedral elements, free of volumetric and shear locking, and an explicit Taylor-Galerkin scheme with time step $2.7 \cdot 10^{-3}\,[\mu s]$. The present model is based on the Newmark and Bathe methods with isogeometric meshes with 8×8, 16×16 or 32×32 elements with order 3 and corresponding time steps of 1.875, 0.46875 and $0.1171875\,[\mu s]$ the time step such that the time step scales with the spatial discretization error according to Equation (5.3).

As seen in the figure, the present models agree with the results of the reference papers. However, few observations are made. Firstly, it can be seen that the present method captures more local spikes due to refinements in space and time. Secondly, both methods over-predict the deflections in the mid-point for times between 240 and 300 microseconds but a good agreement with the results of Filho and Awruch [219] were found over the rest of the time signal. The differences with other methods can be explained by the fact that these authors use solid elements [217] or shell element with different or unknown time-integration schemes [218, 220]. Additionally, differences can be clarified by the fact that isogeometric meshes represent the geometry exactly while FEA meshes do not.

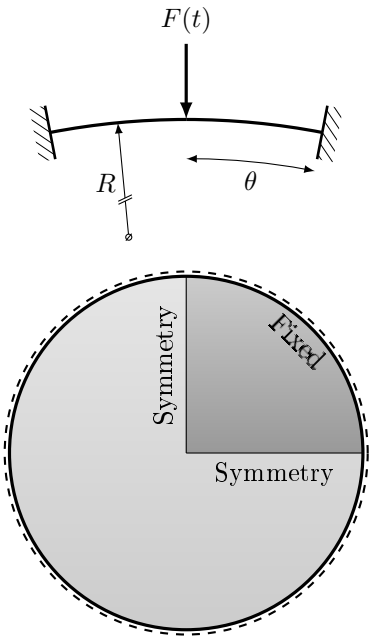

Figure 5.19: Geometry of the spherical cap. The following parameters are used: $R = 4.76\ [m]$, $\theta = 10.9°$, $t = 0.01576\ [m]$, $E = 10\ [MPa]$, $\nu = 0.3$, $\rho = 0.00245\ [kg/m^3]$.

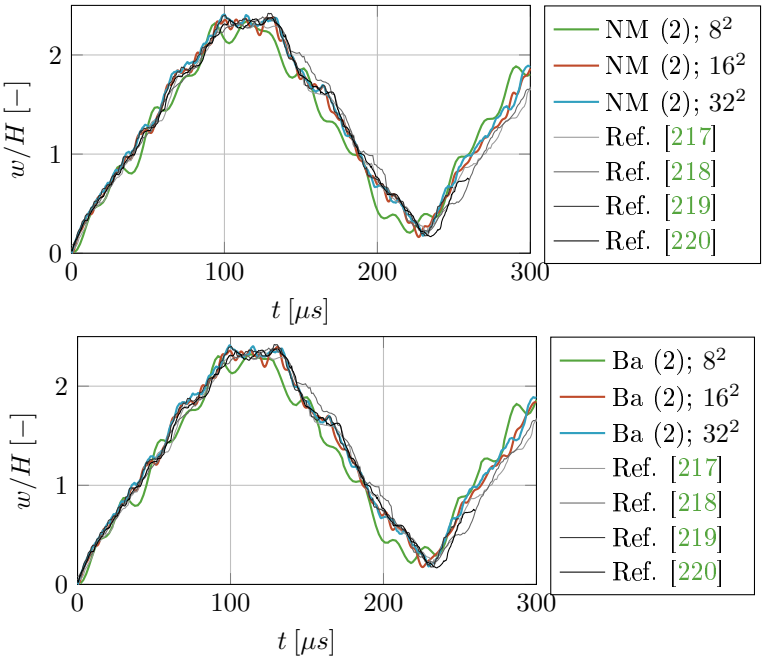

Figure 5.20: Spherical Cap subject to instantaneous load on center (see Figure 5.19) with reference solutions by Mondkar and Powell [217], Yang and Xia [218], Filho and Awruch [219], Wang et al. [220] and present solutions of the Isogeometric Kichhoff-Love shell model for the Bathe (Ba) and Newmark (NM) time integration schemes where N^2 denotes and $N \times N$ mesh. The vertical axis represents the deflection w of the center of the cap normalised with the vertical span and the horizontal axis represents the time in micro-seconds (μs). **Note:** the solution of Filho and Awruch [219] was only present up to $t = 250\ [\mu s]$.

5.6 Concluding Remarks

In this chapter, verification studies were presented for structural analyses implemented in the present isogeometric beam and the thin shell model. Relating to subgoal 4 of this thesis, the following conclusions can be drawn:

- Manufactured solutions and the Shell Obstacle Course were used to verify the results from the *static* beam and shell model, respectively. The results for the beam model show convergence to the manufactured solution. The solutions for the shell have shown good agreement with reference solutions from similar isogeometric shell analyses. Minor differences were observed for the pinched cylinder case, which can be due to slight differences in the geometry. Despite these differences, the errors with respect to the isogeometric benchmark of Kiendl et al. [87] are 0.0% to 0.1% and for the cases of Belytschko et al. [207] 0.0% to 0.6%. Additionally, the benchmark on follower pressure has shown slight differences compared to the model of Bouzidi et al. [211] as a different model was used in their case. Lastly, a case on adaptive refinement showed the potential of adaptive refinement, but an open question is which parameter (e.g. curvature, displacement) should be used for adaptive refinement.

- The *buckling* model for the beam has shown convergence to the analytical solution for moderately fine meshes, but oscillations in the convergence plots for fine meshes. This was explained by the linearization of the buckling problem that is used for linear buckling analysis. A similar observation was made when using an `ANSYS` model. For shell buckling, such oscillations were not found within the present range of knot vector refinements. Although the solutions converged towards the analytical solution, it was found that an increase of the order of the basis function did not necessarily increase the order of convergence. Similar convergence plots as those presented in Section 5.2 were unavailable in similar works of Shojaee et al. [110], Valizadeh et al. [108] and Thai et al. [109] to provide proper comparison of these orders.

- The *post-buckling* algorithm using the arc-length method, was verified using three benchmarks. A shallow roof subject to an increasing mid-point load showed excellent agreement and consistency with the results of Sze et al. [214] and Guo et al. [111]. Additionally, similar results in the post-buckling behaviour of two cases from the work of Pagani and Carrera [216] were observed. Here, the present model was used without the use of initial perturbations. Lastly, a square plate subject to a compressive load was considered to assess the *shooting accuracy* of the combination of the bisection method and the extended iterations. This method showed that bifurcation points were accurately found although a slight underestimation was found for a fourth order basis with the finest mesh while other errors were overestimating. This is possibly because of the tolerance used in the arc-length method.

- Both beam and shell models were considered in the framework of *modal analysis*. In case of the beam model, the error in the discrete domain as well as the errors for the first three eigenfrequencies show excellent agreement with the results of Cottrell et al. [186] in terms of convergence of the eigenfrequencies as well as the spectrum of eigenvalues. The shell model was verified using analytical solutions for a clamped circular plate. In this case, the convergence of the first three eigenfrequencies with respect to the analytical reference solutions showed excellent agreement.

- Lastly, the *dynamic* beam and shell models were considered. All time-integration techniques discussed in Section 4.6 were implemented in the beam model and showed expected convergence with respect to the manufactured solutions, which implies that the methods are correctly implemented. Bathe's and Newmark's method were implemented for the shell model and showed comparable results to previously published results for a spherical cap under an instantaneous load. Furthermore, the methods showed consistency with respect to mesh refinement, although mesh refinement (and hence time-step refinement) showed additional vibrations due to the increased level of spatial and temporal detail.

6 | Application: Wrinkling of Thin Sheets

In this section, the benchmarked thin shell model for post-buckling analysis will be applied on two cases to identify wrinkling behaviour, relating to subgoal 5 of this thesis. The first is the stretched thin sheet, inspired by Cerda et al. [43] (see Figure 6.1), where the edge is incrementally stretched using the arc-length method. The second is a thin membrane with in-plane dimensions in the order of kilometres ($\mathcal{O}(km)$) floating on a fluid-foundation subject to a traction load which is incrementally using the arc-length method (see Figure 6.2). This traction load can resemble a load by wind or current, for instance. The second case is used to illustrate the effects of different design parameters (e.g. material parameters, geometric dimensions) on the wrinkled shape of the membrane. In both cases, the geometry is initially flat, but bifurcation points induce out-of-plane deformations and hence wrinkling.

Based on the results of the parameter variations of the thin sheet subject to a traction load, design considerations for the design of a Very Large Floating Thin Structure (e.g. for offshore solar energy generation) are provided. These design considerations are supported by the results of a floating quarter disk to support the considerations for circular VLFTSs. The design considerations relate to the sixth subgoal of this thesis.

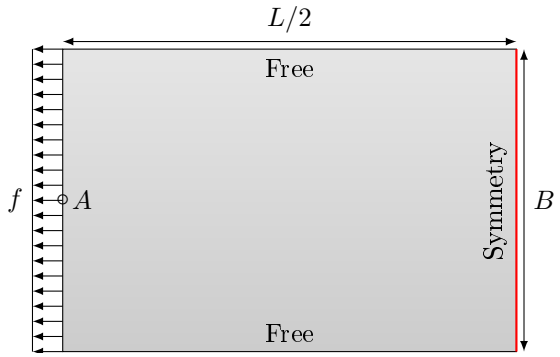

Figure 6.1: Stretched thin sheet modelled with a symmetry axis on the right side. The domain length is $L/2$ and the width is B. The sheet is loaded with a distributed load on the left boundary. Wrinkling profiles are plotted over the red boundary. Strains are measured in point A.

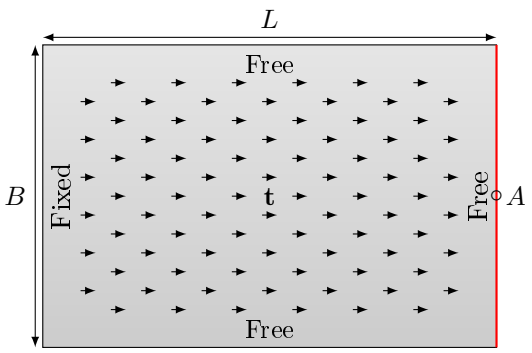

Figure 6.2: Thin sheet with length L and width B subject to traction vector ($\mathbf{t}$). The traction is horizontal in this case. The left edge is simply supported and the other edges are free. The red edge is the edge that is used for plotting of the wrinkling cross-sections. Strains are measured in point A.

6.1 Wrinkling of a Stretched Thin Sheet

Based on the experiment of Cerda et al. [43], the wrinkling pattern of a stretched thin sheet will be investigated here. Similar to the works of Fu et al. [78], Wang et al. [76] and Taylor et al. [77], the aspect ratio $\alpha = L/B$ and the width over thickness ratio $\beta = B/t$ of the plate are used in the analysis. All benchmarks on the thin sheet are modelled as depicted in Figure 6.1. That is, only half of the sheet is modelled by using a symmetry boundary condition on the mid-plane of the sheet. Additionally, the sheet is modelled using a distributed load rather than a displacement since the displacements are applied with elimination in the present model, which causes the residual vector to be unchanged after modifying the load factor in the arc length method. The

end-point strain is measured on the mid-plane of the edge where the load is applied.

Taylor et al. [77] model the stretched thin sheet with length 254 $[mm]$, width 101.6 $[mm]$, Young's modulus 1 $[MPa]$, Poisson's ratio $\nu = 0.5$ and thickness $t = 0.1\,[mm]$, based on the experiments of Zheng [71]. The sheet is stretched until the strain of the displaced edge is 30%. In this study, the stretched sheet is modelled with the same parameters and with the configuration from Figure 6.1. In Figure 6.3a the strain of the boundary where the load is applied is plotted against the dimensionless maximal vertical displacement $\zeta = \max(w)/t$ on the symmetry axis for the isogeometric meshes of 16×16, 32×32 and 64×64 elements with orders 4, 3 and 2, respectively. Additionally, Figure 6.3b depicts a cross-section of the membrane at different strains and contour plots are presented in Figure E.2. Based on these results, four observations are made:

- Firstly, it can be seen from Figure 6.3a that the results show high mesh dependency. The meshes with 16×16 and 32×32 elements show kinks in the curve which corresponds to instantaneous redistribution of the wrinkles, possibly due to an insufficient of basis functions and hence a lack of detail. For the 64×64 mesh, the number of wrinkles is continuously equal to 9.
- Secondly, the curves in Figure 6.3a show that after the sheet buckled and wrinkles appear, the amplitude increases relatively quickly but stagnation is observed. This stagnation is due to the stretching effects in the sheet, which eliminate the wrinkles for higher strains due to stretching forces. Zheng [71] refer to this as *restabilization*.
- Thirdly, it can be seen that the amplitudes are over-estimated compared to the numerical results of Taylor et al. [77] and the experimental results of Zheng [71]. It is expected that this is due to the fact that the sheet in the present case is not modelled with a straight boundary (i.e. based on displacements) and therefore the contraction of the sheet on the symmetry axis is higher. Additionally, the tensional force in the middle axis of the sheet (point A) is expected to be higher, as it elongates more compared to other edges. The effect is illustrated in Figure 6.4.
- To obtain the curve in Figure 6.3b for the finest mesh, the solution was not always stable, i.e. the indicator for buckling was negative in some intervals. In particular, this holds for the intervals $\varepsilon \in [0.072, 0.161]$ and $\varepsilon \in [0.2529, 0.288]$ for the finest mesh. The solution was forced to continue since for secondary bifurcations, the bi-section algorithm did not converge for reasonable arc length steps and with limited computational costs. It should be noted that imposing an initial imperfection might cause a stable track if the amplitude is too large (and hence the imperfection is subjective). Combined with the previous bullet, it is highly recommended to model the sheet with proper boundary conditions and if instabilities are present, to identify the origin of the instabilities.

6.2 Large Floating Sheet Subject to Traction

In order to illustrate the effect of design parameters on wrinkling physics of a floating thin structure, a test case is presented in this section. The test case has similarities with the stretched thin sheet presented in the previous section. However, the sheet is subject to traction (e.g. due to wind or current) and one edge is supported and restrained in width direction. Figure 6.2 gives a schematic sketch. This case is presented since it can be resembled with an experiment in a flume tank.

The parameters that are varied are related to material choices (Young's modulus and Poisson's ratio), geometry choices (thickness and aspect ratio) and the foundation stiffness is varied for the sake of completeness, although $S = \rho g$ can in practice not be influenced for offshore solar platforms[1]. For the sake of comparison, the following non-dimensional quantity is introduced, which represents the ratio between flexural rigidity D and foundation stiffness D. The ratio is a 2D equivalent of the one from Equation (C.7) and hence applicable to shells.

$$\eta = \frac{B}{\left(\frac{D}{S}\right)^{\frac{1}{4}}} \qquad \text{with:} \qquad D = \frac{Et^3}{12(1-\nu^2)}\,[Nm] \qquad \text{and} \qquad S = \rho g\,[N/m^3]. \tag{6.1}$$

[1] When considering a sheet on water, the foundation stiffness is the hydrostatic pressure and hence governed by $S = \rho g$. However, the present set-up allows for experimental verification in a so-called *flume tank* with optionally a different fluid to obtain representative values for non-dimensional quantities.

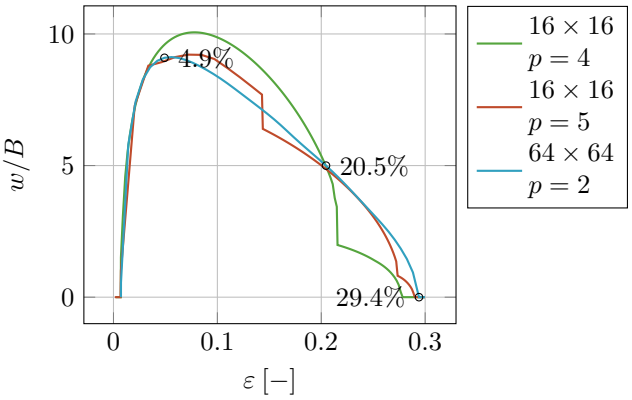

(a) Strain-amplitude diagram.

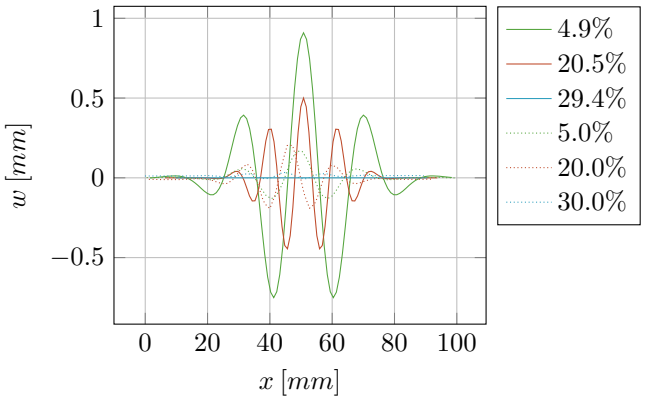

(b) Wrinkle profile diagram.

Figure 6.3: Strain-amplitude diagram (left) and wrinkle profile on the symmetry axis (right) for two isogeometric meshes with 16×16 elementes and orders 4 and 5. The strains wrinkle profiles are depicted for different strain levels (marked in the strain-amplitude diagram) and the experimental values from Zheng [71] are plotted in the wrinkle profile diagram as well.

For the non-dimensional load, the expression in Equation (6.2) is taken. This expression is inspired by the one-dimensional equivalent in Equation (C.6), taking B as the wrinkling length, replacing the reference load P_{ref} by the traction times the area of the sheet $t_{\text{ref}}BL$ and replacing the bending stiffness EI by the flexural rigidity D times the length of the sheet L to incorporate for the aspect ratio of the sheet.

$$p = \frac{P_{\text{ref}}B^2}{DL} = \frac{(t_{\text{ref}}LB)B^2}{DL}. \tag{6.2}$$

Lastly, the strain ε of the sheet is defined by the maximal horizontal elongation ($\max \Delta$) over the length of the sheet. The non-dimensional amplitude ζ of the wrinkled sheet is defined by the maximum vertical amplitude over the red edge of the sheet in Figure 6.2 divided by the length of the wrinkle in its initial state, i.e. B. This gives:

$$\varepsilon = \frac{\max \Delta}{L} \qquad \zeta = \frac{\max w}{B}. \tag{6.3}$$

For the sake of comparison, a *base case* was defined. In this case, the membrane has a length and a width of 10^3 $[m]$, a thickness of 5 $[m]$, a Young's modulus and Poisson's ratio of 0.5 $[GPa]$ and 0.3 (corresponding to Ethylene-Vinyl Acetate (EVA) [221]) and the foundation stiffness corresponds to that of water, i.e. $S = 10^4$ $[kgm]$. In all presented results, an Isogeometric mesh of 16×16 elements with order 4 was used, unless stated otherwise. Furthermore, the values corresponding to the base case will be underlined in the sequel. The results are depicted in Section 6.2 and Figure 6.5.

6.2.1 Discussion of the Base Case

Throughout this section, the influence of different parameters on the response of the thin sheet under traction will be discussed based on three figures. Before proceeding to the results of the parameter variations the plots will be discussed for the base case.

In Figure 6.6a, two plots are depicted. In the sequel, these curves will be referred to as the and *load diagram* (left) the *strain-amplitude diagram* (right). In the load diagram, the *non-dimensional horizontal strain* of the sheet ε (dashed lines) and the *non-dimensional maximal amplitude* ζ (solid lines) are plotted against the non-dimensional load p and referred to as *load-strain* and *load amplitude* curves. Based on the load-strain curve, the strain for a certain load can be reconstructed and can be used in combination with the strain-amplitude diagram. Based on the load-amplitude curve, the critical buckling load can be determined. The strain amplitude diagram can be used to find the critical buckling strains.

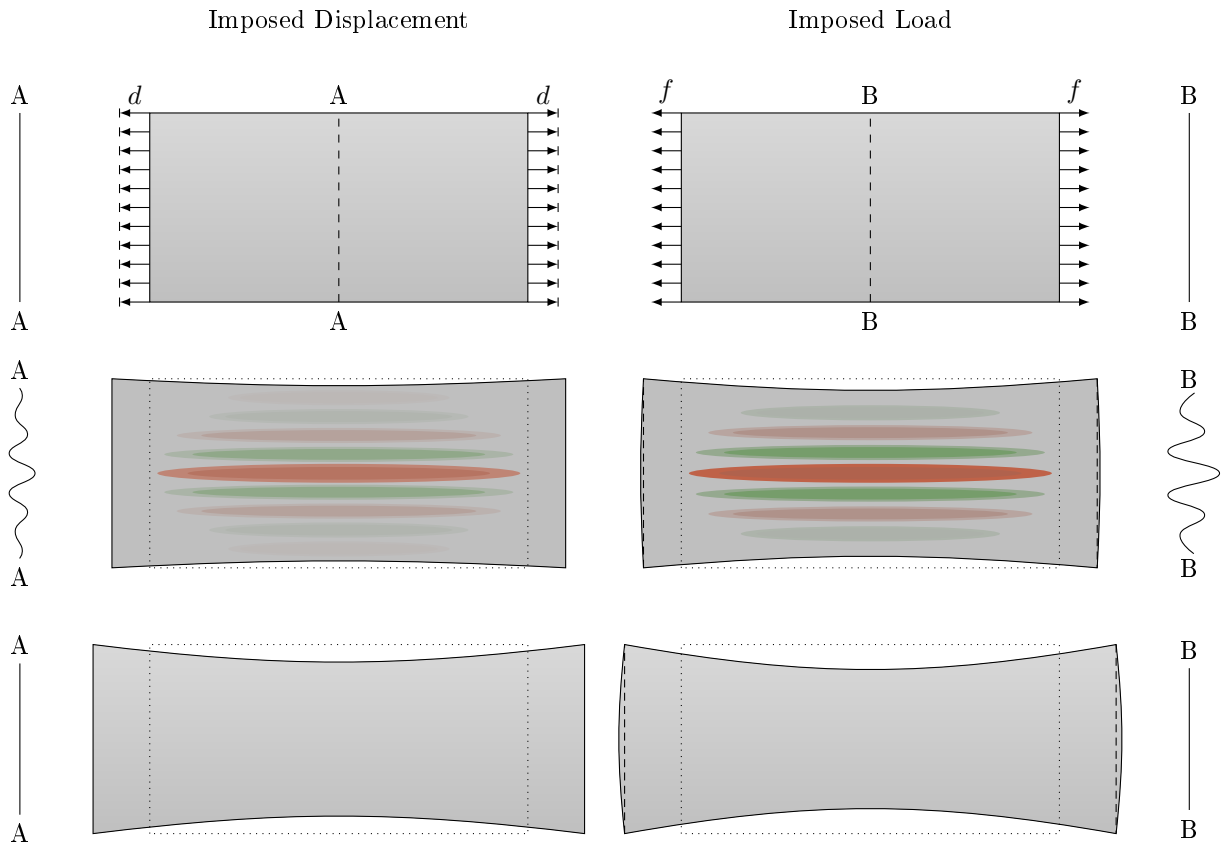

Figure 6.4: Illustration of the effect of imposing a distributed load on the edges compared to a forced displacement. The contraction on the cross section B-B increases compared to that of A-A and hence amplitudes are larger.

Furthermore, Figure 6.5a shows the cross-sections of the free, wrinkled edge of the sheet on specific strain values. Depending on the case, cross-sections will be plotted for 20% or 40% strain. For further reference of the wrinkled configuration, deformed geometries are plotted in the appendix Appendix E. Based on the available data, few conclusions can be drawn:

- Both the strain-amplitude diagram and the load-amplitude diagram show the critical buckling strain and load, respectively, by means of a bifurcation branch. Just after this branch, the slope of the curves decreases over the strain/load.
- The load-strain does not show a bifurcation point since the sheets elongate also before wrinkles are initiated. Furthermore, the slope of the curve decreases over the load, which is a consequence of tensional forces in the sheet that penalises larger amplitudes. This effect also occurs for the thin sheet in Section 6.1 and was introduced by Cerda et al. [43].

6.2.2 The effect of Foundation Stiffness

Based on experimental findings of Pocivavsek et al. [44], it is known that foundation stiffness penalises large wavelengths since these wavelengths are associated with large amplitudes and hence the potential energy in the foundation increases. Although this quantity cannot be varied for designs of offshore solar platforms, it can be used to develop representative scalings for experiments using Equation (6.1). In this case, the foundation stiffness is varied between the values $S \in \{10^3, 5 \cdot 10^3, \underline{10^4}\}$ such that $\eta = \{204.4, 305.7, \underline{363.6}\}$.

In Figure 6.6b the strain versus the amplitude and the load versus the strain and amplitude are plotted and in Figure 6.5b the cross-sections corresponding to a strain of around 20% are presented. The following observations are made:

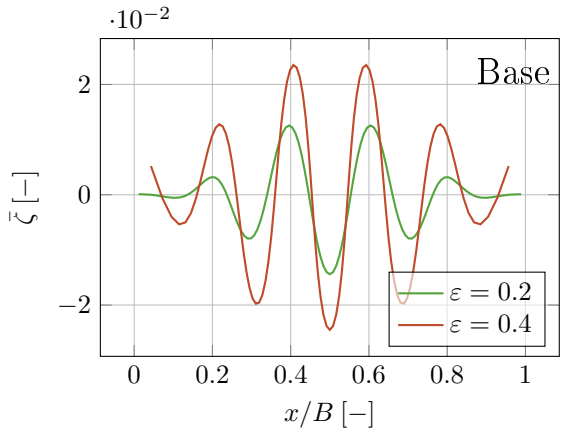

(a) Base Case, for strains of 0.2 and 0.4. Deformed shapes can be found in Figure E.3 in Appendix E.

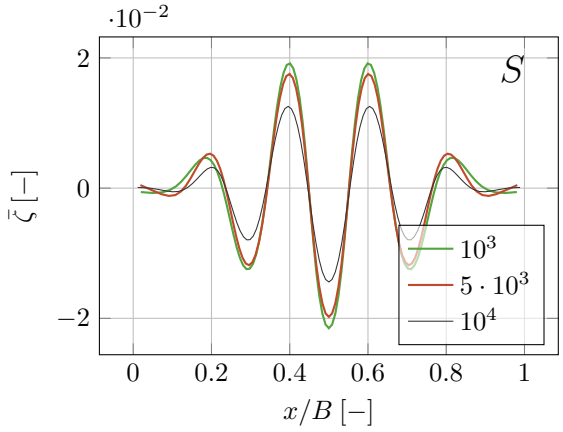

(b) Fluid foundation stiffness S, with unit $[kgm]$, for a strain of 0.2. Deformed shapes can be found in Figure E.4 in Appendix E.

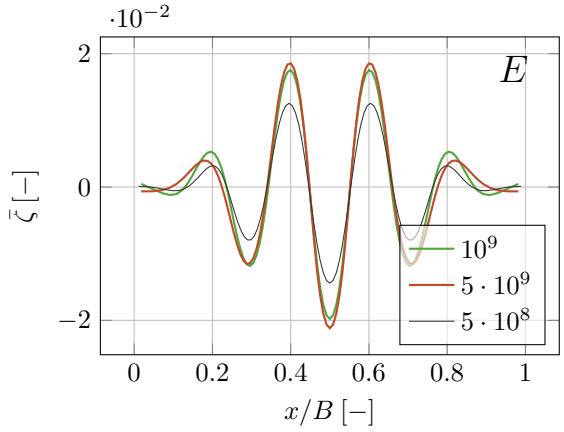

(c) Young's modulus E, with unit $[GPa]$, for a strain of 0.2. Deformed shapes can be found in Figure E.5 in Appendix E.

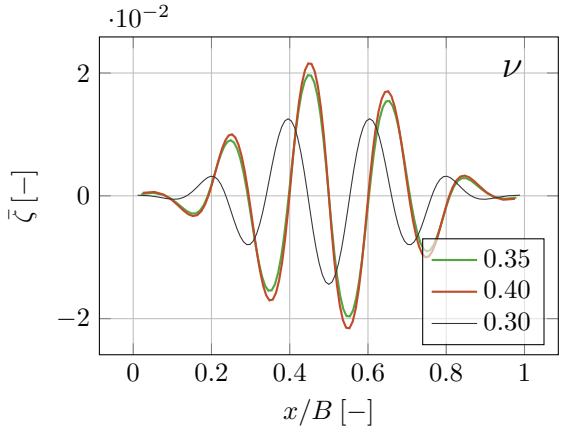

(d) Poisson's ratio ν, dimensionless, for a strain of 0.2. Deformed shapes can be found in Figure E.6 in Appendix E.

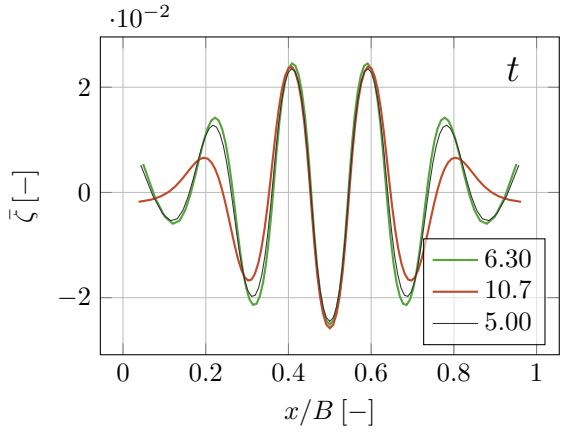

(e) Thickness t, with unit $[m]$, for a strain of 0.4. Deformed shapes can be found in Figure E.7 in Appendix E.

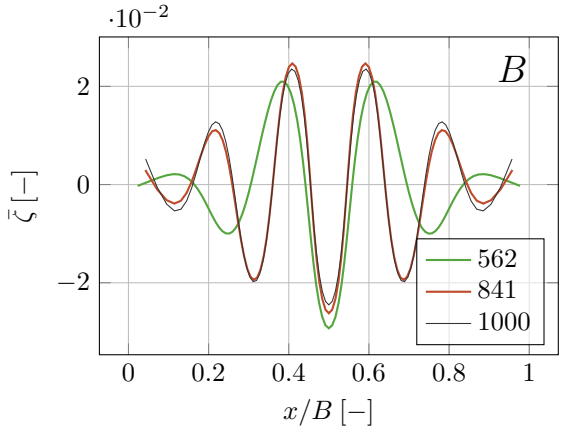

(f) Wrinkling length B, with units $[m]$, for a strain of 0.4. Deformed shapes can be found in Figure E.8 in Appendix E.

Figure 6.5: Wrinkling cross-sections with non-dimensional amplitude $\bar{\zeta} = w/B\ [-]$ and non-dimensional width coordinate. The cross-sections are plotted for strains as indicated in the captions of the figures. The results are presented for (a) the base case and parameter variations of (b) foundation stiffness, (c) Young's modulus, (d) Poisson's ratio, (e) thickness and (f) size. The results are obtained using a 16×16 mesh of order 4

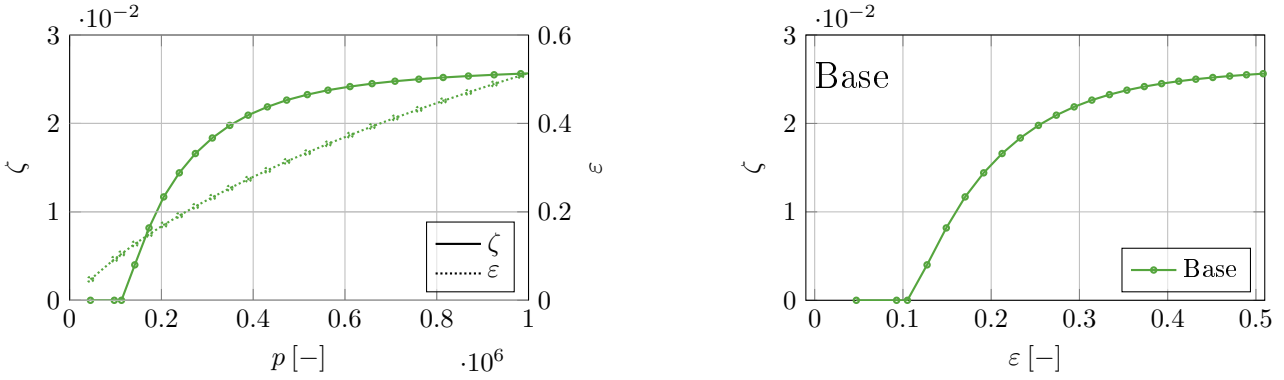

(a) Base case. Deformed shapes can be found in Figure E.3 in Appendix E.

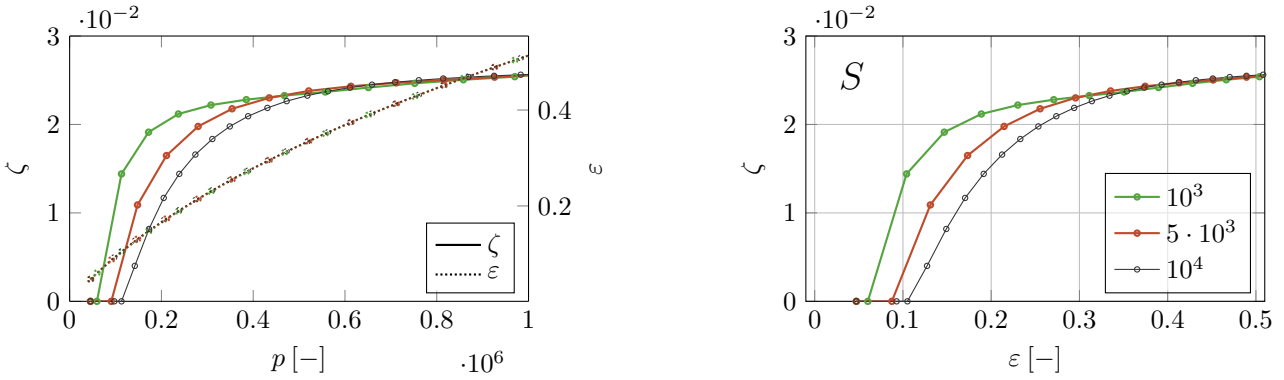

(b) Fluid foundation stiffness S, with unit $[kgm]$. Deformed shapes can be found in Figure E.4 in Appendix E.

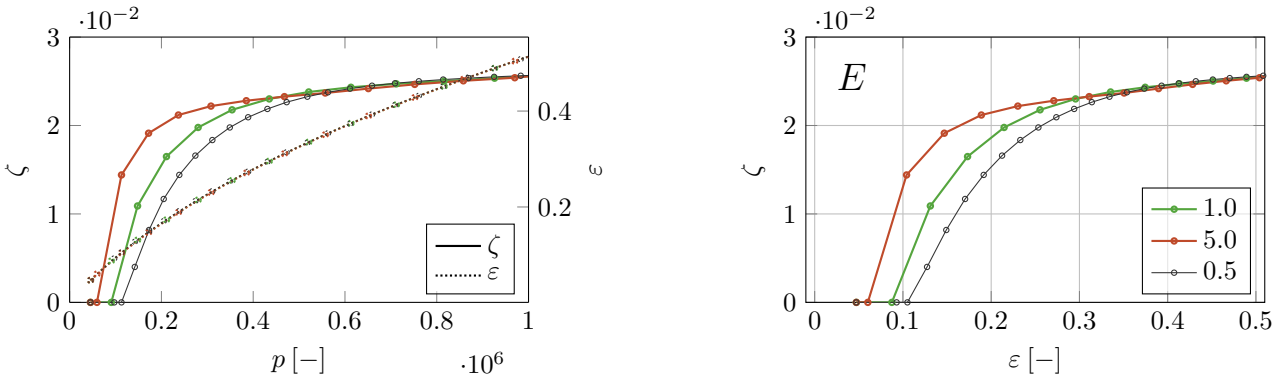

(c) Young's modulus E, with unit $[GPa]$. Deformed shapes can be found in Figure E.5 in Appendix E.

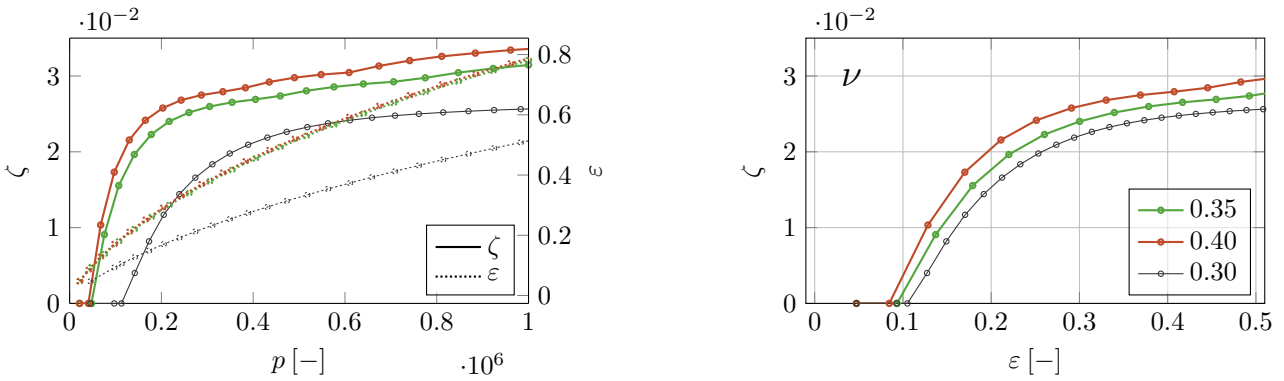

(d) Poisson's ratio ν, dimensionless. Deformed shapes can be found in Figure E.6 in Appendix E.

Figure 6.6: Load diagram (left) presenting non-dimensional amplitude ζ and strain ε against the nondimensional load p and strain diagram (right) presenting non-dimensional amplitude ζ against strain ε. The results are presented for (a) the base case and parameter variations of (b) foundation stiffness, (c) Young's modulus, (d) Poisson's ratio, (e) thickness and (f) size. The results are obtained using a 16×16 mesh of order 4.

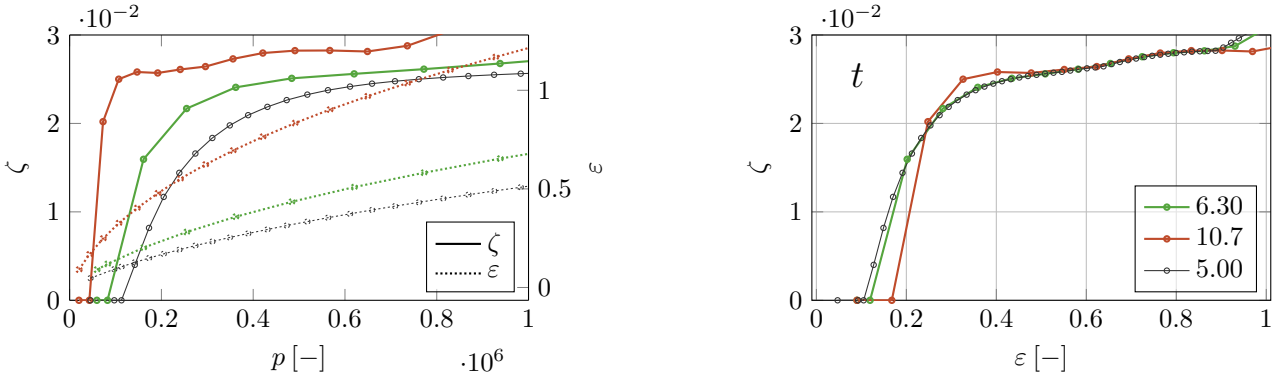

(e) Thickness t, with unit $[m]$. Deformed shapes can be found in Figure E.7 in Appendix E.

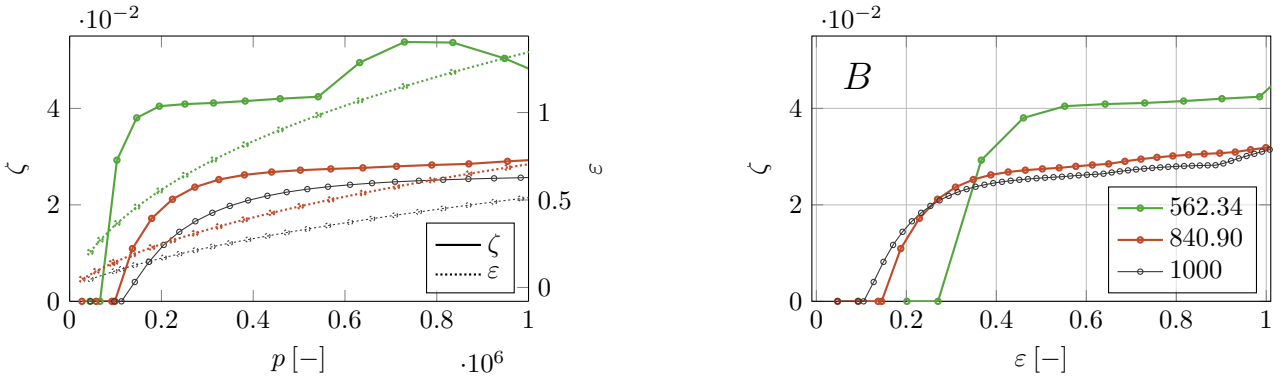

(f) Wrinkling length B, with units $[m]$. Deformed shapes can be found in Figure E.8 in Appendix E.

Figure 6.6: (Continued) Load diagram (left) presenting non-dimensional amplitude ζ and strain ε against the non-dimensional load p and strain diagram (right) presenting non-dimensional amplitude ζ against strain ε. The results are presented for (a) the base case and parameter variations of (b) foundation stiffness, (c) Young's modulus, (d) Poisson's ratio, (e) thickness and (f) size. The results are obtained using a 16×16 mesh of order 4.

- As seen Figure 6.5b, the number of wrinkles increases gradually for increasing S, as seen on the sides of the cross-sections.
- The load diagram in Figure 6.6b shows that for increasing foundation stiffness, the buckling load (i.e. the load when wrinkles initiate) increases, which is in line with the physics discussed by Pocivavsek et al. [44]. Additionally, it can be seen that load-strain curves are equal for all variations and that for large loads the slopes of the amplitude-strain curves are also equal, which is both due to the fact that the foundation stiffness does not influence axial stiffness.
- Considering the strain-amplitude diagram in Figure 6.6b it can hence be observed that wrinkle initiation occurs for lower strains when the foundation stiffness decreases.

6.2.3 The effect of Young's Modulus and Poisson's Ratio

The Young's Modulus and the Poisson's ratio are parameters that can be chosen in the design of a floating sheet for offshore solar generation since it is closely related to material selection. For the base-case of this case-study, the Young's Modulus was chosen to be equal to 0.5 $[GPa]$ and the Poisson's ratio to be 0.3 which are values common for polymers such as Ethylene-Vinyl Acetate (EVA) [221]. However, the choice of foam polymers on the one side or stiffer materials such as non-metallic fibre materials can decrease or increase the Young's modulus and Poisson's ratio. In this case, the effect of varying Young's modulus is assessed for values of $E \in \{5.0, 1.0, \underline{0.5}\}$ $[GPa]$ such that $\eta = \{204.4, 305.7, \underline{363.6}\}$ and varying Poisson's ratio is assessed for values of $\nu \in \{\underline{0.30}, 0.35, 0.40\}$.

Firstly, Figure 6.6c and Figure 6.5c present the wrinkling diagrams and the cross sections for changing Young's modulus, respectively. The following observations are made:

- From the cross-sections of the wrinkles at a strain of 20%, it can be seen that the number gradually decreases on the sides of the cross-sections for increasing Young's modulus, which is in line with observations of Pocivavsek et al. [44].
- Figure 6.6c shows an increasing Young's modulus implies an increased buckling load. This is in line with the results from classical buckling theory. Additionally, it can be seen that the lines for in the load-strain diagram overlap by the choice of p.

Secondly, Figure 6.6d and Figure 6.5d present the wrinkling diagrams and the cross sections for changing Poisson's ratio, respectively. Generally, an increase in the Poisson's ratio implies an increase in the contraction of the membrane orthogonal to the load direction. As seen in the sheet of Cerda et al. [43], this contraction implies wrinkles parallel to the length direction of the sheet. The following observations are made:

- From Figure 6.5d it can be seen that the number of wrinkles for the base case is different than for both varied Poisson ratios. That is, for the base case the number of wrinkles is equal to 9 whereas, for the other cases, this number is equal to 10 (taking into account the edges). This can be due to the fact that a larger Poisson ratio causes the sheet's contraction to increase. Another reason for this difference is that the solutions are not fully converged on the mesh (as also observed for the stretched thin sheet, see Section 6.1), hence a refinement study is recommended but not performed because of constraints in computational time.
- Considering the load diagram in Figure 6.6d, it can be seen that the strains are equal $\nu \in \{0.35, 0.40\}$ and different for $\nu = 0.30$ which is explained by the number of wrinkles. The critical buckling load initiates the load-amplitude curves earlier for increasing Poisson's ratio. Contrary to the cases of the varying Young's modulus or Foundation stiffness, these curves are not overlapping for large loads. The observations can be explained by the fact that an increased Poisson's ratio implies an increased contraction of the sheet and hence compressive stresses in the material exceed the critical buckling values earlier.
- Considering the strain-amplitude diagram similar behaviour is observed but then related to critical strains. The differences with the base case are lower because of the combination of large differences between $\nu\{0.35, 0.40\}$ and $\nu = 0.30$ for both plots in the load diagram.

6.2.4 The Effect of Membrane Thickness

An important design parameter of floating membrane structures is the thickness of the structure. In this work, the Kirchhoff-hypothesis was assumed, which requires that the structure is slender. The base case of the thin sheet under traction has a length and width 1 $[km]$ and a thickness of 5 $[m]$. This implies that the *slenderness* of the plate is 200, which is considered *thin*[2] [87]. An important note that should be made is that the thickness of the sheet will be varied here, assuming that the sheet has a constant, solid, cross-section. A (concept) design, however, might not have a cross-section that is constant and solid, but rather have outer-fibres and an empty, but reinforced, mid-plane to make the structure lighter and cheaper. However, this cross section will have an equivalent flexural rigidity and hence it is assumed here that the flexural rigidity D based on thickness t is equivalent for a yet to be designed cross-section. The thickness parameter will be varied in $t \in \{10.772, 6.292, \underline{5.00}\}$ such that $\eta = \{204.4, 305.7, \underline{363.6}\}$.

In Figure 6.5e the cross-sectional profiles for the sheet on different thickness values are given. Furthermore, Figure 6.6e presents the load diagram and the strain-amplitude plot. The following observations are made:

- As seen in Figure 6.5e, an increase of the thickness clearly implies a decrease in the number of extremes. In this case, the base case consists of 9 extremes whereas the largest thickness value counts 7. For the intermediate thickness, the number of extremes is also equal to 9. One additional interesting observation is that the cross-sections are mainly different towards the outer edges of the sheet.

[2] Kiendl et al. [87] states that the Kirchhoff-Love shell theory is applicable for shells with $L/t > 20$ (thin) and that shells with $L/t > 1000$ (very thin) the deformations cannot be described by geometrically linear behaviour for even small deformations.

- A change of the thickness influences the flexural rigidity to the third power and the through-thickness area of a shell element to the first power. By an increase of the flexural rigidity, the critical buckling that initiates wrinkles increases to the third power. Additionally, axial stiffness is increased due to an increase in the thickness, but its effect is proportional. Considering Figure 6.6e, it is observed that the non-dimensional critical buckling values are decreasing for increasing t, which is due to the non-dimensionalization of p. For larger strains, the curves are not equal, contrary to the cases where Young's modulus and foundation stiffness were varied. The reason for this is the fact that the membrane stiffness and the bending stiffness do not both increase proportionally due to the scaling chosen in p. Lastly, it can be seen that the line for a thickness of $10.7\,[m]$ is not fully flat for large p, which is possibly due to redistribution of the maximum amplitude from the middle to the side of the wrinkle due to stretching effects.

- Considering the strain-amplitude diagram in Figure 6.6e, it can be seen that the critical strain is largest for the largest thickness and that the curves have similar values for larger strains due to the fact that the horizontal axis is scaled by the different slopes in the load-strain diagram.

6.2.5 The Effect of Size

From the theory of plate or beam buckling, it is well-known that length or span of a plate or a beam influences the critical buckling load. When the length of a beam increases, the critical buckling load decreases. Considering the present case, the wrinkles occur in the direction perpendicular to the length of the sheet. Hence, the width B of the sheet is considered as a reference length for dimensionless quantities η and p. In the following, the width of the sheet is hence varied with values $B \in \{562.34, 840.90, \underline{1000}\}$ such that $\eta = \{204.4, 305.7, \underline{363.6}\}$.

In Figure 6.5f the cross-sectional profiles for different values of the thickness are presented and Figure 6.6f presents the load diagram and the strain-amplitude plot. The strain is normalized with the length of the sheet since this measures the elongation in length direction. The following observations are made:

- As seen in Figure 6.5f, the number of wrinkles for the lowest width of the sheet is equal to 7 whereas for the base case and the intermediate width this number is 9. Similar to the case of a varying thickness there is a preference for a symmetric mode shape which was also visible with a finer mesh.

- Considering the load curves in Figure 6.6f a decrease of the width of the sheet implies a decrease in the buckling load for the non-dimensionalization in Equation (6.2). Physically, a decrease of the width of the sheet would increase the buckling load from the perspective of the *span* of the sheet that decreases. However, the total load that is applied to the sheet also decreases since it is defined per unit area. Regarding the load-strain curve, it can be seen that the slope of the curves increases with a decrease in the thickness.

- An additional observation that can be made is that the plot for the lowest width $B = 562.34\,[m]$ shows an amplitude increase around a load p of 0.55. This increase corresponds with a shift of the maximum amplitude in the domain from the middle of the wrinkle to the side of the wrinkle. This is caused by the fact that the amplitudes in the middle of the wrinkle decrease due to stretching and while ones at the side keep increasing. However, it should be noted that this effect occurs for strains beyond 100% which is considered highly inaccurate for Saint-Venant Kirchhoff material models, see Section 3.5.

- Considering the strain-amplitude diagram in Figure 6.6f, it can be seen that the critical strain increases as the width of the sheet decreases. Using the observations made in the previous bullet, this can be explained by the fact that the increase in the slope of the load-strain is larger than the decrease of the critical load. Additionally, it can be seen that the lines do not overlap for large strains, as was seen for Young's modulus and foundation stiffness variations. This is expected to b related to the parametrization of ζ.

- Comparing the results from Figures 6.5f and 6.6f with the diagrams for the foundation stiffness and Young's modulus variation, it can be seen that despite the values of η are the same, a difference in critical buckling load and strain is observed. This is, again, expected to be related to the choice of the parametrization of p.

6.2.6 General Conclusions

Based on the parameter variations, some general conclusion can be drawn:

- The results of a varying foundation stiffness or Young's modulus show equal results for similar values of η. This implies that the scaling using η and p can be properly used in these cases. The results clearly show the balancing physics between the foundation stiffness and the material stiffness, i.e. the flexural rigidity.
- When the thickness is increased according to the non-dimensional parameter η and thus when the flexural rigidity D is changed by t instead of E, results are not equal to those generated by variations of foundation stiffness or Young's modulus. Possibly, the non-dimensional parameter p causes incorrect scaling of the load for the present mechanism.
- Similar to the thickness, variations in the effective wrinkling length, i.e. the width of the sheet, result in different results compared to the cases of varying Young's modulus or foundation stiffness for similar values of η. These differences could be related to improper choice of the scaling p.

Concluding, the present results can be seen as a step towards verification and possibly experimental validation case for thin floating membranes under tension. As mentioned above, the scaling laws presented in this case are expected to be not fully correct as they are not consistent in the prediction of a non-dimensional buckling load p for similar values of a non-dimensional stiffness ratio η between foundation stiffness S and flexural rigidity D. Improvement of these scaling laws is left out of the scope of this present research but is highly recommended for future research. The work of Cerda and Mahadevan [54] should be taken into account here, as it analogies in the effects of foundation stiffness and tensional forces in terms of energies.

Additionally, it is recommended to perform further convergence studies on the meshes that are used in the case study. Implementation of Quasi-Newton or Broyden methods in the present arc-length method would decrease the computational costs of the method such that finer meshes can be used for the analysis. Additionally, adaptive refinement of the mesh using THB-splines might be beneficial when the wrinkles have been formed.

6.3 Floating Quarter Disk

As an application to an offshore solar platform, assuming that the platform is thin, has large in-plane dimensions and a small thickness, the test-case as depicted in Figure 6.7 is specified. That is, a thin, circular membrane is modelled where the inner radius (R_1) is contracted by a distributed load and the outer boundary at radius R_2 is free or constrained. The vertical displacements on the inner boundary are also either free or constrained. The membrane is supported by a spring foundation with stiffness S, representing fluid-pressure.

The domain of interest is a quarter disk rather than a full disk, due to unavailability of periodic basis functions in the present model. The boundaries of the quarter disk are simply supported, i.e. the vertical displacement on the radial boundaries is zero.

In the Figure 6.8, results for the quarter disk for different boundary conditions are presented. The isogeometric mesh is depicted to represent the undeformed disk. As can be seen in this figure, the effect of constraints on the inner and outer boundaries is that the critical load and strain for wrinkle formation increases, which is a logical consequence of the fact that waves in radial dimension are halted on the outer and optionally the inner boundary. Additionally, the results show that for (approximately) equal amplitudes of the wrinkles, the strains of the constraint platforms are higher. All these observations provide background for design considerations of for very large floating sheets in Section 6.4.

6.4 Design Considerations for VLFTSs

Based on the result presented in Sections 6.2 and 6.3, this section intends to give some design considerations for the design of Very Large Floating Thin Structures (VLFTSs) for offshore solar power generation. The content of this section is based on structural design and analysis thoughts of the author, as no references are available on the design of VLFTSs. Therefore, the considerations in this section are conceptual and engineering details

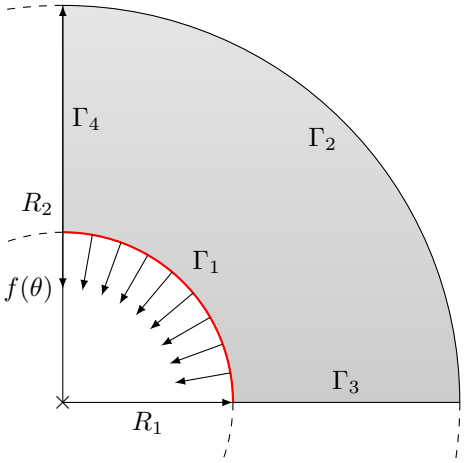

Figure 6.7: Floating disk with inner radius R_1 and outer radius R_2. The inner-boundary of the disk is loaded by a distributed load in radial direction. The straight boundaries are (anti)symmetry boundaries and the outer boundary is free. The disk is resting on a foundation with stiffness S.

are to be investigated further. Hence, these considerations can be seen as guiding thoughts.

When designing a floating platform for any reason, safe and reliable operation of and on the platform is desired under specific circumstances. In this context, this is referred to as *structural reliability*. For offshore solar platforms, this means that the structure and its mooring system should be able to encounter wind, waves and currents and even collisions with other structures in the ocean environment. When considering a ship hull, plates are supported by stiffeners, webs and girders in longitudinal and/or transversal direction to resist global loads (hull bending moments) and local loads (wave impacts) [52]. The structure is called *hierarchical*, since plates are supported by stiffeners, stiffeners are on their turn supported by webs and girders support the complete ship structure. In these structures, buckling of a plate with stiffeners between the system of webs and girders does not necessarily imply sinking or malfunctioning of the complete vessel. In other words, *structural reliability* is guaranteed when a plate fails.

Considering the floating sheets presented in Sections 6.2 and 6.3, it can be seen that initiation of the wrinkles (i.e buckling) and propagation of the wrinkles (i.e. post-buckling) affect the complete structure. Namely, as load increases, out-of-plane deformations of the wrinkles increase globally. As a result, structural reliability might be limited, as water can flow over parts of the platform, or wrinkles transition to folds and solar panels get covered, hence the platform loses its function. In worse cases, increased vertical deformations can lead to structural failure due to fracture or yielding of the material. In the following, design considerations for very large floating thin offshore solar platforms are given to indicate future challenges for the design of such structure from the view of wrinkling.

6.4.1 Arresting Wrinkles

In the case studies covered in this research, wrinkling is a phenomenon that globally affects the shape of the platform. To make wrinkling a local phenomenon and hence to ensure structural reliability, the platform should be designed such that local wrinkle formation does not have a global effect. Hence, wrinkles should be arrested to develop over the complete platform. Arresting wrinkles can be done by introducing local reinforcements.

In Figure 6.9 a circular offshore structure is depicted, with reinforcements denoted by thick solid lines. The reinforcements, in this case, can be locally thicker parts of the structure, or reinforcements using another material with a higher Young's modulus. Wrinkles that are long in the radial direction, have to encounter for instance tangential reinforcements (i.e. rings) which have large bending stiffness. Reinforcements are therefore expected to increase the buckling load by penalising long wrinkle wavelengths. It should be noted that from a numerical point of view, modelling of smaller wrinkles requires finer meshes. However, when the reinforcements

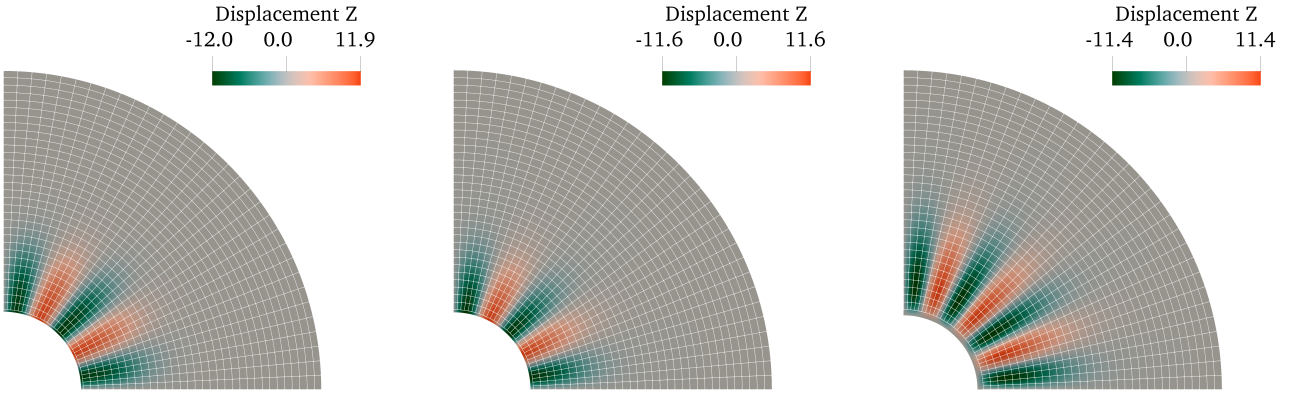

(a) Γ_1 vertically free, Γ_2 free in all directions.
The critical load is $f_c = 1.66 \cdot 10^2\ [MN/m]$, with critical strain $\varepsilon_c = 0.0042[-]$. The figure is plotted for $\varepsilon = 0.0089\ [-]$

(b) Γ_1 vertically free, Γ_2 simply supported.
The critical load is $f_c = 2.87 \cdot 10^2\ [MN/m]$, with critical strain $\varepsilon_c = 0.0077$. The figure is plotted for $\varepsilon = 0.0160$

(c) Γ_1 vertically constrained, Γ_2 simply supported.
The critical load is $f_c = 5.65 \cdot 10^2\ [MN/m]$, with critical strain $\varepsilon_c = 0.0107$. The figure is plotted for $\varepsilon = 0.0561$

Figure 6.8: Wrinkling of a quarter annulus (see Figure 6.7 for the geometry) with dimensions $R_1 = 500\,[m]$, $R_2 = 2000\,[m]$ and thickness $t = 10\,[m]$, Young's modulus $E = 0.5\,[GPa]$, Poisson's ratio $\nu = 0.4$ on a foundation with stiffness $S = \rho g = 10^4\,[kgm]$. The reference load is $f(\theta) = 0.5\,[N/m]$ and the boundaries Γ_3 and Γ_4 are simply supported ($\mathbf{u} = \mathbf{0}$) the boundary Γ_2 is either free or simply supported ($\mathbf{u} = \mathbf{0}$) and the boundary Γ_1 is free or constrained in vertical direction $u_z = 0$. Isogeometric meshes with 32×32 elements and order 4 of the undeformed geometry are plotted in white.

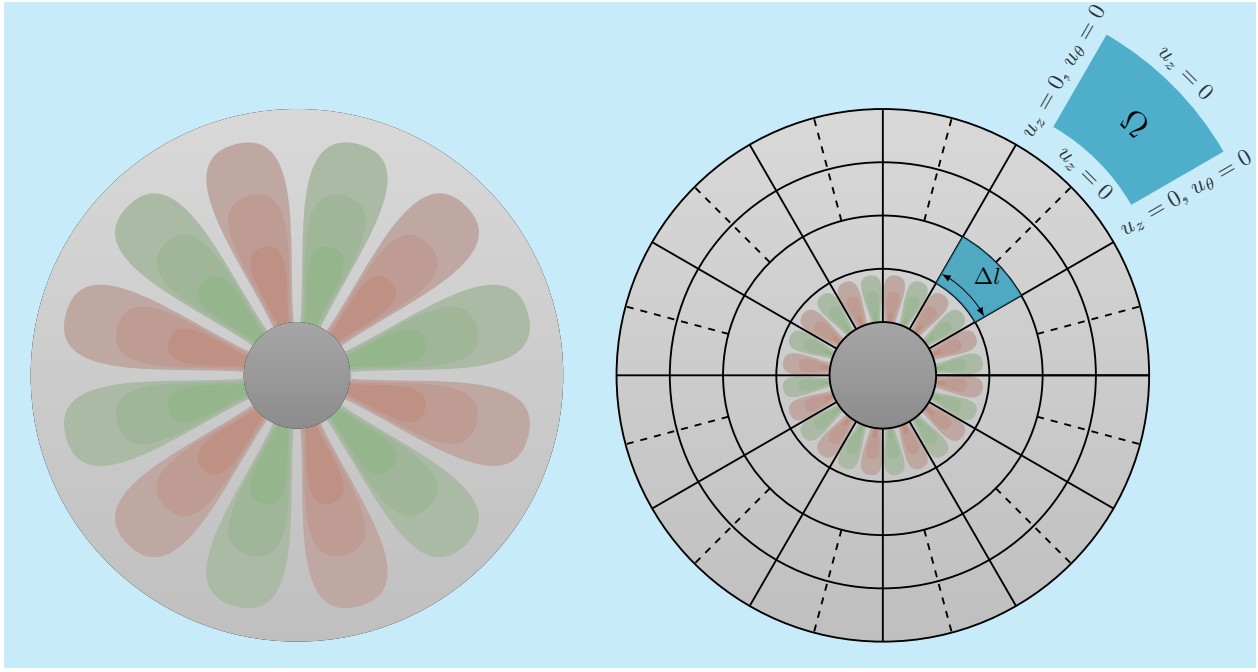

Figure 6.9: Original (continuous) offshore solar platform (left) and reinforced offshore solar platform (right). The dashed reinforcements are optional reinforcements to decrease the *tangential span* (denoted with Δl as an example) and in blue a possible extracted model domain is depicted when assuming a hierarchical structure. The sketches of the wrinkles are based on Figure 6.8.

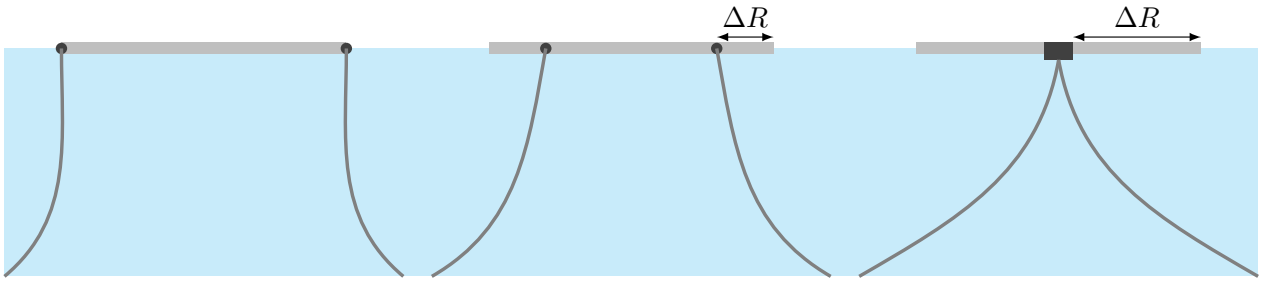

Figure 6.10: Three possible mooring solution for offshore solar platforms. The distance ΔR represents the radial distance between incident waves and the mooring connection. This distance can determine global buckling instability and hence wrinkling patters, but is depending on the reinforcements applied.

are considered as (torsional) constraints, the model domain can be reduced to a single patch (as depicted in Figure 6.9.

Reinforcement in radial and tangential direction implies that the distance between two radial reinforcements is larger when moving further outward on the disk. As commonly known from buckling theory, a larger span will reduce the wrinkling wavelength and hence wrinkling is more likely to occur on larger radii. A solution to cope with this problem is to add additional radial stiffening for larger radii (see Figure 6.9), or to distribute the stiffening less uniformly (e.g. according to the nerve structure of a leaf; c.f. the front page of this thesis). Additionally, reinforcement is drawn uniformly spaced in the tangential and radial direction, but the rings (i.e. radial dimension) can be spaced non-uniformly as well, to improve buckling resistance of each of the patches.

An additional note that should be made is that the reinforcements can be combined with the attachment of patches or modules of the platform and hence increase the manufacturability of the platform compared to a continuous structure. Additionally, the reinforcements can also be used as a walkway to increase the accessibility of the complete platform for inspection and maintenance purposes.

6.4.2 Mooring System Design

A design consideration that is not considered in this work, but that is essential in the future design of floating structures with low flexibility is mooring system design. In particular, interest is the connection of the platform to a mooring system (e.g. an anchor chain). In Figure 6.10, three alternatives are presented for the connection of a mooring system.

Firstly, a design where the mooring lines are connected to the outer ring (i.e. reinforced) is depicted. In this case, it is expected that the mooring system restricts this ring in a vertical direction, which can be a problem when large waves are encountering the platform.

Secondly, a design where the mooring system is connected between the centre and the outer ring of the platform is presented. It should be noted that the mooring lines are still to be connected to a reinforcement. In these cases, the edges are free to displace with the waves and the loads acting on the surface of the platform do not have to be transferred over the full radius.

Lastly, a design where the mooring lines are connected to a central buoy is presented. In this design, the buoy can be designed such that it has sufficient buoyancy to carry installations such as transformers. The disadvantage of such a buoy connection, however, is that the loads have to be transferred throughout the whole radius of the platform. Additionally, it should be noted that the buoyancy of the platform is depending on the depth of the sea since the mooring system itself is expected to weigh more as the depth of the sea increases. For future work, it is recommended to look into these concepts in more detail.

6.4.3 Holes and Point Loads

The last design consideration is regarding local effects such as holes/gaps or point loads. Firstly, holes or gaps in the structure might be required to increase the amount of solar radiation that is going through the platform to provide sunlight to underlying aquaculture. Additionally, holes can also be functional for maintenance purposes as the bottom of the platform can be made accessible for divers. However, the effect of the placement of holes in the structure can influence the wrinkling resistance of the platform as local stress concentrations might appear. It is expected that reinforcement of the structure will reduce the influence of holes on global structural reliability, as wrinkles due to the holes can be arrested by the reinforcement.

Secondly, point loads can be in-plane loads (such as local cable connections), but also loads orthogonal to the surface of the platform. In both cases, the effect of local disturbance of the structure on local structural stability should be considered. It is expected that reinforcements will increase the structural reliability of the platform, as was also the case for the holes. Examples of point loads can be humen or accidental placement of equipment on the platform.

Assuming the dimensions of the platform or patches of the platform are in the order of 100 up to 1000 metres and (man)holes and point loads have a small area (i.e. in the order of 1 metre), numerical challenges appear in terms of the multiple scales of the problem. In these cases, the numerical analysis should be covered by adaptive meshing techniques (see Carraturo et al. [129]) or multi-scale (post-)buckling analysis. No literature was found about the latter topic for Isogeometric or Finite Element Analysis.

6.5 Concluding Remarks

In this section, three applications of the present model on modelling wrinkling phenomena have been presented, relating to the fifth subgoal of this thesis. Additionally, based on the model results and the background information on Very Large Floating Structures (VLFSs) from Chapter 2, design considerations were presented in this section. This relates to the sixth subgoal of this thesis.

Firstly, the thin shell post-buckling model was applied to a derived case of the stretched thin sheet of Cerda and Mahadevan [54] in Section 6.1. Due to the fact that the boundaries do not remain straight when the sheet is elongated, the model results are not comparable to numerical studies from the literature. However, the physics that were observed in these works show a qualitative comparison. The reason for not modelling straight boundaries for this problem is, as mentioned earlier, due to a restriction in the implementation of Dirichlet boundary conditions combined with the arc-length method. Hence, improvement of this implementation is one of the recommendations for the current model as will be discussed in Chapter 8. Additionally, higher levels of mesh refinement or local refinement would give insight into the post-buckling instabilities that were found. However, finer meshes were not considered because of high computational costs. Mesh refinement and the effect of order increase or reduction, possibly using linear FEA, on computational costs are left for further research.

Secondly, a floating sheet subject to a traction load was considered to mimic a possible configuration of a Very Large Floating Thin Structure subject to wind or current in Section 6.2. The foundation stiffness was varied as a model parameter and the Young's modulus, Poisson's ratio, the width and the thickness of the sheet were varied as design parameters. In all parameter variations, the non-dimensional ratio between foundation stiffness and flexural rigidity η was similarly varied and the strain ε and non-dimensional amplitude ζ were plotted against the non-dimensional load p. The main conclusion from this parameter study is that despite constant variation of η and even the flexural rigidity D, differences in the strain and amplitudes were found. Hence, it is recommended to investigate the use of different scaling laws for this case.

Lastly, using the results of the parameter variations of the floating sheet subject to traction and additional results on the impact of different boundary conditions on a floating quarter disk subject to contraction on its inner radius, design considerations for the development of thin offshore structures were presented (see Section 6.4). In brief, these are: (i) adding reinforcement to arrest wrinkles and to introduce structural hierarchy for structural reliability; (ii) consider the effect of different mooring system connections to the (reinforced) platform; and (iii) investigate the effect of holes and point loads on local wrinkling behaviour.

7 | Conclusions

In this thesis, a model for the wrinkling analysis of thin sheets on substrates was presented. The main question that will be answered in the conclusion of this thesis is:

> *How can wrinkling formation of floating thin structures be numerically modelled with Isogeometric Analysis?*

The main objectives separate the development of a mathematical model and the application of this model on the physics of wrinkling of thin sheets on foundations, hence this chapter evaluates these objectives separately later on. In particular, the objectives are formulated as:

1. *Develop a geometrically nonlinear shell model based on Kirchhoff-Love shell theory and Isogeometric Analysis for post-buckling analysis.*

2. *Apply the Isogeometric shell model on common structural analysis computations, and in particular on post-buckling computations of wrinkling formation in floating sheets.*

In the remainder of this chapter, conclusions on the main aims and main question of this work are drawn. Section 7.1 first provides the combined highlights of this work relating to the knowledge gaps identified in Chapter 2 and answering the research question of this thesis. Thereafter, Section 7.2 provides the conclusions related to objective 1 of this research, and Section 7.3 provides conclusions related to objective 2 of this research. All conclusions are constructed by reflecting on the subgoals presented in Chapter 1.

7.1 Highlights

Based on the two objectives, the following highlights are the main conclusions from this research:

- Wrinkling formation of thin, floating sheets is numerically modelled using an Isogeometric Kirchhoff-Love shell model combined with the extended arc-length method (see Section 4.4) for post-buckling analysis. The extended arc-length method does not require initial perturbations of the solution, hence no *a priori* modelling decisions are required. This adds post-buckling analyses to the seamless integration of Computer Aided Design (CAD) and general structural analysis, which is the core idea of Isogeometric Analysis.

- Benchmark studies in Section 5.3 verified the shell model and the arc-length method based on results from the literature. Additionally, three case studies on wrinkling formation in were given in Chapter 6, namely a thin sheet subject to tension, a floating thin sheet subject to in-plane traction and a quarter disk subject to a contraction on the inner radius. The case studies show that the present model predicts wrinkling shapes, but the further implementation of Dirichlet boundary conditions in the arc length method will allow for further verification on wrinkling specifically. Furthermore, the implementation of adaptive meshing techniques using THB-splines (see Section 4.1) is recommended to capture local wrinkling phenomena without a large increase in computational costs.

- Application of the model on other structural analyses showed (static, buckling, modal and dynamic analysis) showed generally good agreement, although the linear buckling method should be verified further (see Section 5.2).

7.2 Mathematical Model Development

The first aim of this thesis focusses on model development of a thin shell model for the post-buckling analysis of thin sheets. In particular:

> *Extend the Kirchhoff-Love shell implementation in the Isogeometric Analysis framework to be applied in post-buckling analysis.*

The first subgoal of this thesis relates to the governing equations and related assumptions for modelling thin, floating structures. The mathematical model that was used in this work is based on the Kirchhoff hypothesis for thin beams and shells (see Chapter 3). In particular, an Euler-Bernoulli beam model was developed and the Kirchhoff-Love shell model of Goyal [142] was further extended (see Chapter 3). The main assumptions in the models are that the beams and shell are sufficiently thin such that their cross-sections do not deform under deformations and hence that only the mid-plane can be modelled. Additionally, rotary inertia of the shell is neglected and a linear relationship between stress and strain is assumed according to the Saint-Venant material model.

The application of isogeometric is discussed in Section 4.1, relating to the second subgoal of this thesis. Both the beam and shell implementation are based on rotation-free isogeometric analysis implementations. That is, B-splines and NURBS are used as the basis for analysis, and rotational degrees of freedom are not solved for but derivatives of the basis are used instead since their continuity is preserved and controllable across element boundaries. By only solving for displacement degrees of freedom, system size is reduced for the Kirchhoff-Love formulation. Additional advantages of Isogeometric Analysis include the exact representation of the geometry and high accuracy for a low number of degrees of freedom, as discussed in Section 2.3

Using the shell model, the arc-length method was implemented amongst other structural analyses. The present implementation of this method for the shell model includes the Crisfield arc-length method including bisection methods, extended iterations and branch switching to compute bifurcation points and to switch branches after these points (see Section 4.4). In Section 5.3 a series of three benchmark problems for the present arc-length method implementation was given. On the first hand, a shallow roof subject to an incremental point load was considered and similar results as published by other authors were obtained. Secondly, a clamped beam subject to an in-plane or out-of-plane point load was considered, where the latter case involves a bifurcation. The results of this benchmark showed that the results of the post-buckling branch are in agreement with the reference paper of Pagani and Carrera [216], without imposing initial perturbations on the beam. Lastly, the *shooting accuracy* of the model was assessed by means of a plate buckling problem. Here, the arc-length method was applied and a bifurcation was found using extended arc-length iterations. The results show accurate prediction of the bifurcation point with errors of 0.01% up to 0.10% for the finest meshes. From these results it can be concluded that the post-buckling method is verified, which fulfils the third and fourth subgoals of this thesis.

In Chapter 6 the model was applied to the cases of the stretching of a thin sheet and wrinkling of a floating sheet. Both cases contain conclusions that are noteworthy from a development point of view. Firstly, the stretched sheet showed large deviations compared to measurements of Zheng [71] due to the fact that arc-length method does not work for incremental displacements on the edges since Dirichlet boundary conditions are imposed by elimination (see Section 6.1). Additionally, it was found that for small wrinkle wavelengths, fine meshes (thus leading to large computational costs) were used to obtain accurate displacement fields and that instabilities had to be suppressed to obtain the results. Therefore, it can be concluded that further consideration of the origin of the instabilities of the stretched thin sheet is required by considering mesh refinement or very low arc-length steps. Both come with additional computational costs.

7.3 Structural Analysis and Wrinkling of Floating Sheets

Focussing on the application of the Isogeometric Euler-Bernoulli beam and Kirchhoff-Love shell models that were developed under the first objective of this thesis, the second objective reads:

> *Apply the Isogeometric shell model on common structural analysis computations, and in particular on post-buckling computations of wrinkling formation in floating sheets.*

Related to the third subgoal of this thesis, Chapter 4 presented different numerical procedures for structural analysis computations, given the (non)-linear stiffness, the mass and a damping matrix from any beam or shell discretization. The analyses that were covered here are static, modal, buckling, post-buckling and dynamic analysis (see Sections 5.1 to 5.5). In case of the post-buckling solver, the Crisfield arc-length method combined with procedures to compute bifurcation points and to switch bifurcation branches. Furthermore, a number of temporal integration schemes (see Section 4.6) were implemented for the beam model and based on the fact that no order reduction has to be applied and hence system size is not doubled, the Newmark and Bathe method were included for the shell model.

Based on the benchmark problems in Chapter 5, the beam and shell model presented in this thesis were verified, relating to subgoal 5. The models were verified using manufactured solutions or benchmark studies from the literature. The following is concluded:

- Firstly, for the beam model, the static analysis showed expected orders of convergence except for second order basis functions. Buckling analysis showed that the beam model consistently predicts critical buckling loads, although inaccuracies were found for the finest meshes. The modal analysis showed expected orders of convergence for a simply supported beam, based on theoretical analysis from literature. Dynamic analysis with the beam model showed expected orders of temporal convergence for all implemented time integration methods.
- Secondly, static analysis for the shell model showed good agreement with the results of other isogeometric shell implementations, but slight differences with respect to Finite Element models. For buckling analysis, the shell model showed convergence towards analytical critical buckling loads, although this convergence did not improve for increasing orders of convergence. Post-buckling analysis benchmarks showed good agreement with reference solutions for cases with and without bifurcations. Similar to the beam model, a modal analysis benchmark showed a convergence of order $2(p-1)$, but a theoretical estimate for this order was absent. Lastly, a benchmark for nonlinear dynamic analysis showed that the present method provides similar results compared to other studies, although differences in elements and time integration methods were present. Additionally, the dynamic analysis showed that refinements increase the prediction of local spatial and temporal features

Although not all structural analyses have been used for application on wrinkling of (floating) thin membranes, the methods have been verified for future use for the analysis of thin shell structures. Especially, the use of the dynamic shell model can be useful for Fluid-Structure Interaction (FSI) computations (see Chapter 8) and modal analysis can be used with the modal expansion method to construct linear dynamic models (see Section 4.5).

Lastly, the phenomenon of wrinkling of thin (floating) sheets is studied, relating to the sixth subgoal of this thesis. The two cases that were presented in Chapter 6 are the stretched thin sheet and a floating sheet subject to traction. In both cases, wrinkles were modelled successfully. However, in the case of the stretched thin sheet, a clear transition to a larger number of wrinkles was seen for coarse meshes. Additionally, this case was modelled using different boundary conditions compared to references from the literature. In case of the sheet subject to traction, the physical mechanisms behind the wrinkling phenomena were identified, but a proper scaling for the non-dimensional load was not found. Based on the physics of wrinkling of a floating sheet, design considerations were presented for an annular offshore solar platform. These considerations are: (i) adding reinforcement to arrest wrinkles and to introduce structural hierarchy for structural reliability; (ii) consider the effect of different mooring system connections to the (reinforced) platform; and (iii) investigate the effect of holes and point loads on local wrinkling behaviour.

8 | Further Research

In this chapter, suggestions for further research are presented, based on the findings of this research and the findings of the literature review. The mindmap in Figure 8.1 is provided to show interactions between different topics presented in this section.

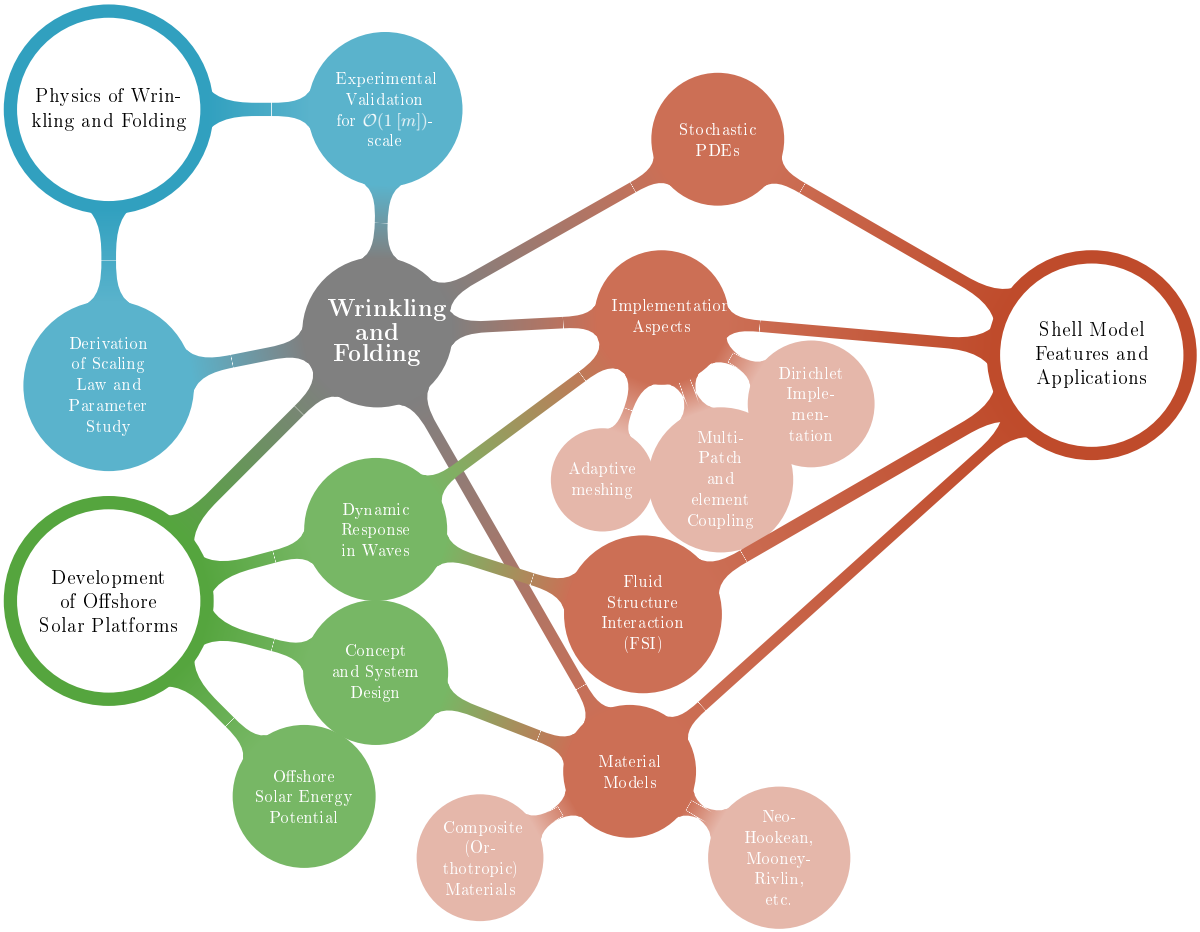

Figure 8.1: Mindmap with different topics presented for further research in this section. Related topics are indicated by connections and motivations can be found throughout this section.

8.1 Shell Model Features and Applications

Firstly, based on the results from this study and the use of the model in Chapter 6, the following future work is recommended:

- The treatment of non-homogeneous *Dirichlet boundary conditions* is done by elimination in the model

developed in this work. For most applications, this technique works correctly. However, in the current implementation, the residual is not updated when Dirichlet boundary conditions are changed using the load factor λ in the arc length method. This results in an unstable arc-length method with complex roots. One way to overcome this problem is to implement the Dirichlet boundary conditions based on L_2-elimination. In this way, the force vector $\mathbf{f}$ contains non-zero entries. An alternative is to implement a method similar to the implementation of clamped boundary conditions, where degrees of freedom on one boundary can be coupled and hence *rigid* boundaries can be modelled (see Figure 6.4).

- Improvements for the post-buckling method that was used in this model are mostly based on robustness and computational costs. Although the method was successfully benchmarked in this study, the case where wrinkling of a thin sheet was investigated (see Section 6.1) showed that secondary bifurcations can occur and that the current implementation was not able to find these points with the finest meshes. Hence, it is recommended to reduce the computational costs of the arc-length method by utilising quasi-Newton or Broyden methods such that the results for finer meshes can be considered. Alternatively, the implementation of an existing and possibly optimized continuation method library can be considered, e.g. using the LOCA package of Trilinos[1].

- To capture local phenomena such as wrinkling without uniformly refining the complete domain and hence increasing computational costs massively, refinement using THB-splines is proposed. Although this concept was proposed in a case in Section 5.1, future work can be done on *adaptive mesh refinement* in combination with time-integration and arc-length methods. The problem that arises, in this case, is that with mesh refinements the number of degrees of freedom (hence matrix and vector sizes) change and therefore time-integration and arc-length methods have to be modified since they assume the same system size every step. A solution for this problem, which shows the strength of Isogeometric Analysis, is to utilise the property that the solution is continuous everywhere and hence can be refined accordingly without making interpolation errors. In this way, the previous load or time steps can be refined to comply with the system size of the new load step. The work of Carraturo et al. [129] can be used as inspiration here.

Additionally, a few recommendations for wider application of the model on engineering applications follow from findings in the literature review of this study. Firstly, one of the goals of this research was to implement different structural analyses for the Kirchhoff-Love shell model. For simple geometries, i.e. single patch geometries, this goal is achieved as shown in the benchmark studies. However, when geometries become more complex, there is the need to connect *multiple patches* or element types in-plane or out-of-plane. For example, when the offshore solar platform will be reinforced by stiffeners or when 'airbags' are used, different shell patches should be connected out-of-plane. These connections can be implemented by the *Bending Strip Method* [88] and non-conforming patch coupling can be done by the master-slave coupling from Coox et al.[90, 91] or using interpolation matrices to transfer mass and stiffness of arbitrarily curved stiffeners to a plate [105].

Secondly, when designing structures with local thickness changes beyond the thin-shell assumptions, implementation of *blended elements* [96] can be beneficial. These elements account for combination or Reissner-Mindlin and Kirchhoff-Love theory. When the structure is reinforced with beams, the methodology from the work of Raknes et al. [97] can be used to combine beam and shell elements. Lastly, implementation of *material models* such as Neo-Hookean or Mooney-Rivlin would allow for more accurate modelling of rubber-like materials or implementation of *composite material models*. This can be of particular interest if offshore solar platforms will be constructed from such materials.

Lastly, the thin shell model could be further developed to solve for *Stochastic Partial Differential Equation* (SPDEs) to identify the occurrence of different wrinkling and folding complexes based on a non-deterministic distribution of thickness or stiffness variations, which was done by Li et al. [118, 119, 120] recently.

[1] The Library of Continuation Algorithms (LOCA) is a library for performing large-scale bifurcation analysis developed by Sandia National Laboratories. The website of LOCA is `http://www.cs.sandia.gov/loca/`. LOCA is a package of the Trilinos Project (`https://trilinos.github.io/`). The webpages were accessed in July 2019.

8.2 Physics of Wrinkling and Folding

Modelling of wrinkles in thin sheets is one of the main topics of this research. A lot of work has been performed and published in other works and based on the findings of this study, the applications to offshore solar platforms and the available literature, some suggestions for further research in this topic are given here.

Firstly, with the implementations mentioned in Section 8.1, especially the Dirichlet boundary conditions implementation, several *experiments* from literature can be resembled with the present model. As mentioned in Section 2.2, the experiments from Wong and Pellegrino [50], Cerda et al. [43], Iwasa [222] (hence numerical results similar to those of Nayyar et al. [72] and Taylor et al. [73]). Using periodic basis functions, an annular sheet under torsion can also be modelled (see the work of Wang et al. [223]), which is expected to be a representative case for the offshore platform.

Furthermore, experiments by Wang and Zhao [224] and Pocivavsek et al. [44] explored the transition of wrinkled sheets on a substrate towards a folded configuration. An extension of the current research would be to investigate this phenomenon for sheets subject to bi-axial loading patterns and to further validate the model using the *scaling laws* and experimental data from Wang and Zhao, Pocivavsek et al. [224, 44]. This can lead to more complex structures of wrinkles and folds. Ultimately, a bi-axial version of the phase-diagram of Wang and Zhao [224] can be derived for this kind of loading situations. Additionally, more applicable to the offshore solar platform, this can be done for annular geometries floating on a substrate. One of the requirements of the investigation of wrinkling and folding complexes is that the model should be capable of modelling delamination or self-contact of the sheet in a far-developed fold as described for the floating uni-directionally loaded sheet by Jambon-Puillet et al. [55]. Regarding the experimental investigation of wrinkling for large floating sheets is that the effect of surface tension can be significant in an experimental setting, but insignificant on full scale. Hence, the Bond number should be taken into account in *experimental scalings*.

8.3 Development of Offshore Solar Platforms

Although the motivation for offshore solar energy, as presented in Chapter 1 was only motivational in this research, some suggestions for future developments based on the cited literature are presented here.

Thirdly, from a modelling perspective, the developed model combined with cable elements can be used to model a floating solar platform on an air-water interface to compute *dynamic loads* on the structure and mooring system in the ocean environment. In this work, the whole study of Fluid-Structure Interaction was left out of scope, but initially, the shell solver was coupled to a simple ideal flow solver using a linear elasticity solver for the domain deformations (using the solver and findings of Shamanskiy et al. [225]). When an isogeometric flow solver - whenever it considers real flow, ideal flow or turbulent flow - is coupled to an isogeometric structural solver in a partitioned way, the interface can be represented identically for both solvers (see Hosters et al. [226] for details), utilising the isogeometric refinement property that maintains the shape of the interface.

Secondly, this research has shown the development of a model to predict wrinkling of sheets floating on water. Additionally, background knowledge was given on the physics of wrinkling. The next step in the development of offshore solar platforms could be to develop a concept design. This design can bring new challenges in the modelling of such structures. These concept designs, on their turn, can be used to develop the present isogeometric model for wrinkling predictions towards a tool that is suitable to model for instance more complex cross-sections (see Section 8.1 for the Bending Strip Method and combinations of elements), composite materlals, but also considering hierarchy in the structure or the need to model local effects (which requires local refinements using THB splines).

Thirdly, based on the available literature sources on offshore solar platforms and additional publications on environmental analyses, it is recommended to perform a study on the *potential of offshore solar energy*. For this analysis, data on cloud cover [7], increased efficiency of cooling and an increase of the albedo effect due to sea water[25] and the methodology of Huld et al. [6] and Miglietta et al. [24] on the land-based solar energy potential can be combined in a similar analysis to investigate the potential of offshore solar energy.

Bibliography

[1] United Nations Framework Convention on Climate Change. Paris agreement, 2015. Accessed: December 2018.

[2] Latvia Presidency of the Council of the European Union. Intended nationally determined contribution of the eu and its member states, March 2015. Accessed: December 2018.

[3] Z. Gao, H. B. Bingham, D. Ingram, A. Kolios, D. Karmakar, T. Utsunomiya, I. Catipovic, G. Colicchio, J. Miguel Rodrigues, F. Adam, D. G. Karr, C. Fang, H. K. Shin, J. Slätte, C. Ji, W. Sheng, P. Liu, and L. Stoev. Committee V.4 report: Offshore Renewable Energy. In M. L. Kaminski and P Rigo, editors, *Progress in Marine Science and Technology: Proceedings of the 20th International Ship and Offshore Structures Congress*, volume II, pages 193–277. IOS Press, 2018. doi: 10.3233/978-1-61499-864-8-193.

[4] R. Campbell, A. Martinez, C. Letetrel, and A. Rio. Methodology for estimating the French tidal current energy resource. *International Journal of Marine Energy*, 19:256–271, sep 2017. ISSN 2214-1669. doi: 10.1016/J.IJOME.2017.07.011.

[5] C. Kalogeri, G. Galanis, C. Spyrou, D. Diamantis, F. Baladima, M. Koukoula, and G. Kallos. Assessing the European offshore wind and wave energy resource for combined exploitation. *Renewable Energy*, 2017. ISSN 18790682. doi: 10.1016/j.renene.2016.08.010.

[6] T. Huld, A. Amillo, T. Huld, and A. M. G. Amillo. Estimating PV Module Performance over Large Geographical Regions: The Role of Irradiance, Air Temperature, Wind Speed and Solar Spectrum. *Energies*, 8(6):5159–5181, jun 2015. ISSN 1996-1073. doi: 10.3390/en8065159.

[7] R. Meerkötter, G. Gesell, V. Grewe, C. König, S. Lohmann, and H. Mannstein. A high resolution European cloud climatology from 15 years of NOAA/AVHRR data. In *Proc. 2004 EUMETSAT Meteorological Conference, Prague, Czech Republic*, volume 31. Citeseer, 2004.

[8] EMODnet Bathymetry Consortium et al. Emodnet digital bathymetry (dtm). *EMODnet Bathymetry.*, 10, 2016.

[9] Global Wind Energy Council. Global wind energy report 2018. Anual Report 14, Global Wind Energy Council, April 2019.

[10] X. Wang, X. Zeng, J. Li, X. Yang, and H. Wang. A review on recent advancements of substructures for offshore wind turbines. *Energy Conversion and Management*, 158:103–119, feb 2018. ISSN 0196-8904. doi: 10.1016/J.ENCONMAN.2017.12.061.

[11] E. I. Zountouridou, G. C. Kiokes, S. Chakalis, P. S. Georgilakis, and N. D. Hatziargyriou. Offshore floating wind parks in the deep waters of Mediterranean Sea. *Renewable and Sustainable Energy Reviews*, 51:433–448, nov 2015. ISSN 1364-0321. doi: 10.1016/J.RSER.2015.06.027.

[12] G. Pisacane, G. Sannino, A. Carillo, M. V. Struglia, and S. Bastianoni. Marine Energy Exploitation in the Mediterranean Region: Steps Forward and Challenges. *Frontiers in Energy Research*, 6:109, oct 2018. ISSN 2296-598X. doi: 10.3389/fenrg.2018.00109.

[13] T. Soukissian, D. Denaxa, F. Karathanasi, A. Prospathopoulos, K. Sarantakos, A. Iona, K. Georgantas, S. Mavrakos, T. H. Soukissian, D. Denaxa, F. Karathanasi, A. Prospathopoulos, K. Sarantakos, A. Iona, K. Georgantas, and S. Mavrakos. Marine Renewable Energy in the Mediterranean Sea: Status and Perspectives. *Energies*, 10(10):1512, sep 2017. ISSN 1996-1073. doi: 10.3390/en10101512.

[14] L. Rusu and F. Onea. Assessment of the performances of various wave energy converters along the European continental coasts. *Energy*, 82:889–904, mar 2015. ISSN 03605442. doi: 10.1016/j.energy.2015.01.099.

[15] E. Rusu and F. Onea. A review of the technologies for wave energy extraction. *Clean Energy*, 2(1):10–19, 2018.

[16] M. N. Ayob, V. Castellucci, and R. Waters. Wave energy potential and 1–50 TWh scenarios for the Nordic synchronous grid. *Renewable Energy*, 2017. ISSN 18790682. doi: 10.1016/j.renene.2016.09.004.

[17] R. C. Lisboa, P. R. F. Teixeira, and C. J. Fortes. Numerical evaluation of wave energy potential in the south of Brazil. *Energy*, 121:176–184, 2017. ISSN 0360-5442. doi: https://doi.org/10.1016/j.energy.2017.01.001.

[18] G. Lavidas. Developments of energy in EU–unlocking the wave energy potential. *International Journal of Sustainable Energy*, 38(3):208–226, mar 2019. ISSN 1478-6451. doi: 10.1080/14786451.2018.1492578.

[19] F. Arena, V. Laface, G. Malara, A. Romolo, A. Viviano, V. Fiamma, G. Sannino, and A. Carillo. Wave climate analysis for the design of wave energy harvesters in the Mediterranean Sea. *Renewable Energy*, 77:125–141, may 2015. ISSN 0960-1481. doi: 10.1016/J.RENENE.2014.12.002.

[20] D. Magagna and A. Uihlein. Ocean energy development in Europe: Current status and future perspectives. *International Journal of Marine Energy*, 11:84–104, sep 2015. ISSN 2214-1669. doi: 10.1016/J.IJOME.2015.05.001.

[21] M. Melikoglu. Current status and future of ocean energy sources: A global review. *Ocean Engineering*, 148:563–573, jan 2018. ISSN 0029-8018. doi: 10.1016/J.OCEANENG.2017.11.045.

[22] N. Guillou, S. P. Neill, and P. E. Robins. Characterising the tidal stream power resource around France using a high-resolution harmonic database. *Renewable Energy*, 123:706–718, aug 2018. ISSN 0960-1481. doi: 10.1016/J.RENENE.2017.12.033.

[23] E. Segura, R. Morales, and J. A. Somolinos. Cost Assessment Methodology and Economic Viability of Tidal Energy Projects. *Energies*, 10(11):1806, nov 2017. ISSN 1996-1073. doi: 10.3390/en10111806.

[24] M. M. Miglietta, T. Huld, and F. Monforti-Ferrario. Local Complementarity of Wind and Solar Energy Resources over Europe: An Assessment Study from a Meteorological Perspective. *Journal of Applied Meteorology and Climatology*, 2017. ISSN 1558-8424. doi: 10.1175/JAMC-D-16-0031.1.

[25] H. Bahaidarah, A. Subhan, P. Gandhidasan, and S. Rehman. Performance evaluation of a PV (photovoltaic) module by back surface water cooling for hot climatic conditions. *Energy*, 2013. ISSN 03605442. doi: 10.1016/j.energy.2013.07.050.

[26] A. Akbarzadeh and T. Wadowski. Heat pipe-based cooling systems for photovoltaic cells under concentrated solar radiation. *Applied Thermal Engineering*, 16(1):81–87, jan 1996. ISSN 13594311. doi: 10.1016/1359-4311(95)00012-3.

[27] A. Sahu, N. Yadav, and K. Sudhakar. Floating photovoltaic power plant: A review. *Renewable and Sustainable Energy Reviews*, 66:815–824, dec 2016. ISSN 1364-0321. doi: 10.1016/J.RSER.2016.08.051.

[28] B. D Patterson, F. Mo, A. Borgschulte, M. Hillestad, F. Joos, T. Kristiansen, S. Sunde, and J. A van Bokhoven. Renewable CO2 recycling and synthetic fuel production in a marine environment. *Proceedings of the National Academy of Sciences of the United States of America*, 116(25):12212–12219, jun 2019. ISSN 1091-6490. doi: 10.1073/pnas.1902335116.

[29] M. Kashiwagi. A time-domain mode-expansion method for calculating transient elastic responses of a pontoon-type VLFS. *Journal of Marine Science and Technology*, 5(2):89–100, dec 2000. ISSN 0948-4280. doi: 10.1007/PL00010631.

[30] O. Waals. Life@sea: future use of our oceans, March 2018. Presented at The Floating Future Seminar 2018, Wageningen, The Netherlands.

[31] Masashi Kashiwagi et al. Research on hydroelastic responses of vlfs" recent progress and future work. In *The Ninth International Offshore and Polar Engineering Conference*. International Society of Offshore and Polar Engineers, 1999.

[32] M. Kashiwagi. A B-spline Galerkin scheme for calculating the hydroelastic response of a very large floating structure in waves. *Journal of Marine Science and Technology*, 3(1):37–49, mar 1998. ISSN 0948-4280. doi: 10.1007/BF01239805.

[33] M. Kashiwagi. Transient responses of a VLFS during landing and take-off of an airplane. *Journal of Marine Science and Technology*, 9(1):14–23, may 2004. ISSN 0948-4280. doi: 10.1007/s00773-003-0168-0.

[34] A. Andrianov. Hydroelastic analysis of very large floating structures. *Doctorale thesis, Delft University of Technology*, 2005.

[35] M. Lamas-Pardo, G. Iglesias, and L. Carral. A review of Very Large Floating Structures (VLFS) for coastal and offshore uses. *Ocean Engineering*, 109:677–690, nov 2015. ISSN 0029-8018. doi: 10.1016/J.OCEANENG.2015.09.012.

[36] T. P. Gerostathis, K. A. Belibassakis, and G. A. Athanassoulis. 3D hydroelastic analysis of very large floating bodies over variable bathymetry regions. *Journal of Ocean Engineering and Marine Energy*, 2(2):159–175, may 2016. ISSN 2198-6444. doi: 10.1007/s40722-016-0046-6.

[37] T. Hamamoto. Stochastic fluid—structure interaction of large circular floating islands during wind waves and seaquakes. *Probabilistic Engineering Mechanics*, 10(4):209–224, jan 1995. ISSN 0266-8920. doi: 10.1016/0266-8920(95)00017-8.

[38] T. I. Khabakhpasheva and A. A. Korobkin. Hydroelastic behaviour of compound floating plate in waves. *Journal of Engineering Mathematics*, 44(1):21–40, sep 2002. ISSN 1573-2703. doi: 10.1023/A:1020592414338.

[39] M. Riyansyah, C. M. Wang, and Y. S. Choo. Connection design for two-floating beam system for minimum hydroelastic response. *Marine Structures*, 23(1):67–87, 2010. ISSN 0951-8339. doi: https://doi.org/10.1016/j.marstruc.2010.01.001.

[40] C. M. Wang and Z. Y. Tay. Hydroelastic analysis and response of pontoon-type very large floating structures. In *Fluid structure interaction II*, pages 103–130. Springer, 2011.

[41] W. Wei, S. Fu, T. Moan, C. Song, and T. Ren. A time-domain method for hydroelasticity of very large floating structures in inhomogeneous sea conditions. *Marine Structures*, 57:180–192, jan 2018. ISSN 09518339. doi: 10.1016/j.marstruc.2017.10.008.

[42] G. K. Batchelor. An Introduction to Fluid Dynamics, 1967. ISSN 00319228.

[43] E. Cerda, K. Ravi-Chandar, and L. Mahadevan. Wrinkling of an elastic sheet under tension. *Nature*, 419(6907):579–580, oct 2002. ISSN 0028-0836. doi: 10.1038/419579b.

[44] L. Pocivavsek, R. Dellsy, A. Kern, S. Johnson, B. Lin, K. Y. C. Lee, and E. Cerda. Stress and fold localization in thin elastic membranes. *Science*, 2008. ISSN 00368075. doi: 10.1126/science.1154069.

[45] Y. L. Li, M. Y. Lu, H. F. Tan, and Y. Q. Tan. A study on wrinkling characteristics and dynamic mechanical behavior of membrane. *Acta Mechanica Sinica*, 28(1):201–210, feb 2012. ISSN 0567-7718. doi: 10.1007/s10409-011-0512-2.

[46] B. Li, Y. P. Cao, X. Q. Feng, and H. Gao. Surface wrinkling of mucosa induced by volumetric growth: Theory, simulation and experiment. *Journal of the Mechanics and Physics of Solids*, 59(4):758–774, apr 2011. ISSN 0022-5096. doi: 10.1016/J.JMPS.2011.01.010.

[47] D. Vella, A. Ajdari, A. Vaziri, and A. Boudaoud. Wrinkling of pressurized elastic shells. *Physical Review Letters*, 2011. ISSN 00319007. doi: 10.1103/PhysRevLett.107.174301.

[48] M. Taffetani and D. Vella. Regimes of wrinkling in pressurized elastic shells. *Philosophical transactions. Series A, Mathematical, physical, and engineering sciences*, 375(2093):20160330, may 2017. ISSN 1364-503X. doi: 10.1098/rsta.2016.0330.

[49] C. Androulidakis, E. N. Koukaras, M. G. Pastore Carbone, M. Hadjinicolaou, and C. Galiotis. Wrinkling formation in simply-supported graphenes under tension and compression loadings. *Nanoscale*, 9(46): 18180–18188, nov 2017. ISSN 2040-3364. doi: 10.1039/C7NR06463B.

[50] W. Wong and S. Pellegrino. Wrinkled membranes I: experiments. *Journal of Mechanics of Materials and Structures*, 1(1):3–25, may 2006. ISSN 1559-3959. doi: 10.2140/jomms.2006.1.3.

[51] D. O. Brush, B. O. Almroth, and J. W. Hutchinson. Buckling of Bars, Plates, and Shells. *Journal of Applied Mechanics*, 1975. ISSN 00218936. doi: 10.1115/1.3423755.

[52] O. F. Hughes, J. K.. Paik, and D. Béghin. *Ship structural analysis and design*. Society of Naval Architects and Marine Engineers, 2010. ISBN 0939773821.

[53] B. K. Hadi. Wrinkling of sandwich column: comparison between finite element analysis and analytical solutions. *Composite Structures*, 53(4):477–482, sep 2001. ISSN 0263-8223. doi: 10.1016/S0263-8223(01)00060-5.

[54] E. Cerda and L. Mahadevan. Geometry and Physics of Wrinkling. *Physical Review Letters*, 2003. ISSN 10797114. doi: 10.1103/PhysRevLett.90.074302.

[55] E. Jambon-Puillet, D. Vella, and S. Protière. The compression of a heavy floating elastic film. *Soft Matter*, 12(46):9289–9296, nov 2016. ISSN 1744-683X. doi: 10.1039/C6SM00945J.

[56] W. Wong and S. Pellegrino. Wrinkled membranes II: analytical models. *Journal of Mechanics of Materials and Structures*, 1(1):27–61, may 2006. ISSN 1559-3959. doi: 10.2140/jomms.2006.1.27.

[57] W. Wong and S. Pellegrino. Wrinkled membranes III: numerical simulations. *Journal of Mechanics of Materials and Structures*, 1(1):63–95, may 2006. ISSN 1559-3959. doi: 10.2140/jomms.2006.1.63.

[58] A. A. Evans, S. E. Spagnolie, D. Bartolo, and E. Lauga. Elastocapillary self-folding: buckling, wrinkling, and collapse of floating filaments. *Soft Matter*, 9(5):1711–1720, jan 2013. ISSN 1744-683X. doi: 10.1039/C2SM27089G.

[59] T. J. W. Wagner. *Elastocapillarity: Adhesion and large deformations of thin sheets*. PhD thesis, University of Cambridge, 2013.

[60] T. J. W. Wagner and D. Vella. Floating carpets and the delamination of elastic sheets. *Physical Review Letters*, 107(4):044301, jul 2011. ISSN 00319007. doi: 10.1103/PhysRevLett.107.044301.

[61] Maroun Abi Ghanem, Xudong Liang, Brittany Lydon, Liam Potocsnak, Thorsen Wehr, Mohamed Ghanem, Samantha Hoang, Shengqiang Cai, and Nicholas Boechler. Wrinkles Riding Waves in Soft Layered Materials. *Advanced Materials Interfaces*, 6(1):1801609, jan 2019. ISSN 2196-7350. doi: 10.1002/admi.201801609. URL https://onlinelibrary.wiley.com/doi/abs/10.1002/admi.201801609.

[62] E. Puntel, L. Deseri, and E. Fried. Wrinkling of a Stretched Thin Sheet. *Journal of Elasticity*, 105(1-2): 137–170, nov 2011. ISSN 0374-3535. doi: 10.1007/s10659-010-9290-5.

[63] H. Diamant and T. A. Witten. Compression Induced Folding of a Sheet: An Integrable System. *Physical Review Letters*, 107(16):164302, oct 2011. ISSN 0031-9007. doi: 10.1103/PhysRevLett.107.164302.

[64] M. Rivetti. Non-symmetric localized fold of a floating sheet. *Comptes Rendus Mécanique*, 341(3):333–338, mar 2013. ISSN 1631-0721. doi: 10.1016/J.CRME.2013.01.005.

[65] B. Audoly. Localized buckling of a floating elastica. *Physical Review E*, 84(1):011605, jul 2011. ISSN 1539-3755. doi: 10.1103/PhysRevE.84.011605.

[66] M. Rivetti and S. Neukirch. The mode branching route to localization of the finite-length floating elastica. *Journal of the Mechanics and Physics of Solids*, 69:143–155, sep 2014. ISSN 0022-5096. doi: 10.1016/J.JMPS.2014.05.004.

[67] Y. Wong, S. Pellegrino, and K. Park. Prediction of winkle amplitudes in square solar sails. In *44th AIAA/ASME/ASCE/AHS/ASC Structures, Structural Dynamics, and Materials Conference*, page 1982, 2003.

[68] Y. W. Wong and S. Pellegrino. Computation of wrinkle amplitudes in thin membrane. In *43rd AIAA/ASME/ASCE/AHS/ASC Structures, Structural Dynamics, and Materials Conference*, page 1369, 2002.

[69] C. G. Wang, H. F. Tan, X. W. Du, and Z. M. Wan. Wrinkling prediction of rectangular shell-membrane under transverse in-plane displacement. *International Journal of Solids and Structures*, 44(20):6507–6516, oct 2007. ISSN 0020-7683. doi: 10.1016/J.IJSOLSTR.2007.02.036.

[70] C. Bisagni. Dynamic buckling of fiber composite shells under impulsive axial compression. *Thin-Walled Structures*, 43(3):499–514, mar 2005. ISSN 0263-8231. doi: 10.1016/J.TWS.2004.07.012.

[71] L. Zheng. *Wrinkling of dielectric elastomer membranes*. PhD thesis, California Institute of Technology, 2009.

[72] V. Nayyar, K. Ravi-Chandar, and R. Huang. Stretch-induced stress patterns and wrinkles in hyperelastic thin sheets. *International Journal of Solids and Structures*, 48(25-26):3471–3483, dec 2011. ISSN 0020-7683. doi: 10.1016/J.IJSOLSTR.2011.09.004.

[73] M. Taylor, B. Davidovitch, Z. Qiu, and K. Bertoldi. A comparative analysis of numerical approaches to the mechanics of elastic sheets. *Journal of the Mechanics and Physics of Solids*, 79:92–107, jun 2015. ISSN 0022-5096. doi: 10.1016/J.JMPS.2015.04.009.

[74] A. A. Sipos and E. Fehér. Disappearance of stretch-induced wrinkles of thin sheets: A study of orthotropic films. *International Journal of Solids and Structures*, 97-98:275–283, oct 2016. ISSN 0020-7683. doi: 10.1016/J.IJSOLSTR.2016.07.021.

[75] Q. Li and T. J. Healey. Stability boundaries for wrinkling in highly stretched elastic sheets. *Journal of the Mechanics and Physics of Solids*, 97:260–274, dec 2016. ISSN 0022-5096. doi: 10.1016/J.JMPS.2015.12.001.

[76] T. Wang, C. Fu, F. Xu, Y. Huo, and M. Potier-Ferry. On the wrinkling and restabilization of highly stretched sheets. *International Journal of Engineering Science*, 136:1–16, mar 2019. ISSN 0020-7225. doi: 10.1016/J.IJENGSCI.2018.12.002.

[77] M. Taylor, K. Bertoldi, and D. J. Steigmann. Spatial resolution of wrinkle patterns in thin elastic sheets at finite strain. *Journal of the Mechanics and Physics of Solids*, 62:163–180, jan 2014. ISSN 0022-5096. doi: 10.1016/J.JMPS.2013.09.024.

[78] C. Fu, T. Wang, F. Xu, Y. Huo, and M. Potier-Ferry. A modeling and resolution framework for wrinkling in hyperelastic sheets at finite membrane strain. *Journal of the Mechanics and Physics of Solids*, 124:446–470, mar 2019. ISSN 0022-5096. doi: 10.1016/J.JMPS.2018.11.005.

[79] Y .P. Cao, X. P. Zheng, F. Jia, and X. Q. Feng. Wrinkling and creasing of a compressed elastoplastic film resting on a soft substrate. *Computational Materials Science*, 57:111–117, may 2012. ISSN 0927-0256. doi: 10.1016/J.COMMATSCI.2011.02.038.

[80] Y. J. Ning, Z. C. Zhang, B. Gu, Alamusi, and F. Jia. Surface instability and wrinkling pattern evolution on a fluid-supported inhomogeneous film. *The European Physical Journal Plus*, 132(4):170, apr 2017. ISSN 2190-5444. doi: 10.1140/epjp/i2017-11448-2.

[81] A. Javili, B. Dortdivanlioglu, E. Kuhl, and C. Linder. Computational aspects of growth-induced instabilities through eigenvalue analysis. *Computational Mechanics*, 2015. ISSN 01787675. doi: 10.1007/s00466-015-1178-6.

[82] B. Dortdivanlioglu, A. Javili, and C. Linder. Computational aspects of morphological instabilities using isogeometric analysis. *Computer Methods in Applied Mechanics and Engineering*, 2017. ISSN 00457825. doi: 10.1016/j.cma.2016.06.028.

[83] T.J.R. Hughes, J.A. Cottrell, and Y. Bazilevs. Isogeometric analysis: CAD, finite elements, NURBS, exact geometry and mesh refinement. *Computer Methods in Applied Mechanics and Engineering*, 194 (39-41):4135–4195, oct 2005. ISSN 0045-7825. doi: 10.1016/J.CMA.2004.10.008.

[84] J. Austin Cottrell, Thomas J.R. Hughes, and Y. Bazilevs. *Isogeometric Analysis: Toward Integration of CAD and FEA*. Wiley, 2009. ISBN 9780470748732. doi: 10.1002/9780470749081.

[85] V. P. Nguyen, C. Anitescu, S. P. A. Bordas, and T. Rabczuk. Isogeometric analysis: An overview and computer implementation aspects. *Mathematics and Computers in Simulation*, 117:89–116, nov 2015. ISSN 0378-4754. doi: 10.1016/J.MATCOM.2015.05.008.

[86] M. C. Hsu, D. Kamensky, F. Xu, J. Kiendl, C. Wang, M. C. H. Wu, J. Mineroff, A. Reali, Y. Bazilevs, and M. S. Sacks. Dynamic and fluid–structure interaction simulations of bioprosthetic heart valves using parametric design with T-splines and Fung-type material models. *Computational Mechanics*, 55(6):1211–1225, jun 2015. ISSN 01787675. doi: 10.1007/s00466-015-1166-x.

[87] J. Kiendl, K.-U. Bletzinger, J. Linhard, and R. Wüchner. Isogeometric shell analysis with Kirchhoff–Love elements. *Computer Methods in Applied Mechanics and Engineering*, 198(49-52):3902–3914, nov 2009. ISSN 0045-7825. doi: 10.1016/J.CMA.2009.08.013.

[88] J. Kiendl, Y. Bazilevs, M.-C. Hsu, R. Wüchner, and K.-U. Bletzinger. The bending strip method for isogeometric analysis of Kirchhoff–Love shell structures comprised of multiple patches. *Computer Methods in Applied Mechanics and Engineering*, 199(37-40):2403–2416, aug 2010. ISSN 0045-7825. doi: 10.1016/J.CMA.2010.03.029.

[89] J. Kiendl, M.-C. Hsu, M. C. H. Wu, and A. Reali. Isogeometric Kirchhoff–Love shell formulations for general hyperelastic materials. *Computer Methods in Applied Mechanics and Engineering*, 291:280–303, jul 2015. ISSN 0045-7825. doi: 10.1016/J.CMA.2015.03.010.

[90] L. Coox, F. Maurin, F. Greco, E. Deckers, D. Vandepitte, and W. Desmet. A flexible approach for coupling NURBS patches in rotationless isogeometric analysis of Kirchhoff–Love shells. *Computer Methods in Applied Mechanics and Engineering*, 325:505–531, oct 2017. ISSN 0045-7825. doi: 10.1016/J.CMA.2017.07.022.

[91] L. Coox, F. Greco, O. Atak, D. Vandepitte, and W. Desmet. A robust patch coupling method for NURBS-based isogeometric analysis of non-conforming multipatch surfaces. *Computer Methods in Applied Mechanics and Engineering*, 316:235–260, apr 2017. ISSN 0045-7825. doi: 10.1016/J.CMA.2016.06.022.

[92] F. Roohbakhshan and R. A. Sauer. Efficient isogeometric thin shell formulations for soft biological materials. *Biomechanics and Modeling in Mechanobiology*, 16(5):1569–1597, oct 2017. ISSN 1617-7959. doi: 10.1007/s10237-017-0906-6.

[93] D.J. Benson, Y. Bazilevs, M. C. Hsu, and T. J. R. Hughes. Isogeometric shell analysis: The Reissner–Mindlin shell. *Computer Methods in Applied Mechanics and Engineering*, 199(5-8):276–289, jan 2010. ISSN 0045-7825. doi: 10.1016/J.CMA.2009.05.011.

[94] L. Beirão da Veiga, A. Buffa, C. Lovadina, M. Martinelli, and G. Sangalli. An isogeometric method for the Reissner–Mindlin plate bending problem. *Computer Methods in Applied Mechanics and Engineering*, 209-212:45–53, feb 2012. ISSN 0045-7825. doi: 10.1016/J.CMA.2011.10.009.

[95] J. N. Reddy. *Theory and Analysis of Elastic Plates and Shells, Second Edition*. CRC Press, nov 2006. ISBN 9780849384165. doi: 10.1201/9780849384165.

[96] D.J. Benson, S. Hartmann, Y. Bazilevs, M.-C. Hsu, and T.J.R. Hughes. Blended isogeometric shells. *Computer Methods in Applied Mechanics and Engineering*, 255:133–146, mar 2013. ISSN 0045-7825. doi: 10.1016/J.CMA.2012.11.020.

[97] S.B. Raknes, X. Deng, Y. Bazilevs, D. J. Benson, K. M. Mathisen, and T. Kvamsdal. Isogeometric rotation-free bending-stabilized cables: Statics, dynamics, bending strips and coupling with shells. *Computer Methods in Applied Mechanics and Engineering*, 263:127–143, aug 2013. ISSN 00457825. doi: 10.1016/j.cma.2013.05.005.

[98] S. Thai, N. I. Kim, and J. Lee. Isogeometric cable elements based on B-spline curves. *Meccanica*, 52(4-5): 1219–1237, 2017. ISSN 15729648. doi: 10.1007/s11012-016-0454-7.

[99] S. J. Lee and K. S. Park. Vibrations of Timoshenko beams with isogeometric approach. *Applied Mathematical Modelling*, 37(22):9174–9190, nov 2013. ISSN 0307-904X. doi: 10.1016/J.APM.2013.04.034.

[100] A.-T. Luu, N.-I. Kim, and J. Lee. Isogeometric vibration analysis of free-form Timoshenko curved beams. *Meccanica*, 50(1):169–187, jan 2015. ISSN 0025-6455. doi: 10.1007/s11012-014-0062-3.

[101] O. Weeger, U. Wever, and B. Simeon. Isogeometric analysis of nonlinear Euler-Bernoulli beam vibrations. *Nonlinear Dynamics*, 2013. ISSN 0924090X. doi: 10.1007/s11071-013-0755-5.

[102] A. Cazzani, M. Malagù, and E. Turco. Isogeometric analysis of plane-curved beams. *Mathematics and Mechanics of Solids*, 21(5):562–577, 2016. doi: 10.1177/1081286514531265.

[103] A. Cazzani, M. Malagù, E. Turco, and F. Stochino. Constitutive models for strongly curved beams in the frame of isogeometric analysis. *Mathematics and Mechanics of Solids*, 21(2):182–209, 2016. doi: 10.1177/1081286515577043.

[104] R. Kolman, S. Sorokin, B. Bastl, J. Kopačka, and J. Plešek. Isogeometric analysis of free vibration of simple shaped elastic samples. *The Journal of the Acoustical Society of America*, 137(4):2089–2100, apr 2015. ISSN 0001-4966. doi: 10.1121/1.4916199.

[105] X. C. Qin, C. Y. Dong, F. Wang, and X.Y. Qu. Static and dynamic analyses of isogeometric curvilinearly stiffened plates. *Applied Mathematical Modelling*, 45:336–364, may 2017. ISSN 0307-904X. doi: 10.1016/J.APM.2016.12.035.

[106] T. J. R. Hughes and G. Sangalli. Mathematics of Isogeometric Analysis: A Conspectus. In *Encyclopedia of Computational Mechanics Second Edition*, pages 1–40. John Wiley & Sons, Ltd, Chichester, UK, dec 2017. doi: 10.1002/9781119176817.ecm2100.

[107] S. Shojaee, E. Izadpanah, N. Valizadeh, and J. Kiendl. Free vibration analysis of thin plates by using a NURBS-based isogeometric approach. *Finite Elements in Analysis and Design*, 61:23–34, nov 2012. ISSN 0168-874X. doi: 10.1016/J.FINEL.2012.06.005.

[108] N. Valizadeh, T. Q. Bui, V. T. Vu, H. T. Thai, and M. N. Nguyen. Isogeometric Simulation for Buckling, Free and Forced Vibration of Orthotropic Plates. *International Journal of Applied Mechanics*, 05(02): 1350017, jun 2013. ISSN 1758-8251. doi: 10.1142/S1758825113500178.

[109] C. H. Thai, H. Nguyen-Xuan, N. Nguyen-Thanh, T. H. Le, T. Nguyen-Thoi, and T. Rabczuk. Static, free vibration, and buckling analysis of laminated composite Reissner-Mindlin plates using NURBS-based isogeometric approach. *International Journal for Numerical Methods in Engineering*, 91(6):571–603, aug 2012. ISSN 00295981. doi: 10.1002/nme.4282.

[110] S. Shojaee, N. Valizadeh, E. Izadpanah, T. Bui, and T. V. Vu. Free vibration and buckling analysis of laminated composite plates using the NURBS-based isogeometric finite element method. *Composite Structures*, 94(5):1677–1693, apr 2012. ISSN 0263-8223. doi: 10.1016/J.COMPSTRUCT.2012.01.012.

[111] Y. Guo, H. Do, and M. Ruess. Isogeometric stability analysis of thin shells: From simple geometries to engineering models. *International Journal for Numerical Methods in Engineering*, jan 2019. ISSN 00295981. doi: 10.1002/nme.6020.

[112] K. Luo, C. Liu, Q. Tian, and H. Hu. An efficient model reduction method for buckling analyses of thin shells based on IGA. *Computer Methods in Applied Mechanics and Engineering*, 309:243–268, sep 2016. ISSN 0045-7825. doi: 10.1016/J.CMA.2016.06.006.

[113] D. J. Benson, Y. Bazilevs, M. C. Hsu, and T. J. R. Hughes. A large deformation, rotation-free, isogeometric shell. *Computer Methods in Applied Mechanics and Engineering*, 200(13-16):1367–1378, mar 2011. ISSN 0045-7825. doi: 10.1016/J.CMA.2010.12.003.

[114] D. Wang, W. Liu, and H. Zhang. Novel higher order mass matrices for isogeometric structural vibration analysis. *Computer Methods in Applied Mechanics and Engineering*, 260:92–108, jun 2013. ISSN 0045-7825. doi: 10.1016/J.CMA.2013.03.011.

[115] İ. Temizer, P. Wriggers, and T. J. R. Hughes. Contact treatment in isogeometric analysis with NURBS. *Computer Methods in Applied Mechanics and Engineering*, 200(9-12):1100–1112, feb 2011. ISSN 0045-7825. doi: 10.1016/J.CMA.2010.11.020.

[116] J. Lu and C. Zheng. Dynamic cloth simulation by isogeometric analysis. *Computer Methods in Applied Mechanics and Engineering*, 268:475–493, jan 2014. ISSN 0045-7825. doi: 10.1016/J.CMA.2013.09.016.

[117] M. Ambati, J. Kiendl, and L. De Lorenzis. Isogeometric Kirchhoff–Love shell formulation for elasto-plasticity. *Computer Methods in Applied Mechanics and Engineering*, 340:320–339, oct 2018. ISSN 0045-7825. doi: 10.1016/J.CMA.2018.05.023.

[118] K. Li, W. Gao, D. Wu, C. Song, and T. Chen. Spectral stochastic isogeometric analysis of linear elasticity. *Computer Methods in Applied Mechanics and Engineering*, 332:157–190, apr 2018. ISSN 0045-7825. doi: 10.1016/J.CMA.2017.12.012.

[119] K. Li, D. Wu, W. Gao, and C. Song. Spectral stochastic isogeometric analysis of free vibration. *Computer Methods in Applied Mechanics and Engineering*, 350:1–27, jun 2019. ISSN 0045-7825. doi: 10.1016/J.CMA.2019.03.008.

[120] K. Li, D. Wu, and W. Gao. Spectral stochastic isogeometric analysis for linear stability analysis of plate. *Computer Methods in Applied Mechanics and Engineering*, 352:1–31, aug 2019. ISSN 0045-7825. doi: 10.1016/J.CMA.2019.04.009.

[121] T. J. R. Hughes, A. Reali, and G. Sangalli. Duality and unified analysis of discrete approximations in structural dynamics and wave propagation: Comparison of p-method finite elements with k-method NURBS. *Computer Methods in Applied Mechanics and Engineering*, 197(49-50):4104–4124, sep 2008. ISSN 00457825. doi: 10.1016/j.cma.2008.04.006.

[122] F. Auricchio, M. Conti, M. Ferraro, S. Morganti, A. Reali, and R. L. Taylor. Innovative and efficient stent flexibility simulations based on isogeometric analysis. *Computer Methods in Applied Mechanics and Engineering*, 295:347–361, oct 2015. ISSN 00457825. doi: 10.1016/j.cma.2015.07.011.

[123] S. Morganti, F. Auricchio, D. J. Benson, F. I. Gambarin, S. Hartmann, T. J.R. Hughes, and A. Reali. Patient-specific isogeometric structural analysis of aortic valve closure. *Computer Methods in Applied Mechanics and Engineering*, 284:508–520, feb 2015. ISSN 00457825. doi: 10.1016/j.cma.2014.10.010.

[124] T. W. Sederberg, J. Zheng, A. Bakenov, and A. Nasri. T-splines and T-NURCCs. *ACM Transactions on Graphics*, 22(3):477, 2003. ISSN 07300301. doi: 10.1145/882262.882295.

[125] Y. Bazilevs, V. M. Calo, J. A. Cottrell, J. A. Evans, T. J. R. Hughes, S. Lipton, M. A. Scott, and T. W. Sederberg. Isogeometric analysis using T-splines. *Computer Methods in Applied Mechanics and Engineering*, 2010. ISSN 00457825. doi: 10.1016/j.cma.2009.02.036.

[126] M. R. Dörfel, B. Jüttler, and B. Simeon. Adaptive isogeometric analysis by local h-refinement with T-splines. *Computer Methods in Applied Mechanics and Engineering*, 199(5-8):264–275, jan 2010. ISSN 0045-7825. doi: 10.1016/J.CMA.2008.07.012.

[127] A. V. Vuong, C. Giannelli, B. Jüttler, and B. Simeon. A hierarchical approach to adaptive local refinement in isogeometric analysis. *Computer Methods in Applied Mechanics and Engineering*, 200(49-52):3554–3567, dec 2011. ISSN 0045-7825. doi: 10.1016/J.CMA.2011.09.004.

[128] C. Giannelli, B. Jüttler, and H. Speleers. THB-splines: The truncated basis for hierarchical splines. *Computer Aided Geometric Design*, 29(7):485–498, oct 2012. ISSN 0167-8396. doi: 10.1016/J.CAGD.2012.03.025.

[129] M. Carraturo, C. Giannelli, A. Reali, and R. Vázquez. Suitably graded THB-spline refinement and coarsening: Towards an adaptive isogeometric analysis of additive manufacturing processes. *Computer Methods in Applied Mechanics and Engineering*, 348:660–679, may 2019. ISSN 0045-7825. doi: 10.1016/J.CMA.2019.01.044.

[130] C. Giannelli, B. Jüttler, S. K. Kleiss, A. Mantzaflaris, B. Simeon, and J. Špeh. THB-splines: An effective mathematical technology for adaptive refinement in geometric design and isogeometric analysis. *Computer Methods in Applied Mechanics and Engineering*, 299:337–365, feb 2016. ISSN 0045-7825. doi: 10.1016/J.CMA.2015.11.002.

[131] M. Bischoff, E. Ramm, and J. Irslinger. Models and Finite Elements for Thin-Walled Structures. In *Encyclopedia of Computational Mechanics Second Edition*, pages 1–86. John Wiley & Sons, Ltd, Chichester, UK, dec 2017. doi: 10.1002/9781119176817.ecm2026.

[132] T. J. R. Hughes, A. Reali, and G. Sangalli. Efficient quadrature for NURBS-based isogeometric analysis. *Computer Methods in Applied Mechanics and Engineering*, 2010. ISSN 00457825. doi: 10.1016/j.cma.2008.12.004.

[133] F. Auricchio, F. Calabrò, T. J. R. Hughes, A. Reali, and G. Sangalli. A simple algorithm for obtaining nearly optimal quadrature rules for NURBS-based isogeometric analysis. *Computer Methods in Applied Mechanics and Engineering*, 2012. ISSN 00457825. doi: 10.1016/j.cma.2012.04.014.

[134] N. Collier, D. Pardo, L. Dalcin, M. Paszynski, and V. M. Calo. The cost of continuity: A study of the performance of isogeometric finite elements using direct solvers. *Computer Methods in Applied Mechanics and Engineering*, 213-216:353–361, mar 2012. ISSN 0045-7825. doi: 10.1016/J.CMA.2011.11.002.

[135] N. Collier, L. Dalcin, D. Pardo, and V. M. Calo. The Cost of Continuity: Performance of Iterative Solvers on Isogeometric Finite Elements. *SIAM Journal on Scientific Computing*, 35(2):A767–A784, jan 2013. ISSN 1064-8275. doi: 10.1137/120881038.

[136] D. Garcia, D. Pardo, L. Dalcin, M. Paszyński, N. Collier, and V. M. Calo. The value of continuity: Refined isogeometric analysis and fast direct solvers. *Computer Methods in Applied Mechanics and Engineering*, 316:586–605, apr 2017. ISSN 00457825. doi: 10.1016/j.cma.2016.08.017.

[137] J. Kiendl. *Isogeometric analysis and shape optimal design of shell structures.* PhD thesis, Technische Universität München, 2011.

[138] G. Holzapfel. *Nonlinear solid mechanics: A continuum approach for engineering.* John Wiley & Sons, Ltd, 2000. ISBN 0471823198. doi: 10.1023/A:1020843529530.

[139] J. Stewart. *Calculus*, volume 8th edition. Cengage Learning, 2015. ISBN 1285740629.

[140] J. N. Reddy. *An Introduction to Nonlinear Finite Element Analysis, 2nd Edn.* Oxford University Press, oct 2014. ISBN 9780199641758. doi: 10.1093/acprof:oso/9780199641758.001.0001.

[141] Y. Başar and D. Weichert. *Nonlinear Continuum Mechanics of Solids.* Springer, 2013. doi: 10.1007/978-3-662-04299-1.

[142] A. Goyal. *Isogeometric Shell Discretizations for Flexible Multibody Dynamics.* doctoralthesis, Technische Universität Kaiserslautern, 2015.

[143] M. H. Sadd. *Elasticity : theory, applications, and numerics.* Elsevier/Academic Press, 2009. ISBN 0080922414.

[144] T. J. R. Hughes. *Finite Element Method : Linear Static and Dynamic Finite Element Analysis.* Dover Publications, 2012. ISBN 9781306348782.

[145] B. Dacorogna. *Introduction to the Calculus of Variations.* World Scientific Publishing Company, 2014. doi: 10.1142/p967.

[146] K. W. Cassel. *Variational methods with applications to science and engineering.* Cambridge University Press, 2013. ISBN 9781107022584.

[147] R. A. Horn and C. R. Johnson. *Matrix Analysis.* Cambridge University Press, New York, NY, USA, 2nd edition, 2012. ISBN 0521548233, 9780521548236.

[148] D. Schillinger, S. J. Hossain, and T. J.R. Hughes. Reduced Bézier element quadrature rules for quadratic and cubic splines in isogeometric analysis. *Computer Methods in Applied Mechanics and Engineering*, 277:1–45, aug 2014. ISSN 0045-7825. doi: 10.1016/J.CMA.2014.04.008.

[149] L. H. Nguyen and D. Schillinger. A collocated isogeometric finite element method based on Gauss–Lobatto Lagrange extraction of splines. *Computer Methods in Applied Mechanics and Engineering*, 316:720–740, apr 2017. ISSN 0045-7825. doi: 10.1016/J.CMA.2016.09.036.

[150] M. Abramowitz, I. A. Stegun, and D. Miller. Handbook of Mathematical Functions With Formulas, Graphs and Mathematical Tables (National Bureau of Standards Applied Mathematics Series No. 55). *Journal of Applied Mechanics*, 1965. ISSN 00218936. doi: 10.1115/1.3625776.

[151] R. C. Hibbeler. *Mechanics of Materials.* Pearson, 2011. ISBN 9780136022305. doi: 10.1017/CBO9781107415324.004.

[152] R. W. Ogden. *Non-linear elastic deformations.* Dover Publications, 1997. ISBN 9780486696485.

[153] A. N. Gent. *Engineering with Rubber: How to design rubber components.* Hanser Publications, Cincinnati, 2012. ISBN 978-3-446-42764-8. doi: 10.3139/9783446428713.

[154] C. De Boor. On calculating with B-splines. *Journal of Approximation theory*, 6(1):50–62, 1972.

[155] M. G. Cox. The numerical evaluation of B-splines. *IMA Journal of Applied Mathematics*, 10(2):134–149, 1972.

[156] L. Piegl and W. Tiller. A Menagerie of Rational B-Spline Circles. *IEEE Computer Graphics and Applications*, 1989. ISSN 02721716. doi: 10.1109/38.35537.

[157] B. Jüttler, U. Langer, A. Mantzaflaris, S. E. Moore, and W. Zulehner. Geometry + Simulation Modules: Implementing Isogeometric Analysis. *PAMM*, 14(1):961–962, dec 2014. ISSN 16177061. doi: 10.1002/pamm.201410461.

[158] P. Wriggers. *Nonlinear finite element methods.* Springer, 2008. ISBN 9783540710004. doi: 10.1007/978-3-540-71001-1.

[159] R. de Borst, M. A. Crisfield, J. J.C. Remmers, and C. V. Verhoosel. *Non-Linear Finite Element Analysis of Solids and Structures: Second Edition.* Wiley, 2012. ISBN 9780470666449. doi: 10.1002/9781118375938.

[160] R. J. Roark, W. C. Young, R. G. Budynas, and A. M. Sadegh. *Roark's formulas for stress and strain.* McGraw-Hill, 2012. ISBN 0071742476.

[161] B. Brendel and E. Ramm. Nichtlineare Stabilitätsuntersuchungen mit der Methode der Finiten Elemente. *Ingenieur-Archiv*, 51(5):337–362, 1982. ISSN 00201154. doi: 10.1007/BF00536659.

[162] E. Riks. The Application of Newton's Method to the Problem of Elastic Stability. *Journal of Applied Mechanics*, 39(4):1060, 1972. ISSN 00218936. doi: 10.1115/1.3422829.

[163] M.A. Crisfield. A Fast Incremental/Iterative Solution Procedure That Handles "Snap-Throug". In *Computational Methods in Nonlinear Structural and Solid Mechanics*, pages 55–62. Pergamon, jan 1981. ISBN 9780080272993. doi: 10.1016/B978-0-08-027299-3.50009-1.

[164] M. A. Crisfield. *Non-linear finite element analysis of solids and structures - Volume 1: Essentials*. John Wiley & Sons, Ltd, 1991. ISBN 9780471929567.

[165] M. A. Crisfield. *Non-linear finite element analysis of solids and structures - Volume 2: Advanced topics*. John Wiley & Sons, Ltd, 1997. ISBN 978-0471956495.

[166] M. Fafard and B. Massicotte. Geometrical interpretation of the arc-length method. *Computers & Structures*, 46(4):603–615, feb 1993. ISSN 0045-7949. doi: 10.1016/0045-7949(93)90389-U.

[167] E. Carrera. A study on arc-length-type methods and their operation failures illustrated by a simple model. *Computers & Structures*, 50(2):217–229, jan 1994. ISSN 0045-7949. doi: 10.1016/0045-7949(94)90297-6.

[168] B. A. Memon and X. Z. Su. Arc-length technique for nonlinear finite element analysis. *Journal of Zhejiang University-SCIENCE A*, 5(5):618–628, may 2004. ISSN 1673-565X. doi: 10.1631/jzus.2004.0618.

[169] H. B. Hellweg and M. A. Crisfield. A new arc-length method for handling sharp snap-backs. *Computers & Structures*, 66(5):704–709, mar 1998. ISSN 0045-7949. doi: 10.1016/S0045-7949(97)00077-1.

[170] K. H. Schweizerhof and P. Wriggers. Consistent linearization for path following methods in nonlinear fe analysis. *Computer Methods in Applied Mechanics and Engineering*, 59(3):261–279, dec 1986. ISSN 0045-7825. doi: 10.1016/0045-7825(86)90001-0.

[171] P. X. Bellini and A. Chulya. An improved automatic incremental algorithm for the efficient solution of nonlinear finite element equations. *Computers & Structures*, 26(1-2):99–110, jan 1987. ISSN 0045-7949. doi: 10.1016/0045-7949(87)90240-9.

[172] E. Riks. Some computational aspects of the stability analysis of nonlinear structures. *Computer Methods in Applied Mechanics and Engineering*, 47(3):219–259, dec 1984. ISSN 0045-7825. doi: 10.1016/0045-7825(84)90078-1.

[173] M. Ritto-Corrêa and D. Camotim. On the arc-length and other quadratic control methods: Established, less known and new implementation procedures. *Computers & Structures*, 86(11-12):1353–1368, jun 2008. ISSN 0045-7949. doi: 10.1016/J.COMPSTRUC.2007.08.003.

[174] Y. T. Feng, D. Perić, and D. R. J. Owen. Determination of travel directions in path-following methods. *Mathematical and Computer Modelling*, 21(7):43–59, apr 1995. ISSN 0895-7177. doi: 10.1016/0895-7177(95)00030-6.

[175] Y. T. Feng, D. Perić, and D. R. J. Owen. A new criterion for determination of initial loading parameter in arc-length methods. *Computers & Structures*, 58(3):479–485, feb 1996. ISSN 0045-7949. doi: 10.1016/0045-7949(95)00168-G.

[176] Y. T. Feng, D. R. J. Owen, and D. Perić. On the Sign of the Determinant of the Structural Stiffness Matrix for Determination of Loading Increment in Arc-Length Algorithms. *Communications in Numerical Methods in Engineering*, 13(1):47–49, jan 1997. ISSN 10698299. doi: 10.1002/(SICI)1099-0887(199701)13:1<47::AID-CNM49>3.0.CO;2-J.

[177] W. F. Lam and C. T. Morley. Arc-Length Method for Passing Limit Points in Structural Calculation. *Journal of Structural Engineering*, 118(1):169–185, jan 1992. ISSN 0733-9445. doi: 10.1061/(ASCE)0733-9445(1992)118:1(169).

[178] Z. Zhou and D. W. Murray. An incremental solution technique for unstable equilibrium paths of shell structures. *Computers & Structures*, 55(5):749–759, jun 1995. ISSN 0045-7949. doi: 10.1016/0045-7949(94)00474-H.

[179] M. A. Crisfield. An arc-length method including line searches and accelerations. *International Journal for Numerical Methods in Engineering*, 19(9):1269–1289, sep 1983. ISSN 0029-5981. doi: 10.1002/nme.1620190902.

[180] P. Wriggers and J. C. Simo. A general procedure for the direct computation of turning and bifurcation points. *International Journal for Numerical Methods in Engineering*, 30(1):155–176, jul 1990. ISSN 0029-5981. doi: 10.1002/nme.1620300110.

[181] W. Wagner and P. Wriggers. A simple method for the calculation of postcritical branches. *Engineering computations*, 5(2):103–109, 1988.

[182] R. L. Burden, J. D. Faires, and A. M. Burden. *Numerical analysis*. Cengage Learning, 10th edition, 2015. ISBN 978-1305253667.

[183] P. Wriggers, W. Wagner, and C. Miehe. A quadratically convergent procedure for the calculation of stability points in finite element analysis. *Computer Methods in Applied Mechanics and Engineering*, 70(3):329–347, oct 1988. ISSN 0045-7825. doi: 10.1016/0045-7825(88)90024-2.

[184] J. Shi. Computing critical points and secondary paths in nonlinear structural stability analysis by the finite element method. *Computers & Structures*, 58(1):203–220, jan 1996. ISSN 0045-7949. doi: 10.1016/0045-7949(95)00114-V.

[185] F. Zhi-Fang and H. Jimin. *Modal Analysis*. Butterworth-Heinemann, 2001. ISBN 0750650796.

[186] J. A. Cottrell, A. Reali, and Y. Bazilevs. Isogeometric analysis of structural vibrations. *Computer Methods in Applied Mechanics and Engineering*, 195(41-43):5257–5296, aug 2006. ISSN 0045-7825. doi: 10.1016/J.CMA.2005.09.027.

[187] K. Subbaraj and M. A. Dokainish. A survey of direct time-integration methods in computational structural dynamics-II. Implicit methods. *Computers and Structures*, 1989. ISSN 00457949. doi: 10.1016/0045-7949(89)90315-5.

[188] M. A. Dokainish and K. Subbaraj. A survey of direct time-integration methods in computational structural dynamics—I. Explicit methods. *Computers & Structures*, 32(6):1371–1386, 1989. ISSN 0045-7949. doi: https://doi.org/10.1016/0045-7949(89)90314-3.

[189] E. Hairer, S. P. Nørsett, and G. Wanner. *Solving Ordinary Differential Equations I. Nonstiff Problems*, volume 8. Springer-Verlag Berlin Heidelberg, 2 edition, 1993. ISBN 978-3-540-56670-0. doi: 10.1007/978-3-540-78862-1.

[190] J. C. Butcher. *Numerical Methods for Ordinary Differential Equations*. John Wiley & Sons, Ltd, 2016. ISBN 9781119121534. doi: 10.1002/9781119121534.

[191] C. Vuik, P. Van Beek, F. J. Vermolen, and J. Van Kan. *Numerical Methods for Ordinary differential equations*. VSSD, 2007.

[192] C. A. Felippa and K. C. Park. Direct time integration methods in nonlinear structural dynamics. *Computer Methods in Applied Mechanics and Engineering*, 17-18:277–313, feb 1979. ISSN 0045-7825. doi: 10.1016/0045-7825(79)90023-9.

[193] J. C. Butcher. On Runge-Kutta processes of high order. *Journal of the Australian Mathematical Society*, 1964. ISSN 14468107. doi: 10.1017/S1446788700023387.

[194] W. Kutta. Beitrag zur näherungweisen Integration totaler Differentialgleichungen. *Mathematical Physics*, 46:435–453, 1901.

[195] A.H. van Zuijlen. *Fluid-structure interaction simulations: Efficient higher order time integration of partitioned systems*. PhD thesis, Delft University of Technology, 2006.

[196] A. Kanevsky, M. H. Carpenter, D. Gottlieb, and J. S. Hesthaven. Application of implicit–explicit high order Runge–Kutta methods to discontinuous-Galerkin schemes. *Journal of Computational Physics*, 225 (2):1753–1781, aug 2007. ISSN 0021-9991. doi: 10.1016/J.JCP.2007.02.021.

[197] N. M. Newmark. A Method of Computation for Structural Dynamics. *J. Engng. Mech.*, 1959. ISSN 0044-7951. doi: 0.1016/j.compgeo.2015.08.008.

[198] K. J. Bathe and M. M. I. Baig. On a composite implicit time integration procedure for nonlinear dynamics. *Computers & Structures*, 83(31-32):2513–2524, dec 2005. ISSN 0045-7949. doi: 10.1016/J.COMPSTRUC.2005.08.001.

[199] E. L. Wilson, I. Farhoomand, and K. J. Bathe. Nonlinear Dynamic Analysis of Complex Structures. *Earthquake Engineering and Structural Dynamics*, 1(3):241–252, 1973. ISSN 00988847. doi: 10.1191/030913201680191745.

[200] K. J. Bathe. Conserving energy and momentum in nonlinear dynamics: A simple implicit time integration scheme. *Computers & Structures*, 85(7-8):437–445, apr 2007. ISSN 0045-7949. doi: 10.1016/J.COMPSTRUC.2006.09.004.

[201] K. J. Bathe. On reliable finite element methods for extreme loading conditions. In *NATO Security through Science Series C: Environmental Security*, 2007. ISBN 1402056540. doi: 10.1007/978-1-4020-5656-7_3.

[202] K. J. Bathe and G. Noh. Insight into an implicit time integration scheme for structural dynamics. *Computers & Structures*, 98-99:1–6, may 2012. ISSN 0045-7949. doi: 10.1016/J.COMPSTRUC.2012.01.009.

[203] G. Noh and K. J. Bathe. Further insights into an implicit time integration scheme for structural dynamics. *Computers & Structures*, 202:15–24, jun 2018. ISSN 0045-7949. doi: 10.1016/J.COMPSTRUC.2018.02.007.

[204] P. J. Roache. Code Verification by the Method of Manufactured Solutions. *Journal of Fluids Engineering*, 2002. ISSN 00982202. doi: 10.1115/1.1436090.

[205] I. Babuska and J. T. Oden. Verification and validation in computational engineering and science: Basic concepts. *Computer Methods in Applied Mechanics and Engineering*, 2004. ISSN 00457825. doi: 10.1016/j.cma.2004.03.002.

[206] B. H. Thacker, S. W. Doebling, F. M. Hemez, M. C. Anderson, Jason E. P., and E. A. Rodriguez. Concepts of Model Verification and Validation. *Concepts of Model Verification and Validation*, 2004. doi: 10.2172/835920.

[207] T. Belytschko, H. Stolarski, W. K. Liu, N. Carpenter, and J. S. J. Ong. Stress projection for membrane and shear locking in shell finite elements. *Computer Methods in Applied Mechanics and Engineering*, 1985. ISSN 00457825. doi: 10.1016/0045-7825(85)90035-0.

[208] L. F. Richardson. The Approximate Arithmetical Solution by Finite Differences of Physical Problems Involving Differential Equations, with an Application to the Stresses in a Masonry Dam. *Philosophical Transactions of the Royal Society A: Mathematical, Physical and Engineering Sciences*, 210(459-470):307–357, jan 1911. ISSN 1364-503X. doi: 10.1098/rsta.1911.0009.

[209] L. Coox, F. Maurin, F. Greco, E. Deckers, D. Vandepitte, and W. Desmet. A flexible approach for coupling NURBS patches in rotationless isogeometric analysis of Kirchhoff–Love shells. *Computer Methods in Applied Mechanics and Engineering*, 325:505–531, oct 2017. ISSN 0045-7825. doi: 10.1016/J.CMA.2017.07.022.

[210] N. Nguyen-Thanh, J. Kiendl, H. Nguyen-Xuan, R. Wüchner, K.U. Bletzinger, Y. Bazilevs, and T. Rabczuk. Rotation free isogeometric thin shell analysis using PHT-splines. *Computer Methods in Applied Mechanics and Engineering*, 200(47-48):3410–3424, nov 2011. ISSN 0045-7825. doi: 10.1016/J.CMA.2011.08.014.

[211] R. Bouzidi, Y. Ravaut, and Christian Wielgosz. Finite elements for 2D problems of pressurized membranes. *Computers & Structures*, 81(26-27):2479–2490, oct 2003. ISSN 0045-7949. doi: 10.1016/S0045-7949(03)00308-0.

[212] B. W. Fichter. Some Solutions for the Large Deflections of Uniformly Loaded Circular Membranes. Technical report, NASA Langley Research Center, jul 1997.

[213] T. Y. Wu and E. C. Ting. Large deflection analysis of 3D membrane structures by a 4-node quadrilateral intrinsic element. *Thin-Walled Structures*, 46(3):261–275, mar 2008. ISSN 02638231. doi: 10.1016/j.tws.2007.08.043.

[214] K. Y. Sze, X. H. Liu, and S. H. Lo. Popular benchmark problems for geometric nonlinear analysis of shells. *Finite Elements in Analysis and Design*, 40(11):1551–1569, jul 2004. ISSN 0168-874X. doi: 10.1016/J.FINEL.2003.11.001.

[215] Y. Zhou, I. Stanciulescu, T. Eason, and M. Spottswood. Nonlinear elastic buckling and postbuckling analysis of cylindrical panels. *Finite Elements in Analysis and Design*, 96:41–50, apr 2015. ISSN 0168-874X. doi: 10.1016/J.FINEL.2014.12.001.

[216] A. Pagani and E. Carrera. Unified formulation of geometrically nonlinear refined beam theories. *Mechanics of Advanced Materials and Structures*, 25(1):15–31, jan 2018. ISSN 15376532. doi: 10.1080/15376494.2016.1232458.

[217] D. P. Mondkar and G. H. Powell. Finite element analysis of non-linear static and dynamic response. *International Journal for Numerical Methods in Engineering*, 11(3):499–520, jan 1977. ISSN 10970207. doi: 10.1002/nme.1620110309.

[218] J. Yang and P. Xia. Corotational Nonlinear Dynamic Analysis of Thin-Shell Structures with Finite Rotations. *AIAA Journal*, 53(3):663–677, mar 2014. ISSN 0001-1452. doi: 10.2514/1.j053147.

[219] L. A. D. Filho and A. M. Awruch. Geometrically nonlinear static and dynamic analysis of shells and plates using the eight-node hexahedral element with one-point quadrature. *Finite Elements in Analysis and Design*, 2004. ISSN 0168874X. doi: 10.1016/j.finel.2003.08.012.

[220] P. Wang, H. Chalal, and F. Abed-Meraim. Simulation of nonlinear benchmarks and sheet metal forming processes using linear and quadratic solid–shell elements combined with advanced anisotropic behavior models. *MATEC Web of Conferences*, 2016. doi: 10.1051/matecconf/20168007001.

[221] H. Warlimont and W. Martienssen, editors. *Springer Handbook of Materials Data*. Springer Handbooks. Springer International Publishing, Cham, 2018. ISBN 978-3-319-69741-3. doi: 10.1007/978-3-319-69743-7.

[222] T. Iwasa. Experimental verification on simplified estimation method for envelope curve of wrinkled membrane surface distortions. *Thin-Walled Structures*, 122:622–634, jan 2018. ISSN 0263-8231. doi: 10.1016/J.TWS.2017.10.049.

[223] C. G. Wang, Y. P. Liu, L. Lan, L. Li, and H. F. Tan. Post-wrinkling analysis of a torsionally sheared annular thin film by using a compound series method. *International Journal of Mechanical Sciences*, 110:22–33, may 2016. ISSN 0020-7403. doi: 10.1016/J.IJMECSCI.2016.02.011.

[224] Q. Wang and X. Zhao. A three-dimensional phase diagram of growth-induced surface instabilities. *Scientific Reports*, 5(1):8887, aug 2015. ISSN 2045-2322. doi: 10.1038/srep08887.

[225] A. Shamanskiy, M. H. Gfrerer, J. Hinz, and B. Simeon. Isogeometric Parametrization Inspired by Large Elastic Deformation. http://arxiv.org/abs/1810.12425, oct 2019.

[226] N. Hosters, J. Helmig, A. Stavrev, M. Behr, and S. Elgeti. Fluid–structure interaction with NURBS-based coupling. *Computer Methods in Applied Mechanics and Engineering*, 332:520–539, apr 2018. ISSN 00457825. doi: 10.1016/j.cma.2018.01.003.

[227] R. Haberman. *Applied partial differential equations with Fourier series and boundary value problems.* Pearson Higher Ed, 2012.

[228] J. N. Reddy. *Principles of Continuum Mechanics.* Cambridge University Press, Cambridge, 2010. ISBN 9780511763212. doi: 10.1017/CBO9780511763212.

[229] E. Jones, T. Oliphant, and P. Peterson. ${$SciPy$}$: Open source scientific tools for ${$Python$}$, 2014.

A | Differential Geometry Examples

In this section, the derivation of the covariant and contravariant bases of two surface descriptions will be given. These are based on the formulations in Section 3.1.

A.1 Polar Coordinates

A circular surface can be described by polar coordinates. Here, we consider a quarter circle, which is described by an angular coordinate ϕ and by a radial coordinate r (the parameters are also denoted by $\theta = (\theta_1, \theta_2) = (\phi, r)$):

$$\mathbf{S}(\theta_1, \theta_2) = \begin{bmatrix} r(\theta_2)\cos\left(\phi(\theta_1)\right) \\ r(\theta_2)\sin\left(\phi(\theta_1)\right) \end{bmatrix} \qquad r \in \mathbb{R}^+,\ \phi \in [0, \pi/2] \tag{A.1}$$

The covariant basis vectors are the vectors $\mathbf{a}_\alpha = \frac{\partial \mathbf{S}}{\partial \theta_\alpha}$. This gives:

$$\mathbf{a}_1 = \begin{bmatrix} \frac{\partial S_1}{\partial \theta_1} \\ \frac{\partial S_2}{\partial \theta_1} \end{bmatrix} = \mathbf{a}_1 = \begin{bmatrix} -r\sin(\phi) \\ r\cos(\phi) \end{bmatrix}$$

$$\mathbf{a}_2 = \begin{bmatrix} \frac{\partial S_1}{\partial \theta_2} \\ \frac{\partial S_2}{\partial \theta_2} \end{bmatrix} = \begin{bmatrix} \cos(\phi) \\ \sin(\phi) \end{bmatrix}$$

The covariant metric tensor $[g_{\alpha\beta}]$ is a second-order tensor containing inner-products of the covariant basis vectors:

$$\begin{aligned} g_{11} &= \mathbf{a}_1 \cdot \mathbf{a}_1 = r^2 \\ g_{12} &= \mathbf{a}_1 \cdot \mathbf{a}_2 = 0 \\ g_{21} &= \mathbf{a}_2 \cdot \mathbf{a}_1 = 0 \\ g_{22} &= \mathbf{a}_2 \cdot \mathbf{a}_2 = 1 \end{aligned}$$

From these values, it can be seen that the basis is orthogonal, i.e. that the cross-coefficients of the metric tensor are zero. The inverse of the covariant metric tensor yields the contravariant metric tensor $[g^{\alpha\beta}]$. The coefficients are:

$$\begin{aligned} g^{11} &= 1/r^2 \\ g^{12} &= 0 \\ g^{21} &= 0 \\ g^{22} &= 1 \end{aligned}$$

Hence, the contravariant basis is:

$$\mathbf{a}^1 = g^{11}\mathbf{a}_1 + g^{12}\mathbf{a}_2 = \frac{1}{r^2}\begin{bmatrix} -r\sin(\phi) \\ r\cos(\phi) \end{bmatrix} + 0 \cdot \begin{bmatrix} \cos(\phi) \\ \sin(\phi) \end{bmatrix} = \frac{1}{r^2}\begin{bmatrix} -r\sin(\phi) \\ r\cos(\phi) \end{bmatrix}$$

$$\mathbf{a}^2 = g^{21}\mathbf{a}_1 + g^{22}\mathbf{a}_2 = 0 \cdot \begin{bmatrix} -r\sin(\phi) \\ r\cos(\phi) \end{bmatrix} + \begin{bmatrix} \cos(\phi) \\ \sin(\phi) \end{bmatrix} = \frac{1}{r^2}\begin{bmatrix} \cos(\phi) \\ \sin(\phi) \end{bmatrix}$$

It can easily be checked that the products of the covariant and contravariant bases satisfy

$$\mathbf{a}^{\alpha} \cdot \mathbf{a}_{\beta} = \delta_{\alpha}^{\beta} = \begin{cases} 1 & \text{if } \alpha = \beta \\ 0 & \text{if } \alpha \neq \beta \end{cases}$$

A.2 Curvilinear Coordinates

A surface description which is non-orthogonal is given by the following formula:

$$\mathbf{S}(\theta_1, \theta_2) = \begin{bmatrix} (r(\theta_2)+1)\cos(\phi(\theta_1)) \\ \frac{(r(\theta_2)+1)^3}{4}\sin(\phi(\theta_2)) \end{bmatrix} \quad \text{where} \quad \phi(\theta_1) = \frac{\pi}{2}\theta_1 \quad \text{and} \quad r(\theta_2) = \theta_2 \quad \text{(See Equation (3.1))}$$

Here, the coordinates $\phi(\theta_1)$ and $r(\theta_2)$ are equivalents of the angular and radial coordinates of a polar coordinate system and a function of parameters θ_1 and θ_2. The covariant basis vectors are the vectors $\mathbf{a}_{\alpha} = \frac{\partial \mathbf{S}}{\partial \theta_{\alpha}}$. This gives:

$$\mathbf{a}_1 = \begin{bmatrix} \frac{\partial S_1}{\partial \theta_1} \\ \frac{\partial S_2}{\partial \theta_1} \end{bmatrix} = \mathbf{a}_1 = \begin{bmatrix} -\frac{1}{2}(\theta_2+1)\pi\sin\left(\frac{1}{2}\theta_1\pi\right) \\ \frac{1}{8}(\theta_2+1)^3\pi\cos\left(\frac{1}{2}\theta_1\pi\right) \end{bmatrix}$$

$$\mathbf{a}_2 = \begin{bmatrix} \frac{\partial S_1}{\partial \theta_2} \\ \frac{\partial S_2}{\partial \theta_2} \end{bmatrix} = \begin{bmatrix} cos\left(\frac{1}{2}\theta_1\pi\right) \\ \frac{3}{4}(\theta_2+1)^2\sin\left(\frac{1}{2}\theta_1\pi\right) \end{bmatrix}$$

The covariant metric tensor $[g_{\alpha\beta}]$ is a second-order tensor containing inner-products of the covariant basis vectors:

$$g_{11} = \mathbf{a}_1 \cdot \mathbf{a}_1 = \frac{1}{4}(\theta_2+1)^2\pi^2\sin^2\left(\frac{1}{2}\theta_1\pi\right) + \frac{1}{64}(\theta_2+1)^6\pi^2\cos^2\left(\frac{1}{2}\theta_1\pi\right)$$

$$g_{12} = \mathbf{a}_1 \cdot \mathbf{a}_2 = -\frac{1}{2}(\theta_2+1)\pi\sin\left(\frac{1}{2}\theta_1\pi\right)\cos\left(\frac{1}{2}\theta_1\pi\right) + \frac{3}{32}(\theta_2+1)^5\pi\cos\left(\frac{1}{2}\theta_1\pi\right)\sin\left(\frac{1}{2}\theta_1\pi\right)$$

$$g_{21} = \mathbf{a}_2 \cdot \mathbf{a}_1 = -\frac{1}{2}(\theta_2+1)\pi\sin\left(\frac{1}{2}\theta_1\pi\right)\cos\left(\frac{1}{2}\theta_1\pi\right) + \frac{3}{32}(\theta_2+1)^5\pi\cos\left(\frac{1}{2}\theta_1\pi\right)\sin\left(\frac{1}{2}\theta_1\pi\right)$$

$$g_{22} = \mathbf{a}_2 \cdot \mathbf{a}_2 = \cos^2\left(\frac{1}{2} * \theta_1 * \pi\right) + \frac{9}{16}(\theta_2+1)^4\sin^2\left(\frac{1}{2}\theta_1\pi\right)$$

The inverse of the covariant metric tensor yields the contravariant metric tensor $[g^{\alpha\beta}]$. The coefficients are:

$$g^{11} = \frac{\pi^2}{64}(\theta_2^2+2\theta_2+1)\Bigg(\cos^2\left(\frac{1}{2}\theta_1\pi\right)\theta_2^4 + 4\cos^2\left(\frac{1}{2}\theta_1\pi\right)\theta_2^3 + 6\cos^2\left(\frac{1}{2}\theta_1\pi\right)\theta_2^2 + 4\cos^2\left(\frac{1}{2}\theta_1\pi\right)\theta_2$$
$$+ 16\sin^2\left(\frac{1}{2}\theta_1\pi\right) + \cos^2\left(\frac{1}{2}\theta_1\pi\right)\Bigg)$$

$$g^{12} = \frac{\pi}{32}(3\theta_2^4+12\theta_2^3+18\theta_2^2+12\theta_2-13)\pi\sin\left(\frac{1}{2}\theta_1\pi\right)\cos\left(\frac{1}{2}\theta_1\pi\right)(\theta_2+1)$$

$$g^{21} = \frac{\pi}{32}(3\theta_2^4+12\theta_2^3+18\theta_2^2+12\theta_2-13)\pi\sin\left(\frac{1}{2}\theta_1\pi\right)\cos\left(\frac{1}{2}\theta_1\pi\right)(\theta_2+1)$$

$$g^{22} = \frac{9}{16}\sin^2\left(\frac{\theta_1\pi}{2}\right)\theta_2^4 + \frac{9}{4}\sin^2\left(\frac{\theta_1\pi}{2}\right)\theta_2^3 + \frac{27}{8}\sin^2\left(\frac{\theta_1\pi}{2}\right)\theta_2^2 + \frac{9}{4}\sin^2\left(\frac{\theta_1\pi}{2}\right)\theta_2 + \frac{9}{16}\sin^2\left(\frac{\theta_1\pi}{2}\right) + \cos^2\left(\frac{\theta_1\pi}{2}\right)$$

Based on the coefficients of the contravariant metric tensor $[g^{\alpha\beta}]$, the contravariant basis is (after simplification):

$$\mathbf{a}^1 = g^{11}\mathbf{a}_1 + g^{12}\mathbf{a}_2 = \begin{bmatrix} \frac{6\sin\left(\frac{\theta_1\pi}{2}\right)}{\pi\left(2\cos^2\left(\frac{\theta_1\pi}{2}\right)-3\right)(\theta_2+1)} \\ -\frac{8\cos\left(\frac{\theta_1\pi}{2}\right)}{\pi(\theta_2+1)^3\left(2\cos^2\left(\frac{\theta_1\pi}{2}\right)-3\right)} \end{bmatrix}$$

$$\mathbf{a}^2 = g^{21}\mathbf{a}_1 + g^{22}\mathbf{a}_2 = \begin{bmatrix} -\frac{\cos\left(\frac{\theta_1\pi}{2}\right)}{2\cos^2\left(\frac{\theta_1\pi}{2}\right)-3} \\ -\frac{4\sin\left(\frac{\theta_1\pi}{2}\right)}{\left(2\cos^2\left(\frac{\theta_1\pi}{2}\right)-3\right)(\theta_2+1)^2} \end{bmatrix}$$

It can be checked that the products of the covariant and contravariant bases satisfy

$$\mathbf{a}^\alpha \cdot \mathbf{a}_\beta = \delta^\beta_\alpha = \begin{cases} 1 & \text{if } \alpha = \beta \\ 0 & \text{if } \alpha \neq \beta \end{cases}$$

B | Structural Derivations

B.1 Continuum mechanics of the thin shell model

B.1.1 Proofs for the Material Tensor $\mathcal{C}$

For the sake of completeness, Theorem 2 is recalled first.

Theorem 2. *The material tensor of Equation* (3.12) *on a local Cartesian basis and the material tensor from Equation* (3.11) *on a curvilinear basis are equivalent.*

Proof. The goal of this proof is to prove that in Equation (3.12), $\tilde{\mathcal{C}}$ is equal to $\bar{\mathcal{C}}$, which is the material tensor from Equation (3.11) in Cartesian coordinates. Therefore, let us consider the definition of the material tensor $\mathcal{C}$ from Equation (3.11). Furthermore, let $\mathbf{e}_i$, $i = 1, 2, 3$ denote a Cartesian basis vector. By construction,

$$e^{\alpha\beta} = \mathbf{e}_\alpha \mathbf{e}_\beta = \begin{cases} 1 & \text{if } \alpha = \beta \\ 0 & \text{if } \alpha \neq \beta \end{cases}.$$

Furthermore, a tensor in basis $\mathbf{a}_\alpha \otimes \mathbf{a}_\beta \otimes \mathbf{a}_\sigma \otimes \mathbf{a}_\tau$ can in general be rewritten to a tensor in basis $\mathbf{e}_\alpha \otimes \mathbf{e}_\beta \otimes \mathbf{e}_\sigma \otimes \mathbf{e}_\tau$ [138, 141]. Hence,

$$\bar{\mathcal{C}} = 2\frac{\lambda\mu}{\lambda + 2\mu} e_{\alpha\beta} e_{\sigma\tau} \mathbf{e}_\alpha \otimes \mathbf{e}_\beta \otimes \mathbf{e}_\sigma \otimes \mathbf{e}_\tau + \mu(e_{\alpha\sigma} e_{\beta\tau} \mathbf{e}_\alpha \otimes \mathbf{e}_\sigma \otimes \mathbf{e}_\beta \otimes \mathbf{e}_\tau + e_{\alpha\tau} e_{\beta\sigma} \mathbf{e}_\alpha \otimes \mathbf{e}_\tau \otimes \mathbf{e}_\beta \otimes \mathbf{e}_\sigma).$$

From this, it can be seen that the material tensor can be written in terms of the curvilinear basis with coefficients $\mathcal{C}$ or in terms of another basis, e.g. the Cartesian basis $\bar{\mathcal{C}}$. Using Equation (3.9), and the fact that the strain tensor is two-dimensional, relevant components of the material tensor $\mathcal{C}$ are:

$$\begin{aligned}
\bar{\mathcal{C}}^{1111} = \bar{\mathcal{C}}^{2222} &= 2\frac{\lambda\mu}{\lambda + 2\mu} \cdot (1 \cdot 1) + \mu(1 \cdot 1 + 1 \cdot 1) = 2\frac{\lambda\mu}{\lambda + 2\mu} + \mu, \\
\bar{\mathcal{C}}^{1122} = \bar{\mathcal{C}}^{2211} &= 2\frac{\lambda\mu}{\lambda + 2\mu} \cdot (0 \cdot 0) + \mu(0 \cdot 0 + 0 \cdot 0) = 2\frac{\lambda\mu}{\lambda + 2\mu}, \\
\bar{\mathcal{C}}^{1112} &= 2\frac{\lambda\mu}{\lambda + 2\mu} \cdot (1 \cdot 1) + \mu(1 \cdot 0 + 0 \cdot 1) = 2\frac{\lambda\mu}{\lambda + 2\mu}, \\
\bar{\mathcal{C}}^{2212} &= 2\frac{\lambda\mu}{\lambda + 2\mu} \cdot (1 \cdot 1) + \mu(0 \cdot 1 + 1 \cdot 0) = 2\frac{\lambda\mu}{\lambda + 2\mu} \\
\bar{\mathcal{C}}^{1211} &= 2\frac{\lambda\mu}{\lambda + 2\mu} \cdot (0 \cdot 1) + \mu(1 \cdot 0 + 1 \cdot 0) = 0, \\
\bar{\mathcal{C}}^{1222} &= 2\frac{\lambda\mu}{\lambda + 2\mu} \cdot (1 \cdot 0) + \mu(0 \cdot 1 + 0 \cdot 1) = 0, \\
\bar{\mathcal{C}}^{1212} &= 2\frac{\lambda\mu}{\lambda + 2\mu} \cdot (0 \cdot 0) + \mu(1 \cdot 1 + 0 \cdot 0) = \mu.
\end{aligned}$$

The following simplifications finish the proof.

$$\begin{aligned} 2\frac{\lambda\mu}{\lambda+2\mu} &= \frac{\nu E}{1-\nu^2}, \\ 2\frac{\lambda\mu}{\lambda+2\mu} + 2\mu &= \frac{E}{1-\nu^2}, \\ \mu &= \frac{E}{1-\nu^2}\frac{1-\nu}{2}. \end{aligned}$$

□

Additionally, Theorem 2 will be proven here, which states that the material tensor $\mathcal{C}$ is symmetric. Let us define the properties *minor* and *major* symmetric first [141]:

Definition 1. *Any fourth-order order tensor $\mathcal{A}$ is said to be* minor symmetrical *or possesses* minor symmetry *if and only if*

$$\mathcal{A}^{\alpha\beta\sigma\tau} = \mathcal{A}^{\beta\alpha\sigma\tau} = \mathcal{A}^{\alpha\beta\tau\sigma}.$$

Additionally, $\mathcal{A}$ is said to be major symmetrical *or possesses* major symmetry *if and only if*

$$\mathcal{A}^{\alpha\beta\sigma\tau} = \mathcal{A}^{\sigma\tau\alpha\beta}.$$

From the book of Başar and Weichert [141], it is known that *any* elastic material tensor possesses minor symmetry. Hyperelastic elasticity tensors in general possesses also major symmetry. This is proven below for the material tensor from Equation (3.11). Let us recall the theorem first

Theorem 3. *The fourth-order material tensor $\mathcal{C}$, defined by*

$$\mathcal{C}^{\alpha\beta\sigma\tau} = 2\frac{\lambda\mu}{\lambda+2\mu}G_{\alpha\beta}G_{\sigma\tau} + \mu(G_{\alpha\sigma}G_{\beta\tau} + G_{\alpha\tau}G_{\beta\sigma}). \qquad \text{(See Equation (3.11))}$$

Is minor *and* major *symmetric.*

Proof. The proof that the material tensor from Equation (3.11) is minor symmetrical, is rather straightforward. Namely, since the covariant metric tensor has the property $G_{\alpha\beta} = G_{\beta\alpha}$, we see that

$$\begin{aligned} \mathcal{C}^{\alpha\beta\sigma\tau} &= 2\frac{\lambda\mu}{\lambda+2\mu}G_{\alpha\beta}G_{\sigma\tau} + \mu(G_{\alpha\sigma}G_{\beta\tau} + G_{\alpha\tau}G_{\beta\sigma}) \\ &= 2\frac{\lambda\mu}{\lambda+2\mu}G_{\beta\alpha}G_{\sigma\tau} + \mu(G_{\beta\sigma}G_{\alpha\tau} + G_{\beta\tau}G_{\alpha\sigma}) = \mathcal{C}^{\beta\alpha\sigma\tau} \\ &= 2\frac{\lambda\mu}{\lambda+2\mu}G_{\alpha\beta}G_{\tau\sigma} + \mu(G_{\alpha\tau}G_{\beta\sigma} + G_{\alpha\sigma}G_{\beta\tau}) = \mathcal{C}^{\alpha\beta\sigma\tau}. \end{aligned}$$

Which proves minor symmetry. To prove that the material tensor from Equation (3.11) also possesses major symmetry, and thus represents a hyperelastic material, indices are again swapped

$$\begin{aligned} \mathcal{C}^{\alpha\beta\sigma\tau} &= 2\frac{\lambda\mu}{\lambda+2\mu}G_{\alpha\beta}G_{\sigma\tau} + \mu(G_{\alpha\sigma}G_{\beta\tau} + G_{\alpha\tau}G_{\beta\sigma}) \\ &= 2\frac{\lambda\mu}{\lambda+2\mu}G_{\sigma\tau}G_{\alpha\beta} + \mu(G_{\sigma\alpha}G_{\tau\beta} + G_{\sigma\beta}G_{\tau\alpha}). \end{aligned}$$

Using symmetry of the metric tensor we indeed see that the equalities hold and hence major symmetry has been proven. □

B.1.2 Variational form

As derived in Section 3.2.5 from the works of Goyal [142] and Kiendl [137], the internal, external and kinetic energies W_{int}, W_{ext} and K, respectively, are given by:

$$\begin{aligned} W_{\text{int}} &= \frac{1}{2}\int_\Omega \underline{\underline{\boldsymbol{n}}} : \underline{\underline{\boldsymbol{\varepsilon}}} + \underline{\underline{\boldsymbol{m}}} : \underline{\underline{\boldsymbol{\kappa}}}\, \mathrm{d}\Omega, \\ W_{\text{ext}} &= -\int_\Omega \mathbf{t}\cdot\mathbf{u}\, \mathrm{d}\Omega, K \qquad\qquad = \frac{1}{2}\int_\Omega \rho\dot{\mathbf{x}}\cdot\dot{\mathbf{x}}\, \mathrm{d}\Omega. \end{aligned} \tag{B.1}$$

Accordingly, the Lagrangian $\mathcal{L}$ is used in Hamilton's principle (see Equation (3.19)) to obtain an energy functional between two *states* or times τ_0 and τ_1 which should be stationary inbetween. Let us here recall the energy functional from Equation (3.20):

$$J(\theta) = \int_{\tau_0}^{\tau_1} \mathcal{L}(\mathbf{u}+\theta\mathbf{v})\, \mathrm{d}t. \qquad \text{(See Equation (3.20))}$$

Consequently, the Gateaux derivative of this term (see Equation (3.21)) needs to be equal to zero to find the path with minimal energy. In this appendix, the Gateaux derivative is evaluated such that Equation (3.22) is obtained.

Firstly, let us start with the internal energy W_{int}. The Gateaux derivative of this term is

$$\begin{aligned} \frac{\mathrm{d}}{\mathrm{d}\theta} W_{\text{int}}(\mathbf{u}+\theta\mathbf{v})\Big|_{\theta=0} &= \frac{\mathrm{d}}{\mathrm{d}\theta}\left\{\frac{1}{2}\int_\Omega \underline{\underline{\boldsymbol{n}}}(\mathbf{u}+\theta\mathbf{v}) : \underline{\underline{\boldsymbol{\varepsilon}}}(\mathbf{u}+\theta\mathbf{v}) + \underline{\underline{\boldsymbol{m}}}(\mathbf{u}+\theta\mathbf{v}) : \underline{\underline{\boldsymbol{\kappa}}}(\mathbf{u}+\theta\mathbf{v})\, \mathrm{d}\Omega\right\}\Big|_{\theta=0} \\ &= \frac{\mathrm{d}}{\mathrm{d}\theta}\left\{\frac{1}{2}\int_\Omega \left(t\mathcal{C} : \underline{\underline{\boldsymbol{\varepsilon}}}(\mathbf{u}+\theta\mathbf{v})\right) : \underline{\underline{\boldsymbol{\varepsilon}}}(\mathbf{u}+\theta\mathbf{v}) + \left(\frac{t^3}{12}\mathcal{C} : \underline{\underline{\boldsymbol{\kappa}}}(\mathbf{u}+\theta\mathbf{v})\right) : \underline{\underline{\boldsymbol{\kappa}}}(\mathbf{u}+\theta\mathbf{v})\, \mathrm{d}\Omega\right\}\Big|_{\theta=0} \\ &= \frac{\mathrm{d}}{\mathrm{d}\theta}\left\{\frac{1}{2}\int_\Omega \left(t\mathcal{C} : \underline{\underline{\boldsymbol{\varepsilon}}}(\mathbf{u}+\theta\mathbf{v})\right) : \underline{\underline{\boldsymbol{\varepsilon}}}(\mathbf{u}+\theta\mathbf{v}) + \left(\frac{t^3}{12}\mathcal{C} : \underline{\underline{\boldsymbol{\kappa}}}(\mathbf{u}+\theta\mathbf{v})\right) : \underline{\underline{\boldsymbol{\kappa}}}(\mathbf{u}+\theta\mathbf{v})\, \mathrm{d}\Omega\right\}\Big|_{\theta=0} \\ &= \frac{\mathrm{d}}{\mathrm{d}\theta}\left\{\frac{1}{2}\int_\Omega \left(t\underline{\underline{\boldsymbol{\varepsilon}}}(\mathbf{u}+\theta\mathbf{v}) : \mathcal{C}^T\right) : \underline{\underline{\boldsymbol{\varepsilon}}}(\mathbf{u}+\theta\mathbf{v}) + \left(\frac{t^3}{12}\underline{\underline{\boldsymbol{\kappa}}}(\mathbf{u}+\theta\mathbf{v}) : \mathcal{C}^T\right) : \underline{\underline{\boldsymbol{\kappa}}}(\mathbf{u}+\theta\mathbf{v})\, \mathrm{d}\Omega\right\} \\ &= \frac{1}{2}\int_\Omega \left(t\underline{\underline{\boldsymbol{\varepsilon}}}' : \mathcal{C}^T\right) : \underline{\underline{\boldsymbol{\varepsilon}}} + \left(t\underline{\underline{\boldsymbol{\varepsilon}}} : \mathcal{C}^T\right) : \underline{\underline{\boldsymbol{\varepsilon}}}' + \left(\frac{t^3}{12}\underline{\underline{\boldsymbol{\kappa}}}' : \mathcal{C}^T\right) : \underline{\underline{\boldsymbol{\kappa}}} + \left(\frac{t^3}{12}\underline{\underline{\boldsymbol{\kappa}}} : \mathcal{C}^T\right) : \underline{\underline{\boldsymbol{\kappa}}}'\, \mathrm{d}\Omega \\ &= \frac{1}{2}\int_\Omega \left(t\underline{\underline{\boldsymbol{\varepsilon}}} : \mathcal{C}\right) : \underline{\underline{\boldsymbol{\varepsilon}}}' + \left(t\underline{\underline{\boldsymbol{\varepsilon}}} : \mathcal{C}^T\right) : \underline{\underline{\boldsymbol{\varepsilon}}}' + \left(\frac{t^3}{12}\underline{\underline{\boldsymbol{\kappa}}} : \mathcal{C}\right) : \underline{\underline{\boldsymbol{\kappa}}}' + \left(\frac{t^3}{12}\underline{\underline{\boldsymbol{\kappa}}} : \mathcal{C}^T\right) : \underline{\underline{\boldsymbol{\kappa}}}'\, \mathrm{d}\Omega \\ &= \int_\Omega \underline{\underline{\boldsymbol{n}}}(\mathbf{u}) : \underline{\underline{\boldsymbol{\varepsilon}}}(\mathbf{u},\mathbf{v})' + \underline{\underline{\boldsymbol{m}}}(\mathbf{u}) : \underline{\underline{\boldsymbol{\kappa}}}'(\mathbf{u},\mathbf{v})\, \mathrm{d}\Omega. \end{aligned}$$

Where the third equality holds by [138, eq. 1.157], the fourth equation is the product rule with the terms with a prime ($'$) denote Gateaux derivatives and in the fifth equality, [138, eq. 1.157] is again used. In the sixth equality the symmetry of $\mathcal{C}$ is used.

For the external energy, the following holds:

$$\begin{aligned} \frac{\mathrm{d}}{\mathrm{d}\theta} W_{\text{ext}}(\mathbf{u}+\theta\mathbf{v})\Big|_{\theta=0} &= \frac{\mathrm{d}}{\mathrm{d}\theta}\left\{\int_\Omega \tau\cdot(\mathbf{u}+\theta\mathbf{v})\, \mathrm{d}\Omega\right\}\Big|_{\theta=0} \\ &= \int_\Omega \tau\cdot\mathbf{v}\, \mathrm{d}\Omega. \end{aligned} \tag{B.2}$$

Lastly, the Gateaux derivative of the kinetic energy is computed based on the assumption that rotational inertia

is negligible (see Equation (3.18)).

$$\begin{aligned}\frac{\mathrm{d}}{\mathrm{d}\theta}K(\mathbf{u}+\theta\mathbf{v})\Big|_{\theta=0} &= \frac{\mathrm{d}}{\mathrm{d}\theta}\left\{\frac{1}{2}\int_\Omega \rho\dot{\mathbf{x}}(\mathbf{u}+\theta\mathbf{v})\cdot\dot{\mathbf{x}}(\mathbf{u}+\theta\mathbf{v})\,\mathrm{d}\Omega\right\}\Big|_{\theta=0} \qquad \approx \frac{\mathrm{d}}{\mathrm{d}\theta}\left\{\frac{1}{2}\int_\Omega \rho\dot{\mathbf{c}}(\mathbf{u}+\theta\mathbf{v})\cdot\dot{\mathbf{c}}(\mathbf{u}+\theta\mathbf{v})\,\mathrm{d}\Omega\right\}\Big|_{\theta=0}\\ &= \frac{\mathrm{d}}{\mathrm{d}\theta}\left\{\frac{1}{2}\int_\Omega \rho\dot{\mathbf{c}}_0+\mathbf{u}+\theta\dot{\mathbf{v}})\cdot(\dot{\mathbf{c}}_0+\mathbf{u}+\theta\dot{\mathbf{v}})\,\mathrm{d}\Omega\right\}\Big|_{\theta=0}\\ &= \int_\Omega \rho\dot{\mathbf{c}}\cdot\dot{\mathbf{v}}\,\mathrm{d}\Omega.\end{aligned}$$

Such that the minimal energy functional becomes

$$\int_{\tau_0}^{\tau_1}\left[\int_\Omega \rho\dot{\mathbf{c}}\cdot\dot{\mathbf{v}}\,\mathrm{d}\Omega - \int_\Omega \underline{\underline{\boldsymbol{n}}}(\mathbf{u}):\underline{\underline{\boldsymbol{\varepsilon}}}(\mathbf{u},\mathbf{v})' + \underline{\underline{\underline{\boldsymbol{m}}}}(\mathbf{u}):\underline{\underline{\boldsymbol{\kappa}}}'(\mathbf{u},\mathbf{v})\,\mathrm{d}\Omega + \int_\Omega \mathbf{p}\cdot\mathbf{v}\,\mathrm{d}\Omega\right]\mathrm{d}\tau = 0. \tag{B.3}$$

Using partial integration of the kinetic energy term and the fact that the variation $\mathbf{v}$ is zero on time steps τ_0 and τ_1, this term can be written as:

$$\int_{\tau_0}^{\tau_1}\left[\int_\Omega \rho\dot{\mathbf{c}}\cdot\dot{\mathbf{v}}\,\mathrm{d}\Omega\right]\mathrm{d}\tau = \left[\int_\Omega \rho\dot{\mathbf{c}}\cdot\mathbf{v}\,\mathrm{d}\Omega\right]_{\tau_0}^{\tau_1} - \int_\Omega \rho\ddot{\mathbf{c}}\cdot\mathbf{v}\,\mathrm{d}\Omega.$$

Where the first term is zero due to the fact that the variation is zero on τ_0 and τ_1. Substitution in Equation (B.3) gives then

$$\int_{\tau_0}^{\tau_1}\left[\int_\Omega \rho\ddot{\mathbf{c}}\cdot\mathbf{v}\,\mathrm{d}\Omega - \int_\Omega \underline{\underline{\boldsymbol{n}}}(\mathbf{u}):\underline{\underline{\boldsymbol{\varepsilon}}}(\mathbf{u},\mathbf{v})' + \underline{\underline{\underline{\boldsymbol{m}}}}(\mathbf{u}):\underline{\underline{\boldsymbol{\kappa}}}'(\mathbf{u},\mathbf{v})\,\mathrm{d}\Omega + \int_\Omega \mathbf{p}\cdot\mathbf{v}\,\mathrm{d}\Omega\right]\mathrm{d}\tau = 0. \tag{B.4}$$

Since Equation (B.4) should be valid for all $\mathbf{v}$ on all times, the variational form is given by:

$$\int_\Omega \rho\ddot{\mathbf{c}}\cdot\mathbf{v}\,\mathrm{d}\Omega + \int_\Omega \underline{\underline{\boldsymbol{n}}}(\mathbf{u}):\underline{\underline{\boldsymbol{\varepsilon}}}(\mathbf{u},\mathbf{v})' + \underline{\underline{\underline{\boldsymbol{m}}}}(\mathbf{u}):\underline{\underline{\boldsymbol{\kappa}}}'(\mathbf{u},\mathbf{v})\,\mathrm{d}\Omega - \int_\Omega \mathbf{p}\cdot\mathbf{v}\,\mathrm{d}\Omega = 0. \tag{B.5}$$

For nonlinear computations, the Jacobian of Equation (B.5) is needed for Newton iterations. The Jacobian is obtained by taking variations $\mathbf{u}+\theta\mathbf{w}$ of Equation (B.5), where $\mathbf{w}$ is admissible.
The first term of Equation (B.5), corresponding to the kinetic energy variation, gives:

$$\begin{aligned}\frac{\mathrm{d}}{\mathrm{d}\theta}\delta K(\mathbf{u}+\theta\mathbf{w},\mathbf{v})_{\theta=0} &= \frac{\mathrm{d}}{\mathrm{d}\theta}\left\{\int_\Omega \rho(\ddot{\mathbf{c}}_0+\ddot{\mathbf{u}}+\theta\ddot{\mathbf{w}})\cdot\mathbf{v}\,\mathrm{d}\Omega\right\}_{\theta=0}\\ &= \int_\Omega \rho\ddot{\mathbf{w}}\cdot\mathbf{v}\,\mathrm{d}\Omega.\end{aligned}$$

The second term of Equation (B.5), corresponding to the internal energy variation, gives:

$$\begin{aligned}\frac{\mathrm{d}}{\mathrm{d}\theta}\delta W_{\mathrm{int}}(\mathbf{u}+\theta\mathbf{w},\mathbf{v})_{\theta=0} &= \frac{\mathrm{d}}{\mathrm{d}\theta}\left\{\int_\Omega \underline{\underline{\boldsymbol{n}}}(\mathbf{u}+\theta\mathbf{w}):\underline{\underline{\boldsymbol{\varepsilon}}}(\mathbf{u}+\theta\mathbf{w},\mathbf{v})' + \underline{\underline{\underline{\boldsymbol{m}}}}(\mathbf{u}+\theta\mathbf{w}):\underline{\underline{\boldsymbol{\kappa}}}'(\mathbf{u}+\theta\mathbf{w},\mathbf{v})\,\mathrm{d}\Omega\right\}_{\theta=0}\\ &= \int_\Omega \underline{\underline{\boldsymbol{n}}}'(\mathbf{w}):\underline{\underline{\boldsymbol{\varepsilon}}}(\mathbf{u},\mathbf{v})' + \underline{\underline{\boldsymbol{n}}}(\mathbf{u}):\underline{\underline{\boldsymbol{\varepsilon}}}(\mathbf{w},\mathbf{v})'' + \underline{\underline{\underline{\boldsymbol{m}}}}'(\mathbf{w}):\underline{\underline{\boldsymbol{\kappa}}}'(\mathbf{u},\mathbf{v}) + \underline{\underline{\underline{\boldsymbol{m}}}}(\mathbf{u}):\underline{\underline{\boldsymbol{\kappa}}}''(\mathbf{w},\mathbf{v})\,\mathrm{d}\Omega.\end{aligned}$$

Such that the Jacobian becomes:

$$j(\mathbf{u},\mathbf{v},\mathbf{w}) = -\int_\Omega \underline{\underline{\boldsymbol{n}}}':\underline{\underline{\boldsymbol{\varepsilon}}}' + \underline{\underline{\boldsymbol{n}}}:\underline{\underline{\boldsymbol{\varepsilon}}}'' + \underline{\underline{\underline{\boldsymbol{m}}}}':\underline{\underline{\boldsymbol{\kappa}}}' + \underline{\underline{\underline{\boldsymbol{m}}}}:\underline{\underline{\boldsymbol{\kappa}}}''\,\mathrm{d}\Omega. \tag{B.6}$$

B.2 Euler-Bernoulli beam model

B.2.1 Derivation of Von Kármán strains

The Von Kármán strains in Cartesian coordinates are used for the derivation of the Euler-Bernoulli beam. Throughout the whole section, the book of Reddy [140] is used. In the derivation of the strains, the Kirchhoff

Hypothesis is assumed to be true and the derivation is not limited to the one-dimensional case, for the sake of generality. Hence, the displacements are governed by (using the bar for three-dimensional coordinate description and quantities without a bar for the mid-plane):

$$\begin{aligned} \bar{u}(x,y,z,t) &= u(x,y,t) - z\frac{\partial w}{\partial x}, \\ \bar{v}(x,y,z,t) &= v(x,y,t) - z\frac{\partial w}{\partial y}, \\ \bar{w}(x,y,z,t) &= w(x,y,t). \end{aligned} \tag{B.7}$$

Furthermore, the derivation is continued by using the Green-Lagrange strain tensor, which, in terms of displacements, is denoted by (using the strain and curvature tensors $\underline{\underline{\boldsymbol{\varepsilon}}}$ and $\underline{\underline{\boldsymbol{\kappa}}}$)

$$\begin{aligned} \varepsilon_{ij} &= \frac{\mathrm{d}\bar{u}_i}{\mathrm{d}x_j} + \frac{\mathrm{d}\bar{u}_j}{\mathrm{d}x_i} + \frac{\mathrm{d}\bar{u}_i}{\mathrm{d}x_j}\frac{\mathrm{d}\bar{u}_j}{\mathrm{d}x_i} && = \frac{1}{2}\left(\nabla\bar{\mathbf{u}} + (\nabla\bar{\mathbf{u}})^T + (\nabla\bar{\mathbf{u}})(\nabla\bar{\mathbf{u}})^T\right), \\ \kappa_{\alpha\beta} &= \frac{\mathrm{d}\bar{w}}{\mathrm{d}x_i}\frac{\mathrm{d}\bar{w}}{\mathrm{d}x_j}. \end{aligned}$$

Where $\bar{\mathbf{u}}^T = [\bar{u}, \bar{v}, \bar{w}]$ and where the coordinates are expressed by $\mathbf{x}^T = [x, y, z]$. If the strains of a material volume in normal directions are small, and for the vertical displacements even zero (see Equation (B.7))

$$\frac{\mathrm{d}u}{\mathrm{d}x}, \frac{\mathrm{d}v}{\mathrm{d}y} \sim \mathcal{O}(\varepsilon), \quad \frac{\mathrm{d}w}{\mathrm{d}z} = 0,$$

And if furthermore the in-plane shear effects are also small, i.e.

$$\frac{\mathrm{d}u}{\mathrm{d}y}, \frac{\mathrm{d}v}{\mathrm{d}x} \sim \mathcal{O}(\varepsilon),$$

Then all terms with $\mathcal{O}(\varepsilon^2)$ vanish from the formulations. Furthermore, for moderate rotations, the following terms have a non-negligible contribution compared to $\mathcal{O}(\varepsilon)$:

$$\left(\frac{\mathrm{d}w}{\mathrm{d}x}\right)^2, \left(\frac{\mathrm{d}w}{\mathrm{d}x}\right)^2, \left(\frac{\mathrm{d}w}{\mathrm{d}x}\frac{\mathrm{d}w}{\mathrm{d}y}\right).$$

These orders have the following consequences for the Green strain tensor [140]:

$$\varepsilon_{11} = \frac{\mathrm{d}u}{\mathrm{d}x} + \frac{1}{2}\left[\cancel{\left(\frac{\mathrm{d}u}{\mathrm{d}x}\right)^2}^{\mathcal{O}(\varepsilon^2)} + \cancel{\left(\frac{\mathrm{d}v}{\mathrm{d}x}\right)^2}^{\mathcal{O}(\varepsilon^2)} + \left(\frac{\mathrm{d}w}{\mathrm{d}x}\right)^2\right] \approx \frac{\mathrm{d}u}{\mathrm{d}x} + \frac{1}{2}\left(\frac{\mathrm{d}w}{\mathrm{d}x}\right)^2 + \mathcal{O}(\varepsilon^2)$$

$$\varepsilon_{12} = \frac{1}{2}\left[\frac{\mathrm{d}u}{\mathrm{d}y} + \frac{\mathrm{d}v}{\mathrm{d}x} + \cancel{\frac{\mathrm{d}u}{\mathrm{d}x}\frac{\mathrm{d}u}{\mathrm{d}y}}^{\mathcal{O}(\varepsilon^2)} + \cancel{\frac{\mathrm{d}v}{\mathrm{d}x}\frac{\mathrm{d}v}{\mathrm{d}y}}^{\mathcal{O}(\varepsilon^2)} + \frac{\mathrm{d}w}{\mathrm{d}x}\frac{\mathrm{d}w}{\mathrm{d}y}\right] \approx \frac{1}{2}\left[\frac{\mathrm{d}u}{\mathrm{d}y} + \frac{\mathrm{d}v}{\mathrm{d}x} + \frac{\mathrm{d}w}{\mathrm{d}x}\frac{\mathrm{d}w}{\mathrm{d}y}\right] + \mathcal{O}(\varepsilon^2)$$

$$\varepsilon_{13} = \frac{1}{2}\left[\frac{\mathrm{d}u}{\mathrm{d}z} + \frac{\mathrm{d}w}{\mathrm{d}x} + \cancel{\frac{\mathrm{d}u}{\mathrm{d}x}\frac{\mathrm{d}u}{\mathrm{d}z}}^{\mathcal{O}(\varepsilon)} + \cancel{\frac{\mathrm{d}v}{\mathrm{d}x}\frac{\mathrm{d}v}{\mathrm{d}z}}^{\mathcal{O}(\varepsilon)} + \cancel{\frac{\mathrm{d}w}{\mathrm{d}x}\frac{\mathrm{d}w}{\mathrm{d}z}}^{0}\right] \approx \frac{1}{2}\left[\frac{\mathrm{d}u}{\mathrm{d}z} + \frac{\mathrm{d}w}{\mathrm{d}x}\right] + \mathcal{O}(\varepsilon)$$

$$\varepsilon_{22} = \frac{\mathrm{d}v}{\mathrm{d}y} + \frac{1}{2}\left[\cancel{\left(\frac{\mathrm{d}u}{\mathrm{d}y}\right)^2}^{\mathcal{O}(\varepsilon^2)} + \cancel{\left(\frac{\mathrm{d}v}{\mathrm{d}y}\right)^2}^{\mathcal{O}(\varepsilon^2)} + \left(\frac{\mathrm{d}w}{\mathrm{d}y}\right)^2\right] \approx \frac{\mathrm{d}v}{\mathrm{d}y} + \frac{1}{2}\left(\frac{\mathrm{d}w}{\mathrm{d}y}\right)^2 + \mathcal{O}(\varepsilon^2)$$

$$\varepsilon_{23} = \frac{1}{2}\Bigg[\frac{\mathrm{d}v}{\mathrm{d}z} + \frac{\mathrm{d}w}{\mathrm{d}y} + \cancel{\frac{\mathrm{d}u}{\mathrm{d}y}\frac{\mathrm{d}u}{\mathrm{d}z}}^{\mathcal{O}(\varepsilon)} + \cancel{\frac{\mathrm{d}v}{\mathrm{d}y}\frac{\mathrm{d}v}{\mathrm{d}z}}^{\mathcal{O}(\varepsilon)} + \cancel{\frac{\mathrm{d}w}{\mathrm{d}y}\frac{\mathrm{d}w}{\mathrm{d}z}}^{0}\Bigg] \approx \frac{1}{2}\left[\frac{\mathrm{d}v}{\mathrm{d}z} + \frac{\mathrm{d}w}{\mathrm{d}y}\right] + \mathcal{O}(\varepsilon)$$

$$\varepsilon_{33} = \cancel{\frac{\mathrm{d}w}{\mathrm{d}z}}^{0} + \frac{1}{2}\Bigg[\cancel{\left(\frac{\mathrm{d}u}{\mathrm{d}z}\right)^2}^{\mathcal{O}(\varepsilon^2)} + \cancel{\left(\frac{\mathrm{d}v}{\mathrm{d}z}\right)^2}^{\mathcal{O}(\varepsilon^2)} + \cancel{\left(\frac{\mathrm{d}w}{\mathrm{d}z}\right)^2}^{0}\Bigg] \approx \mathcal{O}\left(\varepsilon^2\right).$$

Plugging in the expressions for u, v, w and performing some mathematical operations yields the Von Kármán strains:

$$\begin{aligned}
\varepsilon_{11} &= \frac{\mathrm{d}u}{\mathrm{d}x} - z\frac{\mathrm{d}^2w}{\mathrm{d}x^2} + \boxed{\frac{1}{2}\left(\frac{\mathrm{d}w}{\mathrm{d}x}\right)^2}, \\
\varepsilon_{12} &= \frac{1}{2}\left[\frac{\mathrm{d}u}{\mathrm{d}y} - z\frac{\mathrm{d}^2w}{\mathrm{d}x\mathrm{d}y} + \frac{\mathrm{d}v}{\mathrm{d}x} - z\frac{\mathrm{d}^2w}{\mathrm{d}x\mathrm{d}y} + \frac{\mathrm{d}w}{\mathrm{d}x}\frac{\mathrm{d}w}{\mathrm{d}y}\right] = \frac{1}{2}\left[\frac{\mathrm{d}u}{\mathrm{d}y} + \frac{\mathrm{d}v}{\mathrm{d}x} - 2z\frac{\mathrm{d}^2w}{\mathrm{d}x\mathrm{d}y} + \boxed{\frac{\mathrm{d}w}{\mathrm{d}x}\frac{\mathrm{d}w}{\mathrm{d}y}}\right], \\
\varepsilon_{13} &= \frac{1}{2}\left[-z\frac{\mathrm{d}}{\mathrm{d}z}\left(\frac{\mathrm{d}w}{\mathrm{d}x}\right) - \frac{\mathrm{d}w}{\mathrm{d}x} + \frac{\mathrm{d}w}{\mathrm{d}x}\right] = \frac{1}{2}\left[-z\frac{\mathrm{d}}{\mathrm{d}x}\left(\cancel{\frac{\mathrm{d}w}{\mathrm{d}z}}^{0}\right) - \frac{\mathrm{d}w}{\mathrm{d}x} + \frac{\mathrm{d}w}{\mathrm{d}x}\right] = 0, \\
\varepsilon_{22} &= \frac{\mathrm{d}v}{\mathrm{d}y} - z\frac{\mathrm{d}^2w}{\mathrm{d}y^2} + \boxed{\frac{1}{2}\left(\frac{\mathrm{d}w}{\mathrm{d}y}\right)^2}, \\
\varepsilon_{23} &= \frac{1}{2}\left[-z\frac{\mathrm{d}}{\mathrm{d}z}\left(\frac{\mathrm{d}w}{\mathrm{d}y}\right) - \frac{\mathrm{d}w}{\mathrm{d}y} + \frac{\mathrm{d}w}{\mathrm{d}y}\right] = \frac{1}{2}\left[-z\frac{\mathrm{d}}{\mathrm{d}y}\left(\cancel{\frac{\mathrm{d}w}{\mathrm{d}z}}^{0}\right) - \frac{\mathrm{d}w}{\mathrm{d}y} + \frac{\mathrm{d}w}{\mathrm{d}y}\right] = 0, \\
\varepsilon_{33} &= \frac{\mathrm{d}w}{\mathrm{d}z} = 0.
\end{aligned} \tag{B.8}$$

Note that the derivatives of u and v with respect to z are zero as these are the in-plane mid-plane displacements. The derivatives of w with respect to z are zero since Furthermore, the boxed terms are the nonlinear strain contributions.

B.2.2 Derivation of the Strong Form

For the derivation of the Euler-Bernoulli beam equation, only the xz-plane is considered and hence all derivatives with respect to y are equal to zero. This implies that the Von Kármán strains from Equation (B.8) simplify to:

$$E_{11} = \frac{\mathrm{d}u}{\mathrm{d}x} - z\frac{\mathrm{d}^2w}{\mathrm{d}x^2} + \frac{1}{2}\left(\frac{\mathrm{d}w}{\mathrm{d}x}\right)^2.$$

In Section 3.3, the Gateaux derivatives of the strain and curvature are derived in Equation (3.36). Furthermore, expressions for the normal force and the moment in the beam were derived in Equation (3.35). Combining these, variation of the the internal energy in the beam is (see Equation (3.23))

$$\begin{aligned}
\delta W_{\text{int}} &= b\int_x N_{11}\left(\frac{\mathrm{d}\delta u}{\mathrm{d}x} + \frac{\mathrm{d}w}{\mathrm{d}x}\frac{\mathrm{d}\delta w}{\mathrm{d}x}\right) + M_{11}\frac{\mathrm{d}^2\delta w}{\mathrm{d}x^2}\,\mathrm{d}x \\
&= \int_x N_{11}\frac{\partial\delta u}{\partial x} - M_{11}\frac{\partial^2\delta w}{\partial x^2} + N_{11}\frac{\partial w}{\partial x}\frac{\partial\delta w}{\partial x}\,\mathrm{d}x.
\end{aligned} \tag{B.9}$$

In order to derive the governing PDEs (Euler-Lagrange equations, see Reddy [95]) for the Euler-Bernoulli beam with small deformations, the integral form of the internal work needs to be written as a product of δu and δw

to. Hence, using partial integration on Equation (B.9) results in:

$$
\begin{aligned}
(\dots) &= \int_x \frac{\mathrm{d}}{\mathrm{d}x}\left(N_{11}\delta u\right) - \frac{\mathrm{d}N_{11}}{\mathrm{d}x}\delta u - \left[\frac{\mathrm{d}}{\mathrm{d}x}\left(M_{11}\frac{\mathrm{d}\delta w}{\mathrm{d}x}\right) - \frac{\mathrm{d}M_{11}}{\mathrm{d}x}\frac{\mathrm{d}\delta w}{\mathrm{d}x}\right] + \frac{\mathrm{d}}{\mathrm{d}x}\left(N_{11}\frac{\mathrm{d}w}{\mathrm{d}x}\delta w\right) + \\
&\quad - \frac{\mathrm{d}N_{11}}{\mathrm{d}x}\frac{\mathrm{d}w}{\mathrm{d}x}\delta w - N_{11}\frac{\mathrm{d}^2 w}{\mathrm{d}x^2}\delta w\,\mathrm{d}x, \\
&= \int_0^L \int_{-\frac{b}{2}}^{\frac{b}{2}} -\frac{\mathrm{d}N_{11}}{\mathrm{d}x}\delta u + \left[\frac{\mathrm{d}}{\mathrm{d}x}\left(\frac{\mathrm{d}M_{11}}{\mathrm{d}x}\delta w\right) - \frac{\mathrm{d}^2 M_{11}}{\mathrm{d}x^2}\delta w\right] - \frac{\mathrm{d}N_{11}}{\mathrm{d}x}\frac{\mathrm{d}w}{\mathrm{d}x}\delta w - N_{11}\frac{\mathrm{d}^2 w}{\mathrm{d}x^2}\delta w\,\mathrm{d}x \\
&\quad + \left[\int_{-\frac{b}{2}}^{\frac{b}{2}} N_{11}\delta u - M_{11}\frac{\mathrm{d}\delta w}{\mathrm{d}x} + N_{11}\frac{\mathrm{d}w}{\mathrm{d}x}\delta w\,\mathrm{d}y\right]_0^L, \\
&= \int_0^L \int_{-\frac{b}{2}}^{\frac{b}{2}} -\frac{\mathrm{d}N_{11}}{\mathrm{d}x}\delta u - \frac{\mathrm{d}^2 M_{11}}{\mathrm{d}x^2}\delta w - \frac{\mathrm{d}N_{11}}{\mathrm{d}x}\frac{\mathrm{d}w}{\mathrm{d}x}\delta w - N_{11}\frac{\mathrm{d}^2 w}{\mathrm{d}x^2}\delta w\,\mathrm{d}x\mathrm{d}y \\
&\quad + \left[\int_{-\frac{b}{2}}^{\frac{b}{2}} N_{11}\delta u - M_{11}\frac{\mathrm{d}\delta w}{\mathrm{d}x} + \frac{\mathrm{d}M_{11}}{\mathrm{d}x}\delta w + N_{11}\frac{\mathrm{d}w}{\mathrm{d}x}\delta w\,\mathrm{d}y\right]_0^L, \\
&= b\int_0^L -\frac{\mathrm{d}N_{11}}{\mathrm{d}x}\delta u - \frac{\mathrm{d}^2 M_{11}}{\mathrm{d}x^2}\delta w - \frac{\mathrm{d}N_{11}}{\mathrm{d}x}\frac{\mathrm{d}w}{\mathrm{d}x}\delta w - N_{11}\frac{\mathrm{d}^2 w}{\mathrm{d}x^2}\delta w\,\mathrm{d}x \\
&\quad + b\left[N_{11}\delta u - M_{11}\frac{\mathrm{d}\delta w}{\mathrm{d}x} + \frac{\mathrm{d}M_{11}}{\mathrm{d}x}\delta w + N_{11}\frac{\mathrm{d}w}{\mathrm{d}x}\delta w\right]_0^L.
\end{aligned}
$$

Now, the virtual work of the external forces can be determined. Suppose the beam is subject to a transversal pressure on the top ($p_t(x)$) and on the bottom ($p_b(x)$) and a longitudinal traction force on the top ($t_t(x)$) and on the bottom ($t_b(x)$), as well. Furthermore, a hydrostatic foundation is applied on the beam, denoted by $-\rho g w$. Then, the virtual work of these loads becomes:

$$
\begin{aligned}
\delta W_E &= -b\int_0^L p_t\delta w\left(x, y, \frac{h}{2}\right) + p_b\delta w\left(x, y, -\frac{h}{2}\right) \\
&\quad + t_t\delta u\left(x, y, \frac{h}{2}\right) + t_b\delta u\left(x, y, \frac{h}{2}\right) - \rho g w\delta w(x, y, 0)\,\mathrm{d}x \\
&= -b\int_0^L p_t\delta w + p_b\delta w \\
&\quad + t_t\left(\delta u - \frac{h}{2}\frac{\mathrm{d}\delta w}{\mathrm{d}x}\right) + t_b\left(\delta u + \frac{h}{2}\frac{\mathrm{d}\delta w}{\mathrm{d}x}\right) - b\rho g w\delta w\,\mathrm{d}x \\
&= -b\int_0^L \left(p_t + p_b - \frac{h}{2}\frac{\mathrm{d}t_t}{\mathrm{d}x} + \frac{h}{2}\frac{\mathrm{d}t_b}{\mathrm{d}x}\right)\delta w + \left(t_t + t_b\right)\delta u - b\rho g w\delta w\,\mathrm{d}x \\
&\quad - \left[\left(-\frac{h}{2}q_t + \frac{h}{2}q_b\right)\delta w\right]_0^L.
\end{aligned}
$$

Lastly, in order to get the dynamic equation of the Euler beam, the kinetic energy should also be involved. This term was derived in the first term of Equation (B.4) and neglects rotary inertia.

$$
\delta K = b\int_0^L \rho t\left(\ddot{u}\delta u + \ddot{w}\delta w\right)\,\mathrm{d}x.
$$

Now, Hamilton's principle (see Equation (3.19)) becomes:

$$\begin{aligned}\int_{t_1}^{t_2} \delta K - (\delta W_E + \delta W_I)\,\mathrm{d}t = \int_{t_1}^{t_2} \Bigg\{ \int_0^L -\rho\left[bt\ddot{u}_0\delta u + bt\ddot{w}_0\delta w\right] + b\frac{\mathrm{d}N_{11}}{\mathrm{d}x}\delta u + b\frac{\mathrm{d}^2M_{11}}{\mathrm{d}x^2}\delta w \\ + b\frac{\mathrm{d}N_{11}}{\mathrm{d}x}\frac{\mathrm{d}w}{\mathrm{d}x}\delta w + bN_{11}\frac{\mathrm{d}^2w}{\mathrm{d}x^2}\delta w + b\left(p_t + p_b - \frac{h}{2}\frac{\mathrm{d}t_t}{\mathrm{d}x} + \frac{h}{2}\frac{\mathrm{d}t_b}{\mathrm{d}x}\right)\delta w \\ + b\left(t_t + t_b\right)\delta u - b\rho g w\delta w\,\mathrm{d}x \\ + \rho\left[I\frac{\mathrm{d}\ddot{w}_0}{\mathrm{d}x}\delta w\right]_0^L - \left[bN_{11}\delta u - bM_{11}\frac{\mathrm{d}\delta w}{\mathrm{d}x} + b\frac{\mathrm{d}M_{11}}{\mathrm{d}x}\delta w\right]_0^L \Bigg\}\,\mathrm{d}t \\ = 0.\end{aligned}$$

From this principle, the equations of motion follow by collecting the terms multiplied by δu and δw separately from the domain integral.

$$\begin{aligned} b\frac{\mathrm{d}N_{11}}{\mathrm{d}x} - \rho A\ddot{u}_0 + b(t_t + t_b) &= 0, \\ b\frac{\mathrm{d}^2M_{11}}{\mathrm{d}x^2} + b\frac{\mathrm{d}N_{11}}{\mathrm{d}x}\frac{\mathrm{d}w}{\mathrm{d}x} + bN_{11}\frac{\mathrm{d}^2w}{\mathrm{d}x^2} &= \rho A\ddot{w}_0 - b\left(p_t + p_b - \frac{h}{2}\frac{\mathrm{d}t_t}{\mathrm{d}x} + \frac{h}{2}\frac{\mathrm{d}t_b}{\mathrm{d}x}\right) + b\rho g w. \end{aligned} \tag{B.10}$$

Or, combining derivatives:

$$\begin{aligned} b\frac{\mathrm{d}N_{11}}{\mathrm{d}x} - \rho A\ddot{u}_0 + b(t_t + t_b) &= 0, \\ b\frac{\mathrm{d}^2M_{11}}{\mathrm{d}x^2} + b\frac{\mathrm{d}}{\mathrm{d}x}\left(N_{11}\frac{\mathrm{d}w}{\mathrm{d}x}\right) &= \rho A\ddot{w}_0 - b\left(p_t + p_b - \frac{h}{2}\frac{\mathrm{d}t_t}{\mathrm{d}x} + \frac{h}{2}\frac{\mathrm{d}t_b}{\mathrm{d}x}\right) + b\rho g w. \end{aligned} \tag{B.11}$$

Furthermore, N_{11} and M_{11} are defined by:

$$\begin{aligned} N_{11} &= \int_{-\frac{h}{2}}^{\frac{h}{2}} E\left(\frac{\mathrm{d}u}{\mathrm{d}x} - z\frac{\mathrm{d}^2w}{\mathrm{d}x^2} + \frac{1}{2}\left(\frac{\mathrm{d}w}{\mathrm{d}x}\right)^2\right)\mathrm{d}x = Eh\left(\frac{\mathrm{d}u}{\mathrm{d}x} + \frac{1}{2}\left(\frac{\mathrm{d}w}{\mathrm{d}x}\right)^2\right), \\ M_{11} &= \int_{-\frac{h}{2}}^{\frac{h}{2}} Ez\left(\frac{\mathrm{d}u}{\mathrm{d}x} - z\frac{\mathrm{d}^2w}{\mathrm{d}x^2} + \frac{1}{2}\left(\frac{\mathrm{d}w}{\mathrm{d}x}\right)^2\right)\mathrm{d}x = -\frac{Eh^3}{12}\frac{\mathrm{d}^2w}{\mathrm{d}x^2}. \end{aligned}$$

As a result, the equations of motion become:

$$\begin{aligned} -EA\left(\frac{\mathrm{d}^2u}{\mathrm{d}x^2} + \frac{\mathrm{d}w}{\mathrm{d}x}\frac{\mathrm{d}^2w}{\mathrm{d}x^2}\right) + \rho A\ddot{u}_0 &= b(t_t + t_b), \\ -EA\left[\frac{\mathrm{d}w}{\mathrm{d}x}\left(\frac{\mathrm{d}^2u}{\mathrm{d}x^2} + \frac{\mathrm{d}w}{\mathrm{d}x}\frac{\mathrm{d}^2w}{\mathrm{d}x^2}\right) + \frac{\mathrm{d}^2w}{\mathrm{d}x^2}\left(\frac{\mathrm{d}u}{\mathrm{d}x} + \frac{1}{2}\left(\frac{\mathrm{d}w}{\mathrm{d}x}\right)^2\right)\right] + EI\frac{\mathrm{d}^4w}{\mathrm{d}x^4} & \\ \rho A\ddot{w}_0 = b\left(p_t + p_b - \frac{h}{2}\frac{\mathrm{d}t_t}{\mathrm{d}x} + \frac{h}{2}\frac{\mathrm{d}t_b}{\mathrm{d}x}\right) - b\rho g w. & \end{aligned}$$

Or, again, when combining derivatives:

$$\begin{aligned} -EA\left(\frac{\mathrm{d}^2u}{\mathrm{d}x^2} + \frac{\mathrm{d}w}{\mathrm{d}x}\frac{\mathrm{d}^2w}{\mathrm{d}x^2}\right) + \rho A\ddot{u}_0 &= b(t_t + t_b), \\ -EA\frac{\mathrm{d}}{\mathrm{d}x}\left[\left(\frac{\mathrm{d}u}{\mathrm{d}x} + \frac{1}{2}\left(\frac{\mathrm{d}w}{\mathrm{d}x}\right)^2\right)\frac{\mathrm{d}w}{\mathrm{d}x}\right] + EI\frac{\mathrm{d}^4w}{\mathrm{d}x^4} & \\ \rho A\ddot{w}_0 = b\left(p_t + p_b - \frac{h}{2}\frac{\mathrm{d}t_t}{\mathrm{d}x} + \frac{h}{2}\frac{\mathrm{d}t_b}{\mathrm{d}x}\right) - b\rho g w. & \end{aligned} \tag{B.12}$$

Neglecting hydrostatic pressure $b\rho g w$, letting $p = b(p_t + p_b)$ and $t = b(t_t + t_b)$, this simplifies to:

$$\begin{aligned} -EA\left(\frac{\mathrm{d}^2 u}{\mathrm{d}x^2} + \frac{\mathrm{d}w}{\mathrm{d}x}\frac{\mathrm{d}^2 w}{\mathrm{d}x^2}\right) + \rho A\ddot{u}_0 &= t, \\ -EA\frac{\mathrm{d}}{\mathrm{d}x}\left[\left(\frac{\mathrm{d}u}{\mathrm{d}x} + \frac{1}{2}\left(\frac{\mathrm{d}w}{\mathrm{d}x}\right)^2\right)\frac{\mathrm{d}w}{\mathrm{d}x}\right] + EI\frac{\mathrm{d}^4 w}{\mathrm{d}x^4} + \rho A\ddot{w}_0 &= p. \end{aligned} \tag{B.13}$$

This is a result which can also be derived from the derivations by Reddy[140]. It represents the behaviour of the nonlinear Euler-Bernoulli beam including membrane deformations, i.e. stretching. When horizontal deformations are neglected, the following result is obtained:

$$-EA\frac{3}{2}\frac{\mathrm{d}^2 w}{\mathrm{d}x^2}\left(\frac{\mathrm{d}w}{\mathrm{d}x}\right)^2 + EI\frac{\mathrm{d}^4 w}{\mathrm{d}x^4} + \rho A\ddot{w}_0 = p. \tag{B.14}$$

From all of the above and in particular Equation (B.13), it is clear that neglecting membrane stresses, and hydrostatic pressure the first equation vanishes and that the second equation simplifies to the ordinary differential equation

$$EI\frac{\mathrm{d}^4 w}{\mathrm{d}x^4} + \rho A\ddot{w}_0 = p. \tag{B.15}$$

Which is known from many elementary textbooks (Hibbeler [151] amongst others) as the Euler-Bernoulli beam equation.

B.3 Kirchhoff-Love shell model

B.3.1 Variations of the relevant tensors

The strain tensor $\underline{\underline{\varepsilon}}$ is given by (see Equation (3.7))

$$\underline{\underline{\varepsilon}} = \frac{1}{2}\begin{bmatrix} \frac{\partial \mathbf{c}}{\partial\theta_1}\cdot\frac{\partial \mathbf{c}}{\partial\theta_1} - \frac{\partial \mathbf{C}}{\partial\theta_1}\cdot\frac{\partial \mathbf{C}}{\partial\theta_1} & \frac{\partial \mathbf{c}}{\partial\theta_1}\cdot\frac{\partial \mathbf{c}}{\partial\theta_2} - \frac{\partial \mathbf{C}}{\partial\theta_1}\cdot\frac{\partial \mathbf{C}}{\partial\theta_2} \\ \frac{\partial \mathbf{c}}{\partial\theta_1}\cdot\frac{\partial \mathbf{c}}{\partial\theta_2} - \frac{\partial \mathbf{C}}{\partial\theta_1}\cdot\frac{\partial \mathbf{C}}{\partial\theta_2} & \frac{\partial \mathbf{c}}{\partial\theta_2}\cdot\frac{\partial \mathbf{c}}{\partial\theta_2} - \frac{\partial \mathbf{C}}{\partial\theta_2}\cdot\frac{\partial \mathbf{C}}{\partial\theta_2} \end{bmatrix}. \tag{B.16}$$

Since $\mathbf{c} = \mathbf{C} + \mathbf{u}$, the Gateaux derivative is

$$\begin{aligned} &\underline{\underline{\varepsilon}}'(\mathbf{u},\mathbf{v}) = \frac{\mathrm{d}}{\mathrm{d}\theta}\underline{\underline{\varepsilon}}(\mathbf{u}+\theta\mathbf{v})|_{\theta=0} = \\ &\frac{\mathrm{d}}{\mathrm{d}\theta}\frac{1}{2}\begin{bmatrix} \frac{\partial}{\partial\theta_1}(\mathbf{C}+\mathbf{u}+\theta\mathbf{v})\cdot\frac{\partial}{\partial\theta_1}(\mathbf{C}+\mathbf{u}+\theta\mathbf{v}) - \frac{\partial \mathbf{C}}{\partial\theta_1}\cdot\frac{\partial \mathbf{C}}{\partial\theta_1} & \frac{\partial}{\partial\theta_1}(\mathbf{C}+\mathbf{u}+\theta\mathbf{v})\cdot\frac{\partial}{\partial\theta_2}(\mathbf{C}+\mathbf{u}+\theta\mathbf{v}) - \frac{\partial \mathbf{C}}{\partial\theta_1}\cdot\frac{\partial \mathbf{C}}{\partial\theta_2} \\ \frac{\partial}{\partial\theta_1}(\mathbf{C}+\mathbf{u}+\theta\mathbf{v})\cdot\frac{\partial}{\partial\theta_2}(\mathbf{C}+\mathbf{u}+\theta\mathbf{v}) - \frac{\partial \mathbf{C}}{\partial\theta_1}\cdot\frac{\partial \mathbf{C}}{\partial\theta_2} & \frac{\partial}{\partial\theta_2}(\mathbf{C}+\mathbf{u}+\theta\mathbf{v})\cdot\frac{\partial}{\partial\theta_2}(\mathbf{C}+\mathbf{u}+\theta\mathbf{v}) - \frac{\partial \mathbf{C}}{\partial\theta_2}\cdot\frac{\partial \mathbf{C}}{\partial\theta_2} \end{bmatrix}\Bigg|_{\theta=0}. \end{aligned}$$

Evaluating the derivatives with respect to θ and evaluating for $\theta = 0$ gives.

$$\underline{\underline{\varepsilon}}'(\mathbf{u},\mathbf{v}) = \begin{bmatrix} \frac{\partial \mathbf{v}}{\partial\theta_1}\cdot\frac{\partial \mathbf{c}}{\partial\theta_1} & \frac{1}{2}\frac{\partial \mathbf{v}}{\partial\theta_1}\cdot\frac{\partial \mathbf{c}}{\partial\theta_2} + \frac{1}{2}\frac{\partial \mathbf{v}}{\partial\theta_2}\cdot\frac{\partial \mathbf{c}}{\partial\theta_1} \\ \frac{1}{2}\frac{\partial \mathbf{v}}{\partial\theta_1}\cdot\frac{\partial \mathbf{c}}{\partial\theta_2} + \frac{1}{2}\frac{\partial \mathbf{v}}{\partial\theta_2}\cdot\frac{\partial \mathbf{c}}{\partial\theta_1} & \frac{\partial \mathbf{v}}{\partial\theta_2}\cdot\frac{\partial \mathbf{c}}{\partial\theta_2} \end{bmatrix}. \tag{B.17}$$

Note that $\mathbf{c} = \mathbf{C}+\mathbf{u}$, again. The off-diagonal terms, i.e. the $\underline{\underline{\varepsilon}}_{12}$ and $\underline{\underline{\varepsilon}}_{21}$ terms are equal and in Voight-notation, this tensor is usually written as

$$\underline{\underline{\varepsilon}}'(\mathbf{u},\mathbf{v}) = \begin{bmatrix} \varepsilon'_{11} \\ \varepsilon'_{22} \\ 2\varepsilon'_{12} \end{bmatrix} = \begin{bmatrix} \frac{\partial \mathbf{v}}{\partial\theta_1}\cdot\frac{\partial \mathbf{c}}{\partial\theta_1} \\ \frac{\partial \mathbf{v}}{\partial\theta_2}\cdot\frac{\partial \mathbf{c}}{\partial\theta_1} \\ \frac{\partial \mathbf{v}}{\partial\theta_1}\cdot\frac{\partial \mathbf{c}}{\partial\theta_2} + \frac{\partial \mathbf{v}}{\partial\theta_2}\cdot\frac{\partial \mathbf{c}}{\partial\theta_1} \end{bmatrix}. \tag{B.18}$$

The curvature tensor is given by (see Equation (3.7))

$$\underline{\underline{\kappa}} = \begin{bmatrix} \frac{\partial^2 \mathbf{C}}{\partial\theta_1^2}\cdot\hat{\mathbf{N}} - \frac{\partial^2 \mathbf{c}}{\partial\theta_1^2}\cdot\hat{\mathbf{n}} & \frac{\partial^2 \mathbf{C}}{\partial\theta_1\partial\theta_2}\cdot\hat{\mathbf{N}} - \frac{\partial^2 \mathbf{c}}{\partial\theta_1\partial\theta_2}\cdot\hat{\mathbf{n}} \\ \frac{\partial^2 \mathbf{C}}{\partial\theta_1\partial\theta_2}\cdot\hat{\mathbf{N}} - \frac{\partial^2 \mathbf{c}}{\partial\theta_1\partial\theta_2}\cdot\hat{\mathbf{n}} & \frac{\partial^2 \mathbf{C}}{\partial\theta_2^2}\cdot\hat{\mathbf{N}} - \frac{\partial^2 \mathbf{c}}{\partial\theta_1^2}\cdot\hat{\mathbf{n}} \end{bmatrix}.$$

Using $\mathbf{c} = \mathbf{C} + \mathbf{u}$, the Gateaux derivative is

$$\underline{\underline{\boldsymbol{\kappa}}}'(\mathbf{u},\mathbf{v}) = \frac{\mathrm{d}}{\mathrm{d}\theta}\underline{\underline{\boldsymbol{\kappa}}}(\mathbf{u}+\theta\mathbf{v})|_{\theta=0}$$
$$= \frac{\mathrm{d}}{\mathrm{d}\theta}\begin{bmatrix} \frac{\partial^2\mathbf{C}}{\partial\theta_1^2}\cdot\hat{\mathbf{N}} - \frac{\partial^2}{\partial\theta_1^2}(\mathbf{C}+\mathbf{u}+\theta\mathbf{v})\cdot\hat{\mathbf{n}}(\mathbf{C}+\mathbf{u}+\theta\mathbf{v}) & \frac{\partial^2\mathbf{C}}{\partial\theta_1\partial\theta_2}\cdot\hat{\mathbf{N}} - \frac{\partial^2}{\partial\theta_1\partial\theta_2}(\mathbf{C}+\mathbf{u}+\theta\mathbf{v})\cdot\hat{\mathbf{n}}(\mathbf{C}+\mathbf{u}+\theta\mathbf{v}) \\ \frac{\partial^2\mathbf{C}}{\partial\theta_1\partial\theta_2}\cdot\hat{\mathbf{N}} - \frac{\partial^2}{\partial\theta_1\partial\theta_2}(\mathbf{C}+\mathbf{u}+\theta\mathbf{v})\cdot\hat{\mathbf{n}}(\mathbf{C}+\mathbf{u}+\theta\mathbf{v}) & \frac{\partial^2\mathbf{C}}{\partial\theta_2^2}\cdot\hat{\mathbf{N}} - \frac{\partial^2}{\partial\theta_1^2}(\mathbf{C}+\mathbf{u}+\theta\mathbf{v})\cdot\hat{\mathbf{n}}(\mathbf{C}+\mathbf{u}+\theta\mathbf{v}) \end{bmatrix}\Bigg|_{\theta=0}.$$

Evaluating the Gateaux derivative gives

$$\underline{\underline{\boldsymbol{\kappa}}}'(\mathbf{u},\mathbf{v}) = \begin{bmatrix} -\frac{\partial^2\mathbf{v}}{\partial\theta_1^2}\cdot\hat{\mathbf{n}} - \frac{\partial^2\mathbf{c}}{\partial\theta_1^2}\cdot\hat{\mathbf{n}}' & -\frac{\partial^2\mathbf{v}}{\partial\theta_1\partial\theta_2}\cdot\hat{\mathbf{n}} - \frac{\partial^2\mathbf{c}}{\partial\theta_1\partial\theta_2}\cdot\hat{\mathbf{n}}' \\ -\frac{\partial^2\mathbf{v}}{\partial\theta_1\partial\theta_2}\cdot\hat{\mathbf{n}} - \frac{\partial^2\mathbf{c}}{\partial\theta_1\partial\theta_2}\cdot\hat{\mathbf{n}}'\cdot\mathbf{v} & -\frac{\partial^2\mathbf{v}}{\partial\theta_2^2} - \frac{\partial^2\mathbf{c}}{\partial\theta_2^2}\cdot\hat{\mathbf{n}}' \end{bmatrix}.$$

Or, in Voight notation

$$\underline{\underline{\boldsymbol{\kappa}}}'(\mathbf{u},\mathbf{v}) = \begin{bmatrix}\kappa'_{11}\\ \kappa'_{22}\\ 2\kappa'_{12}\end{bmatrix} = \begin{bmatrix} -\frac{\partial^2\mathbf{v}}{\partial\theta_1^2}\cdot\hat{\mathbf{n}} - \frac{\partial^2\mathbf{c}}{\partial\theta_1^2}\cdot\hat{\mathbf{n}}' \\ -\frac{\partial^2\mathbf{v}}{\partial\theta_2^2}\cdot\hat{\mathbf{n}} - \frac{\partial^2\mathbf{c}}{\partial\theta_2^2}\cdot\hat{\mathbf{n}}' \\ -2\frac{\partial^2\mathbf{v}}{\partial\theta_1\partial\theta_2}\cdot\hat{\mathbf{n}} - 2\frac{\partial^2\mathbf{c}}{\partial\theta_1\partial\theta_2}\cdot\hat{\mathbf{n}}' \end{bmatrix}. \tag{B.19}$$

Here, $\hat{\mathbf{n}}'$ denotes the Gateaux derivative of the normal vector $\hat{\mathbf{n}}$. This term is given by [142]

$$\begin{aligned}
\hat{\mathbf{n}}' &= \frac{\mathrm{d}}{\mathrm{d}\theta}\left[\frac{\frac{\partial}{\partial\theta^1}(\mathbf{C}+\mathbf{u}+\theta\mathbf{v})\times\frac{\partial}{\partial\theta^2}(\mathbf{C}+\mathbf{u}+\theta\mathbf{v})}{\left\|\frac{\partial}{\partial\theta^1}(\mathbf{C}+\mathbf{u}+\theta\mathbf{v})\times\frac{\partial}{\partial\theta^2}(\mathbf{C}+\mathbf{u}+\theta\mathbf{v})\right\|}\right]_{\theta=0} \\
&= \frac{1}{\left\|\frac{\partial\mathbf{c}}{\partial\theta^1}\times\frac{\partial\mathbf{c}}{\partial\theta^2}\right\|}\frac{\mathrm{d}}{\mathrm{d}\theta}\left[\frac{\partial}{\partial\theta^1}(\mathbf{C}+\mathbf{u}+\theta\mathbf{v})\times\frac{\partial}{\partial\theta^2}(\mathbf{C}+\mathbf{u}+\theta\mathbf{v})\right]_{\theta=0} + \\
&\quad \left(\frac{\partial\mathbf{c}}{\partial\theta^1}\times\frac{\partial\mathbf{c}}{\partial\theta^2}\right)\frac{\mathrm{d}}{\mathrm{d}\theta}\left[\frac{1}{\left\|\frac{\partial}{\partial\theta^1}(\mathbf{C}+\mathbf{u}+\theta\mathbf{v})\times\frac{\partial}{\partial\theta^2}(\mathbf{C}+\mathbf{u}+\theta\mathbf{v})\right\|}\right]_{\theta=0} \\
&= \frac{\frac{\partial\mathbf{v}}{\partial\theta^1}\times\frac{\partial\mathbf{c}}{\partial\theta^2}+\frac{\partial\mathbf{c}}{\partial\theta^1}\times\frac{\partial\mathbf{v}}{\partial\theta^2}}{\left\|\frac{\partial\mathbf{c}}{\partial\theta^1}\times\frac{\partial\mathbf{c}}{\partial\theta^2}\right\|} + \left[-\frac{1}{\left\|\frac{\partial\mathbf{c}}{\partial\theta^1}\times\frac{\partial\mathbf{c}}{\partial\theta^2}\right\|^2}\frac{\frac{\partial\mathbf{c}}{\partial\theta^1}\times\frac{\partial\mathbf{c}}{\partial\theta^2}}{\left\|\frac{\partial\mathbf{c}}{\partial\theta^1}\times\frac{\partial\mathbf{c}}{\partial\theta^2}\right\|}\left(\frac{\partial\mathbf{v}}{\partial\theta^1}\times\frac{\partial\mathbf{c}}{\partial\theta^2}+\frac{\partial\mathbf{c}}{\partial\theta^1}\times\frac{\partial\mathbf{v}}{\partial\theta^2}\right)\right] \\
&= \mathbf{m}_v - (\hat{\mathbf{n}}\cdot\mathbf{m}_v)\hat{\mathbf{n}}.
\end{aligned} \tag{B.20}$$

Here,

$$\mathbf{m}_v = \frac{\frac{\partial\mathbf{v}}{\partial\theta^1}\times\frac{\partial\mathbf{c}}{\partial\theta^2}+\frac{\partial\mathbf{c}}{\partial\theta^1}\times\frac{\partial\mathbf{v}}{\partial\theta^2}}{\left\|\frac{\partial\mathbf{c}}{\partial\theta^1}\times\frac{\partial\mathbf{c}}{\partial\theta^2}\right\|}. \tag{B.21}$$

For evaluation of the Jacobian matrix, alternatively the tangential stiffness matrix, the Gateaux derivatives of the force and moment tensors, $\underline{\underline{\boldsymbol{n}}}'$ and $\underline{\underline{\boldsymbol{m}}}'$, and the second Gateaux derivatives of the strain and curvature tensors, $\underline{\underline{\boldsymbol{\varepsilon}}}''$ and $\underline{\underline{\boldsymbol{\kappa}}}''$ are required. Firstly, under the Kirchhoff assumptions, the force and moment tensors are defined by Equations (3.13) and (3.14), recalled here for the sake of completeness

$$\begin{aligned}
\underline{\underline{\boldsymbol{n}}} &= \int_{[-\frac{t}{2},\frac{t}{2}]}\underline{\underline{\boldsymbol{S}}}\,\mathrm{d}\theta_3 = \int_{[-\frac{t}{2},\frac{t}{2}]}\mathcal{C}:(\underline{\underline{\boldsymbol{\varepsilon}}}+\theta_3\underline{\underline{\boldsymbol{\kappa}}})\,\mathrm{d}\theta_3 = t\mathcal{C}:\underline{\underline{\boldsymbol{\varepsilon}}} \\
\underline{\underline{\boldsymbol{m}}} &= \int_{[-\frac{t}{2},\frac{t}{2}]}\theta_3\underline{\underline{\boldsymbol{S}}}\,\mathrm{d}\theta_3 = \int_{[-\frac{t}{2},\frac{t}{2}]}\mathcal{C}:(\theta_3\underline{\underline{\boldsymbol{\varepsilon}}}+\theta_3^3\underline{\underline{\boldsymbol{\kappa}}})\,\mathrm{d}\theta_3 = \frac{t^3}{12}\mathcal{C}:\underline{\underline{\boldsymbol{\kappa}}}.
\end{aligned}$$

Since the material tensor $\mathcal{C}$ does not depend on the solution, the Gateaux derivatives of the force and moment tensors are simply given by

$$\underline{\underline{\boldsymbol{n}}}'(\mathbf{u},\mathbf{v}) = t\mathcal{C}:\underline{\underline{\boldsymbol{\varepsilon}}}'(\mathbf{u},\mathbf{v}), \tag{B.22}$$

$$\underline{\underline{\boldsymbol{m}}}'(\mathbf{u},\mathbf{v}) = \frac{t^3}{12}\mathcal{C}:\underline{\underline{\boldsymbol{\kappa}}}'(\mathbf{u},\mathbf{v}). \tag{B.23}$$

The second Gateaux derivatives of the strain tensor is derived from the first derivative from Equation (B.17). Applying a variation of the displacement $\mathbf{u}$ gives the following formulation. Note that the variation is expressed

using the deformed mid-plane $\mathbf{c}$ since there is no need to express it using the displacement vector $\mathbf{u}$ and the undeformed configuration $\mathbf{C}$.

$$\begin{aligned}\underline{\underline{\boldsymbol{\varepsilon}}}'' &= \frac{\mathrm{d}}{\mathrm{d}\theta}\underline{\underline{\boldsymbol{\varepsilon}}}'(\mathbf{u}+\theta\mathbf{w},\mathbf{v})|_{\theta=0} \\ &= \frac{\mathrm{d}}{\mathrm{d}\theta}\begin{bmatrix} \frac{\partial \mathbf{v}}{\partial\theta_1}\cdot\frac{\partial}{\partial\theta_1}(\mathbf{c}+\theta\mathbf{w}) & \frac{1}{2}\frac{\partial \mathbf{v}}{\partial\theta_1}\cdot\frac{\partial}{\partial\theta_2}(\mathbf{c}+\theta\mathbf{w})+\frac{1}{2}\frac{\partial \mathbf{v}}{\partial\theta_1}\cdot\frac{\partial}{\partial\theta_2}(\mathbf{c}+\theta\mathbf{w}) \\ \frac{1}{2}\frac{\partial \mathbf{v}}{\partial\theta_2}\cdot\frac{\partial}{\partial\theta_1}(\mathbf{c}+\theta\mathbf{w})+\frac{1}{2}\frac{\partial \mathbf{v}}{\partial\theta_2}\cdot\frac{\partial}{\partial\theta_1}(\mathbf{c}+\theta\mathbf{w}) & \frac{\partial \mathbf{v}}{\partial\theta_2}\cdot\frac{\partial}{\partial\theta_2}(\mathbf{c}+\theta\mathbf{w}) \end{bmatrix}\Bigg|_{\theta=0}.\end{aligned}$$

Elementary differentiation operations provide the second Gateaux derivative of the strain tensor:

$$\underline{\underline{\boldsymbol{\varepsilon}}}'' = \begin{bmatrix} \frac{\partial \mathbf{v}}{\partial\theta_1}\cdot\frac{\partial \mathbf{w}}{\partial\theta_1} & \frac{1}{2}\frac{\partial \mathbf{v}}{\partial\theta_1}\cdot\frac{\partial \mathbf{w}}{\partial\theta_2}+\frac{1}{2}\frac{\partial \mathbf{v}}{\partial\theta_2}\cdot\frac{\partial \mathbf{w}}{\partial\theta_1} \\ \frac{1}{2}\frac{\partial \mathbf{v}}{\partial\theta_1}\cdot\frac{\partial \mathbf{w}}{\partial\theta_2}+\frac{1}{2}\frac{\partial \mathbf{v}}{\partial\theta_2}\cdot\frac{\partial \mathbf{w}}{\partial\theta_1} & \frac{\partial \mathbf{v}}{\partial\theta_2}\cdot\frac{\partial \mathbf{w}}{\partial\theta_2} \end{bmatrix}.$$

In Voight notation:

$$\underline{\underline{\boldsymbol{\varepsilon}}}'' = \begin{bmatrix} \varepsilon_{11}'' \\ \varepsilon_{22}'' \\ 2\varepsilon_{12}'' \end{bmatrix} = \begin{bmatrix} \frac{\partial \mathbf{v}}{\partial\theta_1}\cdot\frac{\partial \mathbf{w}}{\partial\theta_1} \\ \frac{\partial \mathbf{v}}{\partial\theta_2}\cdot\frac{\partial \mathbf{w}}{\partial\theta_2} \\ \frac{\partial \mathbf{v}}{\partial\theta_1}\cdot\frac{\partial \mathbf{w}}{\partial\theta_2}+\frac{\partial \mathbf{v}}{\partial\theta_1}\cdot\frac{\partial \mathbf{w}}{\partial\theta_2} \end{bmatrix}. \tag{B.24}$$

The second Gateaux derivative of the curvature tensor is derived from the first Gateaux derivative in a similar way.

$$\begin{aligned}\underline{\underline{\boldsymbol{\kappa}}}''(\mathbf{u},\mathbf{v},\mathbf{w}) &= \frac{\mathrm{d}}{\mathrm{d}\theta}\underline{\underline{\boldsymbol{\kappa}}}'(\mathbf{u}+\theta\mathbf{w},\mathbf{v})|_{\theta=0} \\ &= \begin{bmatrix} -\frac{\partial^2 \mathbf{v}}{\partial\theta_1^2}\cdot\hat{\mathbf{n}}(\mathbf{c}+\theta\mathbf{w},\mathbf{v})-\frac{\partial^2}{\partial\theta_1^2}(\mathbf{c}+\theta\mathbf{v})\cdot\hat{\mathbf{n}}'(\mathbf{c}+\theta\mathbf{v}) & -\frac{\partial^2 \mathbf{v}}{\partial\theta_1\partial\theta_2}\cdot\hat{\mathbf{n}}-\frac{\partial^2}{\partial\theta_1\partial\theta_2}(\mathbf{c}+\theta\mathbf{v})\cdot\hat{\mathbf{n}}'(\mathbf{c}+\theta\mathbf{v}) \\ -\frac{\partial^2 \mathbf{v}}{\partial\theta_1\partial\theta_2}\cdot\hat{\mathbf{n}}-\frac{\partial^2}{\partial\theta_1\partial\theta_2}(\mathbf{c}+\theta\mathbf{v})\cdot\hat{\mathbf{n}}' & -\frac{\partial^2 \mathbf{v}}{\partial\theta_2^2}\cdot\hat{\mathbf{n}}-\frac{\partial^2}{\partial\theta_2^2}(\mathbf{c}+\theta\mathbf{v})\cdot\hat{\mathbf{n}}'(\mathbf{c}+\theta\mathbf{v}) \end{bmatrix}\Bigg|_{\theta=0}.\end{aligned}$$

Evaluating the derivatives with respect to θ and substituting $\theta = 0$ gives:

$$\begin{aligned}&\underline{\underline{\boldsymbol{\kappa}}}''(\mathbf{u},\mathbf{v},\mathbf{w}) \\ &\quad= \begin{bmatrix} -\frac{\partial^2 \mathbf{v}}{\partial\theta_1^2}\cdot\hat{\mathbf{n}}'-\left(\frac{\partial^2 \mathbf{w}}{\partial\theta_1^2}\cdot\hat{\mathbf{n}}'+\frac{\partial^2 \mathbf{c}}{\partial\theta_1^2}\cdot\hat{\mathbf{n}}''\right) & -\frac{\partial^2 \mathbf{v}}{\partial\theta_1\partial\theta_2}\cdot\hat{\mathbf{n}}-\left(\frac{\partial^2 \mathbf{w}}{\partial\theta_1\partial\theta_2}\cdot\hat{\mathbf{n}}'+\frac{\partial^2 \mathbf{c}}{\partial\theta_1\partial\theta_2}\cdot\hat{\mathbf{n}}''\right) \\ -\frac{\partial^2 \mathbf{v}}{\partial\theta_1\partial\theta_2}\cdot\hat{\mathbf{n}}-\left(\frac{\partial^2 \mathbf{w}}{\partial\theta_1\partial\theta_2}\cdot\hat{\mathbf{n}}'+\frac{\partial^2 \mathbf{c}}{\partial\theta_1\partial\theta_2}\cdot\hat{\mathbf{n}}''\right) & -\frac{\partial^2 \mathbf{v}}{\partial\theta_1^2}\cdot\hat{\mathbf{n}}'-\left(\frac{\partial^2 \mathbf{w}}{\partial\theta_1^2}\cdot\hat{\mathbf{n}}'+\frac{\partial^2 \mathbf{c}}{\partial\theta_1^2}\cdot\hat{\mathbf{n}}''\right) \end{bmatrix}.\end{aligned}$$

Or in Voight notation:

$$\underline{\underline{\boldsymbol{\kappa}}}'' = \begin{bmatrix} \kappa_{11}'' \\ \kappa_{22}'' \\ 2\kappa_{12}'' \end{bmatrix} = \begin{bmatrix} -\frac{\partial^2 \mathbf{v}}{\partial\theta_1^2}\cdot\hat{\mathbf{n}}'-\left(\frac{\partial^2 \mathbf{w}}{\partial\theta_1^2}\cdot\hat{\mathbf{n}}'+\frac{\partial^2 \mathbf{c}}{\partial\theta_1^2}\cdot\hat{\mathbf{n}}''\right) \\ -\frac{\partial^2 \mathbf{v}}{\partial\theta_1^2}\cdot\hat{\mathbf{n}}'-\left(\frac{\partial^2 \mathbf{w}}{\partial\theta_1^2}\cdot\hat{\mathbf{n}}'+\frac{\partial^2 \mathbf{c}}{\partial\theta_1^2}\cdot\hat{\mathbf{n}}''\right) \\ -\frac{\partial^2 \mathbf{v}}{\partial\theta_1\partial\theta_2}\cdot\hat{\mathbf{n}}-\left(\frac{\partial^2 \mathbf{w}}{\partial\theta_1\partial\theta_2}\cdot\hat{\mathbf{n}}'+\frac{\partial^2 \mathbf{c}}{\partial\theta_1\partial\theta_2}\cdot\hat{\mathbf{n}}''\right) \end{bmatrix}. \tag{B.25}$$

As seen in this formulation, the last tensor to be obtained is the second Gateaux derivative of the normal vector. Similar to the second derivatives of the strain and curvature tensors, the second derivative of the normal vector is also obtained using the first derivative (applying product rules on Equation (B.20))

$$\hat{\mathbf{n}}'' = \mathbf{m}_v - (\hat{\mathbf{n}}'\cdot\mathbf{m}_v + \hat{\mathbf{n}}\cdot\mathbf{m}_v')\hat{\mathbf{n}} - (\hat{\mathbf{n}}\cdot\mathbf{m}_v)\hat{\mathbf{n}}'$$

Where all primes ($\prime$) denote Gateaux derivatives. The variation of the term $\mathbf{m}_v$ is (recall the definition of this term from Equation (B.21)) is:

$$\begin{aligned}\mathbf{m}_v' &= \frac{\mathrm{d}}{\mathrm{d}\theta}\mathbf{m}_v(\mathbf{u}+\theta w,\mathbf{v})\Big|_{\theta=0} \\ &= \frac{\mathrm{d}}{\mathrm{d}\theta}\left[\frac{1}{\|\hat{\mathbf{n}}\|}\left(\frac{\partial \mathbf{v}}{\partial\theta_1}\times\frac{\partial}{\partial\theta_2}(\mathbf{c}+\theta\mathbf{w})+\frac{\partial}{\partial\theta_1}(\mathbf{c}+\theta\mathbf{w})\times\frac{\partial \mathbf{v}}{\partial\theta_2}\right)\right]\Bigg|_{\theta=0} \\ &= \frac{1}{\|\hat{\mathbf{n}}\|}\left(\frac{\partial \mathbf{v}}{\partial\theta_1}\times\frac{\partial \mathbf{w}}{\partial\theta_2}+\frac{\partial \mathbf{w}}{\partial\theta_1}\times\frac{\partial \mathbf{v}}{\partial\theta_2}\right)-\frac{1}{\|\hat{\mathbf{n}}\|^2}\hat{\mathbf{n}}\left(\frac{\partial \mathbf{c}}{\partial\theta_1}\times\frac{\partial \mathbf{w}}{\partial\theta_2}+\frac{\partial \mathbf{w}}{\partial\theta_1}\times\frac{\partial \mathbf{c}}{\partial\theta_2}\right)\left(\frac{\partial \mathbf{v}}{\partial\theta_1}\times\frac{\partial \mathbf{w}}{\partial\theta_2}+\frac{\partial \mathbf{w}}{\partial\theta_1}\times\frac{\partial \mathbf{v}}{\partial\theta_2}\right).\end{aligned}$$

With this term, all necessary terms for the variational form of the Kirchhoff-Love shell have been derived.

C | Analytical Solutions

C.1 Vibrations of a Circular Plate With Clamped Boundaries

In this section, the derivation of the mode shapes and the eigenfrequencies of a circular clamped plate will be given. Derivations are based on general partial differential equations. The reader is referred to the book of Haberman [227] for more details about this topic.

As discussed in many books on finite elements for structures, for instance the books of Reddy[95, 228, 140], the governing Partial Differential Equation (PDE) for a linear plate is:

$$\rho t \frac{\partial^2 w}{\partial t^2} + D\nabla^2\nabla^2 w = p. \tag{C.1}$$

Where ρ is the density of the material of the plate, t is the thickness of the plate, D is the flexural rigidity, w is the vertical displacement of the plate and p is an externally distributed load. Furthermore, ∇^2 is the Laplacian, which reads in polar coordinates:

$$\nabla^2 w = \frac{\partial^2 w}{\partial r^2} + \frac{1}{r}\frac{\partial w}{\partial r} + \frac{1}{r^2}\frac{\partial^2 w}{\partial r \partial \theta},$$

such that,

$$\nabla^2\nabla^2 w = \frac{1}{r^4}\left[r^4\frac{\partial^4 w}{\partial r^4} + 2r^3\frac{\partial^3 w}{\partial r^3} - r^2\frac{\partial^2 w}{\partial r^2} + 2r^2\frac{\partial^4 w}{\partial r^2\partial\theta^2}r\frac{\partial w}{\partial r} - 2r\frac{\partial w}{\partial r\partial\theta^2} + 4\frac{\partial^2 w}{\partial\theta^2} + \frac{\partial^4 w}{\partial\theta^4}\right].$$

Since free vibrations are considered, the surface load $p(x)$ is the zero functions. Then, Equation (C.1) becomes:

$$\rho t\frac{\partial^2 w}{\partial t^2} + \frac{1}{r^4}\left[r^4\frac{\partial^4 w}{\partial r^4} + 2r^3\frac{\partial^3 w}{\partial r^3} - r^2\frac{\partial^2 w}{\partial r^2} + 2r^2\frac{\partial^4 w}{\partial r^2\partial\theta^2} + r\frac{\partial w}{\partial r} - 2r\frac{\partial w}{\partial r\partial\theta^2} + 4\frac{\partial^2 w}{\partial\theta^2} + \frac{\partial^4 w}{\partial\theta^4}\right] = 0.$$

Now, let us assume that the solution in polar coordinates $w(r,\theta,t)$ is a product of the functions $R(r)$, $\Theta(\theta)$ and $T(t)$, i.e. we will solve the equation using *separation of variables*. Furthermore, we denote first and second order derivatives by $'$ and $''$, respectively, and higher order derivatives by the superscripts $^{(3)}$, $^{(4)}$ etc.

$$\rho t R\Theta T'' + D\left[R^{(4)}\Theta T + \frac{2}{r}R^{(3)}\Theta T - \frac{1}{r^2}R''\Theta T + \frac{2}{r^2}R''\Theta'' T + \frac{1}{r^3}R'\Theta T - \frac{2}{r^3}R'\Theta'' T + \frac{4}{r^4}R\Theta'' T + \frac{1}{r^4}R\Theta^{(4)}T\right] = 0.$$

Moving the inertia term (first term) to the right-hand side and dividing both sides by $R\Theta T$ gives:

$$\frac{D}{R\Theta}\left[R^{(4)}\Theta + \frac{2}{r}R^{(3)}\Theta - \frac{1}{r^2}R''\Theta + \frac{2}{r^2}R''\Theta'' + \frac{1}{r^3}R'\Theta - \frac{2}{r^3}R'\Theta'' + \frac{4}{r^4}R\Theta'' + \frac{1}{r^4}R\Theta^{(4)}\right] = -\rho t\frac{T''}{T} = \omega^2.$$

Here, ω is the *eigenfrequency*. From the right equality sign, we see that

$$T = A\exp(i\omega t) + B\exp(-i\omega t).$$

Furthermore, we see that the left-hand side gives:

$$\frac{D}{R\Theta}\left[R^{(4)}\Theta + \frac{2}{r}R^{(3)}\Theta - \frac{1}{r^2}R''\Theta + \frac{2}{r^2}R''\Theta'' + \frac{1}{r^3}R'\Theta - \frac{2}{r^3}R'\Theta'' + \frac{4}{r^4}R\Theta'' + \frac{1}{r^4}R\Theta^{(4)}\right] = \frac{\omega^2\rho t}{D}R\Theta = \lambda^2 R\Theta.$$

For the sake of brievety, define $v(r\theta) = R(r)\Theta(t)$. We see that λ is an eigenvalue of the system

$$(\nabla^2\nabla^2 - \lambda^2)v = 0.$$

Or, when $\gamma^4 = \lambda^2$,

$$(\nabla^2 + \gamma^2)(\nabla^2 - \gamma^2)v = 0. \tag{C.2}$$

Furthermore, by definition of the coordinate system, the coordinate θ is periodical. This implies that the function $\Theta(\theta)$ should also be periodical. Taking this into account, the solution of v has the form:

$$v(r, \theta) = R(r)\exp(im\theta).$$

Where $m \in \mathbb{N}$. Substituting this in Equation (C.2) gives:

$$\left(R'' + \frac{1}{r}R' + \left(\gamma^2 - \frac{1}{r^2}Rm^2\right)\right)\exp(im\theta)\left(R'' + \frac{1}{r}R' - \left(\gamma^2 + \frac{1}{r^2}Rm^2\right)\right)\exp(im\theta) = 0.$$

Now, let $R = A_m(r) + B_m(r)$. Then,

$$A_m'' + \frac{1}{r}A_m' + \left(\gamma^2 - \frac{m^2}{r^2}\right)A_m = 0,$$
$$B_m'' + \frac{1}{r}B_m' - \left(\gamma^2 + \frac{m^2}{r^2}\right)B_m = 0.$$

These functions correspond to the Bessel Differential Equations. Hence, their solutions are

$$A_m = C_1 J_m(\gamma r) + C_3 Y_m(\gamma r),$$
$$B_m = C_2 I_m(\gamma r) + C_4 K_m(\gamma r).$$

Where $J_m(r)$ and $Y_m(r)$, $I_m(r)$ and $K_m(r)$ are the Bessel functions of the first and second kind and the Modified Bessel functions of the first and second kind, respectively. The functions $Y_m(r)$ and $K_m(r)$ have a singularity for $r = 0$, which is in the middle of the plate, and therefore the coefficients C_3 and C_4 must be equal to zero. Therefore, the solution for $R(r)$ becomes:

$$R(r) = C_1 J_m(\gamma r) + C_2 I_m(\gamma r).$$

The coefficients C_1 and C_2 have to be determined based on the boundary conditions of the plate. Suppose the edge of the plate is fully clamped. If the plate has radius a, the following boundary conditions have to be imposed:

$$R(a) = 0 \qquad R'(a) = 0.$$

This yields the following two equations:

$$R(a) = C_1 J_m(\gamma a) + C_2 I_m(\gamma a) = 0,$$
$$R'(a) = C_1 J_m'(\gamma a) + C_2 I_m'(\gamma a) = 0.$$

Since there are two equations and two unknowns, the boundary conditions can be written as a linear system. From the first equation, it can be seen that if $C_1 = I_m(\gamma a)$ and if $C_2 = -J_m(\gamma a)$ the equation is satisfied. The solution of the system is the trivial solution, i.e. $[C_1, C_2] = [0, 0]$. Hence to find the non-trivial solutions, the determinant of the system should be equal to zero.

$$I_m'(\gamma a)J_m(\gamma a) - I_m(\gamma a)J_m'(\gamma a) = 0.$$

The derivatives of the Bessel function of the first kind $J_m(r)$ and the modified Bessel function of the first kind $I_m(r)$ with respect to r are:

$$\frac{\mathrm{d}}{\mathrm{d}r}\left(J_m'(r)\right) = J_{m-1}(r) - \frac{m}{r}J_m(r),$$
$$\frac{\mathrm{d}}{\mathrm{d}r}\left(I_m'(r)\right) = I_{m-1}(r) - \frac{m}{r}I_m(r).$$

Such that the determinant becomes:

$$\left(I_{m-1}(\gamma a) - \frac{m}{a} I_m(\gamma a)\right) J_m(\gamma a) - I_m(\gamma a) \left(J_{m-1}(\gamma a) - \frac{m}{a} J_m(\gamma a)\right) = 0. \tag{C.3}$$

The values of γ for which the determinant is zero are the roots of the equation. In the sequel, we denote the n^{th} of the determinant for m by $\gamma(m,n)$. When a root $\gamma(m,n)$ is known, the corresponding mode shape with modal amplitude α can be computed by:

$$\begin{aligned} v(r,\theta) &= R(r)\Theta(\theta) \quad \text{with:} \\ R(r) &= \alpha \left[I_m(\gamma a) J_m(\gamma_a) - J_m(\gamma a) I_m(\gamma a)\right] \\ \Theta(\theta) &= \exp(im\theta). \end{aligned}$$

If there is a time-dependent forcing term $p(r,\theta,t)$, the equation for $T(t)$ should be solved with the initial condition, such that the transient solution $w(r,\theta,t)$ is obtained. In Table C.1, the roots of the determinant are given for $m \leq 10$ and $n \leq 10$, obtained by an `fsolve` root finder from the `scipy` optimization library in Python [229]. Also note that by the definition of γ, the eigenfrequency ω can be computed:

$$\gamma^4 = \frac{\omega^2 \rho t}{D} \iff \omega^2 = \frac{\gamma^4 D}{\rho t}.$$

Mode shapes are given in Figure 5.17.

Table C.1: Roots $\gamma(m,n)$ for the determinant in Equation (C.3)

3.1962206	6.3064370	9.4394991	12.5771306	15.7164385	18.8565455	21.9970952	25.1379154	28.2789131
4.6108999	7.7992738	10.9580672	14.1086278	17.2557270	20.4010449	23.5453255	26.6889492	29.8321305
5.9056782	9.1968826	12.4022210	15.5794915	18.7439581	21.9014852	25.0548222	28.2054329	31.3541694
7.1435310	10.5366699	13.7950636	17.0052902	20.1923130	23.3662797	26.5321431	29.6926210	32.8493338
8.3466059	11.8367185	15.1498701	18.3959570	21.6084483	24.8014922	27.9822017	31.1545724	34.3210315
9.5257014	13.1073637	16.4750776	19.7582766	22.9978725	26.2116599	29.4087899	32.5944981	35.7720140
10.6870259	14.3551563	17.7764338	21.0971208	24.3647017	27.6002808	30.8149050	34.0149892	37.2045403
11.8345302	15.5845519	19.0580584	22.4161248	25.7121058	28.9701175	32.2029641	35.4181720	38.6204917
12.9709087	16.7987406	20.3230213	23.7180843	27.0425856	30.3233960	33.5749494	36.8058163	40.0214542
14.0980935	18.0000979	21.5736808	25.0052035	28.3581549	31.6619408	34.9325100	38.1794134	41.4087796
15.2175251	19.1904478	22.8118947	26.2792554	29.6604629	32.9872688	36.2770346	39.5402338	42.7836305

C.2 Buckling of a Double Clamped Beam on an Elastic Foundation

In this section, the analytical solution for a double clamped beam on an elastic foundation will be derived. The derivation is based on the derivation given in the work of Rivetti and Neukirch [66]. Additional comments and figures are given when necessary.

The governing equation for a double clamped linear Euler-Bernoulli beam of length L on an elastic foundation without surface forces is given by:

$$\begin{aligned} EI\frac{\mathrm{d}^4 w}{\mathrm{d}x^4} + Sw = 0, \\ w(0) = w(L) = \frac{\mathrm{d}w}{\mathrm{d}x}(0) = \frac{\mathrm{d}w}{\mathrm{d}x}(L) = 0. \end{aligned} \tag{C.4}$$

Here, EI is the bending stiffness of the beam and $S = \rho g b$ is the foundation stiffness of the beam, optionally decomposed by a fluid density ρ, a gravitational acceleration g and the beam width b. Lastly, $w(x)$ denotes the vertical deflection of the beam. Note that the inertia contribution is neglected so that the problem is considered static. Since the beam is linear, stretching effects are limited and hence horizontal forces in the beam are constant. Applying a horizontal force P on the boundary adds a moment contribution in the beam, proportional to the curvature of the beam. The governing ordinary differential equation becomes:

$$\begin{aligned} EI\frac{\mathrm{d}^4 w}{\mathrm{d}x^4} + P\frac{\mathrm{d}^2 w}{\mathrm{d}x^2} + Sw = 0, \\ w(0) = w(L) = \frac{\mathrm{d}w}{\mathrm{d}x}(0) = \frac{\mathrm{d}w}{\mathrm{d}x}(L) = 0. \end{aligned} \tag{C.5}$$

This equation can be made non-dimensional for the applied axial force as well as the foundation stiffness. Let us introduce the non-dimensional parameters for the axial force and for the foundation stiffness, p and η, respectively [66]. Furthermore, the length coordinate is made dimensionless with the length of the beam.

$$p = \frac{PL^2}{EI}, \tag{C.6}$$

$$\eta = \frac{L}{L_{eh}} = \frac{L}{\left(\frac{EI}{S}\right)^{\frac{1}{4}}}. \tag{C.7}$$

Then, the non-dimensional equation from Equation (C.5) becomes:

$$\begin{aligned} \frac{\mathrm{d}^4 w}{\mathrm{d}x^4} + p\frac{\mathrm{d}^2 w}{\mathrm{d}x^2} + \eta^4 w = 0, \\ w(0) = w(1) = \frac{\mathrm{d}w}{\mathrm{d}x}(0) = \frac{\mathrm{d}w}{\mathrm{d}x}(1) = 0. \end{aligned} \tag{C.8}$$

Now, let us make the Ansatz that the solution is of the form $w = \exp(ikx)$. Then, the characteristic polynomial of the ODE in Equation (C.8) becomes:

$$k^4 - pk^2 + \eta^4 = 0.$$

The solutions for k are:

$$\pm k_+ = \pm\sqrt{\sqrt{\left(\frac{p}{2}\right)^2 - \eta^4} + \frac{p}{2}} \quad \text{and} \quad \pm k_- = \pm\sqrt{-\sqrt{\left(\frac{p}{2}\right)^2 - \eta^4} + \frac{p}{2}}. \tag{C.9}$$

From these relations, it follows that $k_+ k_- = \eta^2$ and $k_+^2 + k_-^2 = p$. Furthermore, the solution for w is:

$$w(x) = C_1 \sin\left(\frac{k_+ x}{L}\right) + C_2 \cos\left(\frac{k_+ x}{L}\right) + C_3 \sin\left(\frac{k_- x}{L}\right) + C_4 \cos\left(\frac{k_- x}{L}\right).$$

Substituting this in the boundary conditions of the end at $x/L = 0$ gives:

$$C_2 = -C_4 \quad \text{and} \quad k_+ C_1 = -C_3 k_-.$$

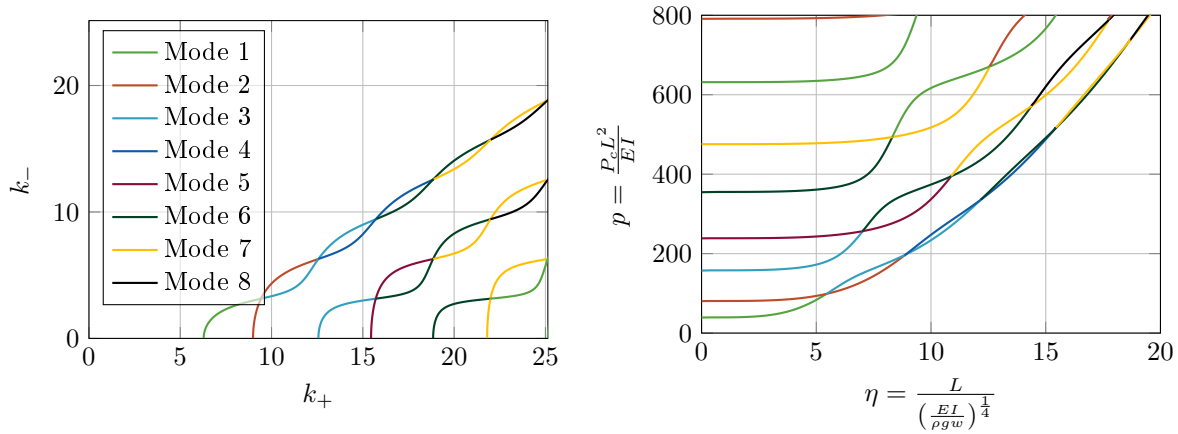

Figure C.1: Relations between k_+ and k_- and between the dimensionless buckling load p and stiffness ratio η.

So that,

$$w(x) = C_1 \sin\left(\frac{k_+ x}{L}\right) + C_2 \cos\left(\frac{k_+ x}{L}\right) - \frac{k_+}{k_-} C_1 \sin\left(\frac{k_- x}{L}\right) - C_2 \cos\left(\frac{k_- x}{L}\right).$$

The boundary conditions at the end $x/L = 1$ give, when re-arranging terms and multiplying the condition $w(1) = 0$ by k_-,

$$\begin{aligned} w(1) &= C_1 \left(k_- \sin\left(k_+\right) - k_+ \sin\left(k_-\right)\right) + C_2 \left(k_- \cos\left(k_+\right) - k_- \cos\left(k_-\right)\right) = 0, \\ \frac{\mathrm{d}w}{\mathrm{d}x}(1) &= \left(k_+ \cos\left(k_+\right) - k_+ \cos\left(k_-\right)\right) + C_2 \left(-k_+ \sin\left(k_+\right) - k_- \sin\left(k_-\right)\right) = 0. \end{aligned} \tag{C.10}$$

These equations can be written as a linear system in C_1, C_2 as follows [1]:

$$\begin{bmatrix} k_- \sin\left(k_+\right) - k_+ \sin\left(k_-\right) & k_- \cos\left(k_+\right) - k_- \cos\left(k_-\right), \\ k_+ \cos\left(k_+\right) - k_+ \cos\left(k_-\right) & k_- \sin\left(k_-\right) - k_+ \sin\left(k_+\right). \end{bmatrix}$$

Since solving the system would give the trivial solution, i.e. $C_1 = C_2 = 0$, the determinant of the system should be zero to find non-trivial solutions. That is:

$$2k_+k_- \left(\cos\left(k_+\right)\cos\left(k_-\right) - 1\right) + \left(k_+^2 + k_-^2\right)\sin\left(k_+\right)\sin\left(k_-\right) = 0. \tag{C.11}$$

From Equation (C.9) we know that $k_+, k_- \geq 0$. Since the first part of the determinant is always less than or equal to zero, it follows that

$$\left(k_+^2 + k_-^2\right)\sin\left(k_+\right)\sin\left(k_-\right) \geq 0.$$

Which is either for $k_+, k_- \in [2n\pi, (2n+1)\pi] \times [(2n+1)\pi, (2n+2)\pi]$ or for $k_+, k_- \in [(2n+1)\pi, (2n+2)\pi] \times [2n\pi, (2n+1)\pi]$ for $n \in \mathbb{N}$. Additionally, from Equation (C.10) it can be seen that the coefficients for the non-trivial solution should be equal to

$$\begin{aligned} C_1 &= -k_- \left(\cos\left(k_+\right) - \cos\left(k_-\right)\right), \\ C_2 &= k_- \sin\left(k_+\right) - k_+ \sin\left(k_-\right). \end{aligned}$$

In order to satisfy the boundary conditions. For Equation (C.11) there is no closed-form solution known. However, the roots of the equation can be found for different values of k_+ and k_- or, using Equation (C.9) for different combinations of p and η. The results are given in Figure C.1. As seen in this figure, an increase of the ratio η implies an increase of the critical nondimensional buckling load since for a fixed η, the first curves are higher.

[1] The bottom-left coefficient is different from the one given by [66] who give $k_+ \cos\left(k_+\right) - k_+ \cos\left(k_-\right)$ which is equal to zero. This is not in correspondence with the boundary conditions

C.3 Buckling of a Fully Restrained, Simply Supported Plate with Aspect Ratio 1

In this appendix, the reference solution for buckling of a plate that is restrained in horizontal directions on all edges is considered. The problem is depicted in Figure C.2. The formulations are based on the book of Hughes et al. [52].

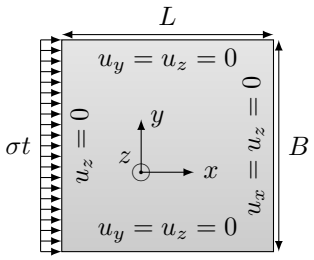

Figure C.2: Model for buckling of a simply supported plate which is restrained in the normal direction of each boundary.

In the sequel, the loads are defined as stresses on the side of the plate. Such that,

$$f = \sigma t$$

Where f is the line load and σ is a distributed load over the plate thickness t. According to Hughes et al. [52] the stress for which the plate will buckle with one wave in transverse direction, i.e. in width direction, is given by:

$$\sigma_{xE1} = \frac{\pi^2 D}{L^2 t}\left(m + \frac{1}{m}\left(\frac{L}{B}\right)\right)^2 = k\frac{\pi^2 D}{L^2 t}\left(\frac{t}{B}\right)^2. \tag{C.12}$$

Where $D = Et^3/12(1-\nu^2)$ is the flexural rigidity of the plate and m is the number of half-waves in length direction. The second equality is a usual form in literature, where

$$k = \left(\frac{mB}{L} + \frac{L}{mB}\right)^2. \tag{C.13}$$

In case of a bi-axially loaded plate, a load is also applied on the side of the plate (along length-direction). This load is referred to as σ_{yE}. In this case, Hughes et al. [52] presents a methodology to compute the critical buckling loads σ_{xE} and σ_{yE} for which buckling occurs.

For the in-plane constrained plate, consider Figure C.3. In this plot, the normalised ratios between the applied horizontal and vertical loads, i.e. $k_x = \sigma_{xE}/\sigma_{xE1}$ and $k_y = \sigma_{yE}/\sigma_{yE1}$ is plotted on the axes. Based on formulations of Hughes et al. [52], the lines for $m = 1$, $m = 2$ and $m = 3$ can be computed. The line with slope 0.3 represents the line for a constrained plate with Poisson's ratio equal to 0.3, since this ratio defines the compressive stresses in y direction (σ_{yE}) due to compressive stress in x direction (σ_{xE}). The intersection of this line with the lines of $m = 1$, $m = 2$ and $m = 3$ are now denoted as $(k_x, k_y)_1$, $(k_x, k_y)_2$ and $(k_x, k_y)_3$. The plot in Figure C.3 is valid for $L/B = 1$.

As an example, for a plate with given D, L and t, the value of σ_{xE1} can be computed. Since $k_x = \sigma_{xE}/\sigma_{xE1}$, the critical buckling loads for modes 1 up to 3 are obtained by

$$\sigma_{xE} = k_x \sigma_{xE1}. \tag{C.14}$$

And the loads σ_{yE} automatically follow via the Poisson's ratio. For the case discussed in Section 5.2, the

parameters are:

$$D = \frac{Et^3}{12(1-\nu^2)} = \frac{200 \cdot 10^9 \cdot 10^{-2}}{12(1-0.3^3)} = 18.315 \cdot 10^3\,[Nm],$$
$$L = 1\,[m],$$
$$m = 1,$$
$$k = 4,$$
$$\sigma_{xE1} = 72.3\,[MPa].$$

The critical stresses σ_c are therefore:

$$\text{Mode 1:} \quad \sigma_c = 0.769 \cdot \sigma_{xE1} = 55.62\,[MPa] \implies f_c = 0.5562\,[MN/m],$$
$$\text{Mode 2:} \quad \sigma_c = 1.453 \cdot \sigma_{xE1} = 105.09\,[MPa] \implies f_c = 1.0509\,[MN/m],$$
$$\text{Mode 3:} \quad \sigma_c = 2.688 \cdot \sigma_{xE1} = 194.37\,[MPa] \implies f_c = 1.9437\,[MN/m].$$

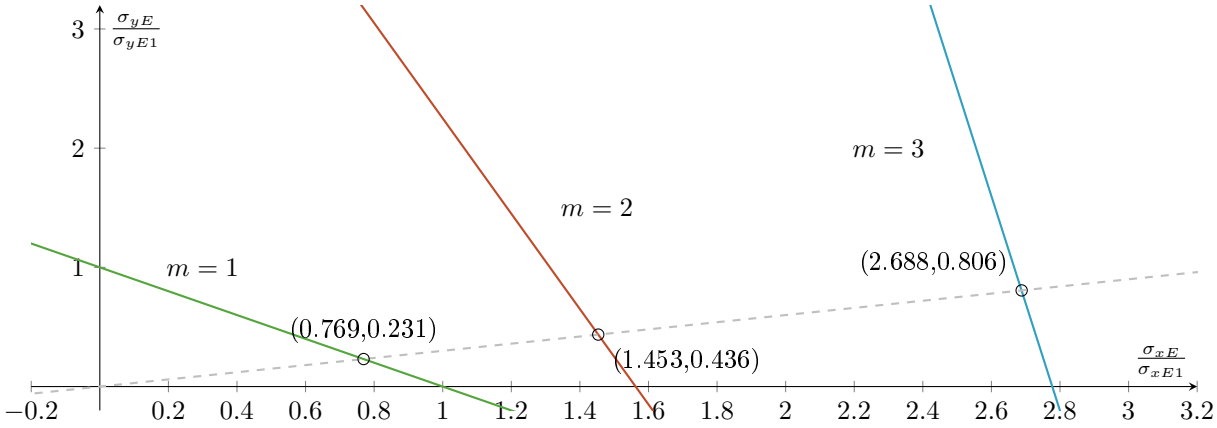

Figure C.3: Normalised buckling diagram for a bi-axially loaded plate with aspect ratio $\beta = L/B = 1.0$. The coloured lines represent buckling mode shapes with 1 up to 3 half-sines in loading direction (m) and 1 half-sine orthogonal to loading direction ($n = 1$). The intersections are marked for a line of $k_y = \nu k_x$, corresponding to a plate with $\nu = 0.3$ loaded in x direction. See Figure 5.9a for the geometric definitions.

D | Derivations for Temporal Analysis

For the Implicit Euler method, we solve

$$\frac{y^{t+\Delta t} - y^t}{\Delta t} = f(y^{t+\Delta t}, t + \Delta t)$$

Based on $\frac{\mathrm{d}y}{\mathrm{d}t} = y(x,t)$. The reduced order system of the equations of motion (see Section 4.6) is

$$\mathcal{F} = \begin{bmatrix} \mathcal{F}_1 \\ \mathcal{F}_2 \end{bmatrix} = \begin{bmatrix} \mathbf{u}^{t+\Delta t} - \mathbf{u}^t - \Delta t \mathbf{v}^{t+\Delta t} \\ \mathbf{v}^{t+\Delta t} - \mathbf{v}^t + \Delta t \mathrm{M}^{-1} \left(\mathbf{N}(\mathbf{u}^{t+\Delta t}) + \mathrm{C}\mathbf{v}^{t+\Delta t} - \mathbf{F}(t + \Delta t) \right) \end{bmatrix} = \mathbf{0} \tag{D.1}$$

Since

$$\begin{aligned} \frac{\mathbf{u}^{t+\Delta t} - \mathbf{u}^t}{\Delta t} &= \mathbf{v}^{t+\Delta t} \\ \mathrm{M}\frac{\mathbf{v}^{t+\Delta t} - \mathbf{v}^t}{\Delta t} + \mathrm{C}\mathbf{v}^{t+\Delta t} + \mathbf{N}(\mathbf{u}^{t+\Delta t}) &= \mathbf{F}(t + \Delta t) \end{aligned}$$

Here, $\mathcal{F}$ is the residual to be solved equal to the zero vector. Furthermore, all vectors on time $t + \Delta t$ are unknown and all on time t are known. $\mathbf{u}$ denotes displacements and $\mathbf{v}$ denotes velocities. M is the mass matrix, C the damping matrix and $\mathbf{N}(\mathbf{u})$ and $\mathbf{F}(t)$ the vectors of internal and external forces.

By the nonlinearity of the system, the vectors $\mathbf{u}^{t+\Delta t}$ and $\mathbf{v}^{t+\Delta t}$ are obtained iteratively using Newton's method. Thus, let $\mathbf{u}_{i+1}^{t+\Delta t} = \mathbf{u}_i^{t+\Delta t} + \Delta\mathbf{u}$ and $\mathbf{v}_{i+1}^{t+\Delta t} = \mathbf{v}_i^{t+\Delta t} + \Delta\mathbf{v}$. Furthermore, the Jacobian of Equation (D.1) is (taking derivatives w.r.t. the variables on $t + \Delta t$):

$$\mathrm{J}_{\mathcal{F}} = \begin{bmatrix} \frac{\partial \mathcal{F}_1}{\partial \mathbf{u}} & \frac{\partial \mathcal{F}_1}{\partial \mathbf{v}} \\ \frac{\partial \mathcal{F}_2}{\partial \mathbf{u}} & \frac{\partial \mathcal{F}_2}{\partial \mathbf{v}} \end{bmatrix} = \begin{bmatrix} \mathrm{I} & -\Delta t \mathrm{I} \\ \Delta t \mathrm{M}^{-1} K_T(\mathbf{u}) & \mathrm{I} - \Delta t \mathrm{M}^{-1} C \end{bmatrix} \tag{D.2}$$

And the residual is

$$\mathbf{R}_i(\mathbf{u}, \mathbf{v}, t + \Delta t) = \begin{bmatrix} \mathbf{u}_i^{t+\Delta t} - \mathbf{u}^t - \Delta t \mathbf{v}_i^{t+\Delta t} \\ \mathbf{v}_i^{t+\Delta t} - \mathbf{v}^t + \Delta t \mathrm{M}^{-1} \left(\mathbf{N}(\mathbf{u}_i^{t+\Delta t}) + \mathrm{C}\mathbf{v}^{t+\Delta t} - \mathbf{F}_i(t + \Delta t) \right) \end{bmatrix}$$

Note that here, $\mathbf{N}(\mathbf{u}_i^{t+\Delta t}) - \mathbf{F}_i(t + \Delta t)$ is the residual of internal and external forces on time $t + \Delta t$. Using the residual and the Jacobian, the displacements and velocities at time $t + \Delta t$ can be obtained using

$$\begin{aligned} \mathrm{J}_{\mathcal{F}} \Delta\mathbf{y} &= -R(\mathbf{y}_i, t + \Delta t) \\ \text{and } \mathbf{y}_{i+1}^{t+\Delta t} &= \mathbf{y}_i^{t+\Delta t} + \Delta\mathbf{y} \\ \mathbf{y} &= [\mathbf{u}, \mathbf{v}] \end{aligned} \tag{D.3}$$

E | Wrinkling Results

E.1 Stretched Thin Sheet

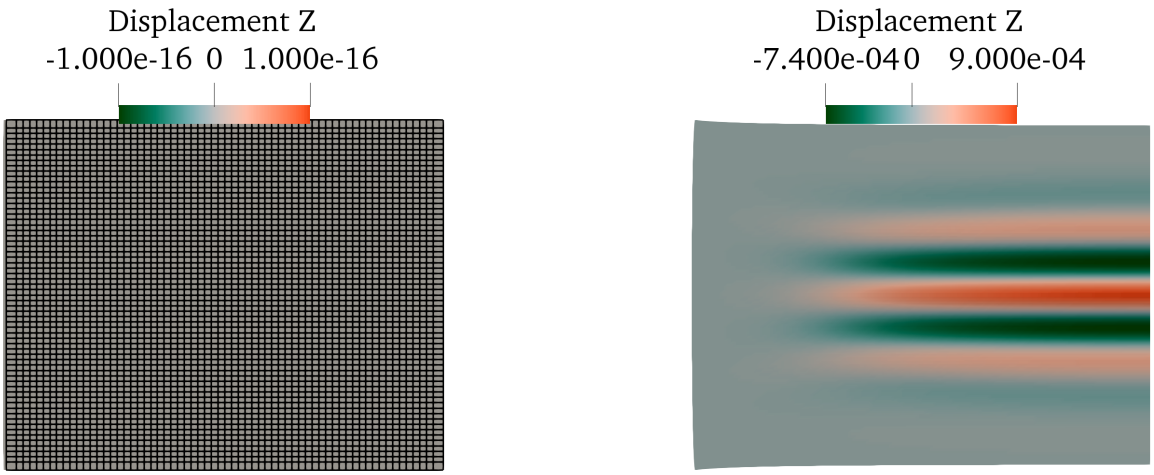

(a) $\varepsilon = 0.0\%$ **(b)** $\varepsilon = 4.9\%$

Figure E.1: Shapes of the sheet for different values of the end-point strain.

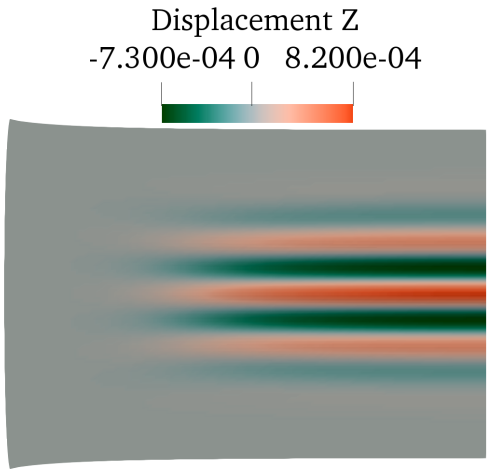

(a) $\varepsilon = 10.2\%$

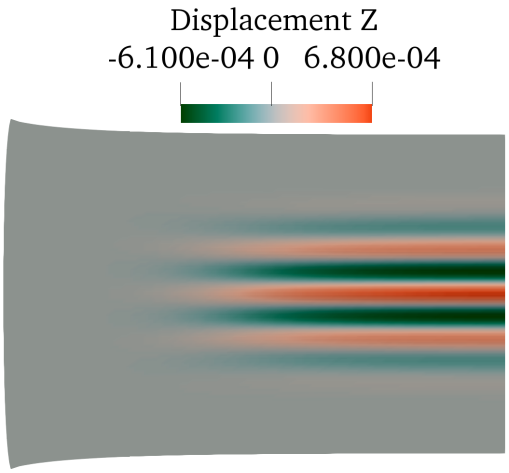

(b) $\varepsilon = 14.8\%$

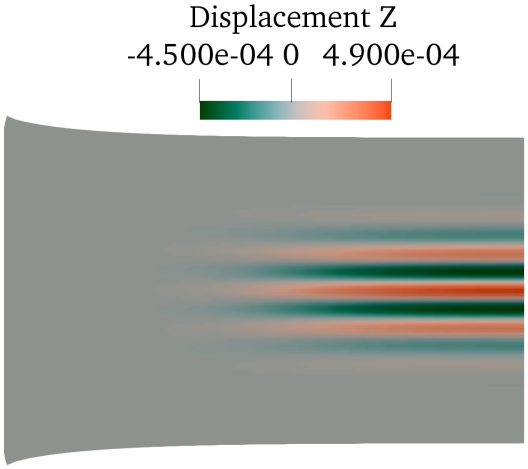

(c) $\varepsilon = 20.4\%$

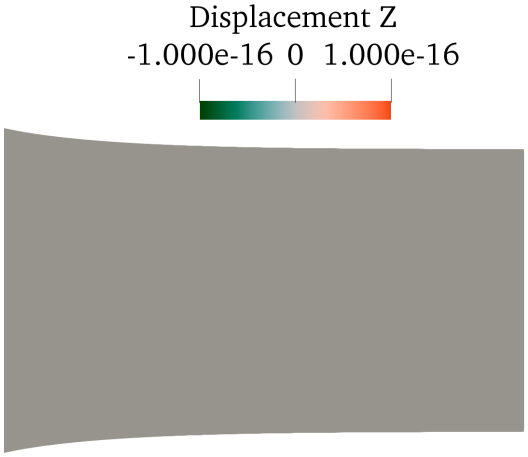

(d) $\varepsilon = 29.4\%$

Figure E.2: Shapes of the sheet for different values of the end-point strain.

E.2 Large Thin Sheet Subject to Traction

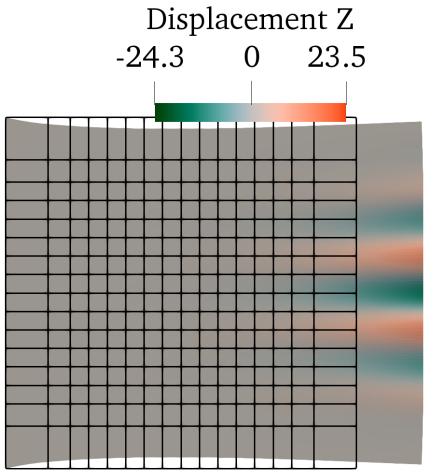

(a) $\varepsilon = 19.15\%$

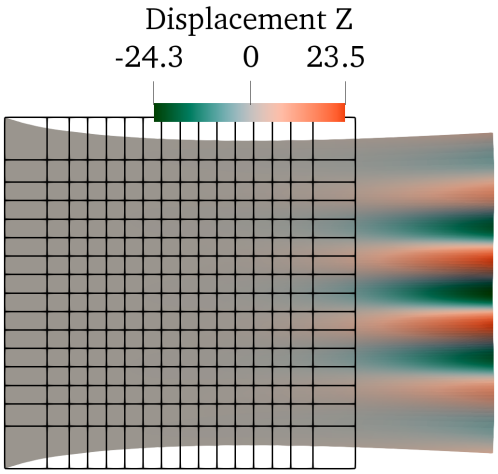

(b) $\varepsilon = 39.3\%$

Figure E.3: Base case.

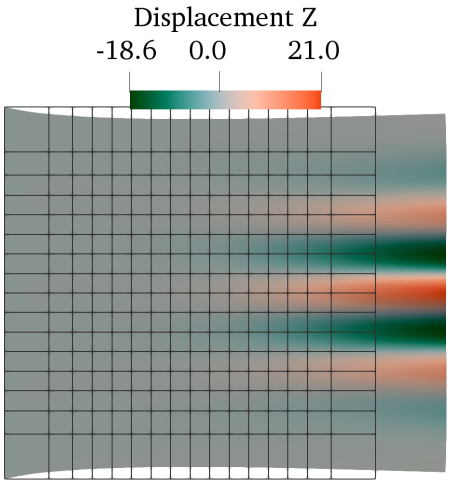

(a) $K = 10^3$; $\varepsilon = 18.9\%$

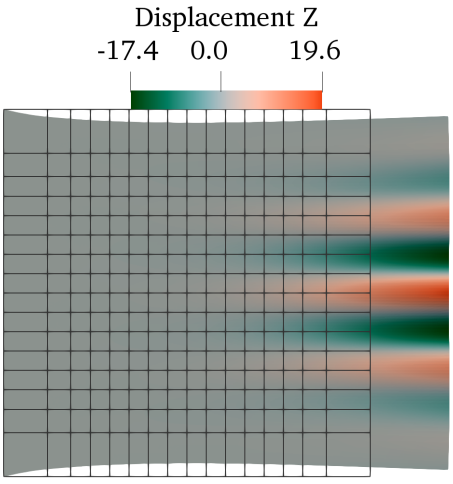

(b) $5 \cdot 10^3$; $\varepsilon = 21.4\%$

Figure E.4: Varying fluid foundation stiffness. Unit $[kgm]$.

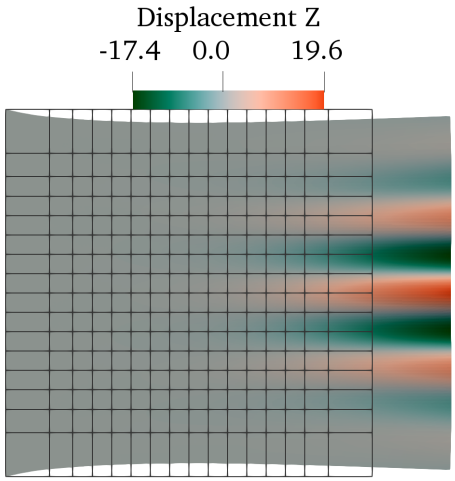

(a) 1.0; $\varepsilon = 21.4\%$

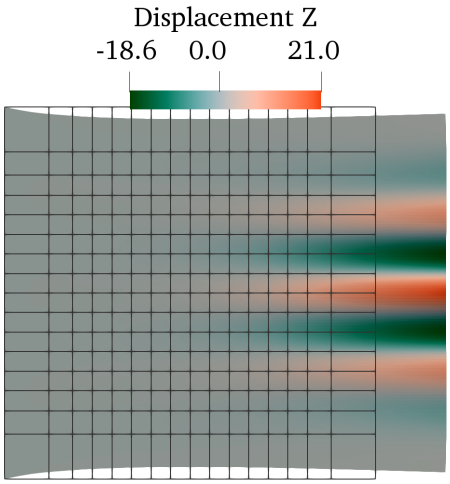

(b) 5.0; $\varepsilon = 18.9\%$

Figure E.5: Varying Young's modulus. Unit $[GPa]$.

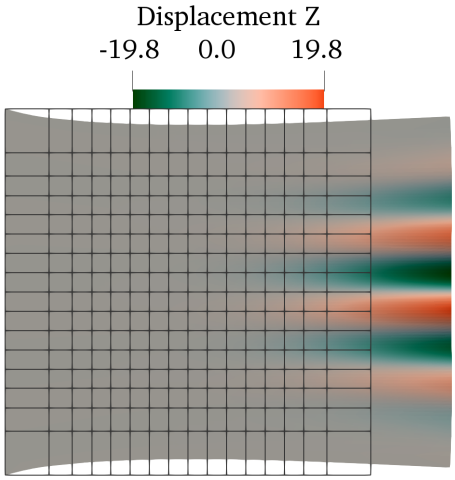

(a) 0.35; $\varepsilon = 22.0\%$

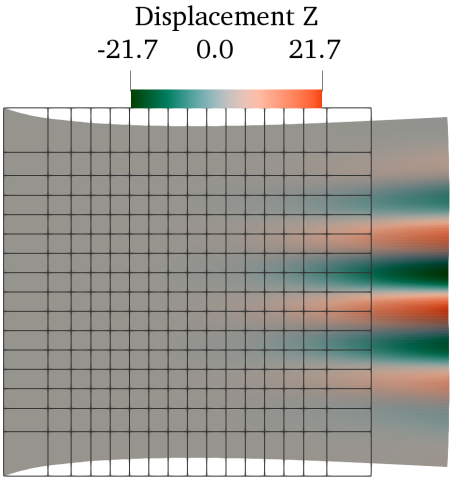

(b) 0.40; $\varepsilon = 21.1\%$

Figure E.6: Varying Poisson's ratio. Dimensionless.

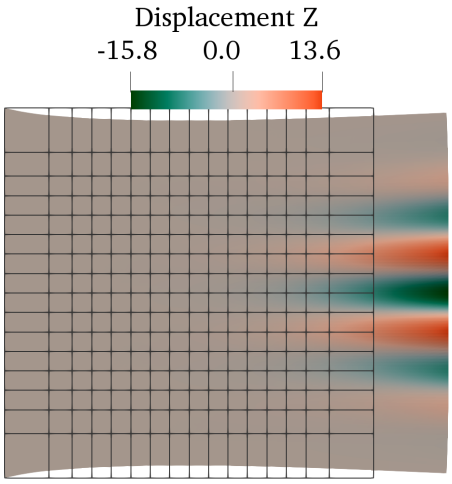

(a) 6.3; $\varepsilon = 20.2\%$

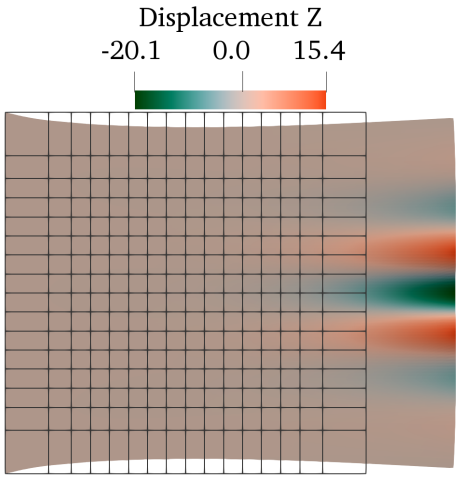

(b) 10.8; $\varepsilon = 24.8\%$

Figure E.7: Varying thickness. Unit $[m]$

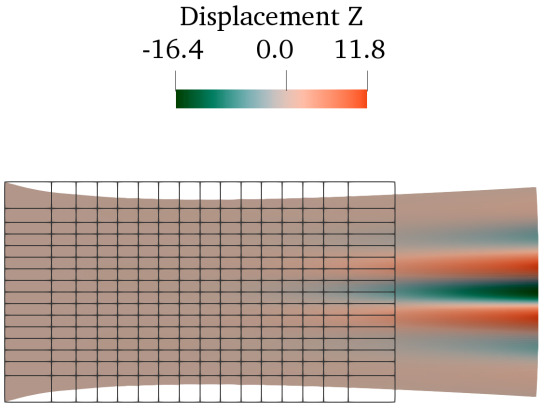

(a) 10^3; $\varepsilon = 36.7\%$

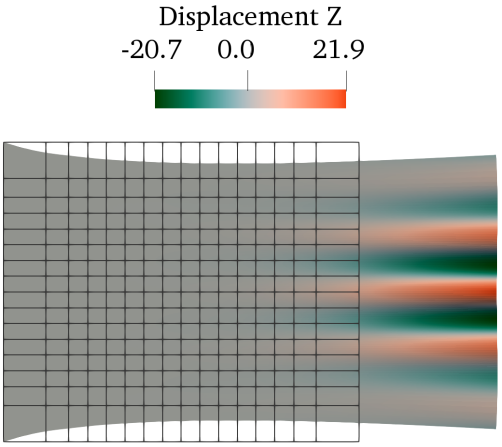

(b) 10^3; $\varepsilon = 38.8\%$

Figure E.8: Varying size.